



# Visual Computing Methods for Radiotherapy Planning

DISSERTATION

zur Erlangung des akademischen Grades

**Doktor der Technischen Wissenschaften**

eingereicht von

**Dipl.-Inf. Matthias Wilfried Schlachter**

Matrikelnummer 01428822

an der Fakultät für Informatik  
der Technischen Universität Wien

Betreuung: Univ.Prof. Dipl.Ing. Dr.techn. Eduard Gröller  
Zweitbetreuung: Dipl.-Math.in Dr. Katja Bühler

Diese Dissertation haben begutachtet:

---

Wolfgang Birkfellner

---

Bernhard Preim

Wien, 5. September 2022

---

Matthias Wilfried Schlachter



# Visual Computing Methods for Radiotherapy Planning

DISSERTATION

submitted in partial fulfillment of the requirements for the degree of

**Doktor der Technischen Wissenschaften**

by

**Dipl.-Inf. Matthias Wilfried Schlachter**

Registration Number 01428822

to the Faculty of Informatics

at the TU Wien

Advisor: Univ.Prof. Dipl.Ing. Dr.techn. Eduard Gröller

Second advisor: Dipl.-Math.in Dr. Katja Bühler

The dissertation has been reviewed by:

---

Wolfgang Birkfellner

---

Bernhard Preim

Vienna, 5<sup>th</sup> September, 2022

---

Matthias Wilfried Schlachter



# Erklärung zur Verfassung der Arbeit

Dipl.-Inf. Matthias Wilfried Schlachter

Hiermit erkläre ich, dass ich diese Arbeit selbständig verfasst habe, dass ich die verwendeten Quellen und Hilfsmittel vollständig angegeben habe und dass ich die Stellen der Arbeit – einschließlich Tabellen, Karten und Abbildungen –, die anderen Werken oder dem Internet im Wortlaut oder dem Sinn nach entnommen sind, auf jeden Fall unter Angabe der Quelle als Entlehnung kenntlich gemacht habe.

Wien, 5. September 2022

---

Matthias Wilfried Schlachter



For Hana & Mayumi





# Acknowledgements

This thesis would not have been possible without the support of many people. First and foremost, I would like to thank my supervisors. I wish to thank Katja Bühler from the VRVis Research Center. She supervised the projects, and her involvement in conceiving the methods, writing, providing guidance and advice ultimately led to this thesis. I would like to thank my thesis supervisor Meister Eduard Gröller from TU Wien for his great support and helpful discussions. I highly appreciate their encouraging feedback and friendly advice from the beginning until the finishing of this thesis.

Furthermore, I want to thank Tobias Fechter. His collaboration represented a cornerstone for many papers, which would not have been possible without his support. A special thank goes also to Miro Jurisic and Renata Raidou for their close involvement leading to papers presented in this thesis, and to Miguel Nunes for all his support and discussions during my time at the VRVis research center. Moreover, I would like to thank all my co-authors S. Adebahr, T. Schimek-Jasch, U. Nestle, O. Oehlke, W. Birkfellner, L. P. Muren, B. Preim, P. M. Putora, D. Camenisch, and S. Peters without whom it would not have been possible to complete my research in its current form.

For the finalization of this thesis, I would especially like to thank Henrik Skibbe for his reviews, corrections, and suggestions. Furthermore, I would like to thank all my current and former colleagues at the VRVis Research Center, but also all the other friends I found there who gave me valuable input and emotional support when it was necessary. Most notably, I wish to thank Michi Schwärzler, Maria Wimmer, Harald Steinlechner, Hendrik Schulze, Martin Trapp, Andreas Grünauer, David Major, and Dimitrios Lenis.

Finally, I want to thank my family for supporting me throughout the creation of this thesis. The biggest thanks belong to my lovely wife, who always supported me over the years. And more recently, my daughter, who supported me in her own way by giving me the motivation I needed to finish this project.

In parts, this work is part of the SUMMER Marie Curie Research Training Network (PITN-GA-2011-290148), which is funded by the 7th Framework Programme of the European Commission (FP7-PEOPLE-2011-ITN). In parts, this work was enabled by the Competence Centre VRVis. VRVis is funded by BMVIT, BMWFW, Styria, SFG, and Vienna Business Agency in the scope of COMET - Competence Centers for Excellent Technologies (854174), which is managed by FFG.



# Kurzfassung

Die Radiotherapie (RT) ist eine der wichtigsten Methoden zur Heilung von Krebs. Es handelt sich um einen komplexen und risikoreichen Behandlungsansatz, der eine präzise Planung vor der Verabreichung der Behandlung erfordert. Visual Computing (VC) ist eine grundlegende Komponente der RT-Planung und bietet Lösungen für alle Teile des Prozesses — von der Bildgebung bis zur Verabreichung.

VC nutzt Elemente der Computergrafik und der Bildverarbeitung, um aussagekräftige, interaktive visuelle Darstellungen medizinischer Daten zu erstellen, und hat sich zu einem einflussreichen Forschungsgebiet für viele fortschrittliche Anwendungen wie die Radioonkologie entwickelt. Interaktive VC-Ansätze stellen eine neue Möglichkeit dar, sachkundige Experten und ihre kognitiven Fähigkeiten in explorative Prozesse einzubinden, die mit rein automatisierten Methoden nicht durchgeführt werden können.

Trotz der bedeutenden technologischen Fortschritte der RT in den letzten Jahrzehnten, gibt es noch viele Herausforderungen zu bewältigen. Bei der RT-Planung müssen Mediziner eine Vielzahl von Informationsquellen für die anatomische und funktionelle Zielvolumenabgrenzung berücksichtigen. Die Validierung und Überprüfung der definierten Zielvolumina und des daraus resultierenden RT-Plans ist eine komplexe Aufgabe. Dies gilt insbesondere dann, wenn sich die Zielgebiete bewegen, wie dies oft bei Tumoren im Brustkorb und im Oberbauch der Fall ist. Ein- bzw. Ausatmung ist hier beispielsweise ursächlich für die Bewegung. Der Umgang mit Unsicherheiten bei der RT-Planung und Verabreichung, insbesondere bei Tumorbewegungen, ist von entscheidender Bedeutung für die Verbesserung der Effizienz der Behandlung und die Minimierung von Nebenwirkungen.

Diese Dissertation leistet einen Beitrag zum Umgang mit RT-Planungsunsicherheiten, indem sie neuartige VC-Methoden vorschlägt. Die Quantifizierung und Visualisierung dieser Arten von Unsicherheiten wird ein wesentlicher Bestandteil der vorgestellten Methoden sein und zielt darauf ab, den RT-Arbeitsablauf in Bezug auf Abgrenzungs- und Registrierungsgenauigkeit, Randdefinitionen und den Einfluss dieser Unsicherheiten auf das dosimetrische Ergebnis zu verbessern. Die in dieser Arbeit vorgestellten Veröffentlichungen befassen sich mit Schlüsselaspekten des RT-Behandlungsplanungsprozesses, bei denen menschliche Interaktion erforderlich ist und VC das Potenzial hat, das Behandlungsergebnis zu verbessern.

Zunächst werden die wichtigsten Anforderungen an ein multimodales Visualisierungs-Framework definiert und implementiert, um das Bewegungsmanagement durch Einbezie-

hung von 4D-Bildinformationen zu verbessern. Das Visualisierungs-Framework wurde entwickelt, um Ärzten die notwendigen visuellen Informationen zur Verfügung zu stellen, mit dem Ziel, die Genauigkeit der Tumorzielabgrenzungen und die Effizienz der RT-Planauswertung zu verbessern.

Darüber hinaus wird in dieser Arbeit das Thema der Genauigkeit der deformierbaren Bildregistrierung (DIR) behandelt. DIR hat das Potenzial, die moderne RT in vielerlei Hinsicht zu verbessern, einschließlich der Volumendefinition, der Behandlungsplanung und der bildgesteuerten adaptiven RT. Die Messung der DIR-Genauigkeit ist jedoch ohne bekannte Validierungsdaten (Ground Truth) schwierig, aber vor der Integration in den RT-Arbeitsablauf notwendig. Die visuelle Bewertung ist ein wichtiger Schritt zur klinischen Akzeptanz. Es wird ein Visualisierungs-Framework vorgeschlagen, das die Erkundung und Bewertung der DIR-Genauigkeit unterstützt. Es bietet verschiedene Interaktions- und Visualisierungsfunktionen für die Erkundung von Kandidatenregionen, um den Prozess der visuellen Beurteilung zu vereinfachen und dadurch die adäquate Verwendung in der RT-Planung zu verbessern und zu fördern.

Abschließend wird das Thema der Schonung von gesundem Gewebe betrachtet. Dies geschieht unter Zuhilfenahme eines neuartigen Visualisierungsansatzes zur interaktiven Erkundung von RT-Plänen. Dabei sollen Regionen des gesunden Gewebes, die weiter geschont werden können, identifiziert werden, ohne die für die Tumorziele definierten Behandlungsansätze zu gefährden. Zu diesem Zweck werden Überlappungsvolumina von Tumorzielen und gesunden Organen in den RT-Plan Evaluierungsprozess einbezogen und das ursprüngliche Visualisierungs-Framework wird um quantitative Ansichten erweitert. Dadurch können quantitative Eigenschaften der Überlappungsvolumina interaktiv erkundet werden, um kritische Regionen zu identifizieren und die Visualisierung für eine detaillierte Überprüfung der Kandidaten zu steuern.

Alle Ansätze wurden in Nutzerstudien zu den einzelnen Visualisierungen und deren Zusammenspiel hinsichtlich Hilfestellung, Verständlichkeit, Intuitivität, Entscheidungsfindung und Schnelligkeit evaluiert und, falls vorhanden, anhand von Ground-Truth-Daten auf ihre Validität hin überprüft.

# Abstract

Radiotherapy (RT) is one of the major curative approaches for cancer. It is a complex and risky treatment approach, which requires precise planning, prior to the administration of the treatment. Visual Computing (VC) is a fundamental component of RT planning, providing solutions in all parts of the process — from imaging to delivery.

VC employs elements from computer graphics and image processing to create meaningful, interactive visual representations of medical data, and it has become an influential field of research for many advanced applications like radiation oncology. Interactive VC approaches represent a new opportunity to integrate knowledgeable experts and their cognitive abilities in exploratory processes, which cannot be conducted by solely automatized methods.

Despite the significant technological advancements of RT over the last decades, there are still many challenges to address. In RT planning medical doctors need to consider a variety of information sources for anatomical and functional target volume delineation. The validation and inspection of the defined target volumes and the resulting RT plan is a complex task, especially in the presence of moving target areas as it is the case for tumors of the chest and the upper abdomen, for instance, caused by breathing motion. Handling RT planning and delivery-related uncertainties, especially in the presence of tumor motion, is essential to improve the efficiency of the treatment and the minimization of side effects.

This dissertation contributes to the handling of RT planning related uncertainties by proposing novel VC methods. Quantification and visualization of these types of uncertainties will be an essential part of the presented methods, and aims at improving the RT workflow in terms of delineation and registration accuracy, margin definitions and the influence of these uncertainties onto the dosimetric outcome. The publications presented in this thesis address key aspects of the RT treatment planning process, where human interaction is required, and VC has the potential to improve the treatment outcome.

First, major requirements for a multi-modal visualization framework are defined and implemented with the aim to improve motion management by including 4D image information. The visualization framework was designed to provide medical doctors with the necessary visual information to improve the accuracy of tumor target delineations and the efficiency of RT plan evaluation.

Furthermore, the topic of deformable image registration (DIR) accuracy is addressed in this thesis. DIR has the potential to improve modern RT in many aspects, including volume definition, treatment planning, and image-guided adaptive RT. However, measuring DIR accuracy is difficult without known ground truth, but necessary before the integration in the RT workflow. Visual assessment is an important step towards clinical acceptance. A visualization framework is proposed, which supports the exploration and the assessment of DIR accuracy. It offers different interaction and visualization features for exploration of candidate regions to simplify the process of visual assessment, and thereby improve and contribute to its adequate use in RT planning.

Finally, the topic of healthy tissue sparing is addressed with a novel visualization approach to interactively explore RT plans, and identify regions of healthy tissue, which can be spared further without compromising the treatment goals defined for tumor targets. For this, overlap volumes of tumor targets and healthy organs are included in the RT plan evaluation process, and the initial visualization framework is extended with quantitative views. This enables quantitative properties of the overlap volumes to be interactively explored, to identify critical regions and to steer the visualization for a detailed inspection of candidates.

All approaches were evaluated in user studies covering the individual visualizations and their interactions regarding helpfulness, comprehensibility, intuitiveness, decision-making and speed, and if available using ground truth data to prove their validity.

# Contents

<b>Kurzfassung</b>	<b>xi</b>
<b>Abstract</b>	<b>xiii</b>
<b>Contents</b>	<b>xv</b>
<b>1 Motivation and Overview</b>	<b>1</b>
1.1 Open Challenges and Thesis Goals . . . . .	2
1.2 Contributions and Thesis Structure . . . . .	10
<b>2 Background and Related Work</b>	<b>15</b>
2.1 Radiotherapy Planning . . . . .	17
2.2 Visual Computing for Radiotherapy Planning . . . . .	23
2.3 Related Work in Visual Computing for RT . . . . .	32
<b>3 A Multi-Modal Visualization Framework for Radiotherapy Planning</b>	<b>43</b>
3.1 Introduction . . . . .	44
3.2 Related Work . . . . .	45
3.3 Data Sets . . . . .	45
3.4 3D Multi-Modal Rendering Core . . . . .	46
3.5 Implementation and Integration . . . . .	47
3.6 Results and Discussion . . . . .	48
3.7 Conclusion and Future Work . . . . .	51
<b>4 4D Multi-Modal Visualization in Radiotherapy Planning</b>	<b>53</b>
4.1 Introduction . . . . .	54
4.2 Methods and Materials . . . . .	56
4.3 Evaluation . . . . .	62
4.4 Results . . . . .	66
4.5 Discussion . . . . .	68
4.6 Conclusion . . . . .	72
<b>5 Visualization of Deformable Image Registration Quality</b>	<b>73</b>
5.1 Introduction . . . . .	74
	xv

5.2	Related Work . . . . .	75
5.3	Visualization System . . . . .	76
5.4	Evaluation . . . . .	85
5.5	Results . . . . .	87
5.6	Discussion . . . . .	89
5.7	Conclusion . . . . .	94
<b>6</b>	<b>Exploration of Overlap Volumes for Radiotherapy Plan Evaluation</b>	<b>95</b>
6.1	Introduction . . . . .	96
6.2	Related Work . . . . .	97
6.3	Data, RT Plan Metrics, and Definitions . . . . .	99
6.4	Visualization: Views . . . . .	101
6.5	Data Exploration and User Interaction . . . . .	108
6.6	Proposed Workflow for RT Plan Evaluation . . . . .	110
6.7	Evaluation and Results . . . . .	112
6.8	Discussion . . . . .	119
6.9	Conclusion and Outlook . . . . .	120
<b>7</b>	<b>Conclusions</b>	<b>121</b>
7.1	Summary of Scientific Contributions . . . . .	121
7.2	Impact on the Field of RT Planning . . . . .	122
7.3	Future Directions . . . . .	123
<b>A</b>	<b>Supplementary Material: Chapter 4</b>	<b>127</b>
<b>B</b>	<b>Supplementary Material: Chapter 5</b>	<b>131</b>
	<b>List of Figures</b>	<b>149</b>
	<b>List of Tables</b>	<b>155</b>
	<b>Bibliography</b>	<b>157</b>
	<b>Curriculum Vitae</b>	<b>181</b>



# Motivation and Overview

Cancer is the second leading cause of death worldwide, and according to the World Health Organization (WHO), 18.1 million people were globally diagnosed with cancer in 2018 [Wor18], with cancer incidence expected to rise in the next decade [SW14]. Radiotherapy, or radiation therapy (RT), is a major curative treatment approach for cancer [DJFB05, ZM16]. Often, it complements surgery, chemotherapy, hormonotherapy, immunotherapy, or is administered in a combination of those [WL15].

Visual Computing (VC) employs elements from computer graphics and image processing to create meaningful, interactive visual representations of medical data, and it has become an influential field of research for many advanced applications like radiation oncology. VC is a fundamental component of RT planning, providing solutions in all parts of the process — from imaging to delivery.

RT is based on the use of ionizing rays, such as photon, electron, or proton radiation, to destroy malignant cells. Prior to dose administration, the treatment must be carefully planned to ensure adequate irradiation of the tumor target and to spare the surrounding healthy tissues, as much as possible.

The planning follows a workflow, which is depicted in Fig. 1.1. After the initial diagnosis and referral, the essential steps in radiation treatment planning [McS11] are image acquisition, the delineation of the relevant target regions, the treatment plan design including dose calculation and the assessment of the computed treatment plan before the actual treatment of the patient. Image-guided adaptive RT (IGART) is a relatively new concept, which tries to account for various types of anatomical changes during the course of delivery providing a more personalized treatment.

The administered radiation dose is measured in Grays (Gy), and varies depending on the type and stage of the cancer or the intent of the treatment. The final prescribed radiation dose will not be administered all at once. Instead, fractionation [THM<sup>+</sup>13, WL15] is used in most treatments, where the total dose is delivered in smaller fractions allowing

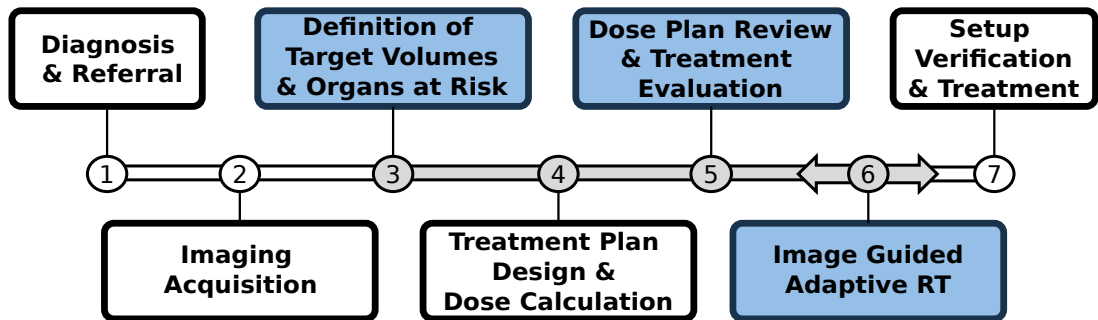


Figure 1.1: The steps of the workflow of RT planning, as adapted from the book of Washington and Leaver [WL15]. Most workflow steps comprise sub-steps [SRM<sup>+</sup>19]. The steps for which visual computing plays an important role are denoted with blue squares.

normal cells to recover and to prevent the repair of tumor cells. Tumors are treated with higher radiation doses, while adjacent healthy organ tissues must receive lower doses, to minimize the side effects of radiation. For instance, there is a high risk of tissue damage leading eventually to secondary cancer, and planning is more important than in any other kind of medical treatment [WL15].

Therefore, precise delineation of the target tumor and all adjacent organs at risk (OARs) is necessary. Depending on the type and location of the tumor, images are acquired using different image modalities such as computed tomography (CT), positron emission tomography (PET), 4D-PET/CT, magnetic resonance imaging (MRI), and are used for the delineation of the target volumes and the surrounding organs. Furthermore, dose calculation through simulation is carried out, in order to assess whether a sufficient dose to destroy the tumor is achieved, while maintaining tolerable doses to the OARs.

This risky and complex nature of RT treatment make it a special field of application within visual computing (VC), as it requires rather sophisticated combinations of a wide range of VC techniques. Furthermore, RT planning steps are often based on image information only, making visualization vital in multiple stages of the planning workflow. Additionally, RT planning involves a multitude of users and data, i.e., developing novel VC methods to support RT planning and also RT research requires interdisciplinary strategies integrating the whole VC portfolio from data, image, and information fusion to interaction, exploration, and visual analytics [SRM<sup>+</sup>19].

## 1.1 Open Challenges and Thesis Goals

The overall goal of this dissertation is to contribute to improving aspects of the RT planning workflow, and therefore to improve the treatment outcome of the patient, by proposing novel visual computing methods. Therefore, an important step is to develop

methods, which address — implicitly or explicitly — various types of uncertainty sources, for instance, coming from segmentation, deformable registration, and breathing motion.

Quantification and visualization of these types of uncertainties will be an essential part of the proposed methods, and aims at improving the radiotherapy workflow in terms of delineation and registration accuracy, margin definitions, and the influence of these uncertainties onto the dosimetric outcome.

The high-level goals can be summarized as follows.

- **Target Volume Definition & RT Plan Evaluation:** Improve the accuracy of tumor target delineations and the efficiency of RT plan evaluation by developing a novel framework for the fusion of multi-modality image information. Contribute to motion management by improving the use of 4D image information.
- **Deformable Image Registration:** Develop new VC concepts for including information about local registration errors, and thereby improve and contribute to its adequate use in RT planning. This includes minimizing additional uncertainties introduced by registration errors, and the use of deformable image registration for motion modelling and in adaptive treatment strategies.
- **Healthy Tissue Sparing:** Improve the treatment plan evaluation process by developing a novel approach to interactively explore RT plans, and identify regions of healthy tissue, which can be spared further without compromising the treatment goals defined for tumor targets.
- **Handling of Uncertainties & Motion Management:** Improve and contribute to the handling of RT planning related uncertainties, especially in the presence of moving targets, by addressing the aforementioned goals.

### 1.1.1 Open Challenges in the Research Field of Radiotherapy

In RT planning, uncertainty is present at all steps of the planning workflow (see Fig. 1.1), and its management is essential for reducing risks and a successful treatment outcome. All involved sources of uncertainty (segmentation, registration, breathing motion) have direct impact on the outcome of the patients' treatment.

An important concept within RT is the use of *Target Volumes*, developed by the *International Commission on Radiation Units & Measurements (ICRU)* [BDK<sup>+</sup>07, GLC<sup>+</sup>04]. Handling of different types of uncertainty is implicitly encoded in these volumes, for instance, via margin volumes. These margin volumes are designed to compensate some types of uncertainty stemming, e.g., from tumor motion or setup errors.

These volumes form the basis for the design of the plan, i.e., prescribing dose values and consecutively the dose calculation (see Step 4 in Fig. 1.1). However, the use of these volumes ultimately leads to another challenge in treatment plan evaluation. Overlaps of targets and OARs might lead to conflicting goals. On the one hand, the target needs to

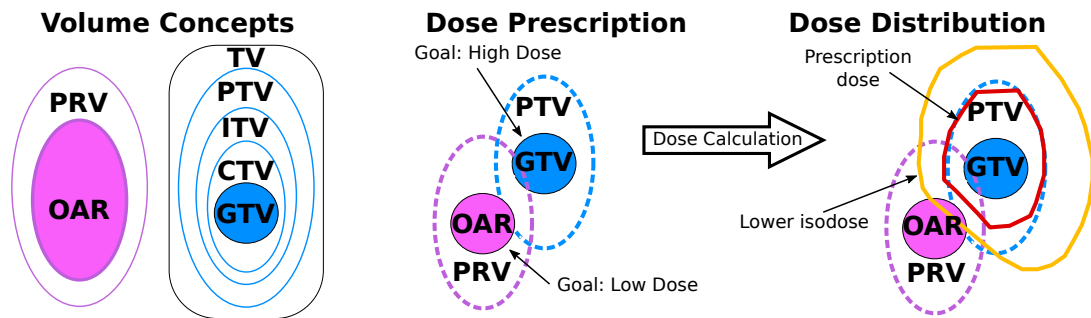


Figure 1.2: Volume concepts used in RT planning. The Gross Tumor Volume (GTV), Clinical Target Volume (CTV), Internal Target Volume (ITV), and Planning Target Volume (PTV), as well as the Organ at Risk (OAR) and Planning Organ at Risk Volume (PRV) are denoted. The Treated Volume (TV) is implicitly defined (by a dose value) after dose calculation. The PTV and ITV account for patient setup errors and other sources of inaccuracy. Overlapping volumes can have an impact on the dose calculation, and might lead to insufficient PTV coverage or undesired dose levels for the OAR.

be sufficiently irradiated, on the other hand, healthy tissue needs to be spared to avoid side effects. Finding a suitable trade-off for the best treatment outcome, represents a real challenge for decision makers.

### Handling of Uncertainties using Volume Concepts

For a better understanding of the underlying challenges, the most important volume concepts and their relation to the various types of uncertainty will be introduced in the following. A schematic overview of these volumes can be found in Fig. 1.2 (left).

The volume that contains the visible, *macroscopic* part of the tumor (within the limits of the employed imaging technique) is called the *Gross Tumor Volume (GTV)*. Images acquired using different image modalities are used for its delineation. For instance, for lung cancer the use of PET/CT is common as depicted in Fig. 1.3. Image registration is involved for mapping the various types of image information into the same coordinate space as the planning CT (pCT). This is necessary, as the pCT is later used for the dose calculation, but introduces an additional source of uncertainty as the underlying algorithm might introduce additional errors.

The *Clinical Target Volume (CTV)* contains the GTV and encompasses *microscopic* extensions into healthy tissues, that are not visible [BDK<sup>+</sup>07, GLC<sup>+</sup>04]. For some types of cancer, including glioblastoma multiforme, existing dose targeting strategies are insufficient, and the use of additional functional imaging modalities has gained interest, such as MR Spectroscopy Imaging (MRSI), to identify regions of high tumor burden or radio-resistance also known as *Biological Target Volumes (BTV)* [LHL<sup>+</sup>00]. The definition of the BTV requires insight into tumor characteristics. With the use of (user defined) metabolite relations derived from MRSI and its fusion with other multi-modal

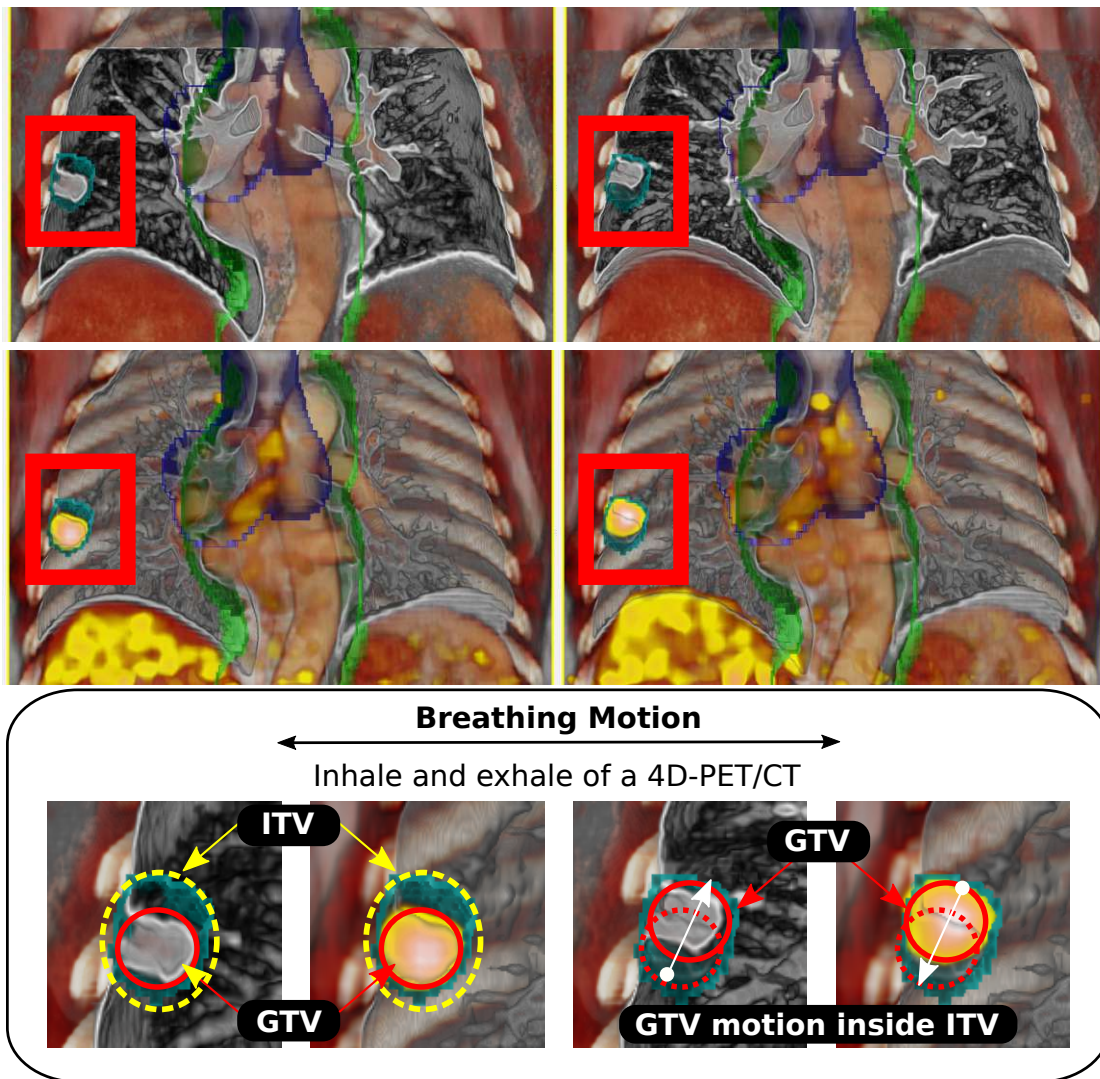


Figure 1.3: Fusion of the planning CT with a 4D-PET/CT (top: 4D-CT, bottom: 4D-PET). The structure encompassing the tumor was defined by using 4D imaging. The images on the left and the right showing the maximum inhale and exhale position during the patients breathing cycle.

image data, it is possible to support BTV delineation [NRS<sup>+</sup>14], which can then be targeted with radiation dose boosts.

The *Internal Target Volume (ITV)* addresses uncertainties due to organ motion [JYW99, RSO<sup>+</sup>96], and is only an intermediate volume that has to be expanded by margins for setup errors [SH02]. The ITV concept is not always required, but is common for lung cancer (see Fig. 1.3), where breathing motion has to be considered [JHP<sup>+</sup>15].

The *Planning Target Volume (PTV)* is the volume encompassing the CTV (and the ITV if employed), which takes into account the fact that the CTV and the involved patient anatomy might vary in position, shape, and size within or between fractions. It accounts specifically for uncertainties, such as patient setup errors [SH02] to ensure that the CTV will receive the prescribed and planned dose, by adding margins to the CTV (or ITV) [Ben08, JYW99, MvM02].

*Organs at risk (OAR)* are normal tissues whose radiation sensitivity may significantly limit the treatment. These can be, for instance, the spinal cord in lung tumor treatment or pelvic organs in prostate tumor treatment. In analogy to the PTV, safety margins can be added around the OAR volumes [MvM02], leading to the concept of the *Planning Organ at Risk Volume (PRV)*.

### 4D Imaging and Motion Management

For non-small lung cancer (NSLC) one of the key challenges is managing intra-fractional motion of tumor tissue and organs. The most prominent image modalities involved in the treatment planning for NSLC are CT and 4D-PET/CT [NWHG09]. One pCT is acquired prior to the planning on which the delineation of the OARs is performed. However, the pCT is only a static image, and does not account for tumor motion. Therefore, GTV delineations can be performed on 4D-PET/CT which allows imaging the patient over the whole breathing cycle. This is depicted in Fig. 1.3, where the maximum inhale and exhale images are fused with the pCT. As mentioned above, the current radiotherapy workflow addresses the tumor motion by applying margins to the delineated GTV to define, for instance, the ITV. The ITV encompassing the tumor as depicted in Fig. 1.3 was defined by using 4D imaging.

The influence and effects of margins and motion uncertainty onto the dosimetric outcome due to breathing motion in lung cancer patients have been investigated [BCTT08, KMJ<sup>+</sup>14], and robust delineation of tumor boundaries is very important. Especially in treatment schemes that deliver a dose in relatively few, high-dose fractions, such as stereotactic body radiotherapy, smaller margins are used around the tumor to spare surrounding normal tissue. When smaller margins are used, however, there is less room for contouring errors. Visual inspection of the delineated structures is therefore a crucial step in treatment-planning, and is also very time-consuming, since this is usually done slice-by-slice.

### Deformable Image Registration

Deformable image registration (DIR) has become an important tool in modern radiotherapy with many applications including target definition, dose planning, dose warping, and IGART [SDP13, VLM<sup>+</sup>15, VKKH13, RA10, SPWF12, GHC14]. During the course of radiotherapy, both the tumor and the surrounding anatomy can change. IGART tries to account for these types of anatomical (intra-fraction and inter-fraction) changes. For instance, both the tumor and the OARs are variable in size and position between

fractions (inter-fraction), e.g., bladder and bowel filling, or due to weight loss and tumor shrinkage [KWCM13].

In IGART, the recent state of anatomy is evaluated by recomputing the accumulated dose (dose warping using DIR) and compared to the planned dose. If the deviation is too high, re-planning might be necessary. The calculation of the true dose distribution for a patient requires accurate DIR to reduce dose warping uncertainties due to the registration algorithm [VLM<sup>+</sup>15].

As mentioned above, breathing motion of tumor tissue and organs represents a real challenge both for target delineation and during delivery (intra-fraction). Motion modeling can be used for better representing the tumor (and patient anatomy) for treatment-planning and for internal margin definitions of GTVs, and therefore reducing the irradiation of healthy tissue [WSvD08]. This usually involves a deformable registration algorithm to measure the displacements vector field (DVF) over the whole breathing cycle, or between maximum inhale and exhale positions (see Fig. 1.4).

Whilst image registration by means of dedicated machines such as PET-CT has been found acceptance in the clinical routine, deformable image registration algorithms have not yet gained wide acceptance. Visual assessment of the DVF is an important step toward clinical acceptance and routine use, as there is usually no ground truth available. However, locally implausible deformations, not readily picked up by observers, represent a significant challenge [RA10].

### Image Fusion of Multi-Modal Image Information

From the above definitions it becomes clear that fusion of the multitude of image information is important for multiple aspects of the planning. A schematic overview of the fusion of the different types of information sources is depicted in Fig. 1.5. The different information sources are relevant for different steps in the workflow (see Fig. 1.1).

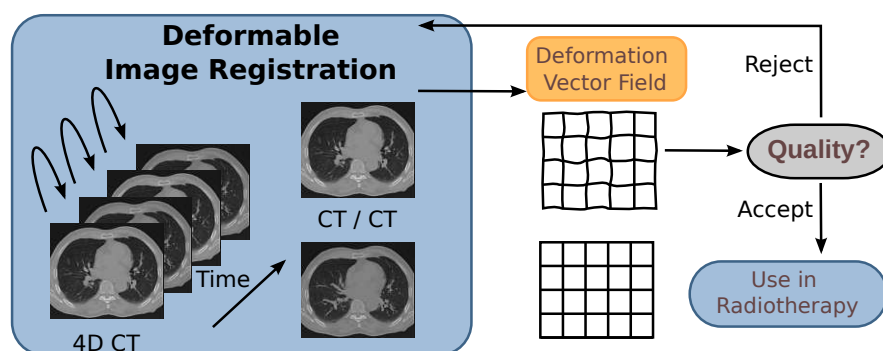


Figure 1.4: Deformable image registration has many applications in radiotherapy. Independent of the application, quality assessment of the resulting displacement vector field is an important step toward clinical acceptance.

For the definition of target volumes and OARs, image information of the *Image Acquisition* steps are important. They need to be mapped to the same coordinate space, which might require image registration, and visualized accordingly. For their verification, these volumes themselves need to be included in the fusion pipeline. Furthermore, the dose distribution may be included in the *Treatment Evaluation* step. If deformable image registration is involved, quality measures might be added to the pipeline to overlay error information. This is especially important when IGART concepts should be used where dose distributions need to be warped, or when motion modelling should be included in the *Target Definition* step (see above).

A natural consequence of having a multitude of information sources, is to provide appropriate interaction techniques and different visualization modes. It is important for users to select data sources, change fusion parameters, change time bins when using 4D imaging (see Fig. 1.3), or combine information such as delineations with image information to implement, for instance, volume masking as depicted in Fig. 1.5.

### Healthy Tissue Sparing

Another challenge, which is faced in clinical reality, is the fact that target volumes and OARs might overlap as depicted in Fig. 1.2 (middle). Some overlaps are more critical than others, and depend also on the OARs involved. These overlaps present a challenge as the shape of the prescribed dose might not be achieved, and on the other side the OARs might receive too high doses in the overlapping regions as shown in Fig. 1.2 (right).

Assessing the adequacy of normal tissue sparing, is considered one of the most difficult parts in quality control with two potential pitfalls [MBLM11]:

1. The OARs are well separated from, or only slightly overlapping, the PTV. In these favorable cases, the potential exists that the treatment planners might not push to provide a dose distribution that spares these organs more than the standard goal, even if additional sparing was possible.

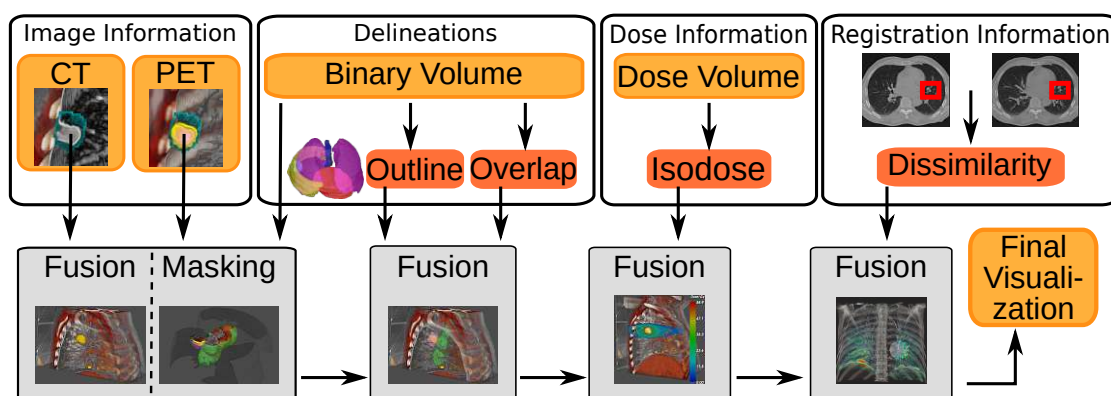


Figure 1.5: Fusion of different types of information sources relevant in RT planning.



- The OARs will be substantially overlapping the PTV. In these cases, the potential exists for treatment planners to expend time and effort attempting to meet goals that are impossible to accomplish without unacceptable sacrifice of another clinical goal.

Including information about overlaps during treatment plan evaluation, for instance, with additional quantitative views as depicted in Fig. 1.6, has the potential to improve the overall quality [WRS<sup>+</sup>09]. Studies have shown the feasibility of overlap sparing without compromising treatment outcome especially for smaller overlaps [HJNL06].

### 1.1.2 Interdisciplinary Research Setting

The presented research in this thesis is the result of tight collaborations with other scientific institutes (see Fig. 1.7). The research was a part of the SUMMER project [SUM12] (Software for the Use of Multi-Modality images in External Radiotherapy), a Marie Curie Research Training Network (PITN-GA-2011-290148) funded by the 7th Framework Programme of the European Commission (FP7-PEOPLE-2011-ITN), which consisted of eight different research institutions located in different European countries (see Fig. 1.7a). SUMMER was created to support the technological and clinical research required for the innovative use of multi-modal images in radiotherapy treatments. The project was devised to produce unique software using several imaging sources (CT, MRI, PET, MR spectroscopy, fMRI, 4D-PET/CT) for biological target volume delineation, based on spatial co-registration of multi-modal morphological and functional images. Furthermore, the author collaborated with other research partners (see Fig. 1.7b) beyond the scope of the SUMMER project.

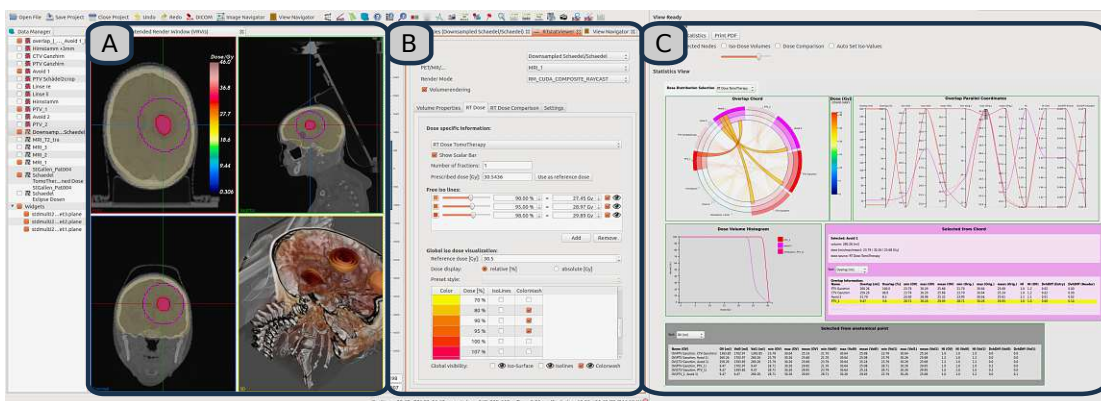


Figure 1.6: Overview of the software as used for the overlap volume exploration. The multi-modal interactive visualization framework is visible in part A, the configuration parameters are implemented in part B, and in part C quantitative visualizations were implemented using the MITK platform.

## Software Development Environment within the SUMMER Project

One of the corner stone objectives of SUMMER was to develop a mutual software console that radiation oncologists, physicians, physicists, radiologists can share to study, annotate and contour images. Running in a unified framework is an important step towards integrating novel research and share results in the form of software prototypes with other project partners. The software development environment for the SUMMER project was the Medical Imaging Interaction Toolkit (MITK) [WVW<sup>+</sup>05]. It is a higher level framework integrating other frameworks such as VTK [SML06] and ITK [MLJ<sup>+</sup>14].

One of the deliverables of the VRVis Research Center was the description of the visualization requirements and the development of a multi-modal interactive visualization framework (see Fig. 1.8). Within this framework GPU-based techniques for the visual computing were implemented and integrated into the MITK framework. This framework builds the basis of the results presented in the remainder of this thesis.

Fig. 1.6 shows an example of the integration in which the multi-modal interactive visualization framework is visible in part A, the configuration parameters are implemented in part B, and in part C quantitative visualizations were implemented using the MITK platform.

## 1.2 Contributions and Thesis Structure

The papers of this thesis are a result of the author's research at the VRVis Research Center (VRVis) in cooperation with the aforementioned scientific partners (see Fig. 1.7a and Fig. 1.7b). All research was thoroughly evaluated with user studies and, if applicable, employing available ground truth data to show its benefit. An overview of contributions of individual chapters and how they relate to the steps in the radiotherapy treatment

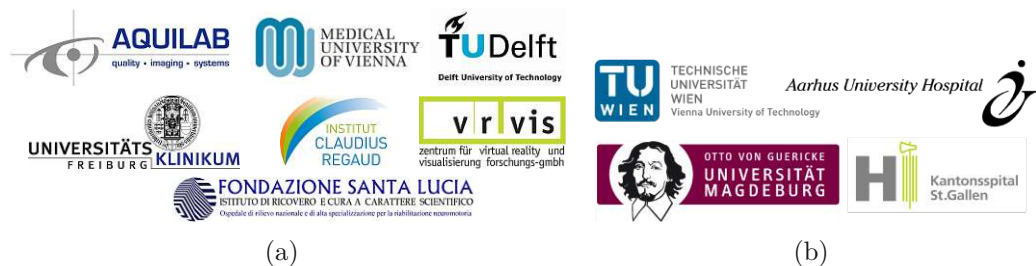


Figure 1.7: (a) The SUMMER consortium consisted of seven different research institutions located in different European countries [SUM12]. Chapters 3–5 are the result of collaborations with the University Medical Center Freiburg, Germany and Chapter 5 with the Medical University of Vienna, Austria. (b) Collaborations with other institutes leading to results presented in this thesis: Kantonsspital St. Gallen, Switzerland; Technical University of Vienna, Austria; University of Magdeburg, Germany; Aarhus University Hospital, Denmark.

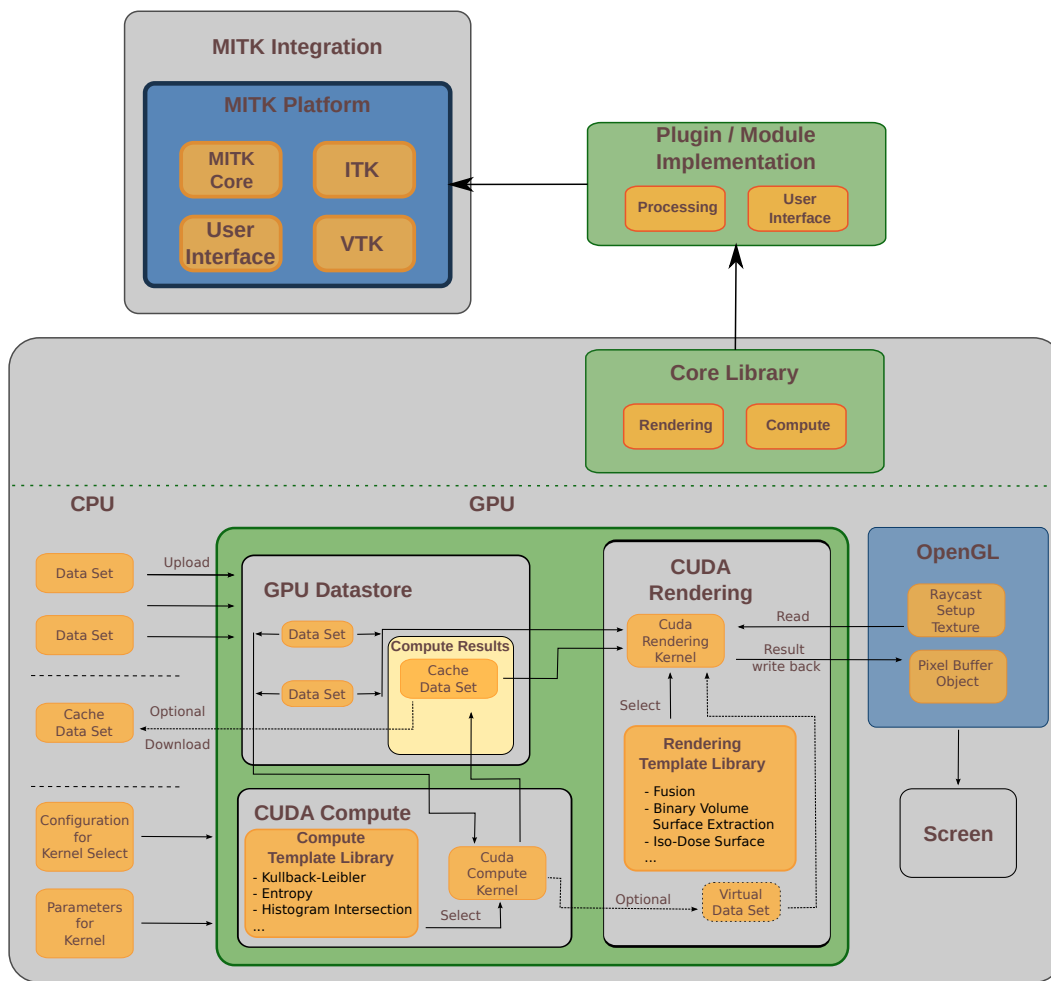


Figure 1.8: Overview of the core software framework and integration.

planning workflow is depicted in Fig. 1.9. The research contributions in this thesis can be summarized as:

- Contributing to the design of a multi-modal visualization framework with a focus on radiotherapy planning. This includes the analysis of requirements and the evaluation of its use.
- Contributing to the design of a framework for the visualization of deformable image registration. This includes the theoretic framework, the design and the evaluation of the proposed methods.
- Contributing to the design and evaluation of a framework for interactive exploration of radiotherapy plans with a focus on overlap volumes, i.e., target volumes and OARs, with the aim of healthy tissue sparing.

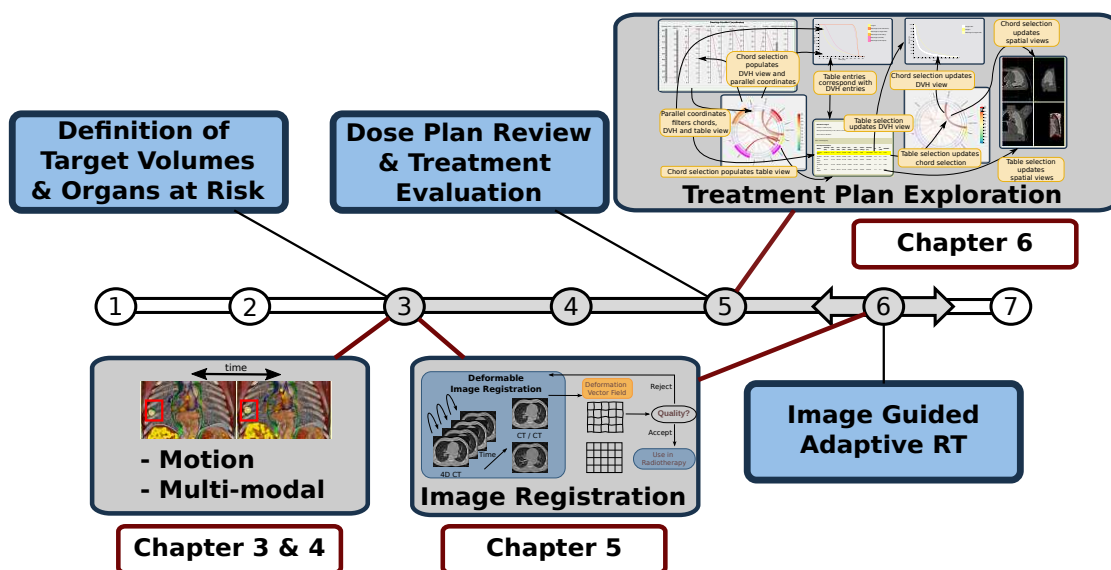


Figure 1.9: Overview of contributions of individual chapters to steps in the radiotherapy treatment planning workflow.

### 1.2.1 Thesis Structure

Chapter 2 provides the relevant background and gives an overview of related work with regard to the scope of the thesis. The main scientific contributions of this thesis will be presented in the Chapters 3–6. They are addressing the challenges outlined above, and their relation to the RT planning steps are depicted in Fig. 1.9. The thesis will conclude with Chapter 7 by reflecting on the contributions, discussing their impact, and show possible directions for future work.

### 1.2.2 Research Contributions of Individual Chapters

**In Chapter 3 and 4:** The design, implementation, and evaluation for a 4D multi-modal visualization framework are presented based on the following publications:

- **M. Schlachter**, T. Fechter, U. Nestle, and K. Bühler. Visualization of 4D-PET/CT, Target Volumes and Dose Distribution: Applications in Radiotherapy Planning. Proceedings of MICCAI Workshop on Image-Guided Adaptive Radiation Therapy, The MIDAS Journal, 2014. [SFNB14]
- **M. Schlachter**, T. Fechter, S. Adebahr, T. Schimek-Jasch, U. Nestle, and K. Bühler. Visualization of 4D multimodal imaging data and its applications in radiotherapy planning. Journal of Applied Clinical Medical Physics, 18(6):183–193, 2017. [SFA<sup>+</sup>17b]

**In Chapter 5:** An approach for deformable image registration is presented. The visualization is based on voxel-wise comparison of local image patches for which dissimilarity measures are computed and visualized to indicate locally the registration results. The framework presented in Chapters 3–4 will be extended with different visualization modes tailored to the given use case. This chapter is based on the following publication:

- **M. Schlachter**, T. Fechter, M. Jurisic, T. Schimek-Jasch, O. Oehlke, S. Adebahr, W. Birkfellner, U. Nestle, and K. Bühler. Visualization of Deformable Image Registration Quality Using Local Image Dissimilarity. *IEEE Transactions on Medical Imaging*, 35(10):2319–2328, 2016. [SFJ<sup>+</sup>16]

**In Chapter 6:** A novel interactive visualization approach for the exploration of radiotherapy treatment plans with a focus on overlap volumes with the aim of healthy tissue sparing is presented. This chapter is based on the following publication:

- **M. Schlachter**, S. Peters, D. Camenisch, P. M. Putora, and K. Bühler. Exploration of Overlap Volumes for Radiotherapy Plan Evaluation with the Aim of Healthy Tissue Sparing. *arXiv*, 2021. [SPC<sup>+</sup>21]

### 1.2.3 Other contributions

Furthermore, the author of this thesis also contributed to the following publications, which will be partially used in Chapter 2:

- **M. Schlachter**<sup>\*</sup>, B. Preim, K. Bühler, and R. G. Raidou<sup>\*</sup>. Principles of Visualization in Radiation Oncology. *Oncology*, 98(6):412–422, 2020. [SPBR20]  
The authors denoted with <sup>\*</sup> contributed equally to this work.
- **M. Schlachter**<sup>\*</sup>, R. G. Raidou<sup>\*</sup>, L. P. Muren, B. Preim, P. M. Putora, and K. Bühler. State-of-the-Art Report: Visual Computing in Radiation Therapy Planning. *Computer Graphics Forum*, 38(3):753–779, 2019. [SRM<sup>+</sup>19]  
The authors denoted with <sup>\*</sup> contributed equally to this work.

The contributions of the surveys are:

- Summarizing the basic principles of visualization within RT planning.
- A comprehensive and comprehensible *taxonomy* of published work in the field of VC, applied to the domain of RT.
- A discussion, underlining the *achievements* of VC in RT so far, highlighting the main *challenges and limitations*, and envisioning *applicability for future work*.

- The identification of *key research directions* for the future based on the taxonomy and discussion.

Additionally, the author of this thesis authored or contributed to the following research publications:

- **M. Schlachter**, M. Reiser, C. Herz, F. Schlürmann, S. Lassmann, M. Werner, H. Burkhardt, and O. Ronneberger. Harmonic Filters for 3D Multichannel Data: Rotation Invariant Detection of Mitoses in Colorectal Cancer. *IEEE Transactions on Medical Imaging*, 29(8):1485–1495, 2010. [SRH<sup>+</sup>10]  
<https://doi.org/10.1109/TMI.2010.2049856>
- **M. Schlachter**, T. Fechter, K. Bühler, and U. Nestle. EP-1711: Fast visual quality inspection of 4D PET/CT contouring of manual and semi-automatic contours. *Electronic Poster: Physics Track: Imaging: Focus on Clinical Applications, Radiotherapy and Oncology*, 111(1):S251–S252, 2014. [SFBN14]  
[https://doi.org/10.1016/S0167-8140\(15\)31829-6](https://doi.org/10.1016/S0167-8140(15)31829-6)
- M. Nunes, B. Rowland, **M. Schlachter**, S. Ken, K. Matkovic, A. Laprie, and K. Bühler. An integrated visual analysis system for fusing MR spectroscopy and multi-modal radiology imaging. *IEEE Conference on Visual Analytics Science and Technology (VAST)*, pages 53–62, 2014. [NRS<sup>+</sup>14]  
<https://doi.org/10.1109/VAST.2014.7042481>
- T. Fechter, J. Dolz, A. Chirindel, **M. Schlachter**, M. Carles, S. Adebahr, M. Mix, and U. Nestle. Fully Automatic Danger Zone Determination for SBRT in NSCLC. *Journal of Radiation Oncology Informatics*, 7(1):1–27, 2015. [FDC<sup>+</sup>15]  
<https://doi.org/10.5166/jroi-7-1-26>

# Background and Related Work

This chapter is based on the publications:

- **M. Schlachter**, B. Preim, K. Bühler, and R. G. Raidou. Principles of Visualization in Radiation Oncology. *Oncology*, 98(6):412–422, 2020. [SPBR20] <https://doi.org/10.1159/000504940>
- **M. Schlachter**, R. G. Raidou, L. P. Muren, B. Preim, P. M. Putora, and K. Bühler. State-of-the-Art Report: Visual Computing in Radiation Therapy Planning. *Computer Graphics Forum*, 38(3):753–779, 2019. [SRM<sup>+</sup>19] <https://doi.org/10.1111/cgf.13726>

The original papers go beyond the scope of this thesis. Therefore, only some parts were re-used and combined to present the relevant background information and related work tailored to this thesis. The parts were adapted in terms of formatting and type-setting to fit this template and to increase readability. Minor corrections, such as fixing typos or unclear wording, were applied.

RT has been used as cancer treatment for more than a century [Sla12]. It is used as *therapeutic treatment* to cure the disease, as *adjuvant therapy* to prevent tumor recurrence, or as *palliative treatment* to relieve patients of symptoms.

The treatment process can be *internal* (e.g., Brachytherapy treatment) or *external* (e.g., External Beam Radiation Therapy or EBRT) [WL15]. In the former case, radioactive sources are positioned precisely inside the area to be treated, affecting only a very localized region [GPM<sup>+</sup>02]. In the latter case, the radiation source is located outside the patient, and delivered using, for instance, a linear accelerator (LINAC), as shown in Fig. 2.1. EBRT is the most widespread treatment in current clinical practice, hence, visual computing (VC) solutions have mostly addressed this. The complex data, the compound processes, and the multitude of user groups involved in RT make it particularly interesting for several fields of research [PB13]. These include image processing, visualization, VC, and machine learning. Recently, there is an increasing demand for more personalized therapy, which will maximize tumor treatment and minimize side effects [THM<sup>+</sup>13, TOG06]. This trend requires the development of new means within the VC domain, while targeted patient treatment includes more and more often additional patient- and tumor-specific information [TOG06]. All this information is complex and heterogeneous, and new strategies for its visualization, exploration, and analysis need to be designed [Rai17]. The topic is also manifold, involving different sources of data and uncertainty, several specialist users, and a variety of applications and challenges — many of which are also applicable to other medical and non-medical domains.

RT planning involves multi-modal and multi-valued data [WL15]. Also, each step of the RT workflow involves heterogeneous sources of information. These might relate, for example, to multi-modal registration and segmentation data [RMB<sup>+</sup>16], to ensemble data from the optimization phase of the dose planning [SRV16], or to modeling data from tumor control probability (TCP) [RCM<sup>+</sup>16] and normal tissue complication probability (NTCP) [Rai18]. Understanding, exploring, and analyzing all these data channels can be a demanding and time-consuming task.

Additionally, uncertainty [Rai18, RPHL14] is present at all steps of the workflow, affecting the accuracy and precision of the final outcome [BCTT08, KMB<sup>+</sup>06, vHRL02]. Uncertainties, which cannot be corrected or minimized, need to be addressed, and their impact has to be predicted. For example, motion management in RT can be challenging for tumors and organs affected by breathing, e.g., the lung [BCTT08, KMB<sup>+</sup>06]. In particular, for treatment methods, which involve critically high doses, such as Stereotactic Body RT (SBRT) for lung cancer, even slight movements cannot be ignored. 4D imaging and deformable registration can be used to model breathing motion [WSvD08], but these might introduce additional uncertainty due to the use of deformable image registration.

Another important aspect is the variety of specialists involved in the different steps of the RT workflow, such as radiologists, radiation oncologists, medical physicists, and dosimetrists. While patient treatment is the primary goal, users have different benefits from the use of VC [PB13]. These may include, e.g., diagnosis, data exploration,



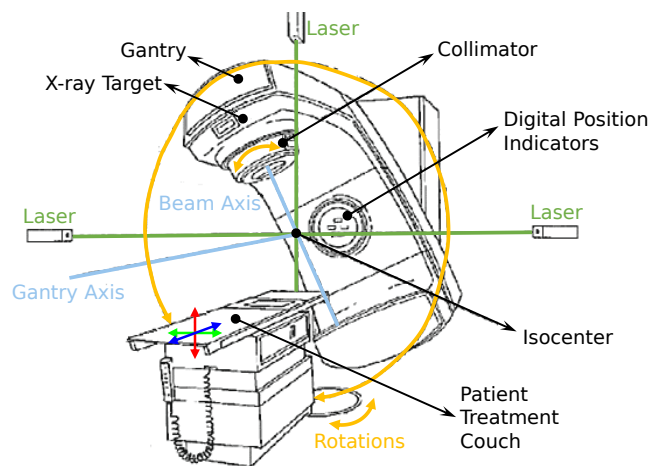


Figure 2.1: Schematic depiction of a linear accelerator (LINAC) used in External Beam Radiation Therapy (EBRT) treatment, with its major components and employed axes [SRM<sup>+</sup>19]. Rotational and translational movements of several parts are depicted with arrows.

verification, or decision-making. Therefore, the needs of different users must be addressed individually, increasing the complexity of the visual design process [DNT09].

## 2.1 Radiotherapy Planning

In the past decade, RT has undergone a steady evolution [THM<sup>+</sup>13], offering flexibility in radiation dose delivery. The advent of new delivery techniques has improved treatment, such as Intensity-Modulated Radiation Therapy (IMRT) and more recently Volumetric Arc Therapy (VMAT) — both subsets of EBRT. These techniques can precisely address tumors, by modulating the intensity of the radiation beam around the tumor volume, while decreasing or avoiding radiation among the surrounding healthy tissues [Web01]. This modulation, i.e., shaping and aiming of radiation beams from several angles of exposure to cumulatively target the tumor, happens in the LINAC by the multileaf collimator see (Fig. 2.1).

Still, RT may result in a number of potential side effects depending on the dose, fractionation, and location. These can range from acute skin irritation [WL15] to secondary cancer decades later [HW03]. To maximize the effectiveness of tumor treatment, while minimizing the damage to surrounding tissues, the radiation dose administration must be carefully planned in dedicated software [WL15]. RT planning follows a workflow, which can be outlined by a series of steps depicted in Fig. 1.1 The time required for the planning procedure differs for each individual patient and is specific to the characteristics of the case and the tumor. An in-depth workflow analysis has been previously presented by Aselmaa et al. [AGL<sup>+</sup>13].

After diagnosis and referral, patient images are acquired [TAKC09]. *Multiple imaging modalities* are often employed, as studies have demonstrated that the combination of different acquisitions can improve detection, diagnosis, and staging [BJE<sup>+</sup>11, BRC<sup>+</sup>12, CKK<sup>+</sup>07, HCE<sup>+</sup>07]. Clinical imaging techniques can be classified into anatomic methods, which measure physical properties of tissue, such as tissue density acquired from Computed Tomography (CT), and functional imaging techniques, which measure functional characteristics, such as metabolism acquired from Positron Emission Tomography (PET) [Eva08]. In a prostate cancer case, multi-modal imaging can include CT Imaging, T2-Weighted Magnetic Resonance Imaging (MRI), Diffusion-Weighted Imaging (DWI), Dynamic-Contrast Enhanced MR Imaging (DCE-MRI), and MR Spectroscopy Imaging (MRSI) [BJE<sup>+</sup>11, BRC<sup>+</sup>12, CKK<sup>+</sup>07, HCE<sup>+</sup>07].

A crucial step of treatment planning is the *definition of target volumes*, i.e., the tumor tissue, and *organs at risk (OARs)*, i.e., volumes representing whole organs or parts, which have to be spared during treatment [Nje08]. The delineation (or *segmentation*) of targets and OARs often employs more than one imaging source, which has proven to be advantageous regarding specificity and sensitivity [LKCG12]. *Data fusion* for the integration and combination of various information channels is also part of this process, while interactive approaches for the *exploration and analysis* of the data are also employed. All aforementioned images need to be *registered* [ZF03], to be transformed into the same coordinate system as the planning CT.

After the localization of the tumor and adjacent organs, one (or more) *initial treatment plan(s)* is (are) designed, using treatment planning software (TPS). Complex constraints and guidelines are employed to determine the geometric, radiobiological, and dosimetric aspects of the treatment — taking into account the OARs, and optimizing for tumor treatment and for healthy tissue preservation [WL15]. For target volumes, a required minimum dose is prescribed, whereas OARs should receive doses as low as possible [BRC<sup>+</sup>12, HMP<sup>+</sup>18]. The tolerance for radiation differs between organs and depends on their tissue properties. This information is also incorporated to prescribe a level of radiation so that no damage is induced to them.

The calculated treatment plan(s) will undergo further *review and approval*. Dose volume histograms (DVH) [DMB<sup>+</sup>91] are often used to summarize the distribution of doses to the target and OARs. Also, the final prescribed radiation dose will not be administered all at once. Fractionation [THM<sup>+</sup>13, WL15] is used in most treatments, where the total dose is spread out in adequate amounts over time, to allow the recovery of normal cells and to prevent the repair of tumor cells between fractions. The step of radiobiological modeling is conducted for the effectiveness assessment of the selected RT strategy, involving TCP modeling [WN93] and NTCP modeling [MYJ<sup>+</sup>10]. TCP models are statistical models that quantify the probability that a tumor is effectively controlled, i.e. treated, given a specific radiation dose, and respectively NTCP models that normal tissue around the tumor is harmed.

*Image-Guided Adaptive RT (IGART)* requires to further verify whether the initial plan is still applicable. Sometimes, changes in the tumor location and shape or anatomical

changes of the patient, e.g., due to weight loss or due to rectal and urinary filling, require further plan modifications between treatment fractions. At the point of treatment delivery, a prior *verification* step ensures that the patient is correctly positioned.

### 2.1.1 Users Involved in RT Planning

Several clinical experts are involved in the steps of the RT workflow [AGL<sup>+</sup>13]. Each specialist has a different role — implying that VC has also different benefits for them. The most relevant specialist groups are:

1. Radiation oncologists (main responsables for the prescription, approval, and supervision of the treatment, involved in *all steps* of the RT workflow).
2. Medical physicists (scientists who advise on the best treatment strategy, involved in *Definition of Target Tumor(s) & Organs at Risk, Treatment Plan Design & Dose Calculation, Dose Plan Review & Treatment Evaluation, Image Guided Adaptive RT*).
3. Radiologists (doctors who specialize in medical imaging acquisition and interpretation, involved in *Diagnosis & Referral, Imaging Acquisition, Definition of Target Tumor(s) & Organs at Risk*).
4. Radiotherapists (or therapy radiographers, specialists who operate the treatment machines, involved in *Setup Verification & Treatment*).
5. Dosimetrists (main responsible for the careful calculation of the dose in the specialized equipment, involved in *Treatment Plan Design & Dose Calculation, Dose Plan Review & Treatment Evaluation, Image Guided Adaptive RT*).

### 2.1.2 Data Involved in RT Planning

The entire workflow of RT planning is based on the imaging acquisitions of the anatomy and pathology of the patient. Yet, each step of the workflow incorporates additional information or data derived from the imaging acquisitions, as depicted in Fig. 1.1. The final outcome of the workflow is a dose plan, which incorporates 2D or 3D radiation dose information. During this entire planning process several imaging and non-imaging data accumulates around the patient [PPB15].

#### Imaging Data

In the image acquisition step, the necessary images needed for radiotherapy planning are acquired from a multitude of sources [HCE<sup>+</sup>07]. These can be CT and MRI data, and data derived thereof, depending on the target anatomy. For example, DWI, DCE, and MRSI are used for prostate and cervical tumor treatment planning [BRC<sup>+</sup>12, BJE<sup>+</sup>11, CKK<sup>+</sup>07]. For lung tumors, the use of functional imaging, such as (4D) PET/CT, can

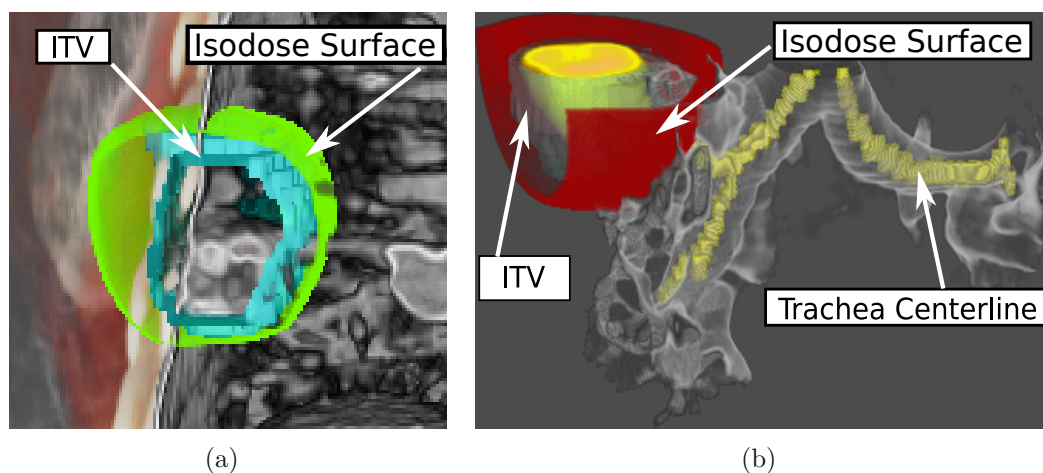


Figure 2.2: (a) Isodose surface encompassing the ITV. This is a less critical example, due to the location of the tumor (at the lung border close to a rib), where the PTV (ITV with setup error margin) is not representing the TV well. (b) Example of a difficult case (central lung), where the tumor is close to an OAR. The PTV and PRV were overlapping in this case. Figures taken from Schlachter et al. [SRM<sup>+</sup>19].

be advantageous for tumor definition [SKO06]. Brain tumors may additionally require Diffusion Tensor imaging (DTI) [MBC15]. Details on each modality can be found in recent surveys [LSBP18, PBC<sup>+</sup>16]. During this step, the planning CT is acquired, a high quality CT which plays an important role in the planning. It serves as the reference coordinate system for target definitions, as well as for other images acquired using different modalities (registration to the planning CT). Furthermore, the tissue densities are used for the dose calculation.

### Target Volumes Concept

As mentioned before, an important concept within RT is the use of *Volume Concepts* (see Fig. 1.2) developed by the *ICRU* [BDK<sup>+</sup>07, GLC<sup>+</sup>04]. Many treatment planning approaches are specifically targeting one (or more) of these volumes.

Many uncertainties, such as patient setup errors [SH02], are handled by adding margins [Ben08, JYW99, MvM02]. Based on the PTV, appropriate beam sizes and beam arrangements will be selected to ensure that the prescribed dose is actually delivered to the CTV [BDK<sup>+</sup>07]. The *Treated Volume (TV)* is planned to receive at least a dose, appropriate for the purpose of the treatment. It is, thus, a volume enclosed by an isodose surface corresponding to that prescribed dose level [BDK<sup>+</sup>07]. For example, if the prescribed dose is 40 Gy, and the minimum dose was 5% below, the TV is then enclosed by a 38 Gy isodose surface. Two examples of a target volume and a defined isodose surface are presented in Fig. 2.2.

In clinical reality, Target Volumes and OARs can overlap or even include each other.

A patient with a brain tumor, for example, has the target inside the brain, which is an OAR itself. The same applies to a lung cancer patient, where the lung itself is an OAR. Some overlaps are more critical than others, such as the brainstem and PTV for brain cases, or trachea and ITV for lung cases. In Fig. 2.2a the tumor is on the lung border, whereas in Fig. 2.2b the tumor is central, and the depicted overlap is more critical. Furthermore, determining the margins is not straightforward and depends on a multitude of factors [vH04]. Overlaps of target volumes and OARs present a challenge as on the one hand the shape of a prescribed dose might not be achieved, and on the other hand the OARs might receive too high doses in the overlapping regions as schematically depicted in Fig. 1.2 (right). Including information about overlaps during treatment plan evaluation has the potential to improve the overall quality [WRS<sup>+</sup>09].

### Uncertainty in RT Planning

RT planning is — among all therapy planning processes — the one where uncertainty, validation, and verification are considered essential by the involved physicians. In literature, there is no widely accepted definition of uncertainty. A definition is given by Griethe et al. [GS06], as *a composition of different concepts, such as error (outlier or deviation from a true value), imprecision (resolution of a value compared to the needed resolution), subjectivity (degree of subjective influence in the data), and non-specificity (lack of distinction for objects)*. In RT planning, we define uncertainty as any source which may cause variations in any step of the workflow and ultimately in the treatment outcome. Uncertainty is an additional data source, present at all steps of the planning workflow. The quantification and communication of uncertainty is essential for the accurate interpretation of the outcome, for reducing the existing uncertainties and risks, and potentially, for improving the outcome.

With regard to imaging modalities, both DWI and DCE imaging have highly varying sensitivity and specificity for tumor detection [KKP<sup>+</sup>08, KVCC08, TAKC09], depending on patient characteristics, on the tissue zone, and on the scanning procedure itself. Poor spatial imaging resolution and image distortions, due to magnetic field inhomogeneities at the interfaces between different tissues are additional problems in DWI [BJE<sup>+</sup>11, CKK<sup>+</sup>07, SFA<sup>+</sup>05]. In addition to this, pharmacokinetic modeling, which is employed in clinical research for the derivation of additional tissue characteristics from DCE data, is also a source of uncertainty [BRP<sup>+</sup>04, TAKC09, TBB<sup>+</sup>99, VTM<sup>+</sup>12]. Often, to minimize uncertainty different imaging modalities are combined [BJE<sup>+</sup>11, BRC<sup>+</sup>12, CKK<sup>+</sup>07, HCE<sup>+</sup>07]. In the delineation of the target volumes and OARs, uncertainties due to patient motion, or due to changes in the anatomy and pathology of the patient are considered within the aforementioned target volume definitions (Section 2.1.2). In the other steps, uncertainty can be caused by an ad-hoc choice, assumptions, stochastic processes, or inter-observer variability, as discussed in a recent work by Raidou et al. [Rai18]. A more detailed review on uncertainty visualization can be found in the survey by Ristovski et al. [RPHL14].

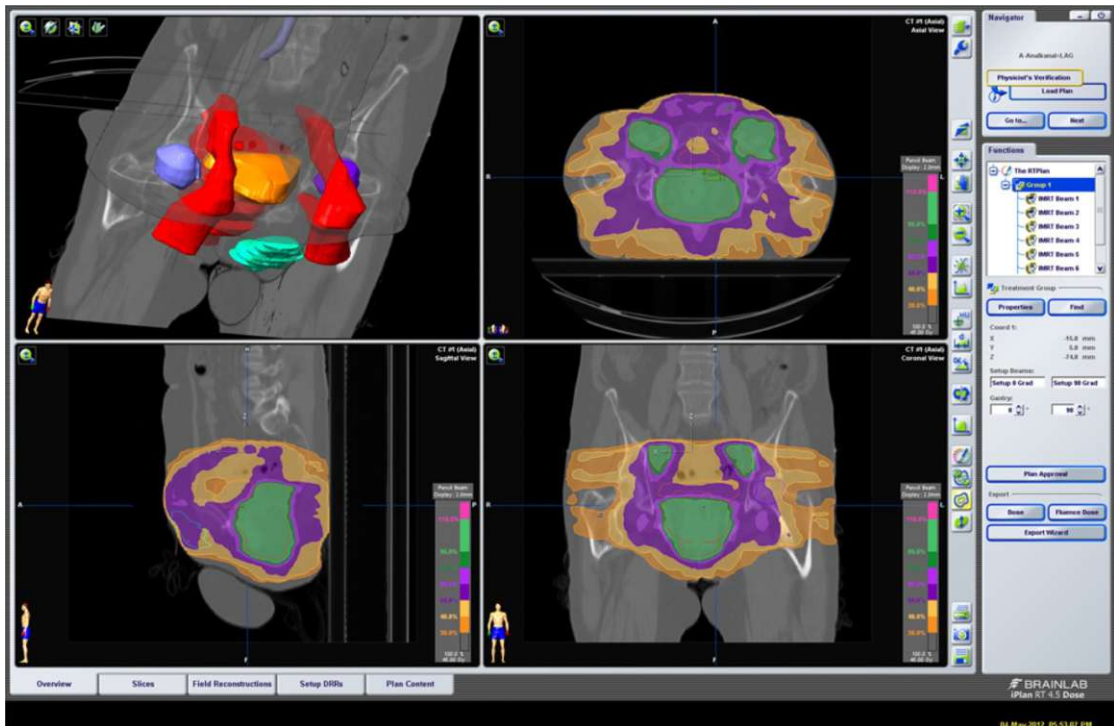


Figure 2.3: The axial, sagittal and coronal slices together with a 3D overview to evaluate the simulated dose distribution used to treat prostate cancer. The 3D overview (upper left) shows the previously segmented anatomical structures along with the three orthogonal slices. The slice views employ isolines and colored regions to display the dose distribution as percentage of the target radiation in the tumor (Courtesy of Mathias Walke, Department of Radiation Treatment Planning, University of Magdeburg, taken from the book of Preim and Botha [PB13]).

### Dose Plans and Dose Volume Histograms

*Dose plans* convey 2D or 3D radiation dose information (dose distribution), as generated from treatment planning systems based on a 3D reconstruction of a planning CT scan. Dose distributions are scalar data maps, where the values indicate in Gy the radiation dose at each location of the patient — in reference to the space of the planning CT. An example of a dose plan is shown in Fig. 2.3. Often, dose plans are regarded together with the so-called *dose volume histograms (DVH)* [DMB<sup>+</sup>91]. A DVH, as shown in Fig. 2.4, summarizes the 3D dose in a 2D plot, relating radiation dose (horizontal axis) to tissue volume (vertical axis). This can be a tumor target or a healthy organ, and the plot can have a differential or cumulative form. A DVH often includes all targets and OARs involved in the radiotherapy plan, where each structure is represented by a color-encoded line.

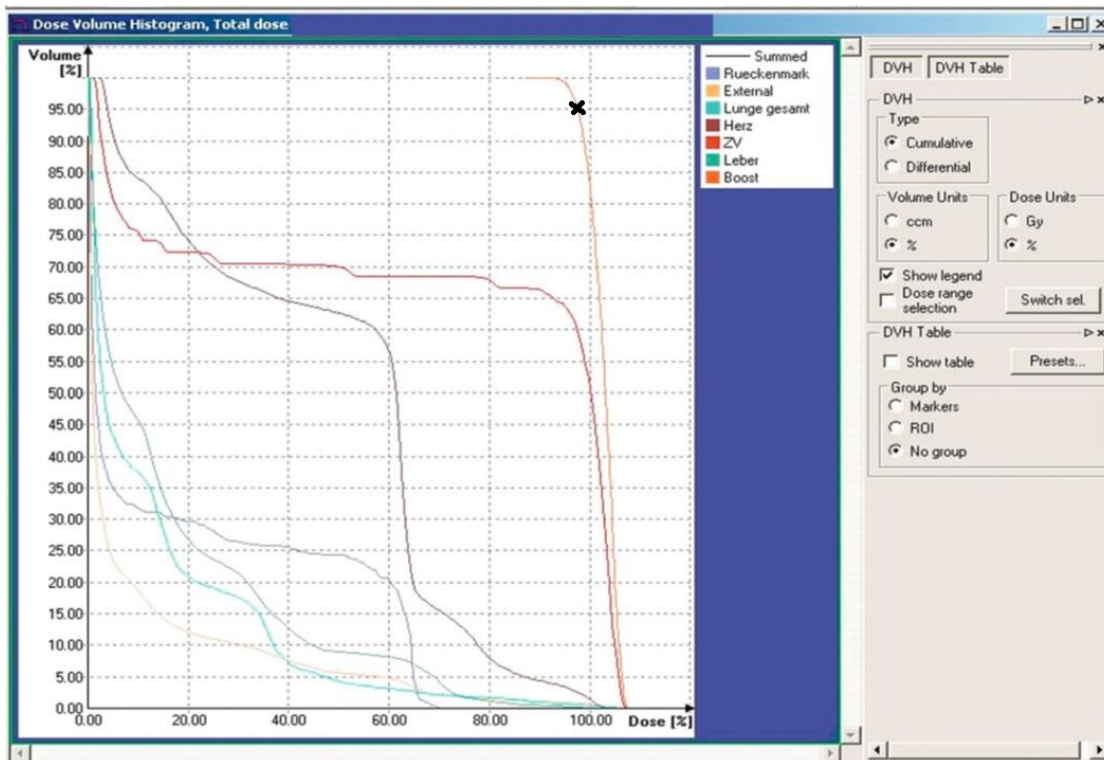


Figure 2.4: The dose volume histogram indicates which percentage of a structure volume receives a certain dose (horizontal axis) to treat an esophageal carcinoma. The orange curve relates to the tumor volume which indicates that 95% of its volume receive at least 95% of the target dose, as shown with the x-mark (Courtesy of Mathias Walke, Department of Radiation Treatment Planning, University of Magdeburg, taken from the book of Preim and Botha [PB13]).

## 2.2 Visual Computing for Radiotherapy Planning

### 2.2.1 Scientific Visualization for Radiotherapy Planning

Volume visualization helps to understand 3D anatomical spatial relationships [LFP<sup>+</sup>90]. For example, in radiotherapy planning, it aids understanding the relationship between the anatomy and the radiation dose distribution. Yet, imaging devices, such as CT scanners, usually create several projections of the human body, which need to be reconstructed into 2D slices to obtain the volumetric dataset. Reconstruction methods, such as filtered back-projection [PB13], are used to create a stack of slices, which are shown in Fig. 2.5. This is done in the following way: assume a reconstructed CT dataset with a  $1.17 \times 1.17 \times 2 \text{ mm}^3$  resolution is given. Thus, the volumetric dataset has an anisotropic resolution, which can be problematic for image — and later, for volume — display and interpretation. To account for anisotropy, transforming the sample position and interpolating on the stack of slices is common in ray traversal, as depicted in Fig. 2.6. Alternatively, resampling the

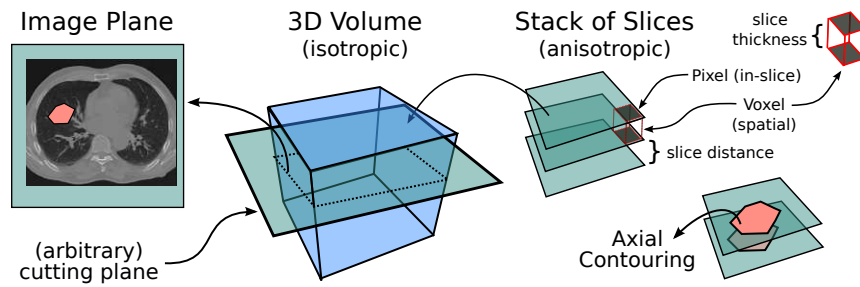


Figure 2.5: Schematic overview of how arbitrary slices can be extracted from 3D volumes, and how volumes are defined by a stack of slices commonly acquired by an imaging device [SPBR20].

slices is also possible, but might lead to loss of information or addition of unnecessary data values. After this step, the data are ready for 2D and/or 3D visualization.

## 2D Representations

In 2D representations, a standard slice-based approach is *multiplanar reformation* (MPR) — a technique that extracts 2D slices from a 3D volume [ZEP10]. Although slices can be extracted in arbitrary orientations, a common way is to show three orthogonal planes — the axial, coronal, and sagittal one — as shown in Fig. 2.7a. Slice-based representations show a section of a volume, defined by the intersection with a plane as depicted in Fig. 2.5. The image information of the volume, e.g., an axial slice, is “reformatted” onto the plane and then displayed in the respective window. During reformatting, slice distance and in-slice resolution are considered, to assure physically correct data display.

Another important aspect is *window/level*. The basic concept of window/level is to apply a linear gray-scale transform function specified by two parameters: the window width (WW) and the window level or window center (WL), to define how a subset of the entire dynamic range of the underlying data will be mapped to pixel intensities in the display. The WW defines the (relative) range of values, e.g., a Hounsfield unit range for CT, and

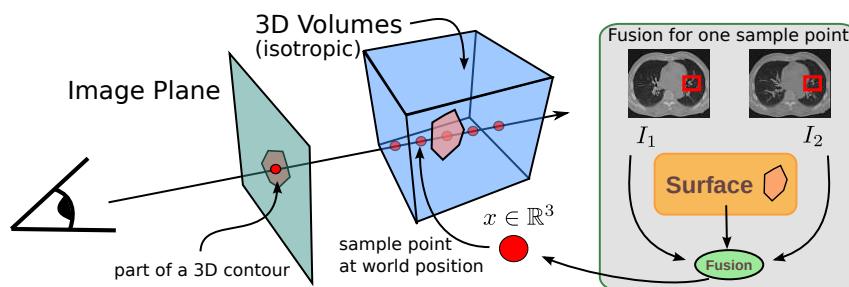


Figure 2.6: Schematic overview of the ray casting algorithm and volume fusion [SPBR20]. The ray is sampled at discrete positions to evaluate the volume rendering integral.



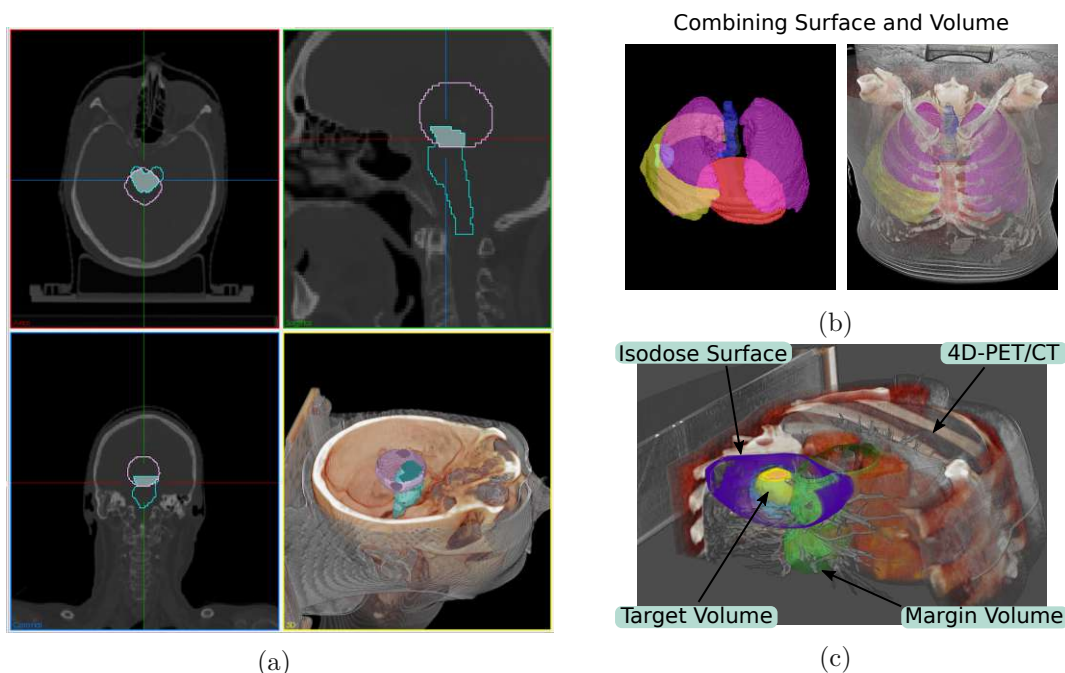


Figure 2.7: (a) MPR views together with volume rendering of a head CT with segmentation data. (b) Surface representation of segmentation data (left) combined with CT data (right). (c) 4D-PET/CT combined with segmentation data and an isodose surface. Figures taken from Schlachter et al. [SPBR20].

the WL is the midpoint of this range. When mapped to gray level values (pixel intensity from 0 to 255 on an 8-bit display), values smaller or equal to  $WL - (WW/2)$  are black (0), values greater or equal to  $WL + (WW/2)$  are white (255), and values in-between are linearly mapped onto their corresponding pixel intensity. This is depicted in Fig. 2.8.

### 3D Representations

We distinguish two general approaches for projecting 3D volume data onto the screen plane: *direct volume rendering* and *surface rendering*, also called indirect volume rendering. The latter usually involves image processing techniques to obtain triangulated surface meshes of distinct data structures [PB13]. Image enhancement and segmentation are out of the scope of this work, but additional information can be found in the book by Gonzalez et al. [GW02].

**Direct Volume Rendering** Direct volume rendering (DVR) creates an interactive visualization of a volume without any intermediate preprocessing step. The method commonly assumes a simplified, physically motivated absorption/emission model of light propagation [Max95]. For DVR, multiple approaches exist, such as splatting, shear-warp, and texture mapping [ZEP10, EHK<sup>+</sup>06]. One of the most prominent and flexible

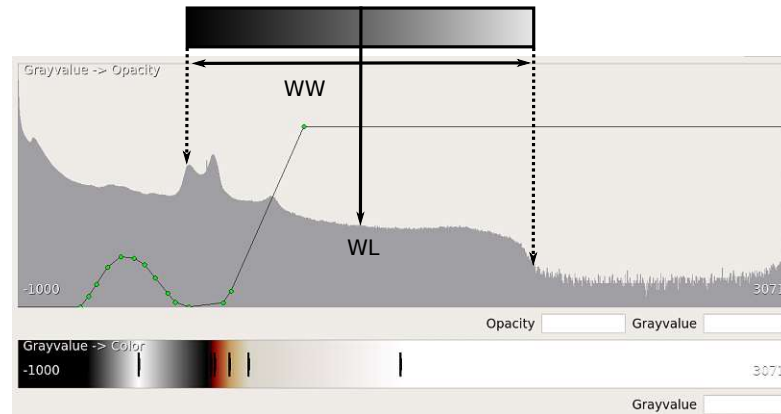


Figure 2.8: A widget used for defining a 1-D transfer function [SPBR20]. The upper part shows the histogram of a CT volume and points can be added to define the opacity transfer function, and the lower part is used to define the color transfer function respectively. The concept of *window/level* is shown on top of the widget. Values outside the window are either black (to the left) or white (to the right).

DVR techniques is ray casting [EHK<sup>+</sup>06], especially since acceleration techniques using graphics hardware exist [KW03]. The idea behind ray casting is to cast a ray for each pixel of the screen from the origin of the camera through the volume. The rendering integral [EHK<sup>+</sup>06] is directly evaluated along the rays traversing the volume, which delivers the final pixel values. A schematic overview for one light ray is depicted in Fig. 2.9 and Fig. 2.6. We refer to the book by Engel et al. [EHK<sup>+</sup>06] for a more detailed description.

Alpha blending [Max95] is a popular optical blending technique, often implemented by using the Riemann sum to discretize the continuous function of the volume rendering integral. Each sample in the approximation is assigned a color and opacity value. The Riemann sum when blending front-to-back for the current sample  $i$  is then given by:  $C_{i+1} = C_i + (c_i \cdot k_i) \cdot (1 - K_i)$  and  $K_{i+1} = K_i + k_i \cdot (1 - K_i)$ . Here  $c_i$  is the color and  $k_i$  the opacity of the current sample, and  $C_i$  and  $K_i$  are the accumulated values. The iteration scheme is depicted in Fig. 2.9 (right) for the composition of the color.

Other simpler projection and compositing techniques exist, such as X-ray projection, and Maximum Intensity Projection (MIP) [ZEP10]. When using MIP, e.g., in Fig. 2.6, only the value with the highest intensity would be considered along the ray, whereas all other sample values would not contribute.

**Transfer Functions** Volumetric data commonly consists of scalar values that represent a physical property, e.g., Hounsfield units denote radiodensity in CT data. In DVR, physical properties are assigned to optical properties, i.e., color and transparency, as shown in Fig. 2.7. Here, bones are displayed opaquely and skin tissue more transparently.

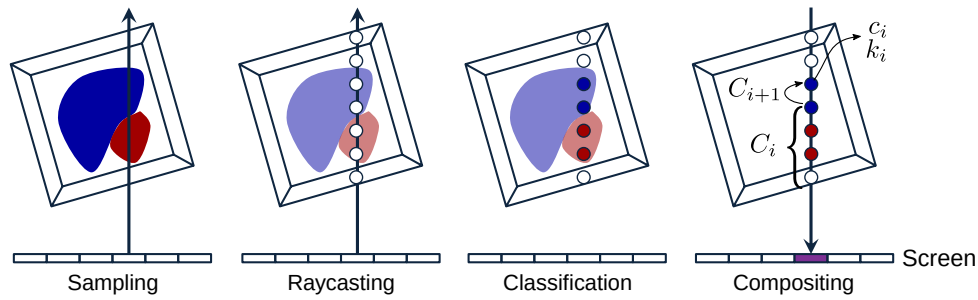


Figure 2.9: The main steps of the volume rendering process [SPBR20].

To obtain this, when the ray “hits” a bone, the accumulated opacity  $K_i$  reaches a maximum value (opaque) — i.e., no further light is visible from “behind” this point.

A widely used approach for assigning optical properties to the data values is by means of *transfer functions* in a process called *classification* [EHK<sup>+</sup>06], as shown in Fig. 2.9. When using a transfer function, each scalar value is assigned a color and opacity, in analogy to the window/level in slice-based representations. A common choice for color and opacity representation is *RGBA*, where the color is represented as combinations of red (R), green (G) and blue (B) channels, together with the opacity or alpha channel (A). The color transfer function  $c : \mathbb{R} \rightarrow \mathbb{R}^3$  and opacity transfer function  $k : \mathbb{R} \rightarrow \mathbb{R}$  are user-defined, and can be specified graphically as depicted in Fig. 2.8. More complex approaches involve *multi-dimensional transfer functions* and can be found in the survey by Ljung et al. [LKG<sup>+</sup>16].

**Surface Representations** Delineations stemming from manual contouring, e.g., on axial slices as shown in Fig. 2.5, or binary volumes from segmentation algorithms are usually transformed into 3D meshes, before rendering. For instance, delineations of Target Volumes in radiotherapy planning are commonly represented as surfaces, as well as isodose surfaces defined by Gray (Gy) values. Surfaces can be visualized opaquely or with transparency, where the latter enables a better overview and understanding of the location of inner surfaces within outer surfaces [PB13]. For correct rendering, all geometry primitives must be depth-sorted to be displayed in the correct spatial order, e.g., from back to front to allow for a correct blending. In Fig. 2.7b (left) surface rendering of multiple, nested, and transparent contours of a lung cancer patient are visualized. Fig. 2.7c shows additionally the isodose surfaces. In the corresponding MPR views, the segmentations (or isodoses) are often visualized as the outline of an area or as a filled (transparent) area overlaid on the slices, as depicted in Fig. 2.7a. Here, the filled regions are used to highlight the overlap of two delineations. More information on surface rendering can be found in the books by Engels et al. [EHK<sup>+</sup>06] and Preim and Botha [PB13], where also concepts for volume data in general are discussed, such as shaded surface display for CT.

## Hybrid and Multi-Volume Representations

**Hybrid Representations** Combining volume with surface rendering is essential in radiation oncology to show, for example, combined isodose surfaces, delineations and volumes in the same view, as depicted in Fig. 2.7c. Technically, combining surfaces as depicted in Fig. 2.7b (left) with volume rendering as depicted in Fig. 2.7b (right), is quite challenging. In the example of ray casting, the algorithm needs to include the surface at the correct depth as schematically depicted in Fig. 2.6, during the evaluation of the ray samples. This usually involves advanced techniques and data structuring to correctly visualize these complex scenarios [KGB<sup>+</sup>09]. Realization for MPR views is simpler, as graphics programming languages, e.g., OpenGL [EHK<sup>+</sup>06], allow for directly overlaying image data with contour data, i.e., meshes or closed polygons.

**Image Fusion and Multi-Volume Rendering** For multi-modal visualization, additional processing is often required. Combining datasets from multiple modalities using separate scanners, requires registration to be performed to align the volumes. This is often costly in terms of processing time, and acceleration techniques might be necessary [FVW<sup>+</sup>11]. But even if the transformation is known, different spatial resolutions, e.g., aligned PET/CT data with a  $4 \times 4 \times 4 \text{ mm}^3 / 1.17 \times 1.17 \times 2 \text{ mm}^3$  resolution, add to the complexity. One way to realize fusion during ray casting is at the *classification level* [SS11], where the optical properties for a sample point of two (or more) volumes are combined as depicted in Fig. 2.6. The fusion of the volume  $I_1$  and  $I_2$  is simply given by a weighted linear combination. Let  $c_1$  and  $c_2$  denote the color value of  $I_1$  and  $I_2$  at world position  $x$  (see Fig. 2.6). Then the fusion of the color is given by  $c_f := \alpha \cdot c_1 + (1 - \alpha) \cdot c_2$ , and can be defined for the absorption respectively. The parameter  $\alpha \in [0, 1] \subset \mathbb{R}$  is user-defined and can be realized, for instance, as a slider for changing the weight. This parameter can also be used for the slice-based visualization of the axial, sagittal and coronal views, where the images are fused respectively. The fusion for slice-based visualizations is usually easier to realize as graphics programming languages allow for directly blending (overlying) whole images. A more detailed overview can be found in the surveys on medical image fusion by James et al. [JD14], on multi-modal data visualization by Lawonn et al. [LSBP18], and on multi-volume ray casting approaches by Lux et al. [LF09].

**Volume Rendering using Graphics Processing Unit (GPU)** Most of the previously discussed algorithms can leverage modern GPUs, and for most of them GPU-based acceleration techniques for volume rendering exist [KW03]. A survey comparing different ray casting techniques using GPUs is provided by Schubert and Scholl [SS11].

## Interaction

An integral part of medical visualization is interaction. One of the most common interaction tasks is to *change visual parameters* [PB13], e.g., changing transfer functions by adding points to the widget shown in Fig. 2.8, and therefore changing the optical

properties assigned to the scalar values of a data set as explained above. A common interaction for slice-based visualization is *panning and zooming*, to refine the visual area of interest by moving the screen or the view on the screen (pan) and zooming into the area of interest. *Navigation* through the volume along the cutting direction for MPR views is another example. Here, the visualizations must be aware of slice distances to correctly display and move the cutting plane, as shown in Fig. 2.5. For volume rendering, interaction techniques such as *3D picking* are common where the closest surface point along the view direction from the 2D mouse position can be selected, and the 2D views will be re-arranged to show the position of the surface point. More advanced interactions include *cutting and clipping* [WEE02], which is used in Fig. 2.7c to “cut open” the volume, or *volume masking*, where certain regions can be assigned to a segmentation to further influence the volume fusion.

### 2.2.2 Visual Analytics for Radiotherapy Planning

Up to this point, we have discussed the visualization of medical data which have a 3D anatomical spatial arrangement, such as CT or MRI data and RT treatment plans. However, additional non-spatial data might be available, such as data from electronic health records of the patient or data from population studies. For these data, the methods discussed in the previous section are not sufficient. Additionally, given the steadily increasing dimensionality and complexity of medical data, new strategies have emerged as a natural response for visualization, exploration, and analysis. For instance, the need to integrate morphological with functional information has given “birth” to multi-modal imaging [LSBP18]. Despite the recent advances in data analysis techniques, the exploration of multi-modal data with the methods of the previous section is still cumbersome. Interactive approaches represent a new opportunity to integrate knowledgeable experts and their cognitive abilities in the exploratory process.

Within this content, visual analytics has been vastly investigated. According to Keim et al. [KKEM10], “Visual analytics combines automated analysis techniques with interactive visualizations for effective understanding, reasoning, and decision-making on the basis of very large and complex datasets”. The process and components of visual analytics are depicted in Fig. 2.10. Visual analytics makes use of the visualizations discussed above, as well as other commonly employed visual representations from the domain of information visualization, such as scatter plots, scatter plot matrices, or parallel coordinates plots. Additionally, it combines these visualizations with other disciplines — most commonly, statistics, data mining, or machine learning. A human-in-the-loop approach is essential in visual analytics solutions, integrating human strengths for sense- and decision-making, with semi-automated data analysis [Mun14, TM04]. This is enabled by interaction. Visual analytics incorporates several fundamental techniques, methods and concepts:

- The *Visual Analytics Seeking Mantra* [KAF<sup>+</sup>08] is summarized as: *Analyze first — Show the important — Zoom, filter and analyze further — Details-on-demand*. Initially, processes for the reduction or abstraction of the data are employed, so

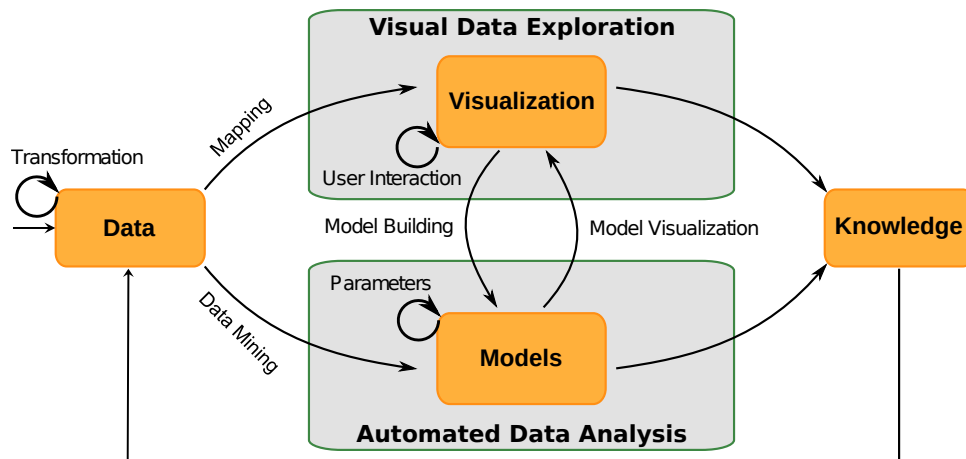


Figure 2.10: The main components of the visual analytics process (redrawn from Schlachter et al. [SPBR20]).

that only the important data can be displayed. For example, data mining serves the purpose of removing outliers or of computing clusters or correlations. Then, users zoom in and filter the data for more detailed information. At the end, all detailed information is shown on demand, through interaction.

- *Multiple (Coordinated) Views* [WBWK00] are widely used in visual analytics. This refers to employing multiple views that allow to observe the data and their in-between relations through different perspectives. Multiple Views are usually combined with Brushing and Linking, discussed below, to facilitate the identification of relationships within the data.
- *Brushing and Linking (B/L)* [BC87] is a concept that involves selecting one or several interesting data subsets in one view and highlighting corresponding subsets in another one. This method is meant to overcome the shortcomings of single techniques and provides more information than the exploration of individual views.
- *Focus + Context (F+C)* [CMS99] is required to present items at different levels of detail. More interesting or relevant data subsets are presented with more detail, while less important ones are presented with less detail. These are, however, retained in the view to provide context for a better understanding and insight.
- *Overview + Detail* [CKB09] is related to the combined use of Multiple Views and Focus + Context. Here, at least two views are presented to the users: one with a rough overview on the entire visualization space, and one with a detailed view of a smaller portion of the space.
- Visual analytics solutions tend to be powerful and complex. Often, target users are not able to fully exploit the potential of such systems. *Guided Visual Analytics*

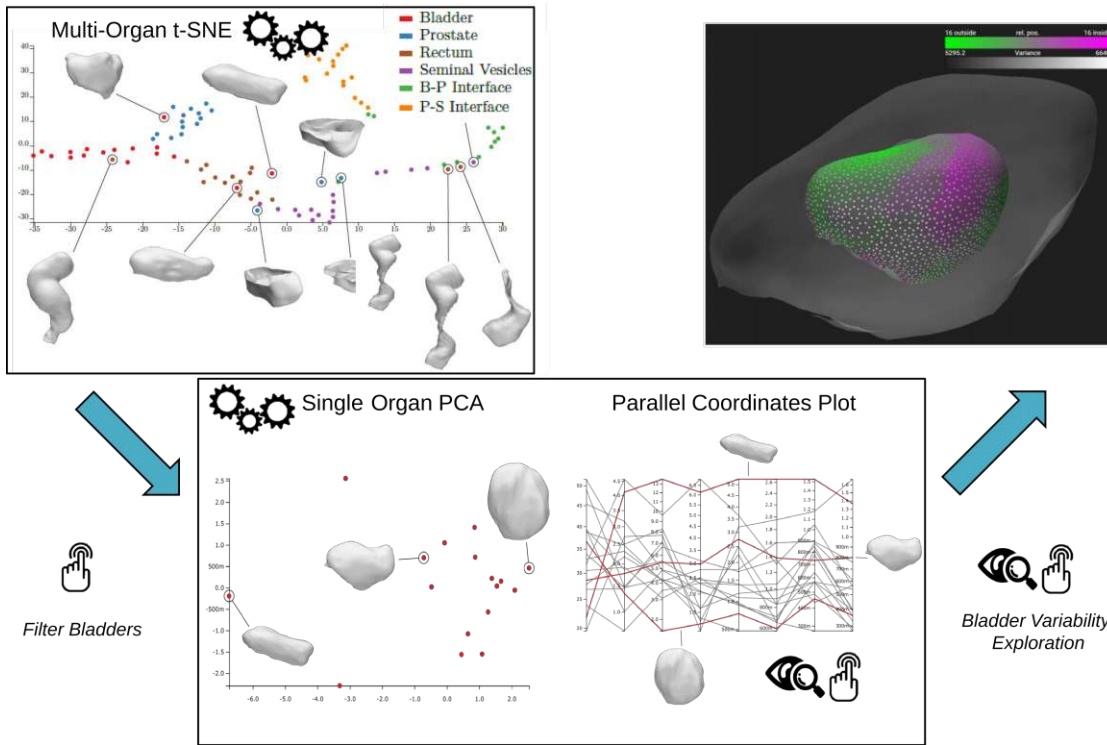


Figure 2.11: An example of a tool for the exploration and analysis of the variability of pelvic organs [RBGR18].

is a concept that puts emphasis on the effective use of such systems by domain experts [CGM<sup>+</sup>17].

Due to the tight and interactive coupling of the components of visual analytics, it is preferable to present a few example applications focusing on two tasks, often encountered in radiation oncology. In this chapter, we focus on (1) radiotherapy-related approaches for the exploration of tissue characterization employed in Target Volumes definition, and (2) strategies for the analysis and assessment of organ segmentation outcomes.

Visual analytics for tissue characterization initially provided solutions, such as the interactive framework by Coto et al. [CGB<sup>+</sup>05] for the exploration and analysis of breast Dynamic Contrast Enhanced (DCE) MRI data. Here, 2D and 3D anatomic representations of the patient data are used together with scatterplots representing the contrast agent enhancement. These are integrated through brushing and linking, enabling the identification and characterization of breast lesions. In other solutions, the entire space of tissue characteristics is visualized after a dimensionality reduction step [NRS<sup>+</sup>14, ODH<sup>+</sup>07, RvD<sup>+</sup>15].

Organ segmentations can be used, e.g., as input to radiotherapy treatment planning. Therefore, their accuracy is crucial. Visual analytics for the analysis and assessment of

automatic segmentations heavily rely on interaction concepts. There are approaches that focus on supporting both cohort and individual patient investigation for the detailed assessment of organ segmentations [RMB<sup>+</sup>16]. Reiter et al. [RBGR18] investigate how the shape and size of organs affect the accuracy of automatic segmentation methods. They propose an approach, which enables quick identification of segmentation errors and their correlation to anatomical features, as depicted in Fig. 2.11. Visual analytics within the domain of radiotherapy has been further investigated by Raidou et al. [RBV17].

### 2.3 Related Work in Visual Computing for RT

In this section, previous work in visual computing for RT is discussed, which is relevant to the contributions of this thesis, i.e, the planning steps presented in Fig. 1.9. The presented selection of papers is based on the literature research and taxonomy reported in the original paper [SRM<sup>+</sup>19].

#### 2.3.1 Taxonomy Description

As discussed in Section 2.1, RT has several particular characteristics with regard to the multitude of involved data, complex and risky processes, and users. This requires the incorporation of many strategies from the domain of VC. For example, registration or multi-modal visualization might be relevant for different steps of the workflow, but each step has specific clinical requirements and targets. Although previous work in the general domain of VC might also be applicable for RT and is referenced in the upcoming sections whenever relevant, it is more appropriate and clinically significant to address each of the steps of the workflow separately. As the entire radiotherapy treatment process is based on this workflow, this division into the clinical steps is anticipated to be more natural for readers both from the VC and the RT domain. The taxonomy is built upon two dimensions:

1. **Steps** of the RT workflow addressed by the proposed methods. This dimension implies also a clinically-relevant categorization based on the available data, upon which the methods were built, as discussed in Section 2.1.2.

The first dimension was reduced to fit the scope of this thesis. This is indicated by the green colors in Fig. 2.12 and in the listing below. The remaining categories are related to the workflow steps addressed in this thesis (see also Fig. 1.9). It comprises the following categories:

- Target and OAR Definition (Section 2.3.2)
  - Data Registration
  - Data Fusion
  - Data Segmentation (enhancement by post-processing omitted)
  - Multi-Parametric Data Exploration and Analysis (omitted in this chapter)



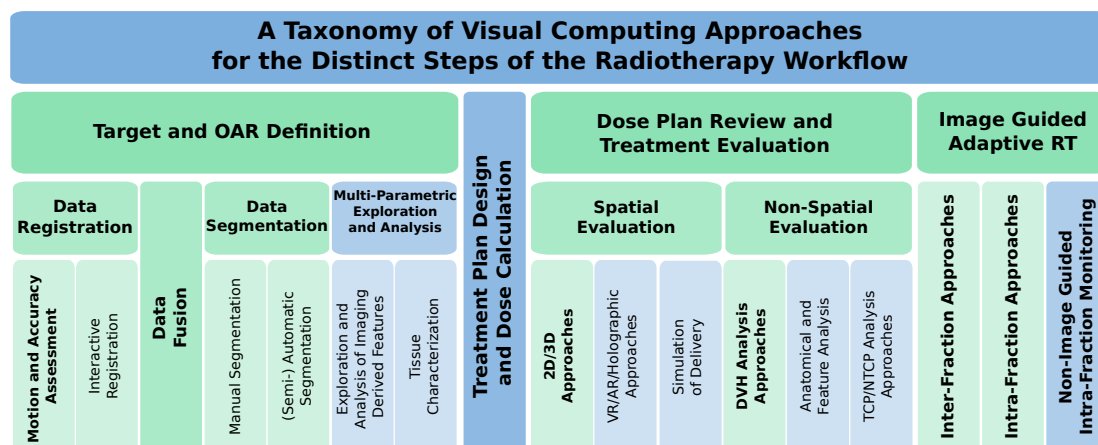


Figure 2.12: Treemap representation of the first dimension of the taxonomy, related to the *Steps* of the RT workflow addressed in VC literature as presented in [SRM<sup>+</sup>19]. The categories in the green squares are related work within the scope of this thesis.

- Treatment Plan Design and Dose Calculation (omitted in this chapter)
- Dose Plan Review and Treatment Evaluation (Section 2.3.3)
  - Spatial Evaluation (subcategories omitted)
  - Non-Spatial Evaluation (subcategories omitted)
- Planning Strategies for Image Guided Adaptive RT (Section 2.3.4, subcategories omitted)

## 2. Adoption of the proposed methods within clinical practice.

Knowing whether previous work has been (partially) integrated into clinical routine is anticipated to give insights into unsolved issues, into challenging future pathways, and into topics that upcoming joint VC/RT research could tackle. This dimension is more related to future directions and is therefore omitted in this chapter and can be found in the previous survey [SRM<sup>+</sup>19].

The full taxonomy description based on 105 papers (out of 601 candidates) with additional categorizations (whether an evaluation was conducted and what kind of evaluation) can be found in the previous survey [SRM<sup>+</sup>19].

### 2.3.2 Target and OAR Definition

After all images are acquired, the tumor with its respective volume definitions and the adjacent OARs are delineated. Multiple sub-tasks are involved in this step, ranging from data exploration and analysis, data registration, data fusion to data segmentation (automatic or manual). These are crucial steps in the workflow, as the subsequent treatment design and dose calculation will be directly influenced by any inaccuracies.

### Data Registration

Previous work related to data registration revolves around two major topics: *motion and accuracy assessment*, and *interactive approaches for registration*.

**Approaches Related to Motion and Accuracy Assessment** — As discussed previously, tumor motion represents a challenge in planning and delivery of radiotherapy [KMB<sup>+</sup>06]. In lung tumor treatment, 4D data for treatment planning in the presence of respiratory motion have been employed to several case studies. Deformable image registration (DIR) is an important component [RCCW05]. The amount of data generated with 4D imaging significantly increases the time needed for image review and target volume delineation, and DIR can be used for contour propagation [OdXJB<sup>+</sup>07] to reduce the workload of manual delineations.

Motion-encompassing methods use DIR to derive a single scan out of a 4D-CT scan for target delineation, which represents the tumor in its time-averaged mid-position [WSvD08]. Furthermore, DIR can be used to model breathing motion. Ehrhardt et al. [EWR<sup>+</sup>08] use DIR for the generation of a mean motion model of the lung, to predict the breathing motion of a patient without the knowledge of 4D information by matching the model. The motion is visualized by color encoding the displacement field magnitudes. Cover et al. [CLS06] demonstrate the standard approach employed for the visualization of motion in 4D-CT lung data, which comprises simple color intensity projections. Although very simplistic, this kind of images are common for the representation of motion or deformation during registration and fusion.

Registration is accompanied by uncertainty, primarily related to the inherent characteristics of the different imaging modalities that are co-registered. In addition to this, different registration algorithms may bring different types of uncertainty, related to localization accuracy or robustness [KBP<sup>+</sup>07]. This might be an important aspect to consider, for instance when used for dose warping [VLM<sup>+</sup>15]. The literature on registration methods is vast [FVW<sup>+</sup>11, KBD16, MV98, SDP13, VMK<sup>+</sup>16, ZF03] and different algorithms can be employed, each with different strengths and implications. In particular, the use of non-rigid registration requires the selection of parameters, which can yield results with large variability [ESS12, RPSWI10]. In other cases, the lack of an objective ground truth in the validation of registration creates the need for manual registrations by experts, which introduces uncertainty that is related to inter-observer variability.

The accuracy of the registration method needs to be analyzed and validated. Visual assessment is one way to verify that the accuracy is sufficient enough for the use in planning. In the study of Hamdan et al. [HBR<sup>+</sup>17] checkerboard visualizations are used to verify the alignment of the registration between MRI and CT images for prostate images together with contours.

**Interactive Registration Approaches** — Interactive rigid image registration of multiple imaging modalities using a volume-view-guided system has been developed by Li et al. [LJYS05]. To distinguish each individual volume in the registration process, mono-color visual representations are used for each image modality, such as red, green,

or blue. The color distribution on the voxel volume or a sub-volume can be used as registration criterion, where the homogeneity of the color distribution is used as an indicator for an optimal match. Interactive DIR using landmarks to steer the algorithm has been presented by Cheung et al. [CK09]. Landmarks can be added, removed, and adjusted between repeated registrations. In their approach, landmark pairs were based on visual correspondences, identified by the user on the images to be registered. The visualization methods used for showing the quality include checkerboard display of the fixed and moving images, 3D visualization of the deformation field using glyphs overlaid on a slice of the target image, and a warped grid to show the transformation warping.

### Data Fusion

Single modality may not provide enough information with respect to tumor tissues, as well as the tissues that surround target organs. Combining different modality images can be a necessary tool in cancer treatment [LSBP18, PBC<sup>+</sup>16]. The specifics of the integration and combination of various channels of data information is done through multi-modality image fusion. Lawonn et al. [LSBP18] recently authored a survey on the visualization of multi-modal medical data. Furthermore, an overview on volume visualization with a focus on medical applications is given by Zhang et al. [ZEP10]. Therefore, we focus on data fusion restricted to radiation treatment planning. Image fusion, i.e., the combination of various images into a single image, is required for an integrated interpretation of the complementary information in the underlying imaged structures. For example, PET/CT or PET/MRI data can be fused to combine functional and anatomical information [LSBP18]. Often, the different modalities are overlaid and presented with a color-encoded scheme. An overview on medical image fusion in general is given by James and Dasarathy [JD14].

An approach that goes beyond the mere color-encoded, overlaid representation of fusion is proposed by Kim et al. [KCEF07]. The authors suggest an entire workflow for interactive multi-volume visualization and the fusion of PET/CT images of lung and brain. The images are initially segmented using a fuzzy *c*-means cluster analysis. Subsequently, the resulting segmentation map, together with the initial PET and CT data, are rendered, fused, and interchanged. In the work of Chavan et al. [CT14], an approach for multi-modality image fusion is employed with the purpose of providing a better visualization (i.e., representation), accurate diagnosis, and appropriate treatment planning. In this work, different *fusion rules* are employed and evaluated against each other in order to determine which are the ones that carry less uncertainty, i.e., noise or visual artifacts, with a focus on uncertainty minimization. Illustrative rendering, which combines anatomical information from CT scans with functional information from PET, is found in the work of Merten et al. [MGLS<sup>+</sup>16]. Illustrative rendering techniques, combining order-independent transparencies with boundary enhancements and silhouettes, are intended to provide an excellent spatial perception and evaluation of tumor position, as well as metabolic and therapeutic agent activity.

Additional information has been incorporated with the inclusion of MRSI data in the

fusion process [NLK<sup>+</sup>14]. Graves et al. [GPN<sup>+</sup>01] present an initial attempt to include 3D MRSI information in the planning process with basic viewing of MRSI data as fixed contours embedded within MRI and CT data. The fusion of multiple MR images (T1, T2, and MRSI) is proposed by Marino et al. [MK11] using a score volume, which takes into account each of the three acquisition types. The MRSI score is based on detecting areas of increased chemical ratios indicating the possibility of cancer.

### Data Segmentation

For the definition of the tumor target and the surrounding organs at risk, conventional approaches involve *manual segmentation* through expert delineation and (*semi-*)*automatic segmentation* methods. An overview on medical image segmentation can be found in Pham et al. [PXP00] or in the book of Birkfellner [Bir14], and — with a focus on interaction — in the work by Olabarriaga and Smeulders [OS01]. A review on deep learning in medical imaging segmentation, focusing on MRI data, was recently given by Lundervold and Lundervold [LL19].

**Approaches Related to Manual Segmentation** — Manual delineations, although conducted by expert radiologists, might result in errors due to inter-observer variability [PM06]. This well-known problem affects the entire RT workflow [GEH<sup>+</sup>02].

**Approaches Related to (Semi-)Automatic Segmentation** — Automated segmentation algorithms can greatly reduce the delineation time and the efforts of a human expert. For example, automatic segmentation based on statistical shape modeling has been proposed by Seim et al. [SKH<sup>+</sup>08] for the segmentation of pelvic bones, or by Vik et al. [VBS<sup>+</sup>12] for the segmentation of pelvic organs. However, if automatic segmentation is employed, the resulting segmentation needs to be verified, before used for dose calculation. Three main sub-topics can be regarded within this category: approaches *aiding* the segmentation of relevant structures, approaches *enhancing* the segmentation outcome by post-processing, and approaches *assessing* the outcome of the segmentation. All three subcategories incorporate user interaction with the segmentations, which has been discussed by Ramkumar et al. [RDK<sup>+</sup>16]. The *enhancement category* was considered out of scope and can be found in the original work [SRM<sup>+</sup>19].

Within the *aiding* category, de Geus et al. [dW96] propose an approach for the detection, modeling, and visual stylization of structures of interest from CT images. Stylization, within the work of de Geus, is defined as a combination of segmentation and 3D visualization, where the resulting segmentation of the critical structures conforms to the bounding volume of the real shape. Moreover, assisted contouring can be employed to reduce some of the manual workload, or adjust the result of automatic segmentations. Zindy et al. [ZMBL00] propose assisted contouring based on scattered data interpolation methods. Instead of warping individual contours, a surface is interpolated through all data points that have already been placed on contour boundaries. This surface can be iteratively refined by adding points on the CT slices. Additionally, sketch-based editing tools for segmentation have been proposed by Heckel et al. [HMTH13], considering image

information for extrapolation, as well as previous and contradictory inputs. Other, more complex approaches involve the work of Akino et al. [AOM<sup>+</sup>14] for the automatic estimation of tumor motion using segmentation of cine-MRI, with the detection of feature points. Motion vectors are calculated and applied to contours, while a potential ITV is calculated from the accumulation of GTVs. This involves the incorporation of motion information from cine-MRI and 4D-CT data. Raidou et al. [RKS<sup>+</sup>16] employ a visual analytics approach to improve classifier design for brain lesion detection using features derived from diffusion imaging. This semi-automatic approach integrates the knowledge and skills of specialist users with automatic methods for smart feature selection and for the evaluation of the classification outcome.

Within the *assessment category*, Raidou et al. [RMB<sup>+</sup>16] propose a visual tool to facilitate the exploration and analysis of the outcomes and errors of automatic segmentation methods, supporting cohort and individual patient investigation for the detailed assessment of their pelvic organ segmentations. This work has been extended later on by Reiter et al. [RBGR18], in a web-based visual analytics approach to facilitate understanding how the shape and size of pelvic organs affect the accuracy of automatic segmentation methods.

### 2.3.3 Dose Plan Review and Treatment Evaluation

In this category, we focus first on the *spatial* evaluation of the dose plan, i.e., the assessment of the planned dose distribution for eventual changes, and then, on the *non-spatial* evaluation of the treatment with respect to actual tumor control and potential complications, which involves topics such as DVH analysis, inter-fractional changes and radiobiological (TCP and NTCP) modeling. Quality assurance today still lacks formalized standards and may vary from institution to institution. A survey analyzing the institutional differences for planar IMRT quality assurance is presented by Nelms and Simon [NS07].

#### Spatial Evaluation

The previously proposed approaches for the visual representation of planning results and for the facilitation of plan reviewing are classified into three main categories. Conventionally, *2D visual representations* of the planned dose distributions have been used, which evolved into or are combined with *3D volume renderings*.

Additionally, *VR/AR and holographic approaches* have been proposed, as well as *simulation approaches* of the delivery step, which can complement the plan evaluation. Both are beyond the scope of this thesis, and the reader is referred to the original article [SRM<sup>+</sup>19].

**2D/3D Approaches** — Hahn et al. [HST87] first proposed 2D color encoded visualization as an aid to the comparison of treatment plans, taking advantage of the conventional cross-sectional representations of the patient contour and selected anatomical features. For the interpretation of the correlation between dose, target, and OARs, and the comparison of several plans, the authors propose the so-called images of regret, where color

is employed to denote limits of acceptability, i.e., areas in which the required dose levels are not satisfied.

Initial approaches on volume rendering in radiation treatment planning have been proposed already in the 90s, with the work of Levoy et al. [LFP<sup>+</sup>90], Miyazawa et al. [MYKO91], and Interrante et al. [IFP95, IFP96, Int97]. Levoy et al. discuss approaches that employ region boundary surfaces for the anatomy, polygonal meshes for the treatment beams, and isovalue contour surfaces for the dose distribution, enhanced by shading, texturing, fogging, and shadowing. Miyazawa et al. propose a 3D visualization system for use in radiotherapy planning simultaneously visualizing original 3D image data, segmentation, and isodose surfaces. Later, Interrante et al. tackled the issue of showing isodose surfaces and anatomical surfaces together — a typical multi-modal visualization problem. Semi-transparent isodose surfaces were the baseline method. They later enhance transparency with ridge and valley lines for better perception of the shape and depth of structures, such as the skin [IFP95], employ artist-inspired curvature-directed strokes, for the same purpose [IFP96], and investigate texturing of layered surfaces [Int97]. Alakuijala et al. [ALH97] present the Beam's light view, a texture mapping method to be used together with traditional 3D radiotherapy renderings from the beam's eye view and room's eye view. The utility of volume rendering as an alternative visualization technique to surface rendering for head and neck radiotherapy planning has also been discussed by Lee et al. [LJP<sup>+</sup>99].

Gambarini et al. [GDF<sup>+</sup>00] present a new toolkit for full volumetric shape and shape-transforming information from multi image sequences of absorbed dose, measured in tissue-equivalent phantoms. The visualization of the different isodose levels on the phantom data are rendered in 3D using a standard marching cubes algorithm. Multi-modal volume visualization is also described by Sibomana et al. [SDB<sup>+</sup>02], where Volumes of Interest (VoIs) are extracted, registered, resliced, and visualized for a head and neck application. The method of Kaiser et al. [KMK<sup>+</sup>04] targets the virtual simulation of a boost field in adjuvant radiotherapy of the breast and the visualization of dose distributions thereof. Lam et al. [LCS<sup>+</sup>13] conduct an evaluation of a multiscale texture analytic procedure for the detection of abnormalities and lesions in CT images of the pelvis, which is based on a visualization platform for the representation of treatment planning, CT image-guided positioning, and treatment delivery.

Recently, Fonseca et al. [FC16] propose SOFT-RT, a Software for IMRT simulations, which produces a 3D rendering of a set of patient images, including the tumor target definitions and the OARs, as well as the features and orientation of the radiation beams. The rendered outcomes represent the tissues exposed to radiation, as well as the amount of absorbed dose in the tumors and the healthy tissues. Abdo-Man [GCC<sup>+</sup>16] involves a pipeline (imaging, organ definition, 3D mesh generation, 3D printing) for the production of a 3D printed anthropomorphic phantom that can be used as a validation tool for dosimetry.

For *risk and/or uncertainty assessment*, several methods have also been presented. Brodin et al. [BMA<sup>+</sup>14] discuss an interactive decision-support tool for individualized risk-based

radiation therapy plan comparison. The tool displays dose-response relationships and other features related to normal tissue side effects, and it is meant for facilitating the optimization of a treatment plan, based on the aforementioned information, using a combination of dose-response curves and 2D views of the dose distribution on the patient anatomy. Zhang et al. [ZMN15] introduce a risk visualization method, based on clinical risk guidelines. The risk distributions are summarized in 2D visual representations on the patient anatomy, and provide a means for the visualization and assessment of the risks of secondary cancer in tissues of the human body. For the comparison and decision-making about an optimal plan among several alternatives, Gopal et al. [GS02] and Silva et al. [SRV16] discuss different approaches. In the work of Gopal et al., treatment plans are represented as points in a multidimensional space called *plan space*, where given specific selection criteria and clinical considerations, the user can obtain the best plan available tailored to the unique anatomy of each patient. Silva et al. propose an approach for the visualization of variability in treatment plans, in order to interactively explore and analyze an ensemble of possible dose plans. This work allows users to analyze the dose plan at two different levels: first, based on the isodoses, i.e., the radiotherapy dose iso-contours, across the alternative dose plans, and, second, directly at a voxel level. The visualization is based on the concept of contour boxplots [WMK13] and on multiple, interactive linked views.

### Non-Spatial Evaluation

With regard to non-spatial evaluation, three major topics have been discussed in previous work. We will concentrate on *DVH-related approaches* in this section.

Approaches that discuss the *analysis of shape and features* of tumors, or of affected organs, and approaches related to *radiobiological modeling*, i.e., the analysis of TCP and NTCP modeling, are beyond the scope of this thesis. The reader is referred to the original article [SRM<sup>+</sup>19].

**Approaches Related to DVH Analysis** — DVHs can be explored as a supplementary and summarized source of information, where no spatial inferences can be made due to the aggregation and representation of the dose against the volume in a graphical 2D plot. However, DVHs are good for the comparison of multiple cases, either alternatives for one patient or for cohort exploration. Maleike et al. [MUO06] propose the simulation and visualization of dose uncertainties due to inter-fractional organ motion. They simulate stochastic properties of the dose distribution to display probabilities of individual voxels, which receive doses above critical levels, as well as a diagram that shows the variability of the DVH.

For the visualization of setup errors, i.e., errors with respect to the patient position during treatment, Samanta et al. [SBR<sup>+</sup>17] propose DVH bands. The impact of setup errors onto the DVH is visualized by introducing random errors and calculating a series of DVHs for each structure, which may help to select the plan with lower influence of setup errors over another one. A similar approach for the visualization of a variety of

possible dosimetric outcomes using DVH bands is proposed by Trofimov et al. [TUDB12]. Here, the intensity of the shading in the bands reflects the relative probability of the outcome.

Mayo et al. [MYE<sup>+</sup>17] follow an approach to develop statistical DVH metrics of previous plans. The current DVH gets visualized on top of the statistical DVHs to quantify the comparison of treatment plans with historical experience and across institutions. Alfonso et al. [AHN15] propose a method for assessment and decision-making in dose calculation. In this work, a dose volume histogram approach is followed. In particular, data from dose volume histograms provided by treatment planning systems with respect to target coverage and organ sparing are combined into a dose distribution index (DDI), i.e., an individual score for the comparison of radiotherapy planning variants.

### 2.3.4 Planning Strategies for Image-Guided Adaptive RT

In this category, we introduce adaptive approaches which try to optimize the treatment either by re-planning or by modification during the delivery. During the course of radiotherapy, both the tumor and the healthy surrounding organs are variable in size and position. This can be attributed to anatomical changes between fractions (inter-fraction) or to changes during beam delivery within one treatment fraction (intra-fraction). The former can happen, e.g., in patients with a tumor in the pelvic area, where the position is dependent on bladder and bowel filling, but changes can also occur due to weight loss and tumor shrinkage [KWCM13]. The latter can happen, e.g., in patients with lung cancer where the tumor moves with breathing. As the anatomy and geometry of a patient is based on medical images acquired at previous stages of the planning workflow, it might not be well-reflected anymore at the time of delivery. More details about IGART in general can be found in Yan [Yan06]. One way to compensate for these uncertainties is by including them into the PTV (or ITV) with appropriate safety margins as explained in the previous sections. Otherwise, Image-Guided Adaptive RT (IGART) tries to optimize dose delivery by taking into account intra- and inter-fractional image data. Current LINACs are equipped with on-board imaging, which can be used for IGART. For instance, cone-beam computed tomography (CBCT) imaging has become an integral part of radiation therapy, with images typically used for offline or online patient setup corrections based on bony anatomy co-registration with the planning CT. For some purposes, the image quality of CBCTs can be insufficient, and the use of contrast-enhanced CBCT imaging for adaptive radiotherapy has been proposed by Soevik et al. [SRS<sup>+</sup>10].

**Approaches Related to Inter-Fraction**— To change the plan or to re-plan according to the recent state of anatomy every time, would be too time-consuming. An alternative is to keep the original plan, but recompute the accumulated dose based on the current state of anatomy. If the deviation of the accumulated dose deviates too much compared to the planned dose, re-planning might be a better option. The calculation of the true dose distribution for a patient requires accurate DIR to reduce dose warping uncertainties due to the registration algorithm [VLM<sup>+</sup>15]. Registration for IGART has different problems



as there are regions within the images to be registered, where explicit correspondences cannot be established [KZD<sup>+</sup>09] for the reasons mentioned above. The work of Song et al. [SSB<sup>+</sup>05] evaluates the efficacy of various image-guided adaptive radiation therapy techniques to deliver and escalate dose to the prostate. Furthermore, the normal tissue sparing potential of adaptive strategies in radiotherapy of bladder cancer has been shown by Wright et al. [WRH<sup>+</sup>08]. Open source software suites, such as DIRART [YBN<sup>+</sup>11] or SlicerRT [PLW<sup>+</sup>12] targeting multiple aspects of IGART including registration and visualization, are freely available. A multi-modality image registration and visualization framework, which is addressing the transfer of structures of RT plans onto follow-up images for re-planning, has been presented by Wang et al. [WLF09]. An alternative to dose warping is Cherenkov imaging, which can estimate the dose in real time in 2D [JZG<sup>+</sup>14] and in 3D [BAG<sup>+</sup>17].

**Approaches Related to Intra-Fraction** — For lung cancer patients, it is more important to monitor the tumor position during the fraction, ensuring a good setup, as well as monitoring of the breathing motion range. Tumor tracking algorithms have been developed that are able to follow the lung tumor based on a combination of in-beam imaging and kilo-voltage (kV) imaging. Furtado et al. [FSS<sup>+</sup>13] implement a real-time tumor motion tracking by 2D/3D registration using on-board kV imaging, which allows for a reduction of the PTV and therefore healthy tissue sparing. Chang et al. [CCT<sup>+</sup>14] propose an approach that integrates real-time ultrasound (US) for the visualization of the target, which is registered to CT images.



# A Multi-Modal Visualization Framework for Radiotherapy Planning

**This chapter is based on the publication:**

**M. Schlachter**, T. Fechter, U. Nestle, and K. Bühler. Visualization of 4D-PET/CT, Target Volumes and Dose Distribution: Applications in Radiotherapy Planning. Proceedings of MICCAI Workshop on Image-Guided Adaptive Radiation Therapy, The MIDAS Journal, 2014. [SFNB14]  
<http://dx.doi.org/10.54294/lgcmk1>

The original paper was adapted in terms of formatting and type-setting to fit this template and to increase readability. Minor corrections, such as fixing typos or unclear wording, were applied, and the abstract was removed.

### 3.1 Introduction

For lung cancer, the most prominent functional imaging system in use is PET along with CT as the anatomical imaging modality. PET/CT imaging with the 18f-fludeoxyglucose (18FDG) tracer is an accurate diagnostic method for non-small cell lung cancer, and is used for the delineation of the gross tumor volume (GTV) [NWHG09]. Respiration causes target areas to move that can not be captured by the planning CT, which is only a static image. 4D imaging techniques can be used to image patients under free breathing conditions and define target volumes representing the lesion over the whole breathing cycle. For example, movement related volume definitions are possible by using time-averaged CT scans for planning [WSvD08]. 4D-PET/CT can be used for delineating the tumor on images of each breathing phase, and the union of the contouring can be used to define target volumes, e.g., the internal target volume (ITV) [NWHG09]. The inspection of target volumes is usually done slice-wise and often combined with a video showing a maximum intensity projection (MIP) of the 4D data sets. However, this makes it hard to capture the real 3D motion of target areas, and might give false impressions about tumor coverage by the defined target volumes. Therefore, a 4D-PET/CT visualization system can assist RT planning and validating treatment plans, especially in the presence of moving structures like tumors of the chest and the upper abdomen.

In this chapter we present a 3D multi-modal visualization framework, which focuses on the validation and inspection of target volumes and dose distribution of RT plans. In order for a 3D visualization to assist physicians in this task, we define the following major requirements, which need to be addressed:

1. Support for 4D (3D+time) PET and CT data sets and fusion of these image modalities: PET and CT signals should be fused in a 3D rendering. Support for changing time bins should be provided for giving access to the whole breathing cycle of the patient.
2. Visualization of segmentation data: Defined structures such as GTV, ITV, planning target volume (PTV), or organs at risk (OAR) should be included and combined with the 3D visualization of PET and CT for evaluating the spatial configuration and ensuring optimal coverage of moving target areas.
3. Visualization of dose information: Visualizing dose information as isodose surfaces together with defined structures like the GTV, ITV, or OARs should allow users to evaluate the spatial configuration and coverage of moving target areas complementary to dose volume histograms (DVH).
4. Clipping and/or masking parts of the volume: Hiding parts of the volume, which might not be relevant in the current situation (e.g., visualize only the PET signal inside a region of interest (ROI)), should be supported.
5. Interactivity and pre-processing: There should be no pre-processing involved such as re-sampling data sets to the same size or offline volume fusion into a new data set.

The parameters such as data sets to be visualized, clipping, and visual appearance, should be modifiable on-the-fly.

The proposed visualization framework performs fusion of 4D-PET/CT images, combined with defined target volumes and segmentation information of OARs. Furthermore, the visualization of dose volumes provides the necessary information for visually reviewing and validating the dose distribution of the computed treatment plan. We present an implementation of such a system, and present results of how it can be used to review target volumes and dose distributions for a lung cancer patient.

## 3.2 Related Work

SlicerRT [PLW<sup>+</sup>12] is a freely available RT research toolkit implemented as an extension to 3D Slicer [FBKC<sup>+</sup>12]. It has functionality for visualizing isodose surfaces and calculating and plotting dose volume histograms (DVH). The visualization is based on the Visualization Toolkit (VTK) [SML06]. The Medical Imaging Interaction Toolkit (MITK) [WVW<sup>+</sup>05] provides a platform similar to 3D Slicer, with a plug-in system, and combines functionality of VTK and ITK [ISNC05]. It provides DICOM data import, visualization, and various plug-ins, e.g., for registration and segmentation, and supports 4D data sets. However, to the best of our knowledge, neither SlicerRT nor 3D Slicer nor MITK support direct volume rendering (DVR) of multiple volume data sets combined with translucent boundary visualization of segmentation data.

State-of-the-art visualization approaches for a number of our requirements exist. Visualization of PET/CT with advanced functionality for fusion with focus on enhancing visibility of ROIs can be found in the work of Jung et al. [JKF12] and Zheng et al. [ZCM13]. Hadwiger et al. [HBH03] and Beyer et al. [BHWB07] combine DVR of multi-modality data sets with segmentation data, and use segmentation information for enabling or disabling volumes per segmentation object, and support different rendering modes such as MIP or iso-surfacing. Translucent boundary visualization of segmentation data and DVR with advanced support for clipping can be found in previous work [TIP05, BBP<sup>t</sup>HR08, KGB<sup>+</sup>09]. 4D approaches focused on extracting and visualizing tumor motion [HWS<sup>+</sup>07] and organ motion [MKN13] in CT images exist as well. However, none of the above-mentioned approaches is available in platforms like 3D Slicer or MITK.

## 3.3 Data Sets

The data sets we focus on consist of the following types: 4D-PET/CT, planning CT, segmentation data sets, and dose volumes. The planning CT has a voxel size of 1.17 mm x 1.17 mm x 3 mm and pixel dimensions of 512 x 512 x 107. Segmentation data sets represent OARs and target volumes such as GTV and ITV. They were converted from the DICOM RT Structure Set format to binary volumes by rasterizing the slice-wise polygons in the planning CT resolution. The 4D-CT consists of 10 time bins with a voxel

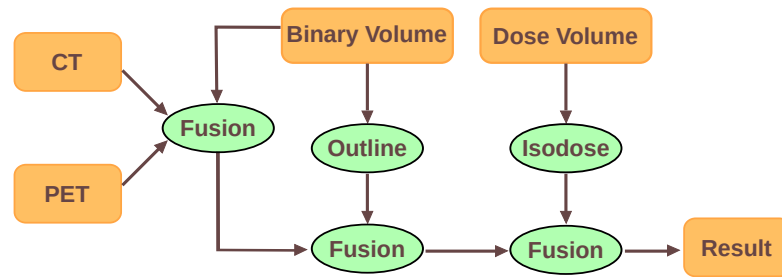


Figure 3.1: Overview of the fusion pipeline used in our ray casting implementation.

size of 1.17 mm x 1.17 mm x 2 mm and pixel dimensions of 512 x 512 x 77. The 4D-PET data set has a voxel size of 4 mm x 4 mm x 4 mm and pixel dimensions of 144 x 144 x 45 consisting of 10 time bins. The dose volume holds the relevant dose distribution information in reference to the planning CT and was exported from the planning system software. It has a voxel size of 2.5 mm x 2.5 mm x 3 mm with pixel dimensions of 212 x 119 x 107.

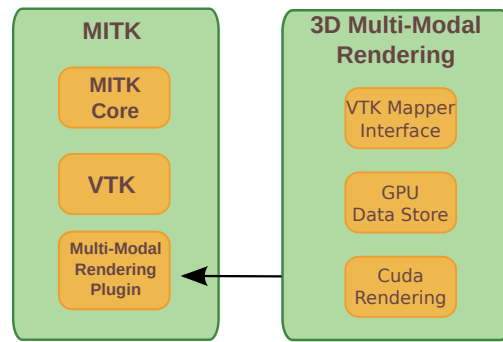
### 3.4 3D Multi-Modal Rendering Core

The functionality of the 3D multi-modal rendering consists of three main parts: fusion of PET and CT, rendering of binary volumes, and isodose rendering of dose volumes.

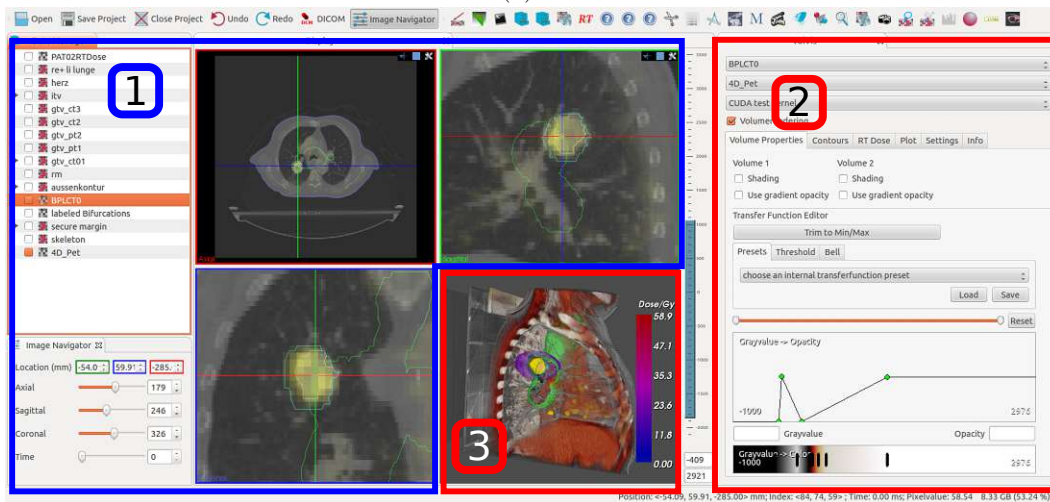
The volume rendering is based on ray casting with front-to-back blending [KW03]. Figure 3.1 gives an overview of the fusion pipeline. The fusion of PET/CT is implemented on the data level. For each voxel, color and opacity values are fused by a weighted linear combination and blended in front-to-back order in the ray casting algorithm. The fusion can be combined with information from binary volumes to define ROIs that encode which modality to visualize. This can be either just one modality (e.g., only PET inside the ITV), or the fused PET/CT, or background for hiding parts of the volume.

Binary volumes, which represent target volumes and segmentation of OARs, are visualized as a surface. Each volume gets rendered in a separate pass into a depth texture and a texture for color and opacity. The first hit of the viewing ray with the surface of the binary volume determines the depth value (similar to rendering the front face of a triangulated mesh). Color and opacity values can be assigned to each binary volume individually. For each intersection point, we include the color and opacity values into the blending scheme of our ray casting algorithm. By this we can blend surfaces at the correct depth, and therefore preserve their spatial ordering.

Dose information is rendered as isodose surfaces. We extract the surfaces during the ray casting pass by testing whether a voxel belongs to a defined isodose surface. If a voxel belongs to a surface, we include the color and opacity of the dose value into the blending scheme of our ray casting pass. The respective dose parameters for the surfaces can be specified as a list of values in Gray units.



(a)



(b)

Figure 3.2: (a) Overview of the core components of our rendering framework and MITK integration. (b) Screen-shot of the MITK platform with the integration of our 3D multi-modal rendering and plug-in.

### 3.5 Implementation and Integration

The 3D multi-modal rendering framework is mostly implemented in CUDA [NVI11], and consists of three main parts (see Fig. 3.2a): the data store module, the rendering module, and an interface to VTK. The data store is responsible for storing volumes in GPU memory and makes them available to our rendering module. Data sets are organized in a unified coordinate system, which takes into account spatial transformations between data sets. The core of the rendering module is responsible for PET/CT fusion, binary volume rendering, and dose volume visualization.

Our visualization framework has been integrated in MITK. Figure 3.2b shows the GUI of the MITK platform. Part 1 of Fig. 3.2b shows already available functionality of MITK. This includes a data set manager, image navigator (3D+time navigation), and 2D slice

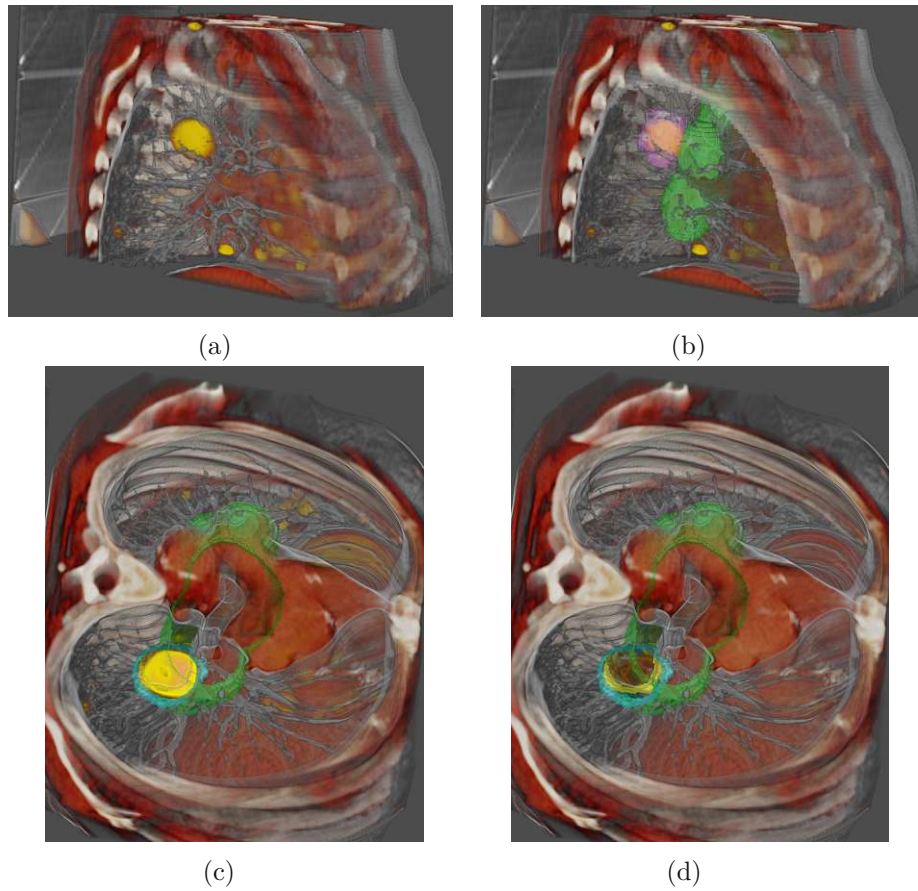


Figure 3.3: Fusion of a different number of modalities: (a) Fusion of PET, CT. (b), (c) PET, CT, and segmentation. (d) CT and segmentation. Different parameters for clipping were applied to hide parts of the thorax.

views. The integration of our multi-modal rendering core is realized via a MITK plug-in, which is the connection between MITK and our rendering core (see Fig. 3.2a). Figure 3.2b Part 2 shows the GUI of our MITK plug-in. It communicates with our rendering core via a VTK interface (see Fig. 3.2a), and is responsible for setting and changing parameters such as data sets, their visual appearance and parameters for clipping and fusion. It is also responsible for calculating and plotting the dose volume histogram for selected target volumes and OARs. Finally, the result of our 3D rendering is integrated and replaces the standard 3D view of MITK (see Fig. 3.2b Part 3).

### 3.6 Results and Discussion

Our 3D multi-modal rendering framework combines information of PET, CT, segmentation, and dose information. Figure 3.3 shows qualitative results of our 3D rendering. The



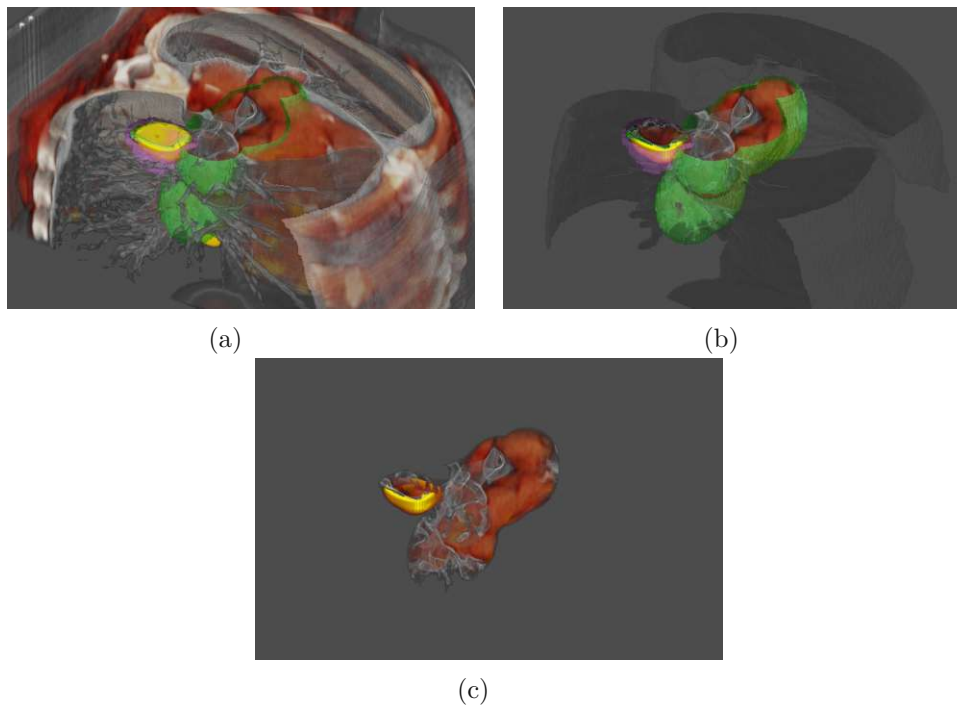


Figure 3.4: (a) Fusion of PET and CT with surface rendering of binary volumes. (b) Fusion of PET and CT with binary volume information. The different binary volumes represent either background, one modality or the fused PET and CT. (c) Same as (b) without surface rendering of binary volumes. Clipping was applied to hide parts of the thorax.

result of the 4D-PET/CT fusion is shown in Fig. 3.3a (Requirement 1). Segmentation data sets, the ITV, and a safety margin around the trachea (SMT), were added in Fig. 3.3b (Requirement 2). Clipping was applied to hide parts of the thorax (Requirement 4). The parameters can be adjusted depending on the ROI (see Fig. 3.3c). Volumes can be enabled or disabled (the PET was disabled in Fig. 3.3d), and the time bins can be changed from within our MITK plug-in (Requirement 5). Seeing the information of modalities inside a target volume can help to verify their coverage of the tumor, or to analyze their spatial configuration in respect to OAR segmentations, especially when they intersect with regions where the delivered dose should be low (see Fig. 3.3d).

Figure 3.4 shows results of the 4D-PET/CT fusion using information of binary volumes (Requirement 4). For comparison, the fusion without segmentation information of PET and CT, together with binary volumes of ITV, GTV, lung, and SMT are shown in Fig. 3.4a. Clipping was used to hide parts of the volume and view the inside of the segmented structures. Figure 3.4b shows the result of fusion with binary volume information together with their surface rendering, and Fig. 3.4c without their surface rendering respectively. The inside of the lung is defined as background (BG), the SMT as CT, the ITV as PET

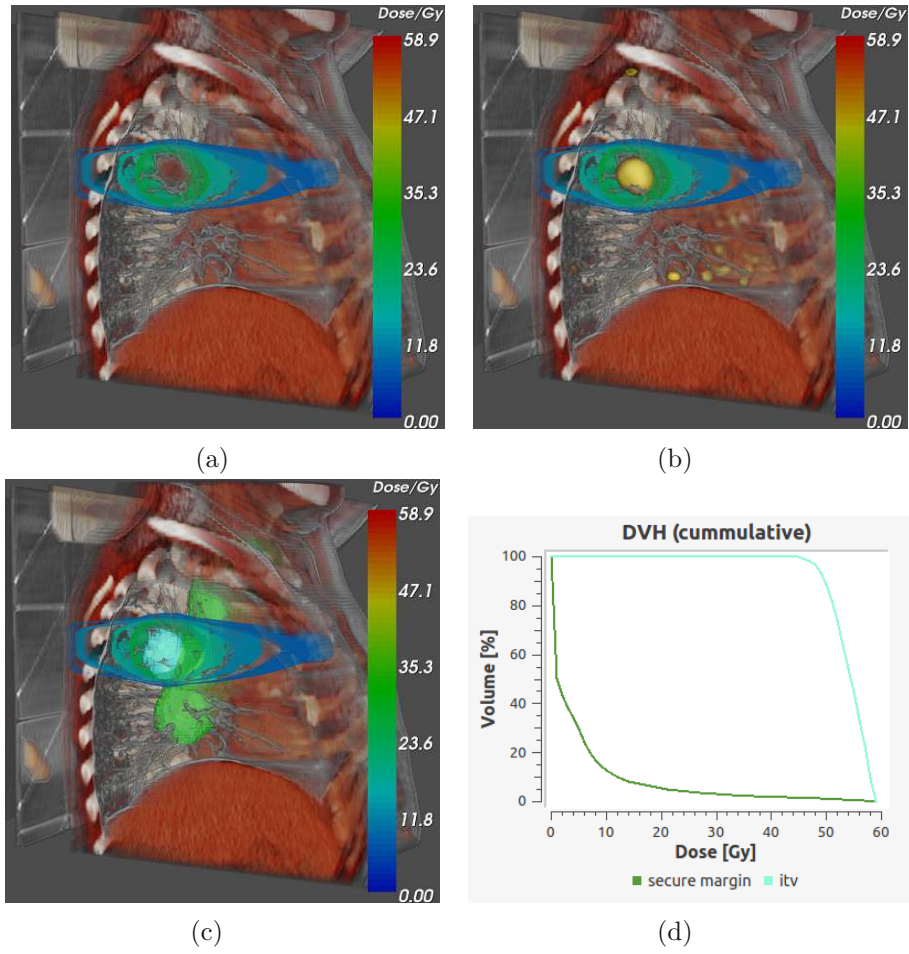


Figure 3.5: Fusion of dose information: (a) Fusion of the planning CT and four different isodose surfaces. (b) Additional fusion of PET. (c) Additional fusion of segmentation data sets. (d) Corresponding DVH of the segmentation data sets from (c).

and the GTV as CT. The assignment of image information is done in the same order, and results in the following mapping:

$$x \in \mathbb{R}^3, \text{label} : \mathbb{R}^3 \rightarrow \mathbb{N}, x \mapsto \begin{cases} 0 \text{ (BG)} & \text{if } x \in \text{lung} \setminus (\text{SMT} \cup \text{ITV} \cup \text{GTV}) \\ 1 \text{ (PET/CT)} & \text{if } x \in \text{SMT} \setminus (\text{ITV} \cup \text{GTV}) \\ 2 \text{ (PET)} & \text{if } x \in \text{ITV} \setminus \text{GTV} \\ 3 \text{ (CT)} & \text{if } x \in \text{GTV} \end{cases}$$

Results of the dose visualization are shown in Fig. 3.5 (Requirement 3). We defined four different isodose values, and used clipping to hide parts of the thorax, which would occlude the target area. A qualitative result of fusing the planning CT with the isodose rendering is shown in Fig. 3.5a. Figure 3.5b shows the result of PET/CT fusion and

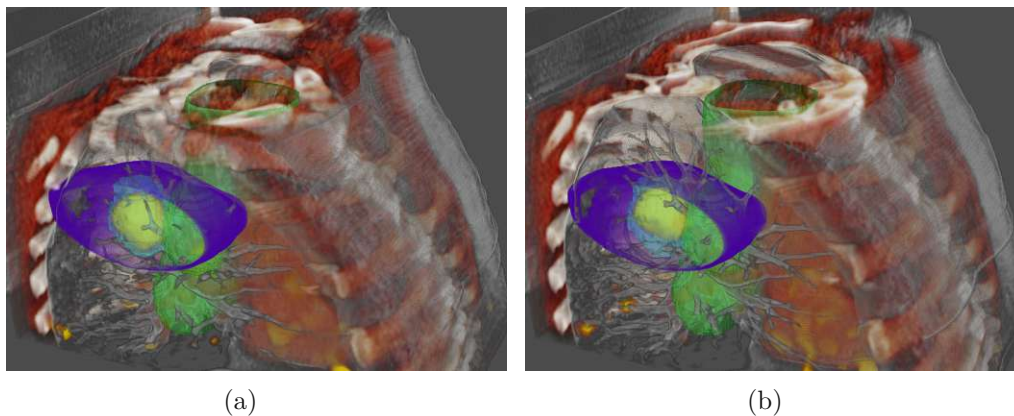


Figure 3.6: Fusion of 4D-PET/CT with segmentation data sets (ITV, SMT) and the 15 Gray isodose surface. (a) and (b) show different time bins of the patients' breathing cycle. Clipping was applied to hide parts of the thorax.

isodose rendering. In Fig. 3.5c the PET was disabled and the binary volumes of ITV and SMT were added. Our MITK plug-in also supports DVH computation and visualization of the segmentation data sets, which were selected for the 3D rendering (see Fig. 3.5d).

Figure 3.6 shows two different time bins of a 4D PET/CT data set, together with segmentation data (ITV, SMT) and the 15 Gray isodose surface. Using the animation plug-in of MITK (or changing time bins manually) provides an interactive 4D visualization of a breathing patient. Comparing Fig. 3.6a with Fig. 3.6b shows how the PET signal moved inside the ITV. This can help to analyze the movement (due to respiratory motion) of target areas inside static structures or dose regions, which are represented by isodose surfaces. For example, the coverage of the ITV with the 4D-PET signal can be reviewed, and, if necessary, adjustments can be made.

### 3.7 Conclusion and Future Work

By including our 3D multi-modality rendering framework into MITK, we implemented the Requirements 1–5 stated in Section 3.1. Making all this available to medical doctors gives them a set of tools, which they can use to interactively explore target volumes and dose distribution data of an RT plan. The proposed functionality can be applied to a multitude of scenarios including: checking the spatial configuration of target volumes defined on volumes of different modalities, checking the coverage of the ITV with the 4D-PET signal (respiratory motion of the tumor area), or the spatial configuration of dose areas inside OARs.

Future implementations could include motion information, e.g., including information from registration algorithms for motion modeling and definition of movement related target volumes, as well as the extraction and visualization of spatial uncertainty. An extended user testing will explore the possible use of this tool in clinical practice.



# Visualization of 4D Multi-Modal Imaging Data: Applications in Radiotherapy Planning

This chapter is based on the publication:

M. Schlachter, T. Fechter, S. Adebahr, T. Schimek-Jasch, U. Nestle, and K. Bühler. Visualization of 4D multimodal imaging data and its applications in radiotherapy planning. *Journal of Applied Clinical Medical Physics*, 18(6):183–193, 2017. [SFA<sup>+</sup>17b]

<https://doi.org/10.1002/acm2.12209>

The original paper was adapted in terms of formatting and type-setting to fit this template and to increase readability. Minor corrections, such as fixing typos or unclear wording, were applied, the abstract was removed, and the introduction was adjusted.

## 4.1 Introduction

Modern radiation therapy aims at delivering high doses very precisely to a target volume with steep dose gradients to the surrounding organs at risk (OARs). Prerequisites therefore are very precise delineations. Although image-guided radiation therapy allows for treatments with high precision, it is only as good as the accuracy with which the target is known [Nje08]. A high degree of uncertainty is associated with the delineation of the target volume [Nje08] and the traditional way to deal with these types of uncertainties is by extending delineations with an appropriate margin. For a moving target, one commonly applied strategy comprises the generation of an internal target volume (ITV) [WL99] from different time bins of 4D imaging data, for instance 4D-CT. However, it remains challenging to efficiently navigate, visualize, and interpret these 4D imaging data [Rat04]. Due to limited time of physicians and lacking tools for dealing with 4D data efficiently, time effort is often reduced by using only the two extreme phases for target delineation [JHP<sup>+</sup>15]. This neglect of large parts of the movement correlated data introduces another source of uncertainty, and might lead to inaccuracy in target volume delineation. Furthermore, as additional information of co-registered functional imaging is increasingly employed in target volume delineation (e.g., 4D-PET), the problem is aggravated, when these additional imaging data should be used in the planning process.

Visualization to efficiently use 4D multi-modal imaging data is to the best of our knowledge not sufficiently implemented in currently available systems. Due to this unmet need, we developed a 4D multi-modal visualization system (4D-VS) that features fusion of 3D/4D multi-modal image information, delineations of tumors and OARs as well as dose distribution data. A high emphasis was laid on interaction to allow for changing time bins, clipping volume information, segmentation, and isodose surfaces.

In this chapter we present a visualization system and its evaluation with respect to specific radiotherapy planning tasks. The rendering framework is based on a revised and extended list of requirements, which was presented in Chapter 3.

### 4.1.1 Clinical Requirements and Tasks

Based on discussions with radiation oncologists, we developed a list of requirements to support radiotherapy planning tasks, which incorporate 4D multi-modality imaging. This includes visualization features, which should be available early in the radiotherapy workflow when target and OARs are delineated, and in a later phase after the dose calculation was performed. Including 4D imaging data should make it especially suitable for cases with moving targets, for instance lung tumors, to ensure high accuracy delineations and coverage over the breathing cycle. Our visualization system is based on the following requirements:

1. Visualization and fusion of 4D (3D+time) multi-modal data sets with easy support for changing time bins and data sets.

2. Joint visualization of segmentation data, such as ITV and OAR, and multi-modal data sets.
3. Joint visualization of dose information (isodose surfaces), multi-modal data, and segmentation data.
4. Clipping and/or masking (using segmentation data) in the volume visualization.
5. Support of mixed resolution data sets without re-sampling and no pre-processing for volume fusion.
6. Interactive modification of parameters for clipping and visual appearance (e.g., fusion parameters).
7. Support for navigation from the volume visualization to the slice views.
8. Support for highlighting volume intersections.

Furthermore, we identified three clinically relevant tasks, which form the basis to evaluate the visualization system:

- T.1 Quality assessment of ITV contours
- T.2 Classification of tumor location
- T.3 Assessment of dose distribution.

Our tasks are motivated by patients who are scheduled for and/or treated by stereotactic body radiation therapy (SBRT). Task T.1, although not specific to SBRT, is very important when using SBRT due to the high doses involved. It will usually be performed simultaneously with the actual delineation task of target volumes. However, if the target is delineated using two extreme phases only, quality assessment for the remaining time bins is an equally relevant task. The classification of tumor location (Task T.2) is relevant to decide whether the patient should be treated with SBRT or receive conventional treatment. The assessment of dose distribution (Task T.3) is also not specific to SBRT, but due to the high doses involved, visualization techniques other than using the dose volume histograms (DVH) can be of interest in complicated cases, where the target is spatially close to an OAR.

#### 4.1.2 Related Work

Visualization of multi-modality data sets and the use of segmentation information for volume masking was presented by Beyer et al. [BHWB07]. Rendering multiple arbitrarily overlapping multi-resolution volumes was covered by Lux and Fröhlich [LF09], and advanced support for clipping the volume visualization using mesh data was presented by Kainz et al. [KGB<sup>+</sup>09]. Specific work on PET/CT visualization with sophisticated

functionality for fusion and clipping can be found in the work of Zheng et al. [ZCM13] and Jung et al. [JKF12].

There have been efforts to bring visualization approaches like the aforementioned ones to frameworks such as the Visualization Toolkit (VTK) [SML06]. However, VTK still lacks multi-volume rendering as reported by the visualization literature and extensions for multi-volume visualization, for instance [BL15], have not found their way into the framework yet. Research platforms, such as 3D Slicer [FBKC<sup>+</sup>12] and the Medical Imaging Interaction Toolkit (MITK) [WVW<sup>+</sup>05], which are tailored to medical applications, often use VTK as basis for the visualization. They offer solutions to more specific clinical applications or workflows, but they also target data processing aspects and try not necessarily to improve the visualization. For example SlicerRT [PLW<sup>+</sup>12] is an extension to 3D Slicer with radiotherapy specific functionality, but it is more focused on data processing.

Commercial software products are used in clinical routine. These are for instance Mirada (Mirada Medical, UK), RayStation (RaySearch Laboratories AB, Stockholm, Sweden), MIM [PPN<sup>+</sup>13], Velocity [KCUP13], and Oncentra MasterPlan (v4.3, Nucletron BV, Veenendaal, the Netherlands). But there is still a gap between what can be found in visualization literature and what has made its way into commercial products. To the best of our knowledge, none of the aforementioned products supports advanced visualization in 3D/4D as intended by our visualization system.

## 4.2 Methods and Materials

The main focus of our visualization system is to improve radiotherapy planning related tasks by including multi-modal volume visualization in an easy-to-use way. It is based on an in-house developed multi-modal rendering framework. Further interaction features are implemented alongside with the user interface within the MITK [WVW<sup>+</sup>04] platform. Parameters, which should be interactively modifiable by the user (Requirement 6), have dedicated user interface elements implemented as MITK plugins. We refer to this as 4D-VS. A video illustrating the main features (explained in the following) is available online [SFA<sup>+</sup>17a].

### 4.2.1 Multi-Modal Data Description

The rendering framework supports different types of data sources and the fusion thereof: imaging data, delineations, and dose distribution. This is represented by the three blocks in Fig. 4.1. Representative data for one patient as used in 4D-VS for the three clinical tasks T.1–T.3, can be found in Table 4.1. Data sets involved have different sizes and spatial resolutions. They cover different anatomical regions of the patient (e.g., 4D-PET/CT covers only a sub-volume of the full-body CT as shown in Fig. 4.2a) and are supported without further pre-processing. For our tasks, PET and CT are used as image information. However, image data from other modalities are also supported. Target and OAR delineations are represented as binary volumes and temporal delineations are



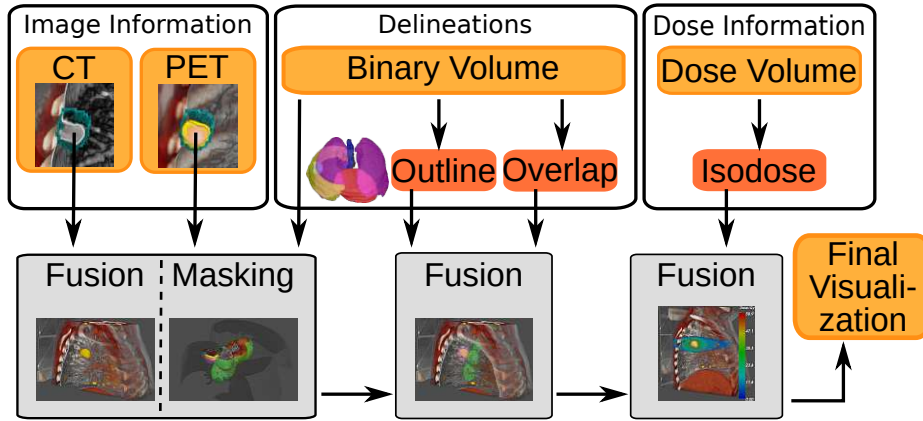


Figure 4.1: Schematic overview of image sources, which are combined in the 4D-VS visualization system.

supported. Dose distribution data sets are provided as 3D volumes with values in Gray (Gy) units, and were calculated using a treatment planning system (Oncentra MasterPlan v4.3).

#### 4.2.2 Multi-Modal Rendering Core

All volume visualizations take advantage of GPU acceleration, and are, for the main part, implemented using CUDA [NVI11]. Each type of data source gets handled in a slightly different way, and will in the end be combined by fusing the different data sources into a final visualization (see Fig. 4.1). The rendering framework organizes data sets in a unified coordinate system in GPU memory, which takes into account mixed spatial resolutions and transformations between data sets in all rendering algorithms (Requirement 5). 4D-VS uses direct volume rendering and fusion [Ehk<sup>+</sup>06] of mixed resolution volume data sets for volume visualization (Requirement 1). The rendering

Table 4.1: Representative imaging sources with sizes and resolutions of one patient used for the three clinical tasks.

Image Source	Resolution in [ $mm^3$ ]	Dimensions in [pixel]	time bins
full-body CT	1.37x1.37x4	512x512x234	–
4D-CT	1.17x1.17x2	512x512x89	10
4D-PET	4x4x4	144x144x45	10
planning CT	0.97x0.97x3	512x512x112	–
delineation	0.97x0.97x3	$\leq$ planning CT	$\leq$ 10
dose volume	5x5x3	90x61x112	–

is based on a GPU accelerated ray casting [KW03] algorithm, which uses the different data sources described above at discrete sample points during the evaluation the volume rendering integral [EHK<sup>+</sup>06].

### 4.2.3 Multi-Modal Data Fusion

For the fusion of image information an accumulation level intermixing technique [SS11] (color fusion) is used. Each sample point in the ray casting algorithm is a weighted linear combination of color and opacity values of the selected images (see Fig. 4.2). The weight of the linear combination can be modified via a slider allowing for adjusting the blending between volumes. The color and opacity values are defined per image source by means of a transfer function [EHK<sup>+</sup>06]. For 4D data sets the time bin can be changed via a slider in the user interface to select which phase of the breathing cycle should be visualized (see Fig. 4.2b and Fig. 4.2c). Example visualizations of the fusion are depicted in Fig. 4.2, where a full body CT is fused with 4D-PET (see Fig. 4.2a and Fig. 4.2b). Image data can be easily exchanged during the rendering. For instance in Fig. 4.2c, the 4D-PET was exchanged with 4D-CT, whereas all other parameters including the time bin, clipping, and user-defined rotations will be kept unchanged. This makes it possible to use multiple image information by simply exchanging the underlying data set. This implements Requirement 5 and parts of Requirement 6.

### 4.2.4 Visualization and Fusion of Delineations

Jointly visualizing delineations and image information (Requirement 2) is implemented by visualizing binary volumes using iso-surface rendering (see Fig. 4.3a). During iso-surface rendering we determine the surface positions of binary volumes, which are used in the ray casting algorithm for fusion with the volume information (see Fig. 4.3b). Color and opacity values can be assigned to each binary volume individually, and modified in the user interface. Determining the surface position preserves the correct depth when combining delineations with volume information using only the resulting color and opacity of the iso-surface rendering for the current sample point (accumulation level intermixing with exclusive opacity [SS11]). For better depth perception, an adapted Blinn-Phong model is used for shading [HBH03, EHK<sup>+</sup>06] during iso-surface rendering.

### 4.2.5 Visualization of Dose Distributions

For implementing Requirement 3, we use iso-surface rendering [EHK<sup>+</sup>06] for defined isovalues given in Gray (Gy) units. Multiple values can be set in the user interface to define more than one surface. Similar to binary volumes, we use fusion of the respective surface colors (accumulation level intermixing with exclusive opacity [SS11]) to jointly visualize isodose surfaces with volume information and delineations (see Fig. 4.4a). Additionally, the DVH for contours loaded within 4D-VS is visualized in a separate window to complement the anatomical views, and this is also necessary for Task T.3.

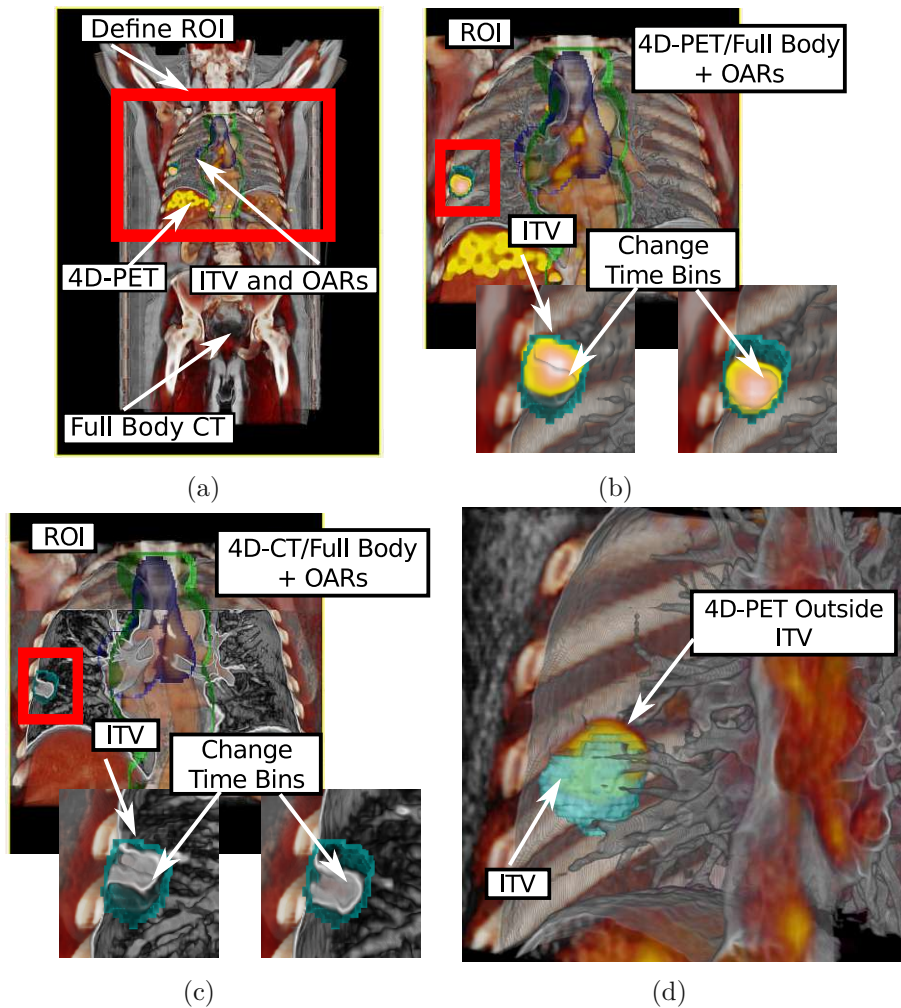


Figure 4.2: In (a) the full body CT is fused with 4D-PET and delineations. Data sets can be clipped to a region-of-interest (ROI) (b). Image information can be exchanged, for instance, in (c) the 4D-CT is used instead of the 4D-PET. A slider can be used to navigate time bins (see (b) and (c)) and access all image information over the whole breathing cycle. An example of an ITV, which does not cover the target, is shown in (d).

#### 4.2.6 Volume Masking using Delineation Information

Binary volumes can further be used for volume masking (similar to clip objects [WEE02]), which partly implements Requirement 4. Thereby the binary volume defines a ROI and can be used to enable or disable certain volume parts (similar approach as in Beyer et al. [BHWB07]). In Fig. 4.4b only the target and an OAR (trachea) is visualized by using their delineation information as a mask. The user can decide which information should be visible inside the mask. In the example only CT information is used for the trachea, whereas PET and CT are used inside the ITV. Furthermore, surface rendering of the

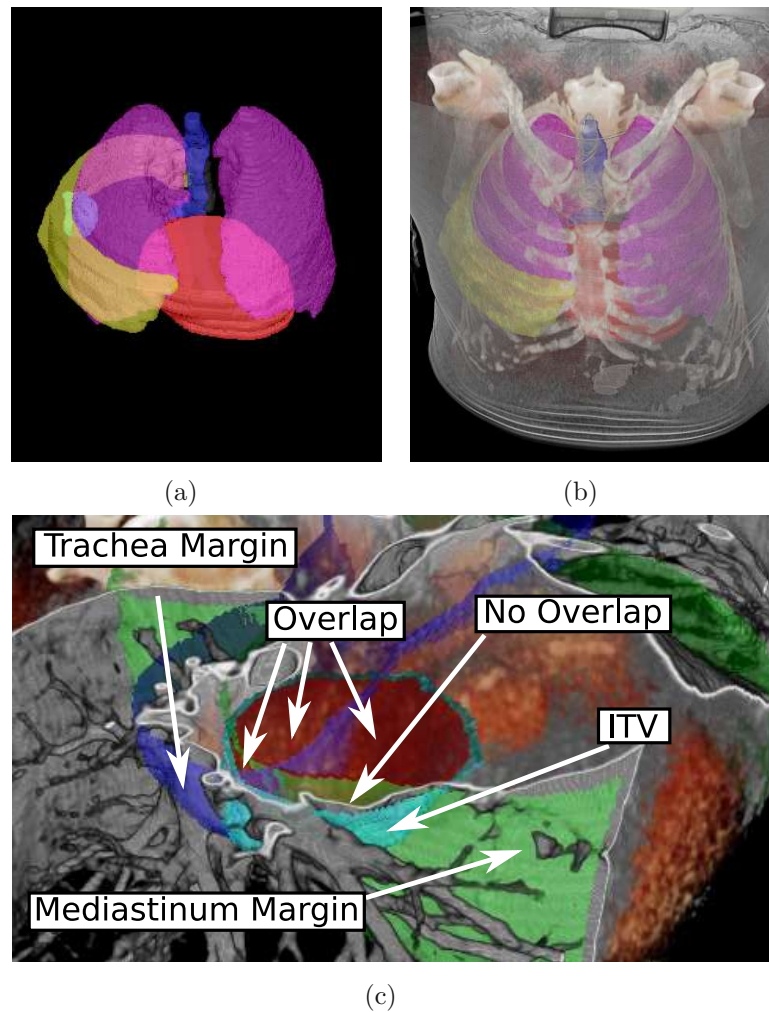


Figure 4.3: Visualization in 4D-VS of binary volumes and fusion with image information are depicted in (a)–(b). Additional features for supporting classification of tumor localization are shown in (c).

delineation can be disabled. This was designed for cases in which the target is close to an OAR (see Fig. 4.4c). Due to the constrained optimization during dose calculation, the resulting distribution might differ from the expected distribution during the prescription phase. In these cases it might be necessary to evaluate the resulting distribution and its spatial configuration more carefully against the target or (a lower dose region) against an OAR (see Fig. 4.4b) to ensure that the treatment goals are still met.

#### 4.2.7 Volume Clipping and User Interaction

For completing Requirements 4 and 6 we implemented interactive clipping of volumes, which can be seen as a user-defined, global ROI. In 4D-VS the visible part of all volumes

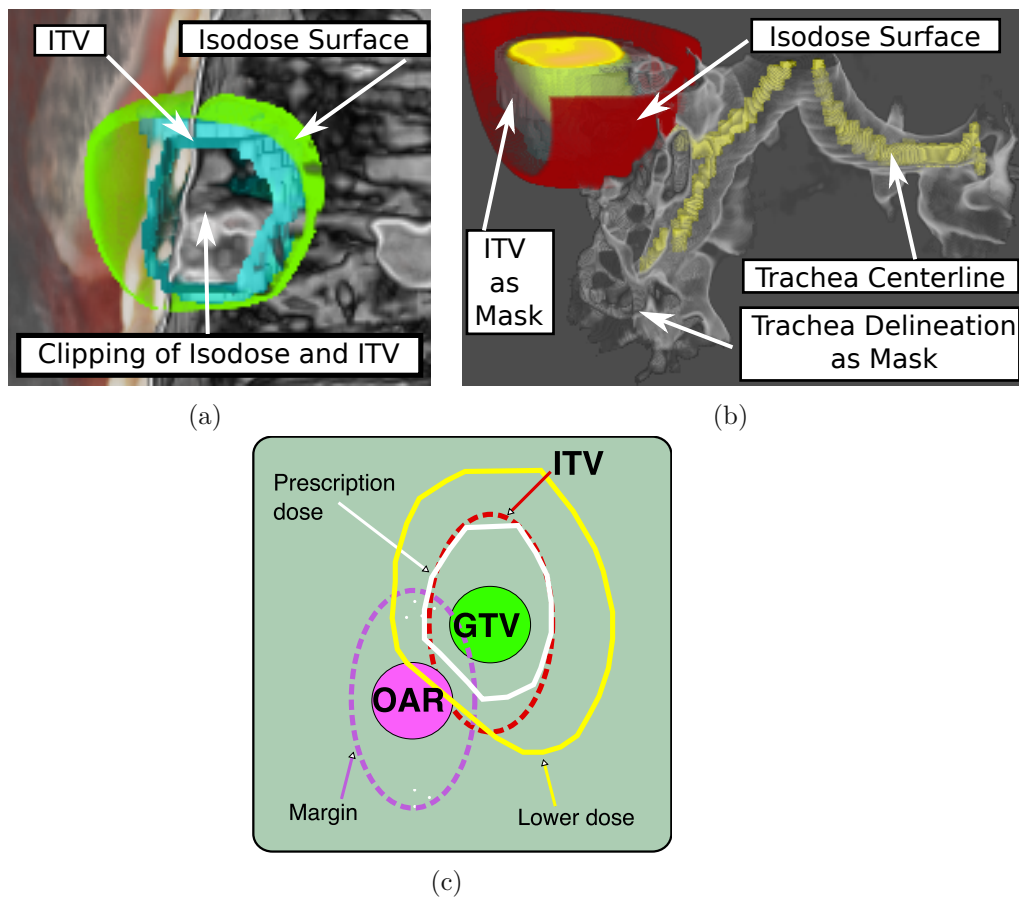


Figure 4.4: Example of the dose distribution visualization using 4D-VS: (a) the 37.5 Gy isodose surface can be evaluated against the planning ITV. A combination of masking, clipping and isodose rendering of a lower dose surface is shown in (b), and a possible configuration of a target close to an OAR is shown in (c).

is defined by a reference volume (usually the planning CT). Other volumes are clipped to the bounding box of the reference volume and visualized only if they are inside the reference. The bounding box of the reference volume can be interactively modified to define a smaller ROI (within the reference volume) to which all data sets are clipped. Users can define the ROI by using two sliders for each of the three coordinate axes. Each slider moves one of the planes, which define the bounding box of the reference volume. In Fig. 4.2a the CT defines the reference volume and can be modified to show only a smaller part of the volume (see Fig. 4.2b and Fig. 4.2c). This was designed to remove occluding volume information or iso-surfaces that are not relevant for a certain task. This type of clipping by a global ROI applies for volume information, delineations, and dose distributions and can be combined with volume masking (see Fig. 4.4a and Fig. 4.4b). For target and OAR delineations we implemented interactive point picking (see Fig. 4.5) to

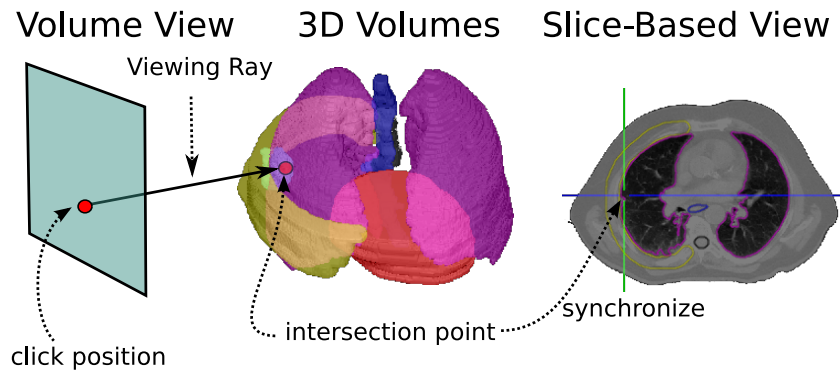


Figure 4.5: The schematic overview of binary volume picking as implemented in the 4D-VS visualization system.

support the navigation from the 3D visualization to the 2D views (Requirement 7). The closest surface point along the view direction from the 2D mouse position can be selected, and the 2D views will be re-arranged to show the position of the surface point. This was designed for Task T.1, when additional information from the slice-based visualization is needed to assess the quality or the delineation should be modified after a region is identified where the target is not fully covered (see Fig. 4.2d).

#### 4.2.8 Volume Intersection Highlighting

The idea behind Requirement 8 is that the classification of tumor location (see Task T.2) can be determined by the distances of the target to the bronchial tree and the mediastinum [TMY<sup>+</sup>06]. Binary volumes for bronchial tree and mediastinum were determined automatically with the approach of Fechter et al. [FDC<sup>+</sup>15], and expanded with margins defined in Timmerman et al. [TMY<sup>+</sup>06]. We use these margin volumes as additional information. However since they are automatically defined, visual assessment is still required. We include these margin volumes in a separate rendering mode, which highlights the intersection volume of the ITV with either one of the margin volumes (see Fig. 4.3c) for Task T.2.

### 4.3 Evaluation

A user evaluation was conducted for investigating the potential benefit of using the 4D visualization features as implemented in 4D-VS by performing the three previously defined tasks T.1–T.3. For comparison to 4D-VS, Oncentra MasterPlan (v4.3, Nucletron BV, Veenendaal, the Netherlands) was used in our evaluation, and will be denoted C-TPS for the remainder of this chapter. C-TPS is the software currently used in clinical routine covering the tasks T.1–T.3.

As mentioned before, our tasks are motivated by patients with malignant pulmonary lesions who are scheduled for and/or treated by stereotactic body radiation therapy

(SBRT). Having very precise delineations (Task T.1), is very important when using SBRT due to the high doses involved. We reduced Task T.1 to a verification task only for the following reasons. First of all, we wanted the test users to concentrate on the visualizations and not on the contouring. Additionally, this reduced the time our test users needed to invest. Furthermore, if the target is delineated using two extreme phases only, quality assessment for the remaining time bins is an equally relevant task to the delineation itself, and is also relevant if using, for instance, an automated 4D segmentation algorithm.

The classification of tumor location (Task T.2) is relevant to decide whether the patient should be treated with SBRT or receive conventional treatment. In this way, Task T.2 is a follow-up task on T.1.

After the dose calculation, the treatment plan will be verified and as a sub-task of the verification also the dose distribution (Task T.3). The assessment of dose distribution in Task T.3 is not specific to SBRT. But due to the high doses involved, visualization techniques other than using the dose volume histograms (DVHs) can be of interest in complicated cases, where the target is spatially close to an OAR. For this task, users were explicitly asked to take the extended volume visualization features into account in addition to the DVHs. Furthermore, we were interested in whether taking the spatial configuration into account was considered helpful by our test users. Task T.3 is a follow-up task on T.2 and T.1. All three tasks have in common, that they use a visual approach for verification.

### 4.3.1 Patient Data and Ground Truth

18 patient cases with malignant pulmonary lesions scheduled for SBRT were selected for testing of Task T.1 and T.2. For reducing observer bias we divided them in two groups (one group for 4D-VS and one for C-TPS), where each group consists of five central and four peripheral cases. As image information we provided a full-body CT and a 4D-PET/CT (see Table 4.1).

For Task T.1 we presented two ITVs for each patient, which results in 18 separate test cases per patient group and system respectively.  $ITV_1$  was generated by a majority vote (3/4) algorithm using manual delineations of four physicians in the context of a contouring exercise. The information used for contouring consisted of 4D-PET/CT, ungated CT, and ungated PET.  $ITV_2$  was generated based on PET information only using a 4D-PET segmentation algorithm [FCC<sup>+</sup>14]. The planning ITV used for treatment of the patients was used as ground truth for estimating the quality of  $ITV_1$  and  $ITV_2$ .

The conversion from DICOM RT Structure Sets to binary volumes was done by rasterization of each planar contour with the slice resolution of the planning CT (see Table 4.1). The axial resolution of binary volumes was the same as the axial planar contour distances, since they were generated on the planning CT. Afterwards we reduced the size of the binary volume by keeping the minimal part of the volume, which represents the actual segmentation information to reduce the memory consumption. This means we only need

Table 4.2: Task description summary and quality scale. The certainty for all tasks was given as binary answer, i.e., either uncertain or certain.

Task Description	Quality Scale
<b>T.1</b> Assess the quality of ITV <sub>1</sub> /ITV <sub>2</sub> and give a rating. Indicate certainty.	1–5 (excellent–poor)
<b>T.2</b> Classify the lesions into central and peripheral. Indicate certainty.	– (not applicable)
<b>T.3</b> Assess the quality of the dose distribution and give a rating. Indicate certainty.	1–5 (excellent–poor)

to store a volume with the size of the minimal bounding box containing the voxels that belong to the contour, and adjust the offset for a correct transform into the patient coordinate system.

The quality of ITV<sub>1</sub> and ITV<sub>2</sub> was determined by calculating the dice coefficient (DC) and the (average/maximum/95%) Hausdorff distances (HD) with the planning ITV. We tried to have a similar distribution of ITV quality for the two test groups by using the DC as an indicator. For 4D-VS (first group) ITV<sub>1</sub> had an average DC of 0.76 ( $\pm 0.09$  SD) and ITV<sub>2</sub> had an average DC of 0.5 ( $\pm 0.19$  SD). The combined test data set (ITV<sub>1</sub> and ITV<sub>2</sub>) for 4D-VS had an average DC of 0.63 ( $\pm 0.2$  SD). Respectively for C-TPS (second group) ITV<sub>1</sub> had an average DC of 0.74 ( $\pm 0.14$  SD) and ITV<sub>2</sub> had an average DC of 0.59 ( $\pm 0.11$  SD). The combined test data set (ITV<sub>1</sub> and ITV<sub>2</sub>) for C-TPS had an average DC of 0.67 ( $\pm 0.14$  SD).

For classification of tumor location (Task T.2) the same data sets were used, however, we additionally provided margin volumes for the bronchial tree and the mediastinum, which were determined automatically with the approach of Fechter et al. [FDC<sup>+</sup>15] (see Section 4.2.8) for using volume intersection highlighting. A ground truth for tumor location was determined by an experienced radiation oncologist different from the test users. Classification was done according to the rules stated by Timmerman et al. [TMY<sup>+</sup>06] using distance measuring tools.

For Task T.3, we selected only patients treated with SBRT, resulting in eight out of the 18 cases, which were only considered for SBRT. Data sets were again split up to reduce bias (four patients for 4D-VS and for C-TPS). As image information we provided the planning CT and all relevant delineations (see Table 4.1) of the target (planning ITV was used) and OARs. For all SBRT plans the 3D dose distribution was calculated with Oncentra MasterPlan.

### 4.3.2 User Evaluation

Two experienced radiation oncologists (denoted as  $U_1$  and  $U_2$ ) performed the three tasks as described in the introduction. They were asked to give a quality rating for the ITV delineation in Task T.1 and for the dose distribution in Task T.3. The scale of the



Table 4.3: Survey questions with answers. Answers given as ( $U_1 / U_2$ ) or “–” if not applicable

Questions	4D-VS	C-TPS
<b>Q1</b> How well can you imagine the 4D-configuration of the structures. Rating 1:best – 5:worst	(1/3)	–
<b>Q2</b> Does the tool have all the functionality for the ITV rating	(y/y)	(y/y)
<b>Q3</b> Does the 4D-VS help to comprehend the test cases	(y/y)	–
<b>Q4</b> Does the tool have all the functionality for central/peripheral classification	(y/y)	(y/y)
<b>Q5</b> Does the functionality of 4D-VS help making the decision	(y/y)	–
<b>Q6</b> Does the tool have all the functionality for dose evaluation	(n/n)	(y/y)
<b>Q7</b> Does the functionality of 3D isodose help making the decision	(y/y)	–

rating was from “1” (excellent) to “5” (poor), where a rating of “3” was defined as acceptable. Additionally, they were asked whether they are certain about their decision for the current task. This is summarized in Table 4.2. All tasks were performed with C-TPS and 4D-VS. After all tasks were performed, users were asked to answer survey questions (see Table 4.3) for each of the systems. The survey had also a general remarks section for free comments.

The visualization as presented in this chapter was developed outside the hospital, and the two radiation oncologists were not involved in the development of the software. The design choices were made in collaboration with technical and medical contacts (different from the test users) situated within the hospital. Hence, we needed to explain the software features in a training session as the test users were unfamiliar with it. During this training session, we explained the features by performing the tasks T.1–T.3 on a test data set, which was not part of the evaluation set. Suggestions for the usage were made depending on the task. The testing itself was then performed unsupervised by each individual expert. A comparison of visualization features that are available in the two systems, and which are relevant for tasks T.1–T.3 can be found in Table 4.4.

### 4.3.3 Visualization Parameter Calibration

The level and window values for PET images, which were provided by the scanner, were used in 4D-VS and C-TPS to provide a comparable windowing [MNR<sup>+</sup>09] for the slice views. In 4D-VS, these values are additionally coupled with the transfer function used for 4D volume visualization. The opacity value range was set depending on these values. Below the lower window value, PET information is transparent, and above the upper window value it has a constant opacity of 0.7. For CT images, the windowing used in the slice views could be adjusted freely in both 4D-VS and C-TPS, to ensure optimal parameters for the visibility (transparency) of certain tissue types. Additionally, the CT

Table 4.4: Feature Comparison of 4D-VS and C-TPS.

Features	Task	4D-VS	C-TPS
2D Multi-Modality Fusion	T.1, T.2, T.3	yes	yes
3D Multi-Modality Fusion	T.1, T.2, T.3	yes	no
4D Multi-Modality Fusion (2D+time and 3D+time)	T.1	yes (slider)	no
2D/3D Visualization of Delineations	T.1, T.2, T.3	yes	yes
2D/3D Fusion of Delineation and Volume	T.1, T.2, T.3	yes	yes
Mask Volumes with Delineations in 3D	T.1	yes	no
Highlighting Intersections of Delineations in 3D	T.2	yes	no
3D Visualization of Isodose Surfaces	T.3	yes	yes
ROI Definition (Clipping) for 3D Volumes	T.1, T.2, T.3	yes	yes (single volume)
ROI Definition (Clipping) for 3D Delineations	T.1, T.2, T.3	yes	no
ROI Definition (Clipping) for 3D Isodose Surfaces	T.3	yes	no
Interactive Point Picking of 3D Delineations	T.1, T.2	yes	yes
Changing Fusion Parameters	T.1	yes	yes (only 2D)

transfer function for volume visualization could be modified in 4D-VS.

## 4.4 Results

The average quality rating of ITVs over all test cases is shown in Table 4.5 (see supplementary material for results concerning individual cases in Appendix A). The combined and per user average with standard deviations (SD) were both calculated. The consensus of the rating between the users was measured by calculating a conformity index (CI), which was defined as the average of the difference in the rating between  $U_1$  and  $U_2$ . The CI indicating the consistency was calculated per ITV and system over all cases, and is listed for  $ITV_1$  and  $ITV_2$  in Table 4.5. The ratings are more consistent between the

Table 4.5: Results of ITV and dose distribution ratings using different systems.

System	Task	Average Ratings						CI
		$U_{1/2}$		$U_1$		$U_2$		
		Avg	SD	Avg	SD	Avg	SD	
4D-VS	T.1 (ITV <sub>1</sub> )	4.06	1.26	3.78	1.20	4.33	1.32	0.56
	T.1 (ITV <sub>2</sub> )	4.78	0.55	4.67	0.71	4.89	0.33	0.22
	T.1 (ITV <sub>1/2</sub> )	4.42	1.02	4.22	1.06	4.61	0.98	0.39
	T.3	2.38	0.52	2.50	0.58	2.25	0.50	0.75
C-TPS	T.1 (ITV <sub>1</sub> )	2.44	1.38	1.67	1.12	3.22	1.2	1.78
	T.1 (ITV <sub>2</sub> )	4.44	0.98	4.00	1.22	4.89	0.33	0.89
	T.1 (ITV <sub>1/2</sub> )	3.44	1.56	2.83	1.65	4.06	1.21	1.33
	T.3	3.13	0.99	3.00	0.82	3.25	1.26	0.25

Table 4.6: Dice and Hausdorff distance comparisons to the planning ITV for rejected and accepted ITVs.

Structure Comparison Metric	System	Accepted ITVs				Rejected ITVs			
		Min	Max	Avg	SD	Min	Max	Avg	SD
Dice	4D-VS	<b>0.73</b>	0.89	0.81	0.07	0.18	0.84	0.59	0.19
	C-TPS	<b>0.48</b>	0.86	0.73	0.13	0.38	0.82	0.60	0.12
Hausdorff (Average)	4D-VS	1.31	<b>4.04</b>	2.04	1.03	1.16	7.29	3.68	1.91
	C-TPS	0.83	<b>8.22</b>	2.37	1.68	1.39	9.17	3.68	2.56
Hausdorff (Maximum)	4D-VS	4.00	<b>11.72</b>	7.23	2.92	4.17	23.48	11.88	5.80
	C-TPS	4.21	<b>52.45</b>	10.89	11.08	5.33	52.45	15.17	12.33
Hausdorff (95%)	4D-VS	2.85	<b>7.66</b>	4.45	1.79	2.93	14.49	7.01	3.30
	C-TPS	2.30	<b>25.31</b>	5.97	5.22	2.94	25.31	8.57	6.15

experts, using 4D-VS than using C-TPS. 4D-VS lead to lower ratings and acceptance rates for ITV<sub>1</sub> compared to C-TPS. The automatically generated ITV<sub>2</sub> received low ratings in both systems. However, the acceptance rates were even lower in 4D-VS. The level of certainty was slightly higher in C-TPS. We defined a rating of 3 (acceptable) as the rejection threshold for ITVs, and calculated the resulting minimum, maximum, average, and standard deviations (SD) of DC and HD measurements for accepted and rejected ITVs (see Table 4.6). Using 4D-VS all patients were classified correctly, and users indicated that they are certain about their decision in all but one case. Using C-TPS one patient was misclassified as peripheral instead of central, and users indicated that they are certain about their decision for all test cases. The average quality rating of

Table 4.7: Acceptance and certainty rates for ITV and dose distribution assessments using different systems.

System	Task	Acceptance		Certainty	
		U <sub>1</sub>	U <sub>2</sub>	U <sub>1</sub>	U <sub>2</sub>
4D-VS	T.1 (ITV <sub>1</sub> )	0.33	0.22	0.78	0.78
	T.1 (ITV <sub>2</sub> )	0.11	0	0.78	0.78
	T.3	-	-	0.5	1.0
C-TPS	T.1 (ITV <sub>1</sub> )	0.88	0.67	1.0	1.0
	T.1 (ITV <sub>2</sub> )	0.44	0	0.78	0.89
	T.3	-	-	1.0	0.5

dose distributions and the corresponding certainty rates are shown in Table 4.7. The overall questions and answers are listed in Table 4.3. The average rating for tempo-spatial comprehensibility of 4D-VS was 2. The feature completeness for ITV assessment and classification of tumor localization was indicated as present in both systems, however not for dose distribution assessment (Q6) in 4D-VS. The additional functionality of 4D-VS was indicated as helpful for all three tasks.

## 4.5 Discussion

In this chapter we presented a 4D multi-modal rendering framework with additional navigation and interaction features, i.e., 4D-VS, for the use in radiotherapy planning. 4D-VS was applied to three specific tasks, which were also performed using the standard tool C-TPS to investigate possible benefits. Lower quality ITVs were more likely to be detected using 4D-VS. Ratings were more consistent for both ITVs (see CI values for Task T.1 in Table 4.5). Furthermore, the classification of tumor location had a higher accuracy using 4D-VS.

For Task T.1 (quality rating of ITVs) the planning ITV was chosen as ground truth for all DC and HD measurements due to its high quality guaranteed by institutional standards. The quality of individual ITVs used in our study was measured by the DC and HD with the planning ITV (see supplementary material for measurements for each data set in Appendix A). The test ITVs had varying quality depending on their generating source, which was either an algorithm or a majority vote (see Section 4.3.1).

The average DC values (see Table 4.6) for accepted ITVs using 4D-VS was 0.81 ( $\pm 0.07$  SD) and 0.73 ( $\pm 0.13$  SD) for C-TPS. The average HD values (see Table 4.6) for average, maximum and 95% for accepted ITVs using 4D-VS were 2.04 ( $\pm 1.03$  SD), 7.23 ( $\pm 2.92$  SD) and 4.45 ( $\pm 1.79$  SD). For C-TPS the respective HD values were 2.37 ( $\pm 1.68$  SD), 10.89 ( $\pm 11.08$  SD) and 5.97 ( $\pm 5.22$  SD). The smallest DC value (the highest HD values for average, maximum, and 95% for contours rated as accepted, i.e., a quality rating

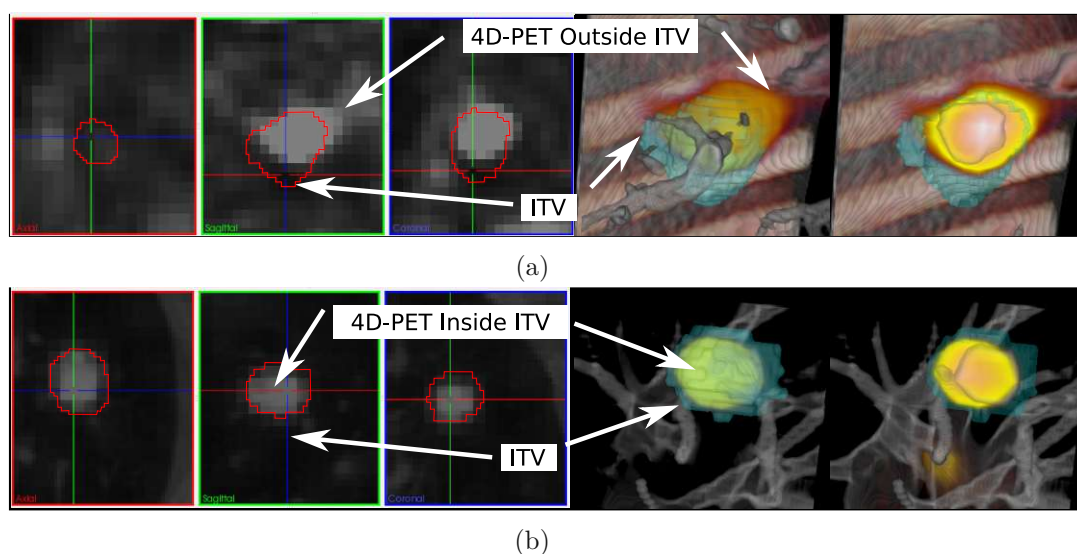


Figure 4.6: Example visualization 4D-PET/CT and ITVs: 2D views and with 4D-VS. Examples show a rejected ITV (a) with a  $DC = 0.65$  and an accepted ITV (b) with a  $DC = 0.76$ .

$\leq 3$ , represents a lower bound for the quality reached in our test set. For 4D-VS the lower bound was 0.73 (4.04, 11.72 and 7.66) and 0.48 (8.22, 52.45 and 25.31) for C-TPS respectively (see bold values in Table 4.6).

Furthermore, the CI values for Task T.1 are lower for 4D-VS, which indicates that the ratings of the ITVs become more consistent between users when using 4D visualization.  $ITV_2$  received lower ratings in both systems, which was expected due to the in general lower DC (higher HD) with the planning ITV. Overall, the detection of low quality ITVs improved and users tend to agree more in their ratings when using 4D-VS.

Furthermore, the survey suggests that the features of 4D-VS provide a better tempo-spatial overview, and that additional volume masking, definition of ROI, and 4D multi-modal visualizations are helpful for ITV assessment (see Table 4.3). An example visualization of a rejected ITV (rating=5) is depicted in Fig. 4.6a, and of an accepted ITV (rating=2) is depicted in Fig. 4.6b. The PET signal is additionally shown in the slice views on the left. In Fig. 4.6a, one can clearly see that the contour does not cover the high uptake region of the PET. Although, there is the possibility to detect this by using slice views, it is more prominent in the volume visualization (see also Fig. 4.2d). Using the additional ROI definition in 4D-VS, volumes and contours can be clipped to define a view, which “cuts” the contour open. With 4D-VS it is at the same time possible to navigate through all the time bins of a 4D dataset, while leaving the rest of the parameters and settings unchanged. This means, by sliding through time, the breathing motion of the patient can be simulated, and the contours can be evaluated against the full 4D dataset. Although, it is possible in C-TPS to load each time bin and evaluate it, in terms of tempo-spatial

comprehensibility and time effort the 4D-VS approach was regarded as advantageous by the users. Besides the missing temporal navigation in C-TPS, volume visualization is available. For a better discussion of the key differences we added example visualizations in Fig. 4.7 showing the ITV depicted in Fig. 4.6b. In C-TPS volume rendering is limited to a single dataset, and therefore it is not possible to fuse information of PET and CT (only slice-wise, see Table 4.4). The contours are only rendered at the correct spatial depth, if no transparency is applied. In Fig. 4.7a all contours are opaque, and in Fig. 4.7b the heart is partially transparent, whereas the rest is unchanged. The heart will now be visualized on top of the volume (Fig. 4.7b) and not at its correct spatial position as in Fig. 4.7a. It is possible to define ROIs in C-TPS. However, they are only applied to volume information, and therefore it is not possible to “cut open” contours as it is in 4D-VS (compare Fig. 4.6). A comparison of available features can be found in Table 4.4. An evaluation of the survey indicates that 4D-VS provides better spatial comprehensibility (Q1–Q3 in Table 4.3) and simplifies the ITV assessment. The users indicated in the survey that the ITV assessment is much faster using 4D-VS than using C-TPS.

For Task T.2 (classification of tumor location) the differences of the two systems were less prominent, when comparing the quantitative results. All tumors were classified correctly using 4D-VS, and only one out of nine patients was wrongly classified with C-TPS. Although, the intersection highlighting was indicated as helpful for making a decision (Q5), the quantitative comparison does not show a significant improvement. In Fig. 4.3c we give an example of how 4D-VS was used to investigate overlapping regions.

For Task T.3 (quality rating of dose distribution), there is no straightforward way to define a ground truth. Therefore, we can only quantitatively compare if the ratings are below or above acceptance, and measure the CI. We observed that the average ratings of the dose distribution are slightly higher and have a slightly higher CI between users (more disagreement) using 4D-VS than C-TPS (see Table 4.5 Task T.3). This could suggest that using the additional features, presented new information which is not present in the other system and led to more disagreement. There is no clear evidence that the certainty improved, and we only observed that  $U_1$  was more certain when using C-TPS, and  $U_2$  when using 4D-VS (see Table 4.7 Task T.3). Fig. 4.7 shows example volume visualizations with isodose surfaces and contours as available in C-TPS for a qualitative comparison to the features of 4D-VS. Isodose surfaces can be visualized as meshes or as solid surfaces. The ROI is only applied to the volume information. Fig. 4.4a shows how the combination of multi-modal fusion, transparent contours, and isodose surfaces as available in 4D-VS can help to investigate the dose distribution. In cases where an OAR is close to the target (see Fig. 4.4c), additional volume masking can be used in 4D-VS for showing only spatially relevant information. The OAR and the target can be masked (see Fig. 4.4b) to investigate a tumor and its dose distribution close to the trachea. Although our study gives no clear evidence that this improves the quality assurance of dose distributions, in our survey the visualization was remarked as helpful for decision-making (Q7). Especially for central tumors where high precision is

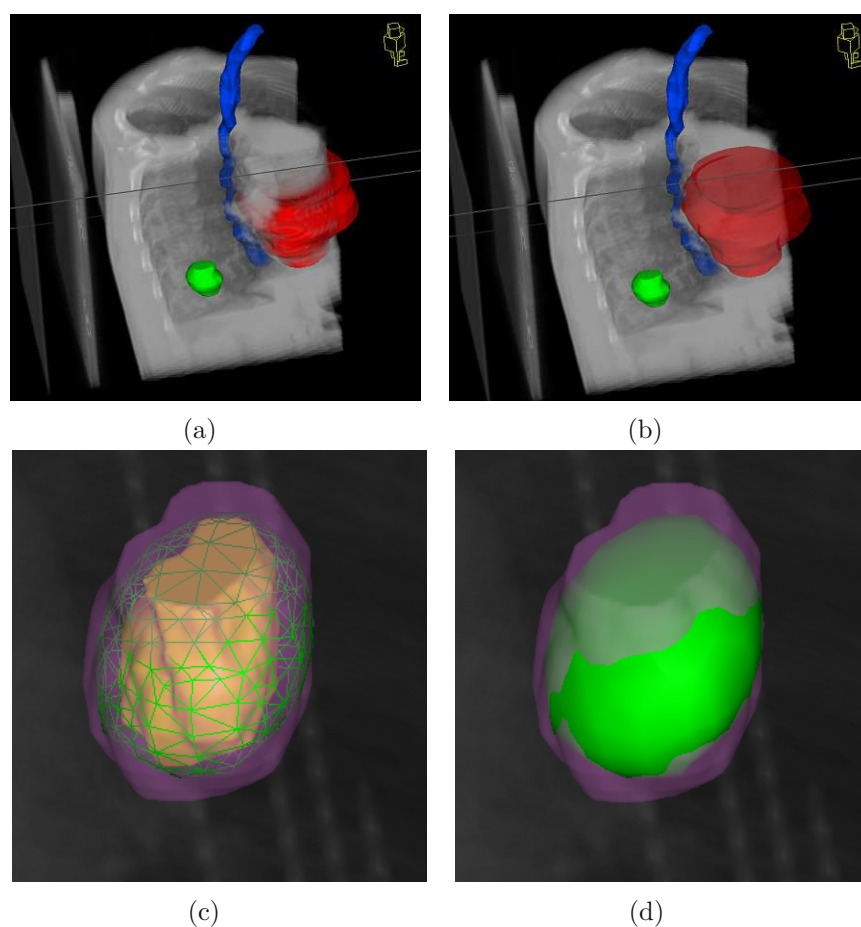


Figure 4.7: Using C-TPS for Tasks T.1 and T.2: Contours are visualized together with the planning CT. Clipping is applied, however, only the CT is affected. The ITV is depicted in green, the heart in red and the esophagus in blue. In (b), the heart is made slightly transparent. When compared to (a), the volume covering the heart is not shown correctly anymore. C-TPS does not preserve the depth information of the heart when made transparent. Using C-TPS for Task T.3: Green is the 37.5 Gy isodose. The planning target volume is depicted in violet, and the ITV in yellow. In (c) the isodose surface is visualized as mesh, and as solid surface in (d)

necessary, this may increase the spatial perception of the dose distribution, as the spatial information is not directly visible in the DVH. However, the question about feature completeness for dose distribution assessment (Q6) using 4D-VS was answered “no” by both users. They remarked volume overlaps should be supported by an additional display showing overlap volumes in numbers and volume to dose relationships. A noteworthy limitation is that our test data included only 3D calculated dose distributions derived from routine 3D RT-planning. Those were combined with 4D image information, and thus the judgment would not include 4D accumulated doses, but only gives a rough idea

of the relation of the target to the location of the dose distribution.

Even though users were unfamiliar with 4D-VS, after a short introduction, they established their own workflow for tasks T.1–T.3. The good spatial overview and additionally using clipping for defining ROIs was remarked as being very helpful. It was also pointed out that additional training might increase the quality and could further reduce time effort.

### 4.6 Conclusion

Our proposed visualizations were generally well approved by the test users. They emphasized the helpfulness of the temporal visualization features of multi-modal images and the fusion with target and OAR delineations as well as improved spatial comprehensibility. Our study also found that lower quality of ITVs are more likely to be detected when using dedicated 4D visualizations as implemented in 4D-VS, which emphasizes volume visualization of temporal multi-modal data sets. The spatial comprehensibility might also improve tasks like the classification of tumor location, which had a higher accuracy using 4D-VS as compared to C-TPS. Additionally, the functionality of 3D dose visualization improved the decision-making about the quality of the plan. Especially for central tumors, where OARs are close to the target volumes, this might further improve the visual assessment of the dose distribution, since the DVH does not provide spatial context.



# Visualization of Deformable Image Registration Quality using Local Image Dissimilarity

This chapter is based on the publication:

M. Schlachter, T. Fechter, M. Jurisic, T. Schimek-Jasch, O. Oehlke, S. Adebahr, W. Birkfellner, U. Nestle, and K. Bühler. Visualization of Deformable Image Registration Quality Using Local Image Dissimilarity. *IEEE Transactions on Medical Imaging*, 35(10):2319–2328, 2016. [SFJ<sup>+</sup>16]

<https://doi.org/10.1109/TMI.2016.2560942>

The original paper was adapted in terms of formatting and type-setting to fit this template and to increase readability. Minor corrections, such as fixing typos or unclear wording, were applied, and the abstract was removed.

## 5.1 Introduction

Deformable image registration (DIR) has become an important research area in modern radiotherapy such as image-guided adaptive radiotherapy (IGART) or stereotactic body radiotherapy (SBRT) for volume definition, dose planning, and dose warping [SDP13, VLM<sup>+</sup>15, VKKH13, RA10, SPWF12, GHC14].

Since precise dose delivery and sparing of the surrounding healthy tissue and organs are required, very precise delineations are necessary. Tumor mobility represents a significant challenge in planning and delivery of radiotherapy, and target delineation encompassing tumor and organ motion for more accurate planning and dose delivery is advised [KMB<sup>+</sup>06]. 4D imaging and the definition of the internal target volume (ITV) for instance, is one way to account for respiratory motion in the planning processes [GHC14]. However, the amount of data generated with 4D imaging significantly increases the time needed for image review and target volume delineation [GHC14]. DIR can be used for contour propagation [OdXJB<sup>+</sup>07] and reduces the workload for manual delineations. Alternatively to the ITV approach, other motion-encompassing methods use DIR to derive a single scan out of a 4D-CT scan for target delineation, which represents the tumor in its time-averaged mid-position [WSvD08]. With DIR, it is also possible to define personalized internal margins adapted to patient specific breathing patterns [BSJS08]. Furthermore, the integration of motion into dose calculation is advantageous [GHC14], and the feasibility of 4D dose accumulation using DIR has been demonstrated both in phantom and patient studies [GHHL08]. Especially in IGART workflows, where the actual dose delivered is monitored and adapted, this has great potential to improve the treatment [GHC14]. Again, DIR can be used to propagate contours and warp the dose to the cone-beam computed tomography, which is acquired in each treatment session to determine or recompute the actual dose delivered [GHC14]. In any case, DIR accuracy has to be evaluated carefully, since the choice of DIR implementation leads to significant differences in the warped dose [VLM<sup>+</sup>15].

The issue of assessing the quality of DIR in daily clinical practice remains. For DIR, expert visual assessment is an important step towards clinical acceptance and routine use, but incorrect deformations, not perceived by observers, represent a significant challenge [RA10]. The goal of this work is to provide clinicians with a visualization framework that simplifies the process of visual assessment of DIR accuracy. Dissimilarity measures of local image patches are computed and used to indicate possible incorrect deformations by volume fusion with the original images. Rendering modes with slice-to-volume navigation were implemented for detailed exploration of critical regions. Interaction features including navigation between the original volumes and user-defined clipping further enhance the system. For demonstrating the viability of our approach, we performed an evaluation with three radiation oncologists. Their task was to indicate DIR accuracy of lung regions using our system. The lung is challenging to evaluate visually and the quality of DIR is often judged only by structures bordering the lung (e.g., bronchi). The presented results show that our system provides an efficient and intuitive way to investigate DIR accuracy.

## 5.2 Related Work

The most common way to evaluate DIR is to use landmarks to measure the accuracy [Fit01]. Efforts have been made for defining reference standards with large sets of expert-determined landmark pairs [CCG<sup>+</sup>09, MvGR<sup>+</sup>11]. This makes comparative evaluation of the spatial accuracy of DIR algorithms possible, but is limited to the test cases. Even though semi-automatic approaches exist [MvGK<sup>+</sup>11], the time effort is too high to define it for an individual patient every time DIR accuracy needs to be evaluated, and therefore it is not suitable for daily routine. Deformable phantoms can be used for evaluating DIR accuracy [KHB<sup>+</sup>08, KCUP13]. However, constructing a deformable phantom, which can duplicate various clinical scenarios, is difficult because of the complexity involved [VKKH13]. Evaluation of DIR accuracy based on computational modeling was proposed [VKKH13, STCS<sup>+</sup>03]. Although, this provides a generic evaluation, an algorithm's performance on real clinical data cannot be measured in this way [MvGK<sup>+</sup>11]. The accuracy of DIR is often approximated using surrogate measures [Roh12], such as tissue label overlap scores, image similarity, image difference, or inverse consistency error. Image similarity is not a reliable criterion when applied globally (e.g., to the whole image), and local approaches should be employed [Roh12]. For instance, patch based approaches allow the similarity to be measured in a small neighborhood around each voxel position [WN12], and are also used in our approach. A commonly employed visualization technique is to assign complementary colors to the fixed and moving image (e.g., red/green) and use color blending of the slices to emphasize intensity differences [WSS<sup>+</sup>06, YBN<sup>+</sup>11]. In the work of Smit et al. [SHS<sup>+</sup>14], orange and blue colors are used as complementary colors. Adding them results in a shade of gray whenever both are of the same intensity, and in a shade of blue or orange if intensities differ. This is only applicable if the images (and tissue) have the same intensity ranges, since it depends directly on the point-wise intensity difference. Another approach is the checkerboard visualization [YBN<sup>+</sup>11, SPWF12], where the images are shown in alternating sequence arranged in a checkerboard pattern. This is helpful to assess the alignment of corresponding edges, but registration errors in more homogeneous regions of the image are not visible [HKK09]. Often the displacement vector field (DVF) is investigated directly. DVFs can be visualized as a deformed grid, where the grid points are displaced according to the estimated deformation. This can also be found in commercial software tools, such as Mirada (Mirada RTx, Mirada Medical, UK, 2015), RayStation (rayDeformable, RaySearch, Stockholm, Sweden, 2015), MIM [PPN<sup>+</sup>13], and Velocity [KCUP13].

Visualizing the transformation directly as glyphs in 2D and 3D is also commonly used [KLPF14], and is, for instance, available in SlicerRT [PLW<sup>+</sup>12]. Using the DVF directly does not provide insight about the actual accuracy, it rather gives an overview to which amount and direction regions are displaced. For example, color-coded visualization of the magnitude values of the DVF or mapping corresponding displacement values onto a 3D surface model, was proposed by Handels et al. [HWS<sup>+</sup>07] to visualize lung tumor mobility and organ motion. DIRART [YBN<sup>+</sup>11] is a software suite for DIR and IGART research, which combines most of the aforementioned visualization techniques.

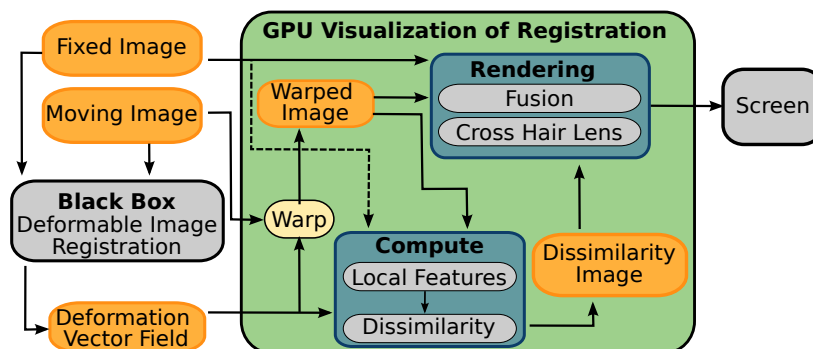


Figure 5.1: Overview of the visualization system. The input data is on the left and indicated by arrows going inside the green box. The green box depicts the core parts of the system, and arrows indicate input and output of the modules.

Additionally, it includes color-coded visualization of quantified properties of the DVF, such as the Jacobian [LHG<sup>+</sup>05] or inverse consistency [YLL<sup>+</sup>08]. Visualization of DVF properties can also be found in the work of Schreibmann et al. [SPWF12] and Hub et al. [HKK09]. The first approach is based on the detection of vortexes, and their intensities (quantified by using the curl operator) are visualized as a vortex map overlaid on the original anatomy to identify problematic regions. The second one automatically estimates the uncertainty of the resulting DVF, which results in the visualization of uncertainty maps for the accuracy.

## 5.3 Visualization System

### 5.3.1 System Design

The visualization system is divided up into two main modules: A rendering module and a compute module (see Fig. 5.1). The rendering system is responsible for direct volume rendering (DVR) and volume fusion. The compute module is responsible for calculating local dissimilarity measures between the fixed and the warped image.

The DIR algorithm itself is treated as a “black box”, and we assume that the algorithm has been applied before using the system. In general DIR can be described as the process of finding the optimal geometric transformation  $T : \mathbb{R}^3 \rightarrow \mathbb{R}^3$  between the fixed  $I_f$  and the moving  $I_m$  image, that maximizes the correspondences between them [RA10]. The output is assumed to be a DVF representing  $T$ . When applied to the moving image, it will generate the warped image  $I_w(\mathbf{x}) = I_m(T(\mathbf{x}))$ .  $I_f$ ,  $I_m$  and the DVF  $T$  are used as input information for the visualization system, and depicted as in-going arrows in Fig. 5.1.

We measure dissimilarity of  $I_f$  and  $I_w$  in a local neighborhood, a patch,  $\Omega \subset \mathbb{R}^3$  around a 3D position  $\mathbf{x} \in \mathbb{R}^3$  (see Fig. 5.2a). The dissimilarity values are computed over the

whole image at discrete sample points and used by the rendering module as additional volume information (denoted as “Dissimilarity Image” in Fig. 5.1). Independent of the dissimilarity measure  $D_{diss}$  being used, it should increase with increasing dissimilarity. This is especially useful for the visualization, as the values of  $D_{diss}$  can be directly used for defining opacity. The required properties can be summarized by the following.

$$\begin{aligned} D_{diss}(I_f|_{\Omega}, I_w|_{\Omega}) &\geq 0 \\ D_{diss}(I_f|_{\Omega}, I_w|_{\Omega}) &= 0 \Leftrightarrow I_w|_{\Omega} \sim I_f|_{\Omega} \\ D_{diss}(I_f|_{\Omega}, I_w|_{\Omega}) &= D_{diss}(I_w|_{\Omega}, I_f|_{\Omega}) \end{aligned} \quad (5.1)$$

It is not required that  $D_{diss}$  is a metric on the original image space (see e.g., the definition of structural equivalence by Wachinger et al. [WN12]). For instance, mutual information [CT05] in its original formulation, would not fulfill the second requirement, since the higher  $D_{diss}$  the more similar the patches are, and therefore a reformulation will be necessary.

### 5.3.2 Direct Volume Rendering and Volume Fusion

For direct volume rendering (DVR), we use a GPU accelerated ray casting approach [KW03] to directly evaluate the volume rendering integral along the viewing rays at discrete sample points [EHK<sup>+</sup>06]. Each sample  $x_s \in \mathbb{R}^3$  in the approximation is assigned a color  $c_{x_s} \in \mathbb{R}^3$  (commonly RGB space) and opacity value  $k_{x_s} \in \mathbb{R}$

$$c_{x_s} = F_c(I_f, I_w, D_{diss}, \mathbf{p}, x_s) \quad (5.2)$$

$$k_{x_s} = F_k(I_f, I_w, D_{diss}, \mathbf{p}, x_s) \quad (5.3)$$

Here  $F_c$  denotes the fusion function for the color and  $F_k$  denotes the fusion function for the opacity. They depend on the input images  $I_f, I_w$ , the dissimilarity measure  $D_{diss}$  (see Fig. 5.2a), and a parameter vector  $\mathbf{p}$ , which represents user-defined parameters employed in the fusion function.

### 5.3.3 Transfer Functions

There are certain transfer functions involved, which influence the final color and opacity of a sample point. One set is used for assigning color and opacity to the fixed and the warped image.  $c_f : \mathbb{R} \rightarrow \mathbb{R}^3$  denotes the color, and  $k_f : \mathbb{R} \rightarrow \mathbb{R}$  denotes the opacity for the fixed image  $I_f$ . The respective functions for the warped image  $I_w$  are denoted as  $c_w$  and  $k_w$ . They are user-defined and rely entirely on the intensity values of  $I_f$  and  $I_w$  respectively. If  $I_f$  and  $I_w$  have the same value range, or are images acquired with the same modality, for instance CT, then  $c_f = c_w$  and  $k_f = k_w$  are identical (an example is provided in Appendix B). Given a sample point  $x_s \in \mathbb{R}^3$ , the color values at the sample position  $c_f|_{x_s}, c_w|_{x_s}$  and opacity values  $k_f|_{x_s}, k_w|_{x_s}$  are given as

$$c_f|_{x_s} = c_f(I_f(x_s)), \quad k_f|_{x_s} = k_f(I_f(x_s)) \quad (5.4)$$

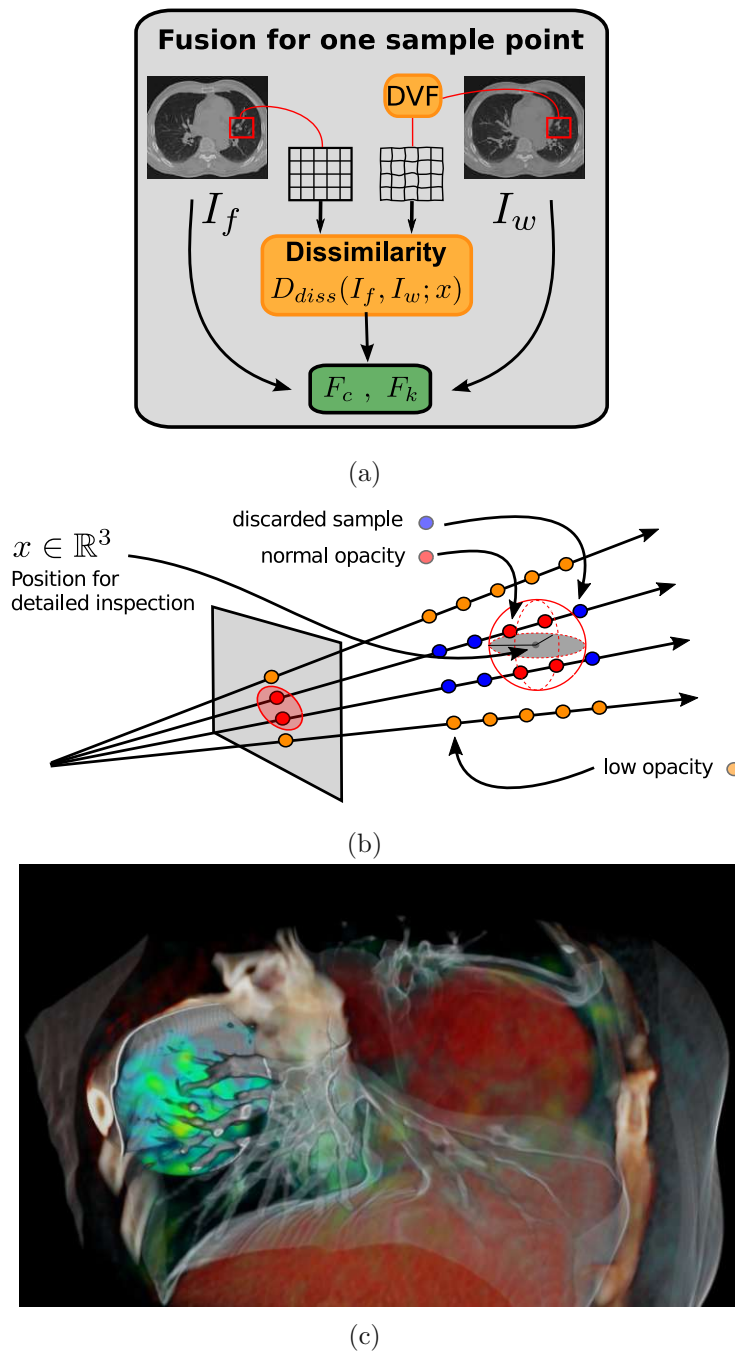


Figure 5.2: Core parts of the visualization system: (a) fusion for one sample point as used in the ray casting. (b) Principle of the cross-hair lens visualization. (c) Example visualization of the cross-hair lens for detailed inspection. Inside the sphere normal opacity values are used. Occluding samples are discarded, and all other samples have lower opacity.

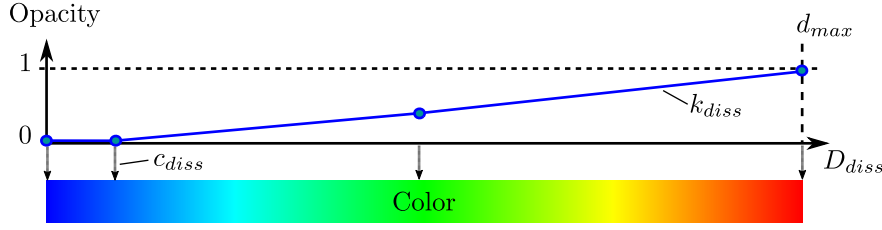


Figure 5.3: Example of functions for  $c_{diss}$  and  $k_{diss}$ . We can define  $k_{diss} : \text{range}(D_{diss}) \rightarrow [0, 1]$  and  $c_{diss} : \text{range}(D_{diss}) \rightarrow [0, 1]^3$  (RGB space). If the range of  $D_{diss}$  is known and bounded  $d_{max} := \sup\{\text{range}(D_{diss})\} < \infty$  we can, for instance, define a piece-wise linear mapping for the opacity with  $k_{diss}(0) = 0$  and  $k_{diss}(d_{max}) = 1$ .

$$c_w|_{x_s} = c_w(I_w(x_s)) , \quad k_w|_{x_s} = k_w(I_w(x_s)) \quad (5.5)$$

The color transfer function  $c_{diss} : \mathbb{R} \rightarrow \mathbb{R}^3$  and the opacity transfer function  $k_{diss} : \mathbb{R} \rightarrow \mathbb{R}$  are used to assign color and opacity depending on the value of the dissimilarity measure  $D_{diss}$  (see Fig. 5.3). Given a sample point  $x_s \in \mathbb{R}^3$ , the color value  $c_{diss}|_{x_s}$  and opacity value  $k_{diss}|_{x_s}$  at the sample position are given as

$$c_{diss}|_{x_s} = c_{diss}(D_{diss}(I_f|_{\Omega_s}, I_w|_{\Omega_s})) \quad (5.6)$$

$$k_{diss}|_{x_s} = k_{diss}(D_{diss}(I_f|_{\Omega_s}, I_w|_{\Omega_s})) \quad (5.7)$$

with  $\Omega_s$  being the patch centered at  $x_s$ . Considering our requirements in Eq. (5.1) we can give meaningful predefined functions for  $c_{diss}$  and  $k_{diss}$  by defining them as  $k_{diss} : \text{range}(D_{diss}) \rightarrow [0, 1]$  and  $c_{diss} : \text{range}(D_{diss}) \rightarrow [0, 1]^3$ . If the range of  $D_{diss}$  is known and bounded  $d_{max} := \sup\{\text{range}(D_{diss})\} < \infty$  we can, for instance, define a linear mapping for the opacity with  $k_{diss}(0) = 0$  and  $k_{diss}(d_{max}) = 1$ . This will make regions for which we have high similarity transparent and regions with high dissimilarity more opaque, and thereby more visible. This is also advantageous for color values assigned to the range of  $D_{diss}$ , since a unique relationship to dissimilarity values can be achieved.

### 5.3.4 Fusion of the Fixed and Warped Image

The fusion of the fixed  $I_f$  and warped image  $I_w$  is simply given by a weighted linear combination. Let  $c_f$  and  $k_f$  denote the color and opacity transfer function of  $I_f$  (see Eq. (5.4)), and  $c_w$  and  $k_w$  of  $I_w$  (see Eq. (5.5)). Then the fusion of the color and opacity is given by:

$$c_{fw} := \alpha \cdot c_f + (1 - \alpha) \cdot c_w \quad (5.8)$$

$$k_{fw} := \alpha \cdot k_f + (1 - \alpha) \cdot k_w \quad (5.9)$$

where the parameter  $\alpha \in [0, 1] \subset \mathbb{R}$  is user-defined.

### 5.3.5 Visualization of Point-wise Dissimilarity

The principal idea is to include information about the registration quality into the visualization system by a point-wise evaluation of the dissimilarity function  $D_{diss}(I_f, I_w; \mathbf{x})$  and defining a transfer function for color  $c_{diss}$  and opacity  $k_{diss}$  depending on the dissimilarity value (see Eq. (5.6) and Eq. (5.7)). For the fusion of the dissimilarity function we used two different approaches. The first is to calculate a weighted linear combination similar to the fusion of the fixed and warped image to overlay the quality as a color-coded dissimilarity map (see Fig. 5.4a and Fig. 5.4b). Regions with a high similarity are assigned low opacity values and the color blue, and regions with high dissimilarity are colored red with high opacity value. The fusion of the dissimilarity with  $I_f$  and  $I_w$  is then given by

$$c = \beta \cdot c_{fw} + (1 - \beta) \cdot c_{diss} \quad (5.10)$$

$$k = \beta \cdot k_{fw} + (1 - \beta) \cdot k_{diss} \quad (5.11)$$

The parameter  $\beta \in [0, 1] \subset \mathbb{R}$  is again user-defined. At this point, substituting backwards all previous definitions will define the fusion functions in Eq. (5.2) and Eq. (5.3) with  $\mathbf{p} = \{c_f, k_f, c_w, k_w, c_{diss}, k_{diss}, \alpha, \beta\}$ , for a sample point at position  $x_s$  and a given dissimilarity measure  $D_{diss}$ . The resulting color  $c_{x_s}$  and opacity  $k_{x_s}$ , which will be used in the ray casting algorithm, is the point wise evaluation of Eq. (5.10) and Eq. (5.11) (see also Fig. 5.2a).

### 5.3.6 Opacity Weighting by Dissimilarity

The opacity  $k$  can also be defined by using  $k_{diss}$  as point-wise weight of the opacity of the fixed and the warped image

$$k = k_{fw} \cdot k_{diss} \quad (5.12)$$

to show only regions where we have possible mis-registration (see Fig. 5.4c), and make well registered regions transparent. In this case, the color transfer function will be set to the one defined for the fixed and warped image  $c = c_{fw}$  in Eq. (5.8). The main advantage of this approach is to get an overview of possible mis-registered regions before exploring the results in detail.

### 5.3.7 Cross-Hair Lens

The cross-hair lens is a special visualization mode that connects the cross-hair position set in the slice views with the volume rendering. The selected position defines a sphere in the 3D volume (see Fig. 5.2b). There are two modes available. The first one, discards all samples along the viewing ray, which would occlude or are behind the sphere (discarded samples in Fig. 5.2b), and also lowers the opacity of surrounding samples to highlight the location of the sphere (low opacity samples in Fig. 5.2b). This mode gives spatial location and context of the selected position, and provides normal rendering inside the sphere (see Fig. 5.2c). The second mode is for a detailed inspection of regions with a high indication



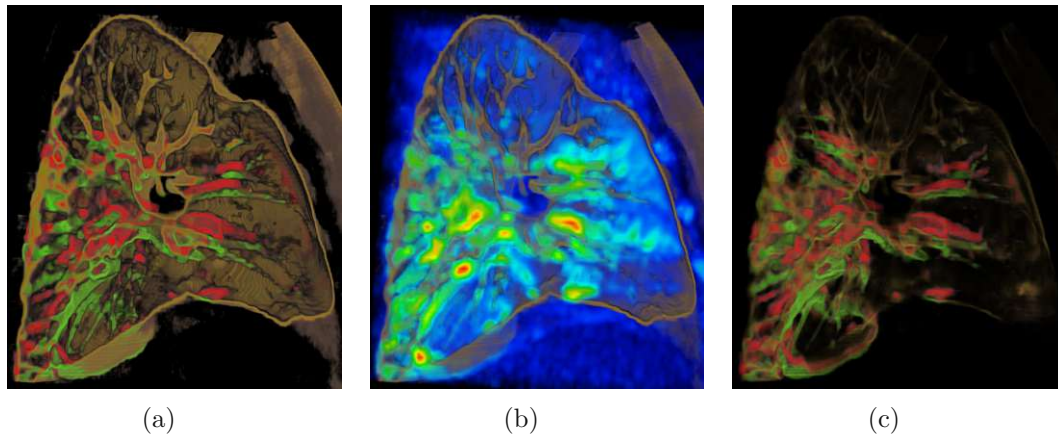


Figure 5.4: For demonstration purposes (a) shows the linear fusion of the fixed and warped image only for lung tissue. The fixed image is set to red, and the warped one to green so that similar regions will appear in yellow tones. In (b) the dissimilarity measure ranging from blue (similar) to red (dissimilar) is visualized together with the fixed and warped image. In (c) the dissimilarity measure is used to weight the opacity of (a).

for registration mismatch. An example of a small lung structure disappearing in the warped image, can be seen in Fig. 5.5. Once a candidate region has been selected, this mode will center and zoom the 3D view around the selected cross-hair point. Additionally, a region of interest (ROI) is defined by the sphere radius and an additional margin. The rest of the volume is discarded in this mode. All interaction parameters are then only applied to the defined ROI.

### 5.3.8 User-defined Region of Interest and Interaction

In addition to the cross-hair lens, it is possible to define a ROI for removing non-relevant or occluding parts of the volumes. An axis-aligned clipping box can be defined by the user, which will crop the volume to any rectangular ROI. Defining ROIs is possible for the whole scene, see for instance the clipped volume in Fig. 5.6, or it can be combined with the cross-hair lens. In Fig. 5.5 the sphere is clipped for better viewing its center point.

### 5.3.9 Image Dissimilarity Measures

We implemented a number of dissimilarity measures in the visualization system, which fulfill the requirements stated in Eq. (5.1). These are reference implementations and can be replaced by any measure, which fulfills the requirements. In the following,  $X$  and  $Y$  denote discrete random variables with possible values  $\{x_1, \dots, x_n\}$  and  $\{y_1, \dots, y_n\}$ , and  $p$  and  $q$  are probability density functions (PDF). Calculating the dissimilarity is based on image patches, which means for a position  $\mathbf{x}_c \in \mathbb{R}^3$  we define a patch  $\Omega \subset \mathbb{R}^3$  as a sub-volume with its center being  $\mathbf{x}_c$ . We only have a discrete number of sample points

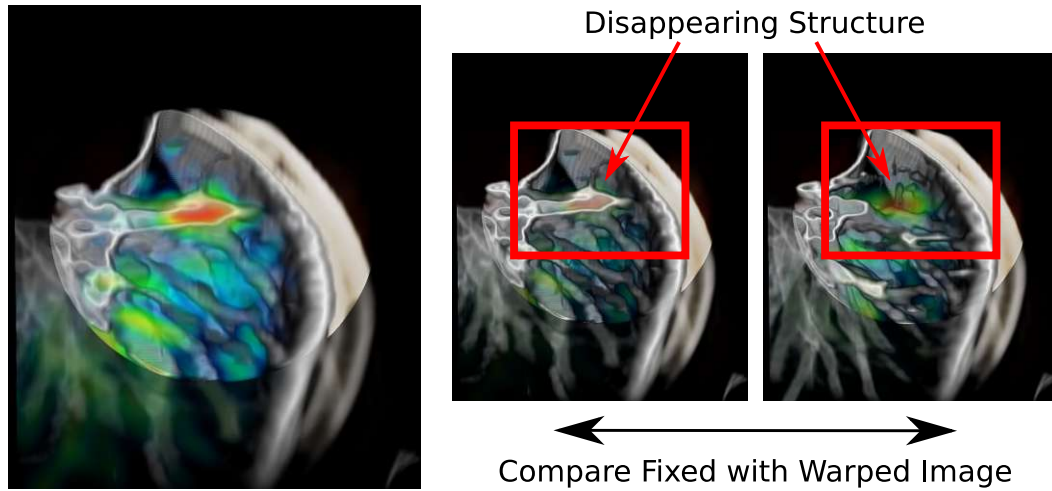


Figure 5.5: The cross-hair lens visualization mode is designed to check in detail a volume position with a high dissimilarity value. Interaction features allow comparing the fixed and warped image. Here, the region with high dissimilarity was due to a structure disappearing in the warped image.

per patch,  $|\Omega| = N \in \mathbb{N}$ , and all definitions are point-wise since  $\Omega$  was defined around the center point  $\mathbf{x}_c$ .

*Intensity Difference (Abs):* A very simple point-wise measure is the absolute difference of intensity values. Here  $\Omega = \{\mathbf{x}_c\}$  is only defined by a single point.

$$D_{Abs}(I_f|_{\Omega}, I_w|_{\Omega}) = |I_f(\mathbf{x}_c) - I_w(\mathbf{x}_c)| \quad (5.13)$$

*Sum of Squared Differences (SSD):* A measure often used in DIR algorithms [SDP13] is the SSD. It represents the mean of the squared intensity differences over a patch.

$$D_{SSD}(I_f|_{\Omega}, I_w|_{\Omega}) = \frac{1}{N} \cdot \sum_{\mathbf{x} \in \Omega} (I_f(\mathbf{x}) - I_w(\mathbf{x}))^2 \quad (5.14)$$

*Normalized Cross Correlation (NCC):* The NCC (Pearson's r) is also found in DIR algorithms [SDP13] as objective function, however needs a slight reformulation to obey the requirements from Eq. (5.1).

$$D_{NCC}(I_f|_{\Omega}, I_w|_{\Omega}) = \frac{1}{2} \cdot (1 - \text{NCC}(I_f|_{\Omega}, I_w|_{\Omega})) \quad (5.15)$$

This remaps the NCC range of  $[-1, 1]$  to the range  $[0, 1]$ , where a value of 0 means the patches are similar in a statistical sense, and 1 means they are dissimilar.

*Kullback-Leibler Divergence (KL):* The KL [CT05] is a measure for dissimilarity of PDFs [CS02]. Given that  $p_{\Omega}$  and  $q_{\Omega}$  are the PDFs estimated for  $I_f|_{\Omega}$  and  $I_w|_{\Omega}$ , we

can compute the dissimilarity using the KL. However, the KL is not symmetric, but can easily be made symmetric by computing the following (the sum is also known as J-divergence [Lin91]).

$$D_{KL}(I_f|_{\Omega}, I_w|_{\Omega}) = \frac{1}{2} \cdot (\text{KL}(p_{\Omega}, q_{\Omega}) + \text{KL}(q_{\Omega}, p_{\Omega})) \quad (5.16)$$

*Histogram Intersection (HI)*: HI is a normalized similarity measure [CS02], and its upper and lower bounds makes it especially suitable for defining transfer functions. HI calculates the similarity between two PDFs, and needs to be inverted to calculate the distance between them (see requirements defined in Eq. (5.1)). With  $p_{\Omega}$  and  $q_{\Omega}$  defined as in Eq. (5.16), this is given as follows.

$$D_{HI}(I_f|_{\Omega}, I_w|_{\Omega}) = 1 - \sum_{i=1}^n \min(p_{\Omega}(x_i), q_{\Omega}(x_i)) \quad (5.17)$$

*Entropy Difference (EN)*: Using Shannon entropy [CT05] as structural representation and taking it as objective function for DIR was proposed by Wachinger et al. [WN12]. With  $H_{I,\Omega}(X)$  denoting the Shannon entropy of a patch  $\Omega$  and an image  $I$  the distance between the two patches in terms of entropy difference is given as follows.

$$D_{EN}(I_f|_{\Omega}, I_w|_{\Omega}) = |H_{I_f,\Omega}(X) - H_{I_w,\Omega}(Y)| \quad (5.18)$$

*Variation of Information (VI)*: The mutual information (MI) [CT05] is also commonly used in DIR algorithms [SDP13], but as mentioned before MI does not fulfill our requirements. However, the variation of information [VEB10] is based on MI and fulfills them. With  $MI_{I_f,I_w,\Omega}(X,Y)$  denoting the MI of  $I_f$  and  $I_w$  for a patch  $\Omega$ , VI is given as follows.

$$D_{VI}(I_f|_{\Omega}, I_w|_{\Omega}) = H_{I_f,\Omega}(X) + H_{I_w,\Omega}(Y) - MI_{I_f,I_w,\Omega}(X,Y) \quad (5.19)$$

### 5.3.10 Example Visualizations

An example visualization using HI with a patch size of 7 mm x 7 mm x 7 mm and 60 histogram bins is depicted in Fig. 5.6. The volume was set to the fixed image, and additional clipping was applied to the 3D view. The cross-hair lens can then be used to investigate the regions with high dissimilarity. Fig. 5.7 shows a close up of a deformed rib from Fig. 5.6. The overlays with the axial, sagittal, and coronal views are shown in Fig. 5.7a for the fixed (upper row) and the warped (lower row) image. The corresponding 3D visualizations using the cross-hair lens are depicted in Fig. 5.7b on the left for the fixed and on the right for the warped image. Example visualizations for all other measures can be found in Appendix B.

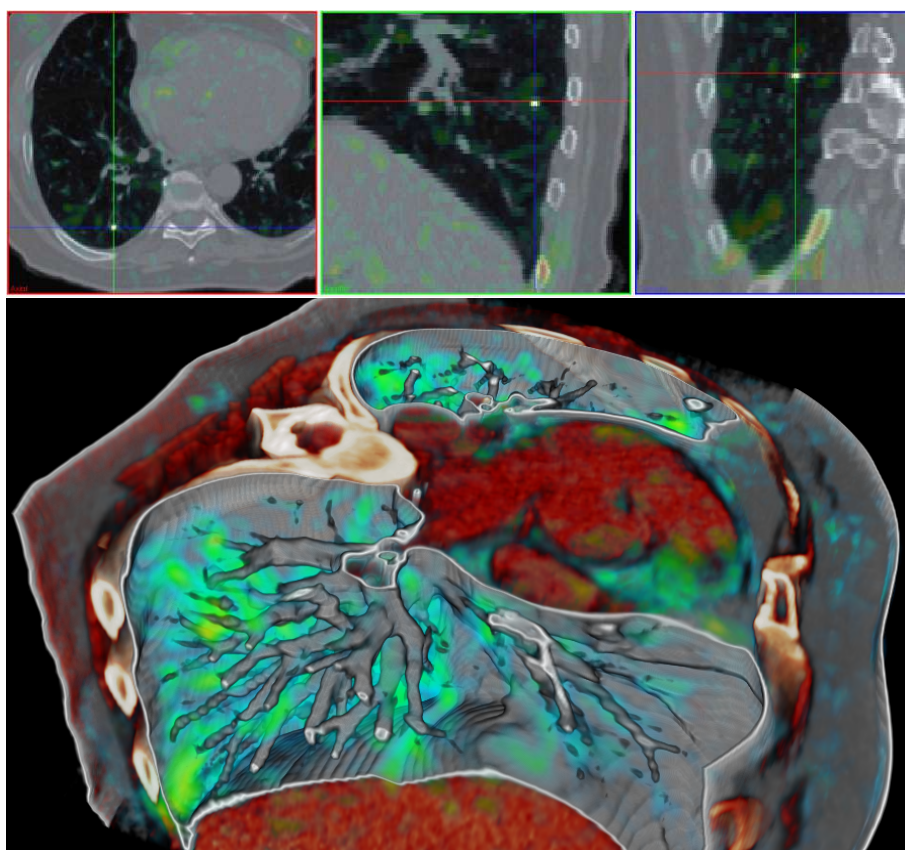


Figure 5.6: Example visualization using  $D_{HI}$  with a patch size of 7 mm x 7 mm x 7 mm. The top row shows the 2D views and the bottom the 3D view of the system. The volume was set to the fixed image, and additional clipping was applied to the 3D view.

### 5.3.11 Implementation Notes

The core components of the visualization system are implemented using NVIDIA's CUDA, and the user interface (UI) is embedded into the MITK [WWW<sup>+</sup>05] platform. The integration in MITK is accomplished via its plugin mechanism. The core part of our system (see Fig. 5.1 green box) is connected to the rendering pipeline and the user interaction system. Core specific parameters such as the transfer functions, sliders for  $\alpha$  and  $\beta$ , or the visualization mode, are accessible via the UI components of the plugin, and can be modified. Data sets are stored on the GPU with their original voxel spacing and aligned in a common coordinate system. Computations are performed on a grid that is defined by the fixed image. Each voxel defines a sample point in the grid for which a computation of dissimilarity is performed. All computations for a single patch are performed with a defined sampling given in mm units (set to the smallest in-plane resolution of the data set), with the center being a point of the computation grid. Intermediate results are cached in the data store and used in the rendering module

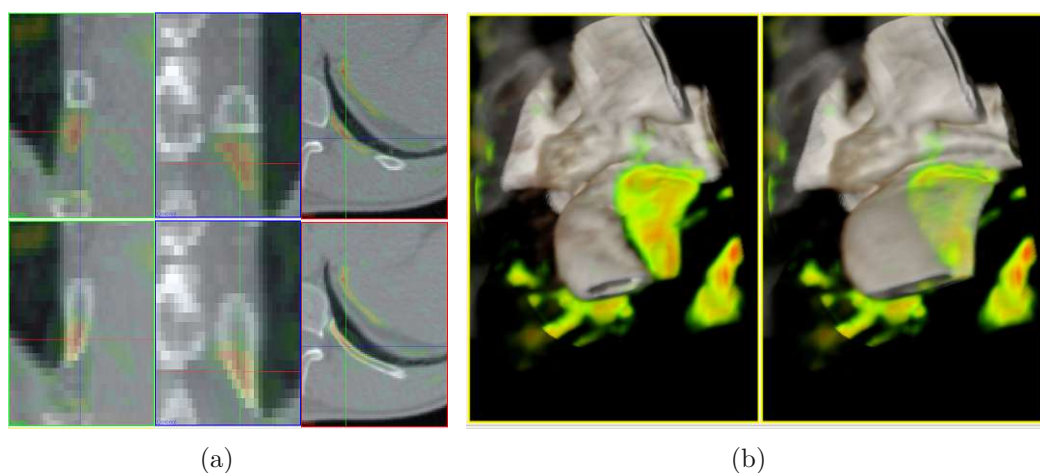


Figure 5.7: Close up of the deformed rib from Fig. 5.6. The top row in (a) shows the 2D views of the fixed image and the bottom of the warped image. (b) shows the cross-hair visualization, which was centered at the rib, for the fixed image on the left and the warped one on the right.

for speed up, and refreshed if either parameters or input images change.

## 5.4 Evaluation

We conducted a user study to show the usefulness of our approach. Three radiation oncologists, all familiar with image registration and methods such as the checkerboard visualization, participated in the study.

### 5.4.1 Data Sets

For the evaluation, we used five thoracic CT images with ground truth data provided by the DIR-Lab (Cases 1–5) [CCG<sup>+</sup>09] with a slice thickness of 2.5 mm, and an in-plane resolution ranging from 0.97 mm to 1.16 mm (256x256x106 voxels). The ground truth for each case consists of 300 anatomical landmark correspondences, which have been annotated by thoracic imaging experts [CCG<sup>+</sup>09]. DIR was performed on each of the CT scan pairs between the maximum inhale and maximum exhale phase of the breathing cycle.

### 5.4.2 Initial Registrations and Landmark Errors

For the registration we employed two different methods. Our visualization method is independent of the choice of the registration method (see Fig. 5.1). Since these registrations form the basis of the user evaluation, we decided to include results from different methods and varying overall quality. The overall quality was measured by statistics (average, standard deviation, minimum and maximum) of the target registration

error (TRE) per data set. For each landmark pair  $(\mathbf{x}, \mathbf{x}')$ , we used the transformation of the corresponding algorithm to calculate the warped landmark position  $\mathbf{x} + T(\mathbf{x})$  and calculate the TRE

$$TRE = \|\mathbf{x} + T(\mathbf{x}) - \mathbf{x}'\| .$$

Cases 1 and 4 were registered using a demons-based approach [VPPA08], which is included in MITK [WVW<sup>+</sup>05]. Cases 2, 3, and 5 were registered using *plastimatch* [SKS10], a B-Spline based deformable registration method, which is included in *SlicerRT* [PLW<sup>+</sup>12]. The mean TRE is ranging from 1.52 mm to 8.28 mm. A full summary of the accuracy for the different cases using all available landmarks is included in Appendix B.

### 5.4.3 Parameter Estimation and Method Preselection

In order to estimate the parameters of the dissimilarity measures  $D_{diss}$  (patch size and number of histogram bins), we used one of the DIR-Lab data sets to generate an artificial volume set with known transformation. First, we registered the data set using *plastimatch* [SKS10], and used the resulting transformation  $T$  to generate a new fixed image from the moving image by applying  $T$ . Basically, the warped image was set to be the fixed image. Additionally, the landmarks from the moving image were warped using  $T$ , generating a new set of landmarks with no observer variability (see also the description of DIR-Lab data [CCG<sup>+</sup>09]). Then we computed for each dissimilarity measure and varying parameters for patch size and number of bins, the correlation coefficient (CC) with the landmark distance. The CC was used to rank the different measures for varying parameters. For our user testing we chose the top two performing measures with the corresponding parameters. Performance was ranked in terms of CC and speed, and the best performing methods were found to be HI and EN (see Eq. (5.17) and Eq. (5.16)).

### 5.4.4 User Study

The task of the study was to give quality ratings for DIR accuracy for all five cases. For each case, HI, EN, and, for comparison, the checkerboard visualization and color blended images (CB+CB) were used. CB+CB are widely used approaches for visual inspection of registration quality, besides intensity difference images, and found in research papers as well as in commercial products.

For evaluation purposes, we divided the lung into smaller regions. It was separated into left and right, with a further subdivision into upper, middle and lower lung. Fig. 5.8a shows the regions we defined. This further subdivision into six regions for each of the five data sets leads to an overall number of 30 regions, which were evaluated individually. The participants were asked to give ratings for each region (Table 5.1 Q1) on a scale from 1 to 5 (1="worst", 3="acceptable", 5="visually no difference"). After each case, they were asked which of the visualizations they would choose to make a final decision, and whether individual visualizations were helpful for the case at hand (Table 5.1 Q2 and Q3). Once all data sets were evaluated, an additional questionnaire was filled out concerning different aspects of the visualization methods. The experts should give ratings

Table 5.1: Questionnaire (Short)

Q1	Rating of DIR Accuracy (per Lung Region)	(Rating: 1–5)
Q2	Which method would you use for final decision-making?	
Q3	Was method X helpful for the current case?	
Q4	Helpfulness for identifying registration errors	(Rating: 1–5)
Q5	How intuitive is visualization X	(Rating: 1–5)
Q6	How fast did you find errors with method X?	(Rating: 1–5)
Q7	Does visualization X give a good spatial overview?	
Q8	Is visualization X suitable for finding small detailed errors?	
Q9	Sliding between fixed and moving is helpful / necessary?	
Q11	Do you trust the proposed visualizations more than CB+CB?	
Q12	Potential for integrating the system into the planning work-flow?	
Q13	Is the cross-hair lens visualization helpful / necessary?	
Q14	Is the opacity weighting visualization helpful / necessary?	

on a scale from 1 to 5 (“worst” to “best”) for each of the methods with respect to (Q4) helpfulness for identifying registration errors, (Q5) intuitiveness of the visualization, and (Q6) the speed of the method (see Table 5.1). Furthermore, we asked survey questions (see Q7–Q14 in Table 5.1) to evaluate (Q7) the spatial overview of the visualization, (Q8) how suitable it is to find small detailed errors, (Q11) whether they trust the proposed visualizations more than the CB+CB method, and (Q9, Q12–Q14) the helpfulness of certain features of the visualization system. The questions in Table 5.1 were shortened, and the version with the original questions is included in Appendix B.

## 5.5 Results

### 5.5.1 Quality Ratings

Results of the ratings for each case averaged over all region ratings can be found in Fig. 5.8b. A rating of “3” defined the acceptance threshold for the accuracy. Case 1–3 have been rated as acceptable by all methods. When compared with the table in Appendix B of individual TRE measures, CB+CB seems to be overestimating the quality for Case 1 with a rating of 4.7. The region holding the maximum TRE was rated in

Table 5.2: Average and maximum landmark (LM) error in mm for accepted regions.

	Combined = Left+Right Lung (Left Lung / Right Lung)		
	CB+CB	EN	HI
AVG	2.33 (2.63 / 1.99)	2.16 (2.40 / 1.88)	<b>1.81</b> (1.87 / 1.74)
Max	6.87 (6.87 / 4.09)	6.87 (6.87 / 3.87)	<b>3.33</b> (3.02 / 3.33)
LMs	1326	1178	994

average with 4, whereas the average rating was 3.3 for the other two methods. Case 4 has been rejected by all methods, and was according to the TRE the registration with the worst quality with an average landmark error of 8.28 mm. If we take results of the study by Tilly et al. [TTA13] as a guideline, the mean error needs to be  $\leq 2$  mm to obtain an uncertainty better than 3 %. Case 5 has a mean TRE of 3.28 mm, and was therefore overestimated by CB+CB and EN. Only when using HI, the quality of Case 5 was rated as not acceptable. Table 5.2 shows an overview of the average and maximum TRE found over all regions rated as accepted.

Fig. 5.9a shows average values of the answers given by the participants to Q2–Q3. HI was always considered to be helpful, EN in 93 % of the cases, whereas CB+CB in only 20 % of the cases. The method used for final decision-making was in 60 % of the cases reported as HI, 33 % EN, and only in 7 % CB+CB. CB+CB was only reported for one data set, Case 4, which had the worst accuracy.

### 5.5.2 Method Evaluation

The results of the user ratings for the individual visualization techniques in terms of helpfulness (Q4), intuitiveness (Q5), and speed (Q6) for finding errors are depicted in Fig. 5.9b. In terms of speed and helpfulness, the proposed visualization methods, EN and HI, were clearly superior to CB+CB. Overall the HI method received the highest ratings with 4.6 for helpfulness and 5.0 for speed. All methods received a rating  $\geq 4$  for intuitiveness, with a slightly better rating for the methods HI and EN.

### 5.5.3 Survey

Results of the survey questions (Q7–Q14) are shown in Fig. 5.9c. The proposed methods gave a good spatial overview (Q7), and the overall opinion of the experts shows that the system is suitable for finding small detailed errors (Q8). Note that CB+CB was consistently considered as not suitable. The interaction with the slider to change between the fixed and the warped image was considered as very helpful (Q9). Also, the cross-hair lens was considered helpful (Q13) and was used intensively during the testing. One of the experts answered with “no” for Q13, and noted in the comments this was due to the



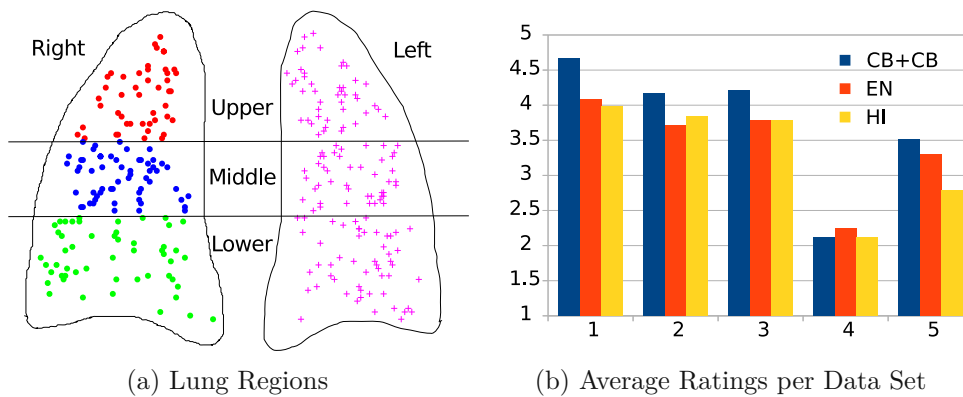


Figure 5.8: (a) Lung regions used for the user evaluation. (b) Average ratings per data set. The average was calculated over region ratings of all users that participated in the study.

word “necessary” in the formulation of the question, but also stated that it is definitely helpful. The opacity weighting (Q14) was not intensively used during the user testing, and was not considered helpful even though the user comments suggest that it gives a good overview in the beginning. Overall, our methods have been well accepted, and all experts indicated that they are trusting our visualization more than CB+CB (Q11).

## 5.6 Discussion

### 5.6.1 Computation Time

The computation time for the different measures is listed in Table 5.3. All measurements were computed on an NVIDIA GTX980 with a patch size of 7 mm, a patch sampling of 1 mm, and a grid size of 256x256x106. The measures  $D_{Abs}$ ,  $D_{SSD}$ , and  $D_{NCC}$  are independent of the histogram bins, and are the fastest.  $D_{EN}$  and  $D_{HI}$  are comparable, and perform in less than 2 s.  $D_{KL}$  is slightly slower (it needs to be computed twice for symmetry) but is still acceptable.  $D_{VI}$  needs to compute the mutual information and is for higher bin sizes relatively slow compared to the other measures (26 s for 128 histogram bins). Depending on the application, speed can be a crucial criterion. For instance, for verifying the registration of a 4D-CT with ten time bins to a planning CT, the computation time should be low.

### 5.6.2 Qualitative Comparison of Dissimilarity Measures

We presented different dissimilarity measures, which can be used for the visualization.  $D_{Abs}$  and  $D_{SSD}$  are based on intensity differences, and  $D_{NCC}$  is based on the correlation.  $D_{KL}$  and  $D_{HI}$  compare the PDFs of the patches, whereas  $D_{EN}$  and  $D_{VI}$  are comparing patches based on the differences of information or shared information. For a qualitative

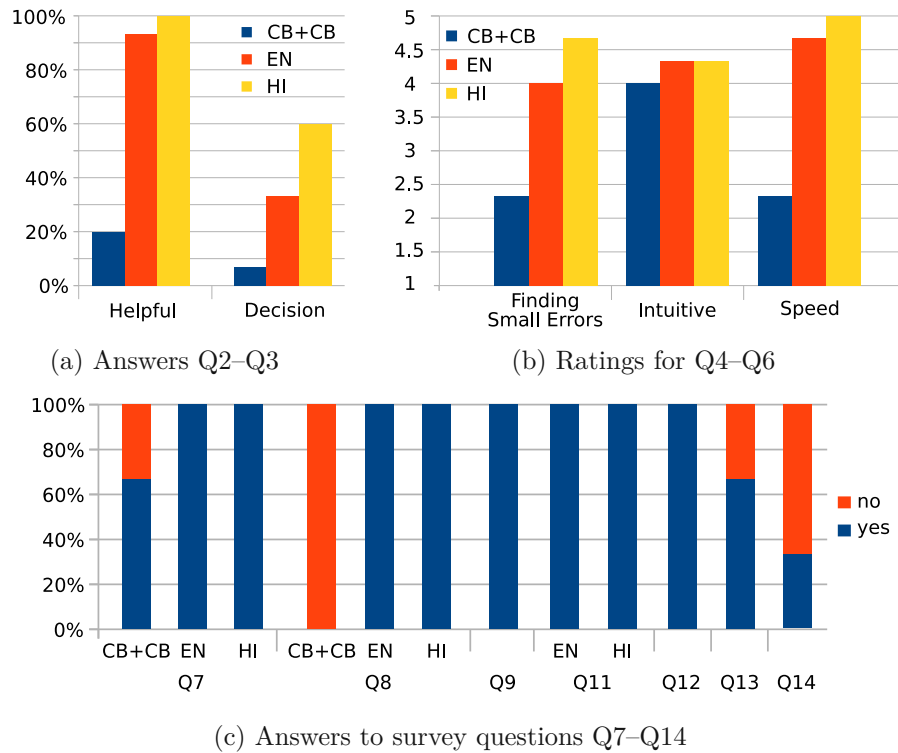


Figure 5.9: Answers to Survey Questions. (a) Average over answers given by all users for Q2-Q3. (b) Average over ratings given by all users for Q4-Q6. (c) Average over answers given by all users for Q7-Q14.

comparison of the resulting visualizations, we provide for each measure an example visualization in Appendix B.

There are different aspects of the measures that are important for the visualization to ensure inter-patient comparability, as well as the ability to detect possible errors. The range of  $D_{Diss}$  is directly related to the definition of transfer functions (see Eq. (5.7) and Eq. (5.6)), and therefore important to ensure a comparable mapping of possible errors to opacity and color values between different patients. In Fig. 5.10 we used a small lung region in which a mis-registration occurred (see Fig. 5.10a) to demonstrate how the boundness of the range of  $D_{diss}$  influences the visualization of the error. In Fig. 5.10b the result of  $D_{SSD}$  is visualized using for  $d_{max}$  (see Fig. 5.3) the highest value found in the data set. This leads clearly to the error not receiving an appropriate visualization (see Fig. 5.10b) as the opacity is too low, and the color indicates a neglectable error. For demonstration purposes, we set  $d_{max}$  to a value of 250 to limit the range of  $c_{diss}$  (see Fig. 5.10e) and  $k_{diss}$ . Now the result shown in Fig. 5.10c gives clearly a more appropriate visualization of the error at hand and indicates a non-neglectable error. For  $D_{SSD}$  the opacity and color range will strongly depend on the highest difference found in the data set, and may vary for each patient if no limit for the value range is defined. However,

Table 5.3: Computation time for Dissimilarity Measure with a patch size of 7 mm and patch sampling of 1 mm and grid size 256x256x106.

Histogram Independent		Histogram Bins		32	128
Measure	Duration (s)	Measure	Duration (s)		
$D_{Abs}$	$1.2 \cdot 10^{-3}$	$D_{EN}$	1.17	1.53	
$D_{SSD}$	0.32	$D_{HI}$	1.16	1.48	
$D_{NCC}$	0.63	$D_{KL}$	1.33	2.15	
		$D_{VI}$	2.95	26.22	

$D_{SSD}$  (also  $D_{Abs}$ ) has the problem that there is no theoretical upper bound, and a limit for the value range is not easily defined. The Hounsfield units (HU) ranging from air to cortical bone could be used to define an upper limit for  $D_{SSD}$  as 4000 HU. However, we measured the maximum of  $D_{SSD}$  per data set to be in the range of 237–789 HU, which would still not provide an appropriate visualization of the error shown in Fig. 5.10b. An additional logarithmic scale applied to the range of  $D_{SSD}$  could help to address this issue (the value 250 HU would correspond to 66% of the logarithmic scale of 4000 HU). For  $D_{EN}$  it is possible to determine its upper bound. For a given number of  $n$  histogram bins,  $d_{max}$  (see Fig. 5.3) can be defined as the entropy of a uniform distribution with  $n$  possible values. In our case the upper bound of  $D_{EN}$  was 4.81 bits. Note, that for  $D_{KL}$  and  $D_{VI}$  upper bounds can be determined in a similar way for discrete random variables. The theoretical upper bound for  $D_{EN}$  might be unrealistic (see Fig. 5.10f), as we assume that one patch has maximum entropy and the second patch has zero entropy. The highest difference in entropy we measured was 3.12 bits. Although this will give transferable values, it eventually leads to values only covering the lower part  $c_{diss}$  and  $k_{diss}$  in realistic scenarios. Again, a logarithmic scale could be applied to address this issue. The range of  $D_{HI}$  is  $[0, 1]$  (see Fig. 5.10g), and is additionally independent of the number of bins used in the histogram. Furthermore, it is intuitive for a user to modify the transfer function to show, for instance, only errors which are above a 10% threshold. This is easily accomplished by defining  $k_{diss}$  to be zero on the interval  $[0, 0.1]$  (see Fig. 5.3). Of the measures we investigated,  $D_{HI}$  is best suited in terms of being reproducible concerning color values, which is important if such a system should be used also by non-expert users. For  $D_{NCC}$  another problem arises when mapping its range to opacity as in Fig. 5.3. The values around 0.5 mean that there is no correlation between the patches. This leads to high dissimilarity values where there is background noise, and might not be intuitive to interpret by users.

Equally important is the ability to detect registration mismatches. We used a preselection step to determine parameters of the measures, and at the same time, to rank the measures according to their CC with TRE (see table in Appendix B). We selected only the best performers to reduce the amount of user testing. The measures  $D_{Abs}$ ,  $D_{SSD}$ , and  $D_{NCC}$

performed poorly in terms of CC in our preselection step.  $D_{KL}$  performed in the preselection slightly better than  $D_{EN}$ . However,  $D_{EN}$  was chosen for speed reasons, and to include a measure based on information difference in the user testing. Qualitatively,  $D_{HI}$  seems to have the best detection also outside the lung.  $D_{VI}$  seems to perform well when qualitatively comparing the example visualizations, it was however the poorest performer in terms of CC.

For the visualization both aspects, the ability to detect registration mismatches and inter-patient comparability, are important, when used for detecting possible errors. If only one of them is fulfilled, either the ability to detect errors or the presentation to user, the detection rate of the system will be influenced. Besides these basic properties, the overall performance will also be influenced by the additional, and more specific visualization modes, which were implemented in our system, such as the cross-hair lens, ROIs, and user interaction.

### 5.6.3 Properties of the Deformation Vector Field

In this work we exclusively considered image similarity, and want to discuss the possibility of also including properties of the DVF itself. Certain errors can be detected by taking the DVF into account. The Jacobian [LHG<sup>+</sup>05] can be used to investigate whether the deformations are physiologically plausible. Considering the example in Fig. 5.7, by visualizing the determinant of the Jacobians, and using prior knowledge about Hounsfield units, it is feasible to detect implausible deformations, such as expanding bones (see Appendix B for an example visualization). This will however depend on the modality if such a relation between the type of tissue and the absolute value of the measurement can be established. The magnitude of the DVF can be used to investigate regions where large displacements were estimated by the algorithm. The magnitudes, for instance, could be used for opacity weighting as described in Eq. (5.12), by replacing  $k_{diss}$  with a function  $k_{magn}$ , which maps magnitudes to opacity values. Regions with low magnitudes would appear more transparently, or could be discarded by setting the lower range of the magnitudes to zero. Regions with high magnitudes could be investigated more easily. However, this should be done with great care. Low magnitudes do not necessarily imply correct registrations, nor do high amplitudes imply possible incorrect registrations (see the example of the large displacement close to the diaphragm in Appendix B). Once accuracy is confirmed, DVF properties will be useful to gain insights about physiological changes or in describing motion patterns.

### 5.6.4 Normalization and Multi-Modality

Computing the measures defined in Eq. (5.16)–(5.19) usually requires the estimation of a PDF. In general, normalization needs to be considered for cases of multi-modal registrations. This can be done either with a local or a global approach [WN12]. For PDF estimation, we followed a Parzen window approach [Par62] for the histogram estimation.

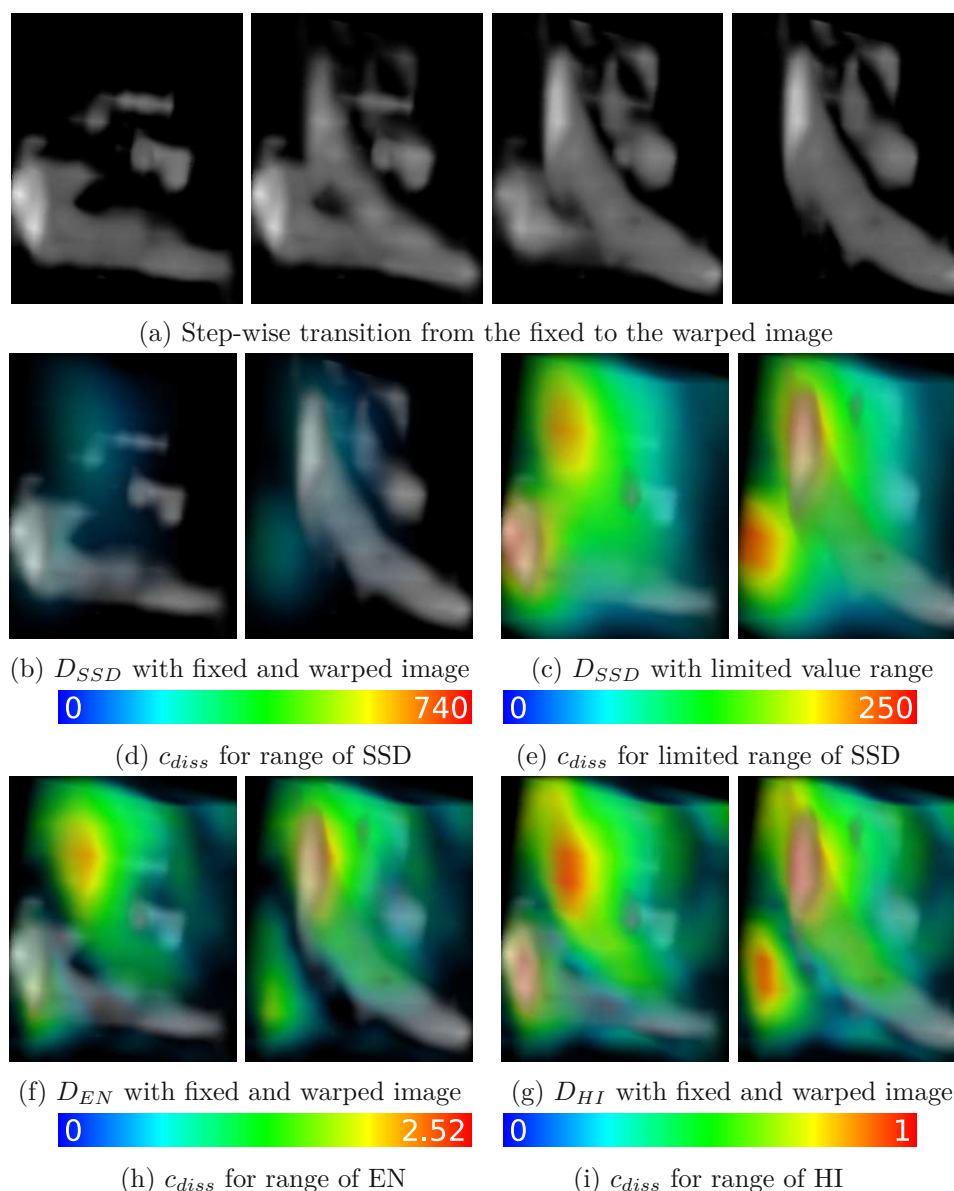


Figure 5.10: Illustration of the influence of the transfer functions and the relation to the range of  $D_{diss}$ . (a) shows a cropped region with a vessel, which was not correctly registered. From left to right a step-wise transition from the fixed to the moving image is depicted ( $\alpha$  was set to 1, 0.75, 0.25, and 0 in Eq. (5.8) and Eq. (5.9)). (b) shows the overlay of  $D_{SSD}$  and the corresponding color transfer  $c_{diss}$  in (d). In (c) the overlay shows  $D_{SSD}$  with a different value set for  $d_{max}$ , as an example of how the boundness of  $D_{diss}$  will influence the final visualization. The corresponding  $c_{diss}$  is shown in (e). The overlay depicted in (f) is for  $D_{EN}$  and in (g) for  $D_{HI}$ , with the corresponding  $c_{diss}$  shown in (h) and (i) respectively. All overlay images were generated with  $\beta = 0.5$  and  $\alpha = 1$  for the left, and  $\alpha = 0$  for the right image.

The measures defined in Eq. (5.13)–(5.15) rely directly on image intensities and are not directly applicable in multi-modality cases.

### 5.6.5 Shortcomings and General Remarks

We only used landmark information defined in the lung, and have no quantitative information about how these measure perform on other regions. Likely, the parameters need to be adjusted for other organs or modalities. This can be done with a similar approach as the preselection step explained in Section 5.4.3. Especially with multi-modality imaging, the measures Eq. (5.16)–(5.19) might perform differently.

## 5.7 Conclusion

We proposed a novel visualization approach to support clinicians with the visual assessment of DIR accuracy, and to provide them with the necessary tools for identifying locally implausible deformations in critical regions. Our system makes suggestions for possible candidate regions, and provides interaction and visualization techniques to support detailed inspection of these regions. The presented results show that our system provides an efficient and comprehensible way to investigate DIR accuracy visually.

Future work should include the extension to multi-modal registrations, which will require investigating additional dissimilarity measures or making adaptations. An additional benefit might be introduced by using neighborhood descriptors such as MIND [HJB<sup>+</sup>12] to describe the structure of patches modality-independent.

CHAPTER **6**

# Exploration of Overlap Volumes for Radiotherapy Plan Evaluation with the Aim of Healthy Tissue Sparing

**This chapter is based on the publication:**

**M. Schlachter**, S. Peters, D. Camenisch, P. M. Putora, and K. Bühler.  
Exploration of Overlap Volumes for Radiotherapy Plan Evaluation with the  
Aim of Healthy Tissue Sparing. arXiv, 2021. [SPC<sup>+</sup>21]  
<https://arxiv.org/abs/2112.12590>

The original paper was adapted in terms of formatting and type-setting to fit this template and to increase readability. Minor corrections, such as fixing typos or unclear wording, were applied, the abstract was removed, and the introduction was adjusted.

## 6.1 Introduction

Radiotherapy (RT) involves high doses of radiation, thus, there is a high risk of tissue damage and severe toxicity to the surrounding organs, leading eventually to secondary cancer [BCD<sup>+</sup>10]. Despite the significant technological advancements of RT over the last decades, there are still many challenges to address [SRM<sup>+</sup>19]. One such challenge is the adequacy of normal tissue sparing in the proximity to a tumor [MBLM11], due to the inherently conflicting nature of maximizing tumor control while minimizing normal organ damage [GW19].

The volume concepts and planning workflow were already introduced in more detail in Chapter 1 and 2, but for a better understanding of the underlying problem, we repeat the most important concepts briefly. Additional details for guidelines, definitions, and naming conventions can be found, e.g., in Gahbauer et al. [GLC<sup>+</sup>04], Burnet and Neil [Bur04], and Berthelsen et al. [BDK<sup>+</sup>07].

The process of RT planning has four major steps as depicted in Fig. 6.1a. After the image acquisition, and after the contouring of target volumes and organs at risk (OARs), the delivery is designed in terms of prescribing doses to the targets and setting dose constraints for OARs. After the prescription, the dose distribution is calculated by applying an appropriate calculation algorithm [RvdMS<sup>+</sup>07]. The result is the (simulated) absorption of dose in tissue, which will be carefully evaluated before delivery. Quality assurance is a crucial part during the whole treatment planning process. However, it is widely accepted that the decision-making process is subjective, and would benefit from efficient and reliable assessment tools [AHN15]. Important volume definitions (see Fig. 6.1b) are the gross tumor volume (GTV), the visible part of the tumor, and the clinical target volume (CTV), the tissue volume that contains microscopic tumor extensions. The CTV extended by an internal margin to include physiologic variations, such as breathing, is called the internal target volume (ITV) and common in lung cancer patients. The planning target volume (PTV) is defined by adding a margin to the CTV (or ITV) for including geometrical uncertainties such as the setup margin related to positioning the patient. If a margin is added to an OAR then the volume is designated as the planning risk volume (PRV).

Treatment plan evaluation is mainly based on inspection of the dose volume histogram (DVH) [AHN15]. A weakness of the DVH approach is the lack of spatial information, as the information where within the structure the dose is received is lost. Furthermore, DVH based analyses inherently assume that organ function is uniformly distributed within an organ, which is not the case for some organs [BCD<sup>+</sup>10].

In this chapter we focus on the problem of overlapping target and OAR volumes. Especially in cases where the PTV and the PRV overlap as depicted in Fig. 6.1c, there are conflicting dose constraints that might lead to high doses in small sub-volumes of OARs. Studies have shown the feasibility of overlap sparing without compromising treatment outcome especially for smaller overlaps [HJNL06]. However, if the OARs are only slightly



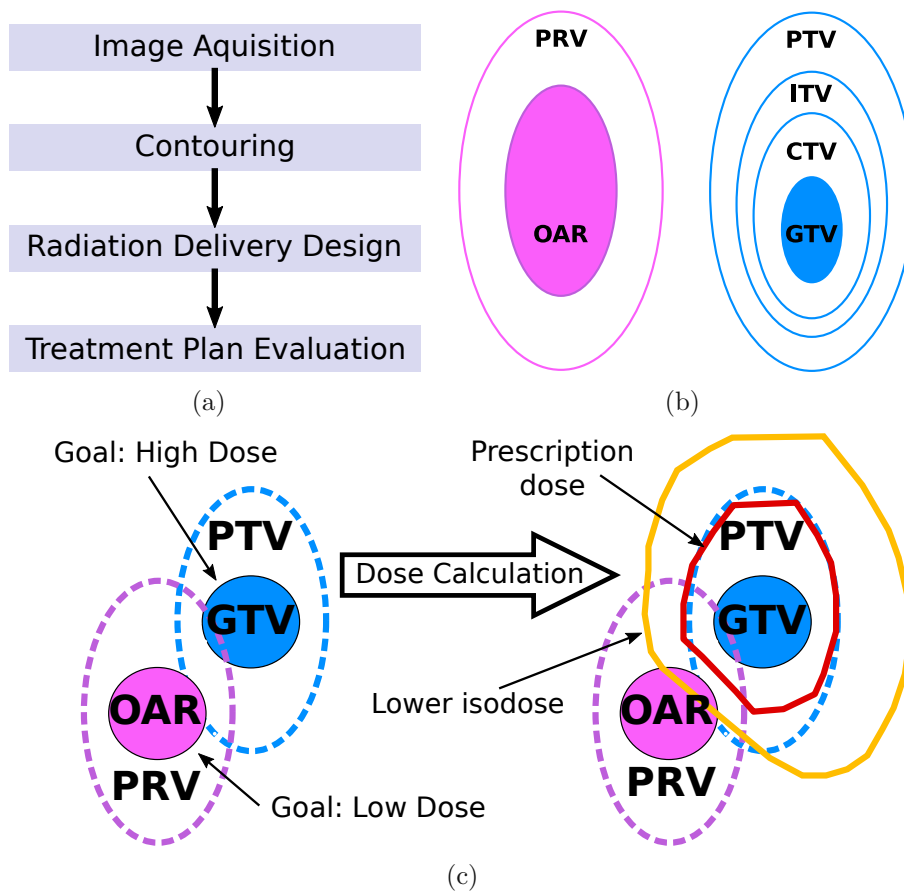


Figure 6.1: (a) The four major (consecutive) RT planning steps prior to treatment. (b) Schematic overview of important RT volume definitions. (c) Conflicting treatment goals: PTV requires high dose, whereas PRV requires low dose. After dose calculation the desired treatment goals might not be as prescribed.

overlapping with the PTV, the potential exists that the treatment planners might not push to spare these organs more than the standard goal [MBLM11].

We present an approach to interactively explore these overlap volumes to ensure an adequate planning outcome for both the target and OARs. The novelty of our approach lies in the combination of visual analytics methods with traditional volume visualization and interaction techniques, enabling a fast, interactive, visual, and flexible exploration of treatment plans driven by relevant dose and physical properties.

## 6.2 Related Work

Healthy tissue sparing can be addressed in multiple ways. One way is to solve the underlying problem with a modeling approach, i.e., in a non-exploratory way by calculating,

e.g., a quality score based on prior knowledge. Another way is to use an exploratory visualization approach, which includes the planners expert knowledge in the decision-making process.

### 6.2.1 Modeling or Knowledge Based Approaches

A recent review of modeling or knowledge-based approaches can be found in the surveys by Wang et al. [WZHZ19] and by Ge and Wu [GW19] covering automated rule implementation, reasoning, and modeling of prior knowledge in clinical practice. An automated scoring system for the comparison of multiple tentative plans, based on DVHs to provide estimates on PTV coverage as well as on sparing of OARs was proposed by Alfonso et al. [AHN15]. The Overlap Volume Histogram (OVH) was proposed by Kazhdan et al. [KSM<sup>+</sup>09] to provide a representation of OARs relative to the tumor volume. Using the OVH, a reference database is searched to identify patients with similar geometries. Retrieved patients are used to guide planners in determining whether lower doses delivered to the OARs are feasible in the new plan [WRS<sup>+</sup>09]. A numerical quality indicator was developed by Song et al. [SSC<sup>+</sup>15] using a geometry-dosimetry model, which characterizes potential plans as optimal or suboptimal achieving patient-specific quality control. A model to assess the quality of a treatment plan using prior patient data was proposed by Petit et al. [PWK<sup>+</sup>12]. It could accurately predict the achievable doses using an OARs orientation and distance to the PTV, leading to a considerable decrease in dose to the OARs. A predictive model to guide management of the overlap region between target volume and OAR was proposed by Mattes et al. [MLE<sup>+</sup>14]. The degree of overlap can be used to accurately guide physicians and to limit the extent of the overlap region prior to optimization. A knowledge-driven decision support system was proposed by Deshpande et al. [DDSL16], which quantifies the spatial relationships between the tumor and OARs through features that account for distance, volume, overlap, location, shape, and orientation. These features are used to identify database cases similar to a new patient, and help to estimate an acceptable dose distribution.

### 6.2.2 Related Visualization Approaches

An overview of visual computing in RT can be found in recent surveys by Schlachter et al. [SRM<sup>+</sup>19, SPBR20], and for domain independent multi-modality visualization in the surveys by Preim et al. [PBC<sup>+</sup>16] and Lawonn et al. [LSBP18].

For the exploration of physical and/or dose properties of overlap volumes, applicable concepts were developed in other domains, such as set visualization or visualizing relationships. For instance, the analysis of similarities and differences arising from comparisons of genomes [KSB<sup>+</sup>09], or the visualization of adjacency relations [Hol06] using a chord diagram for displaying the interrelationships between data can be applied to visualize overlap relations. Overlap volumes represent spatial sets with certain attributes, i.e., physical and dose specific measurements, and therefore set visualization techniques can be applied. A systematic overview of state-of-the-art techniques for visualizing

different kinds of set relations can be found in the survey by Alsallakh et al. [AMA<sup>+</sup>15]. Especially interesting for this work is the concept of visualizing overlaps of arbitrary sets using interactive visual analysis [AAMH13]. An approach, which combines quantitative views with spatial views applied to target volume definitions using information from MR-Spectroscopy, can be found in the work by Nunes et al. [NRS<sup>+</sup>14].

## 6.3 Data, RT Plan Metrics, and Definitions

Our visualizations consist of several views, which can be categorized into spatial views and quantitative views. The spatial view is used for visualizing spatial information, which includes multi-modal image information, segmentation information (tumor and OAR delineations), and 3D dose distributions [SPBR20]. The quantitative views present relevant information about the structures and overlap volumes. This section presents the necessary background and definitions, whereas the details about each view can be found in Section 6.4.

### 6.3.1 Data

Volumetric data is the basis for the spatial views in our application. In general, the spatial views make use of multi-modal imaging sources, e.g., 4D-PET/CT, delineations, and dose distribution [SFNB14]. Delineation colors and names are pre-defined and loaded from DICOM-RT. The delineations are converted to binary volumes with respect to the planning CT resolution. Dose distribution data is used for both spatial and quantitative views.

### 6.3.2 Important Overlap Relations

In the following, a structure is defined as spatial set  $S \subseteq \mathbb{R}^3$ . The overlap relation of two structures  $S_i, S_j \subset \mathbb{R}^3$  is defined by  $S_i \sim S_j \iff S_i \cap S_j \neq \emptyset$ , where  $i, j \in \{1 \dots N\}$ ,  $i \neq j$ , and  $N$  is the number of structures. If a structure is selected in one of the views, it is denoted as reference structure  $S_r$ , where  $r \in \{1 \dots N\}$ . In the following  $S_i, S_j, S_r$  are used to denote structures for  $i, j, r \in \{1 \dots N\}$  with  $i \neq j \neq r$ .

**Volume-to-Volume Overlaps** These overlaps are defined by the intersection of delineation volumes such as the PTV and OAR. We define an overlap volume as  $OV(S_i, S_j) := S_i \cap S_j$ .

**Volume-to-Dose Overlaps** These overlaps are defined between structures  $S_i$  and dose regions  $R_d$  (see Fig. 6.2) as  $OV(S_i, R_d)$ . Given a dose distribution  $f_D : \mathbb{R}^3 \rightarrow \mathbb{R}$  representing the absorbed dose  $d$  at position  $x \in \mathbb{R}^3$ , a dose region  $R_d := \{x \in \mathbb{R}^3 \mid f_D(x) \geq d, d \in \mathbb{R}\}$  is defined as the volume where the dose is at least  $d$  Gy.

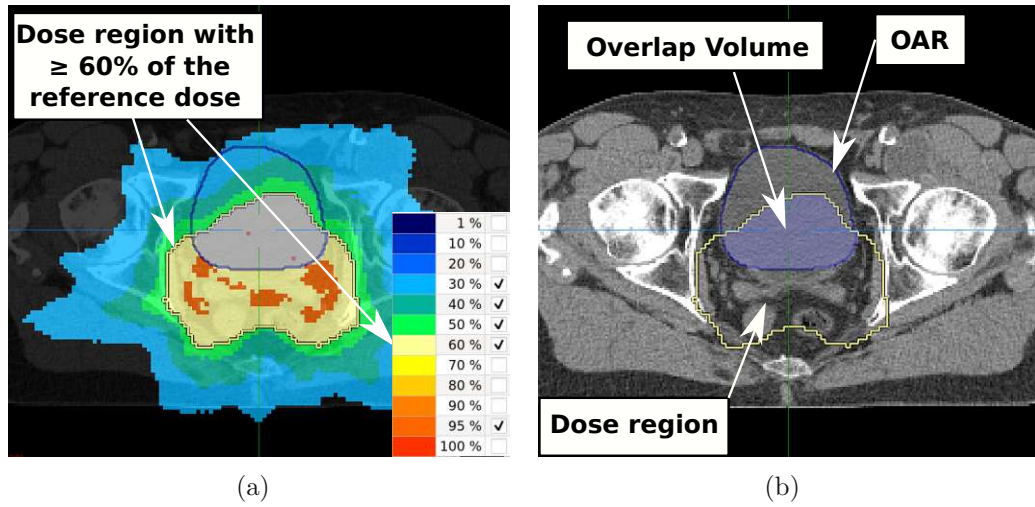


Figure 6.2: Volume-to-Dose Overlaps are defined dose regions  $R_d$  (a) (yellow outline where dose is  $\geq d$ ) and other structures (b).

**Overlaps by Point Selection** The slice views are used to define the set  $OV_x$  of all structures, which overlap in the current cross-hair position  $x$ . This set is used to display all available overlap information in a table view without cluttering the spatial views. The set is updated when the cross-hair is moved, and individual overlaps can be displayed on-demand. Given  $x \in \mathbb{R}^3$  the set  $OV_x := \{S_i \mid S_i \sim S_j \wedge x \in S_i \cap S_j\}$  includes all structures, which overlap each other in the point  $x$ .

### 6.3.3 Treatment Plan Evaluation Metrics

In the quantitative views we make use of treatment plan evaluation metrics, e.g., for filtering or sorting overlaps. A number of quantitative metrics can be considered, and an overview can be found, for instance, in the work of Moore et al. [MBLM12]. The measures summarized in this section represent a proposal for finding candidate overlaps, i.e. overlaps for which lower doses are feasible, and are exchangeable without changing the concept of our approach.

**Quantification of Dose** The following metrics are included in our visualizations:

- $d_{min}, d_{mean}, d_{max}$ : The minimum, mean, and maximum dose value in a structure or overlap volume.
- $D_p$ : The minimum dose in  $p$  percent of the volume.
- $V_d$ : The volume receiving at least  $d$  Gy.
- HI: The Homogeneity Index [KSS<sup>+</sup>12] representing the uniformity of the dose distribution in the volume.

**Quantitative Metrics for Overlap Volumes** We include the absolute volume in ml of the overlap volume  $OV(S_i, S_j)$ , and the overlap in percentage in regard to the selected structures. These values give an indication of whether the volume is worth to consider investigating further, as for instance, a very small overlap could be regarded as irrelevant or vice-versa.

**Histogram Intersection for DVHs** We are especially interested in the deviation of the DVHs of the original structure and the overlap DVHs. If the deviation is high, then the overlap is a candidate for further inspection. The histogram intersection [BOV03] is a measure to describe how similar two distributions are [CS02]. We include the inverse of the histogram intersection in the quantitative views to calculate the difference (or distance) between two DVHs. The difference is defined as

$$D_{HI}(S_i, S_j) = 1 - \sum_{k=1}^n \min(p_i(d_k), p_j(d_k)) ,$$

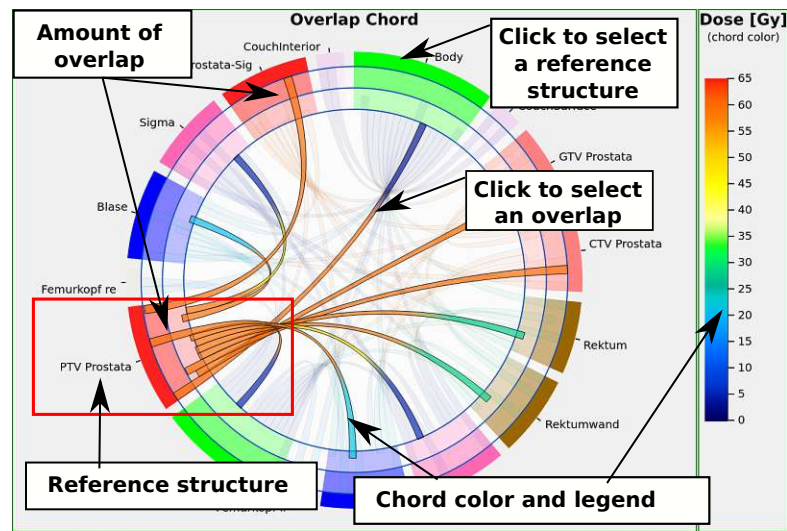
where  $p_i$  and  $p_j$  are the normalized DVHs of structure  $S_i$  and  $S_j$ , and  $n$  is the number of bins of the histogram.

## 6.4 Visualization: Views

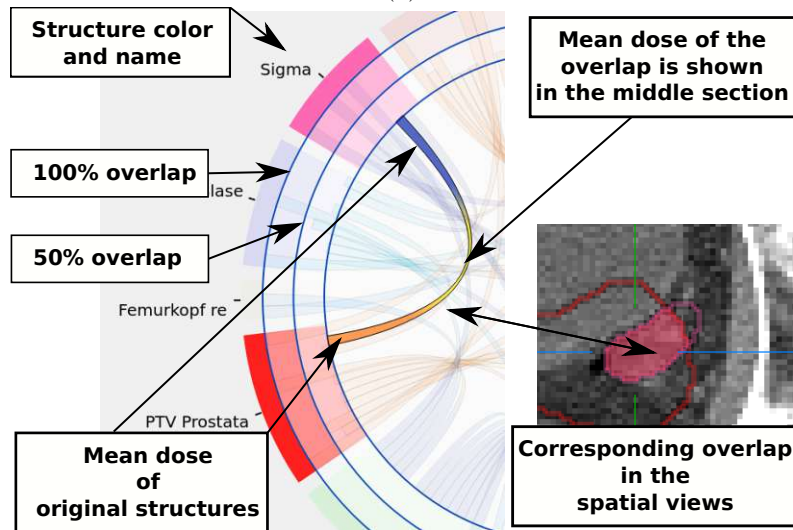
In an early stage, a questionnaire was sent out to two experienced radiation oncologists to gather information about quantitative properties to identify overlaps for which the dose could potentially be reduced. Based on the gathered information we developed a first prototype. The prototype was presented further to a radiation oncologist and a medical physicist from a different institution to gather informal feedback, and to improve the implementation.

We make use of the concept of multiple coordinated views to represent the metrics for overlap relations introduced in Section 6.3. The goal is to support the identification of overlap regions, where the dose for an OAR can be further reduced without compromising the treatment outcome for the target (see Fig. 6.1). The different views are connected (see Section 6.5) to interactively explore overlap regions in the treatment plan at hand.

The quantitative views are used to represent and encode relevant information about the overlap volumes and plan evaluation metrics. They consist of multiple views: A chord diagram, parallel coordinates, two separate table views, and a DVH view. The chord diagram is used for a fast overview of overlapping structures (see Fig. 6.3). The parallel coordinates for displaying and selecting quantitative measures for each overlap volume (see Fig. 6.4). One table view for showing all overlap volumes in relation to a selected reference volume (see Fig. 6.5), and one table view for showing all overlapping volumes in reference to the anatomical reference point defined by the slice view intersection. And the DVH view for showing the DVHs of selected volumes (see Fig. 6.7). The spatial views consist of slice views and volume visualization. They are used for visualizing the spatial information as described in Section 6.3.1.



(a)



(b)

Figure 6.3: The chord diagram with a selected reference structure (a), and the outer ring indicating the amount of overlap (b). The colors represent the mean dose.

### 6.4.1 Chord Diagram

The chord diagram is used as an overview of all structures currently under consideration (see Fig. 6.3), which includes target volumes, OAR volumes, and dose regions  $R_d$ . The chord diagram was chosen as it provides a compact overview of all overlap relations, and helps to select the reference structure in a convenient way (see Fig. 6.3a). A chord connection represents an overlap between two volumes, and therefore a volume by itself.

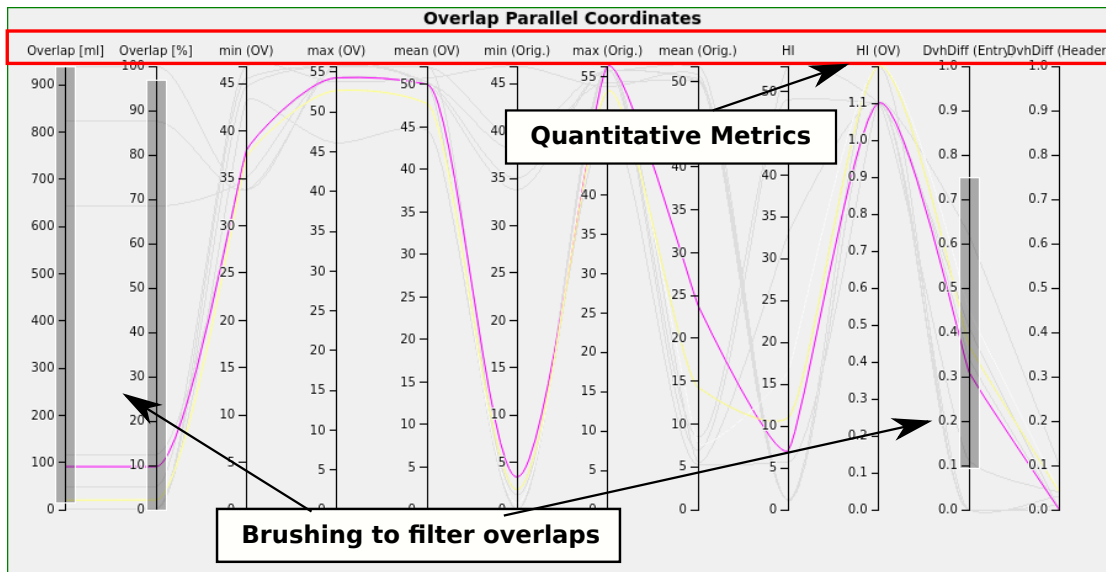


Figure 6.4: The parallel coordinates after selecting a reference structure. Filtering overlaps by evaluation metrics updates the other views. The resulting line color is determined by mixing the colors of the original structures.

The color of the chord has three sections and shows the mean dose value  $d_{mean}$  of the overlap volume  $OV(S_i, S_j)$  in the middle part, and  $S_i$  and  $S_j$  respectively on the outer parts. The color coding gives an indication of how different the mean dose values of the original volumes are compared to the overlap.

The ring of the chord diagram consists of three sections. The outer section is for representing the structure with its assigned name and color (see Fig. 6.3b). A structure can be selected as reference structure by clicking on this section. The portion of arc length allocated to a structure is determined by the number of volumes it overlaps with. The inner two sections are for encoding the amount of overlap of the structures in percentage (see Fig. 6.3b). The three blue circles represent 0%, 50% and 100% percent of overlap, and provide an overview of the amount of overlap.

### 6.4.2 Parallel Coordinates View

Parallel coordinates (PC) are a widely used visualization technique for multivariate data, and a well-known visualization for exploratory data analysis [HW13]. We use a PC view to visualize for each overlap volume  $OV(S_i, S_j)$  the corresponding metrics. The PC was chosen due to its easy-to-understand way of representing multidimensional points (in our case the metrics for each overlap relation), its scalability (easy to add more metrics), and the effective selection of value ranges (brushing) for each metric. Each dimension in the PC view (see Fig. 6.4) corresponds to metrics calculated for  $OV(S_i, S_j)$ , including values for  $S_i$  and/or  $S_j$  depending on whether a reference structure was selected.

**Selected from Chord**

**Selected: PTV 50Gy**  
 volume: 939.58 [ml]  
 dose [min/max/mean]: 33.80 / 55.76 / 50.02 [Gy]  
 dose source: RT Dose

**Reference Structure**

**Quantitative Metrics**

Sort: Overlap [ml]

Overlap information:												
Name	Overlap [ml]	Overlap [%]	min (OV)	max (OV)	mean (OV)	min (Orig.)	max (Orig.)	mean (Orig.)	HI	HI (OV)	DvhDiff (Entry)	DvhDiff (Header)
Body Original	939.58	100.0	33.80	55.76	50.02	0.01	56.37	8.48				
PTV Thwand li	823.16	87.6	33.80	55.76	50.01	33.80	55.76	50.02				
CTV TV	642.27	68.4	35.01	55.76	50.32	35.01	55.76	50.30				
PTV Supra	116.41	12.4	37.94	54.30	50.09	37.94	54.30	50.09	1.1	1.1	0.00	0.00
Avoid2	91.26	9.7	37.94	54.30	50.04	3.44	56.37	23.86	7.1	1.1	0.31	0.00
CTV_LAW	46.87	5.0	47.85	52.78	50.17	46.85	52.78	50.17	1.1	1.1	0.04	0.01
Lungen bds	20.23	2.2	37.21	52.69	47.78	0.66	53.21	7.82	16.5	1.2	0.45	0.04
<b>Lunge li</b>	<b>20.23</b>	<b>2.2</b>	<b>37.21</b>	<b>52.69</b>	<b>47.78</b>	<b>2.12</b>	<b>53.21</b>	<b>14.29</b>	<b>11.0</b>	<b>1.2</b>	<b>0.37</b>	<b>0.04</b>
HD	2.16	0.2	45.53	55.76	52.17	0.01	55.76	52.17				
NS_Wire	1.61	0.2	44.67	55.76	52.03	39.37	55.76	52.17				
Herz	0.02	0.0	43.15	46.11	44.62	1.55	48.71	5.26				

**Filtered Overlaps**

**Selected Overlap**

Figure 6.5: Table view TV-I: The reference structure selected in the chord diagram is listed at the top. All table entries correspond to outgoing chords and lines in the parallel coordinates view (greyed-out values are from brushing shown in Fig. 6.4). The entry highlighted in yellow is the currently selected overlap, which updates the spatial and DVH views.

If a reference structure  $S_r$  is selected in the chord diagram (see Fig. 6.3a), each line in the PC view corresponds to a visible chord in the diagram, i.e., all  $S_r \sim S_i$  where  $i$  corresponds to a visible chord. In the PC view, the amount of overlap in ml and percentage is displayed in regard to  $S_r$ . For  $OV(S_r, S_i)$  and  $S_i$ , the values displayed are  $d_{min}$ ,  $d_{mean}$ ,  $d_{max}$  and  $HI$ . Furthermore, for  $S_r$  and  $S_i$  the values  $D_{HI}(S_r, OV(S_r, S_i))$  and  $D_{HI}(S_i, OV(S_r, S_i))$  are displayed.

If no reference structure is selected, all overlap volumes  $OV(S_i, S_j)$  are displayed in the PC view. Even though  $S_i \sim S_j$  is symmetric, some plan evaluation metrics such as the overlap in % differ depending on whether it relates to  $S_i$  or  $S_j$ . For this reason, each  $S_i \sim S_j$  is represented with two lines in the PC view. One for the values for  $OV(S_i, S_j)$  with  $S_i$ , and one for  $OV(S_i, S_j)$  with  $S_j$ . Both lines can be identified with the same chord in the chord diagram. Since there is no reference structure selected, the dimension for  $D_{HI}(S_r, OV(S_r, S_i))$  is not displayed.

### 6.4.3 Table Views

We include two table views in our application. The first view shows all overlaps of a reference structure  $S_r$  (see Fig. 6.5), the other view shows all overlaps at a 3D world position  $x \in \mathbb{R}^3$  (see Fig. 6.6). Entries in both tables can be selected, which updates connected views.



The screenshot shows a table with the following data:

Name (OV)	OV [ml]	Vol0 [ml]	Vol1 [ml]	m
OV(Body Original, BODY)	16729.42	16734.28	32303.59	0
OV(Body Original, Lunge bds)	2556.74	16734.28	2556.74	1
OV(Lunge bds, BODY)	2556.74	2556.74	32303.59	0
OV(BODY, Avoid2)	1664.33	32303.59	1664.33	1
OV(Body Original, Avoid2)	1663.41	16734.28	1664.33	3
OV(Body Original, Lunge li)	1106.71	16734.28	1106.71	2
OV(Lunge li, Lunge bds)	1106.71	1106.71	2556.74	2
OV(Lunge li, BODY)	1106.71	1106.71	32303.59	2
OV(Lunge li, Avoid2)	510.69	2556.74	1664.33	3
OV(Lunge li, Avoid2)	507.39	1106.71	1664.33	5

Figure 6.6: Table view TV-II: All overlaps defined by the current intersection of the slice views are displayed.

**Reference Structure (TV-I)** This table view lists all overlapping structures of a reference structure  $S_r$  selected in the chord diagram. The selected  $S_r$  is displayed above the table together with relevant information, such as total volume in ml and dose quantities (see Fig. 6.5). Each row represents an overlap  $S_r \sim S_j$  with the reference structure, and displays metrics for the overlap volume  $OV(S_r, S_j)$  and for the structure  $S_j$ . The displayed metrics are the same as displayed in the PC view with a selected  $S_r$  as described in Section 6.4.2. The table can be sorted by each value, and entries can be selected.

**3D World Position (TV-II)** The second table view depends on a 3D point  $x \in \mathbb{R}^3$  to define the set  $OV_x$  (see Section 6.3.2). The point  $x$  is always defined by the current intersection of the slice views. The values displayed in this view are the same as in TV-I, but with additional columns. Since there is no  $S_r$  defined, values such as  $d_{min}$  or volume in ml are displayed for both  $S_i$  and  $S_j$  (see Fig. 6.6). This way, only one row per overlap volume is displayed and includes all values for the original structures. This is similar to the PC view, where two lines are added when no  $S_r$  is selected.

#### 6.4.4 Dose Volume Histogram (DVH) View

DVHs [DMB<sup>+</sup>91] provide a useful summary representation of the 3D dose distribution, and have been widely used for external beam treatment planning. In our application, the DVH view (see Fig. 6.7) is dynamically populated, i.e., the DVHs being displayed depend on selections made in other views. If a single overlap is selected, e.g., in the chord diagram (see Fig. 6.3b), only the DVHs of the corresponding structures are displayed as depicted in Fig. 6.7. If no selection is made, DVHs of all original structures are displayed, which is comparable to DHV views found in commercial systems. The label in the color legend can be used to select a single DVH and fade the remaining ones, if, for instance,

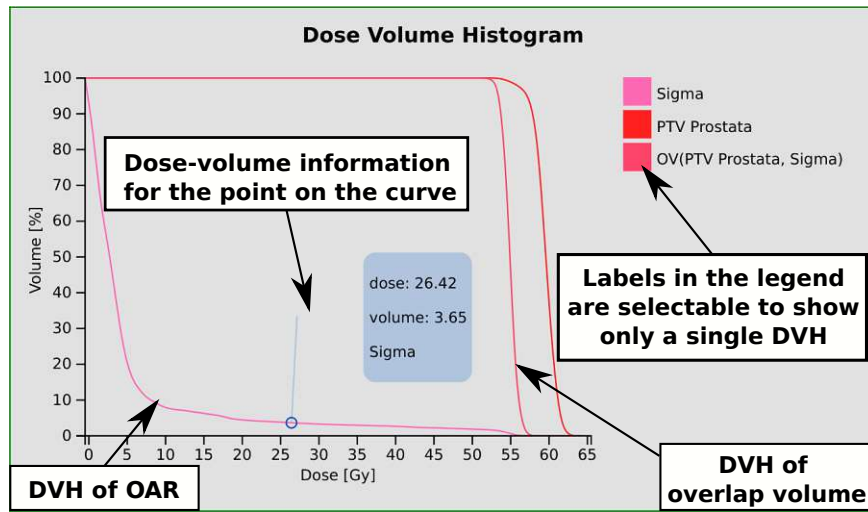


Figure 6.7: DVH view with a selected overlap volume of the PTV and an OAR. The resulting line color of the overlap DVH is determined by mixing the colors of the original structures.

the pre-defined colors of the structures are too similar. Additionally, a tooltip shows information of the closest point on the (closest) curve to the current mouse position (see Fig. 6.7). The point might not be unique when the curves overlap, which can be solved by selecting a single DVH. In the tooltip window, the values for dose ( $D_p$ ), volume ( $V_d$ ), and structure name are shown.

#### 6.4.5 Spatial Views

The spatial views are based on basic principles [SPBR20] used for visualizing data in the domain of RT planning. The views follow a standard layout as generally used in imaging workstations and commercial RT planning tools. The layout provides a screen divided into four quadrants, three showing slice views, and one showing a 3D view of the data (see Fig. 6.8). The general approach is to pre-select at least one anatomical image for display, for instance, the planning CT to provide an anatomical context. Other images can be added, such as an MRI, and are displayed using image fusion [SFA<sup>+</sup>17b]. The information displayed in the spatial views is linked with the quantitative views and depends on the selections made therein. Structures, i.e., target volumes, OARs, and overlap volumes are automatically added or removed, depending on selections made in the quantitative views.

**Slice Views** The slice views show image information in coronal, sagittal, and axial orientation (see Fig. 6.8). Dose distribution information can be added on demand, and displayed either as colorwash, i.e., a color is assigned to pre-defined dose regions  $R_d$ , or as outline as depicted in Fig. 6.9. However, this should not be necessary, since the

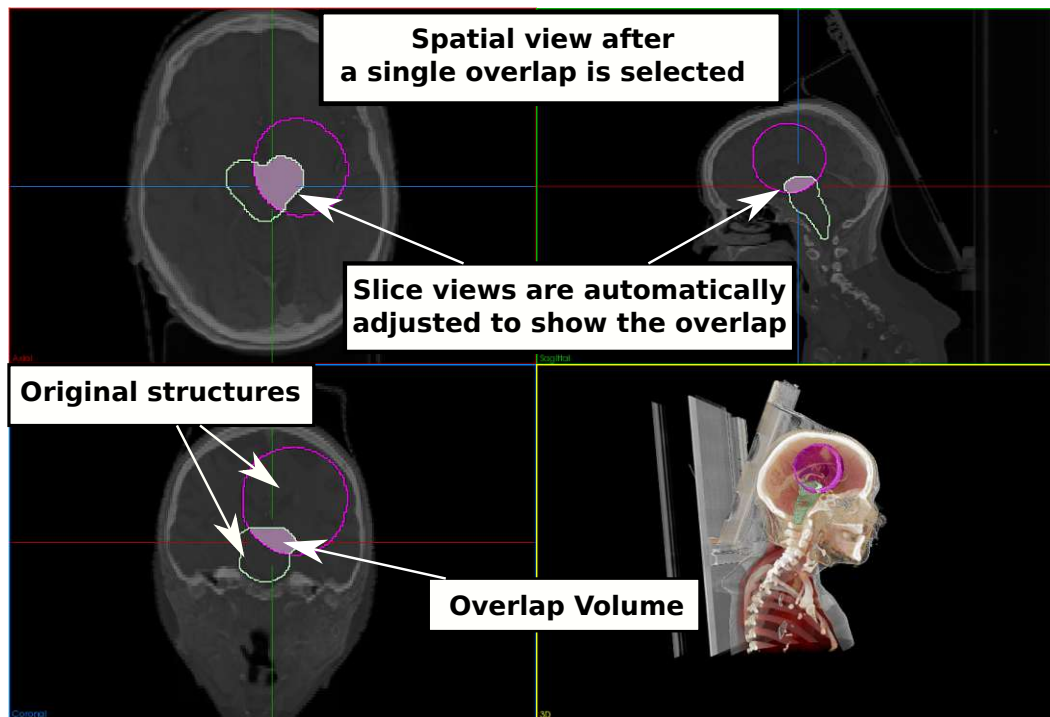


Figure 6.8: Spatial views after selecting an overlap. The original structures are displayed alongside the overlap volume. The overlap is used to focus the slice views in its center and displayed as filled semi-transparent area after its selection in the quantitative views.

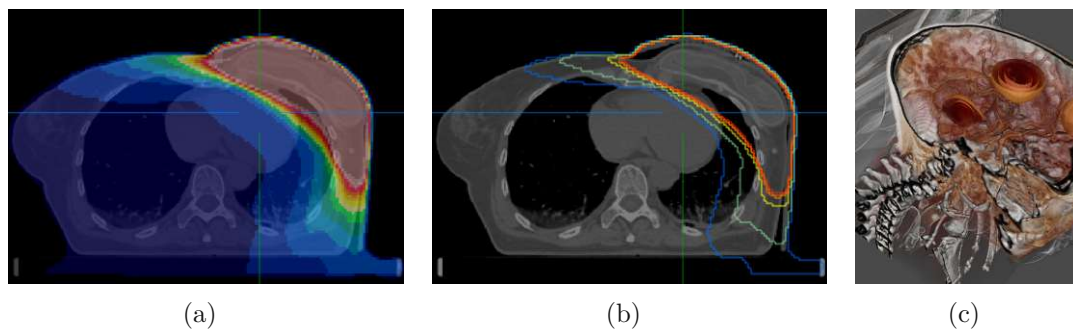


Figure 6.9: Dose visualization can be enabled if required either as colorwash (a) or isolines (b) in the slice views, or as iso-surfaces in the 3D view (c).

quantitative views always show relevant dose information, and furthermore dose regions  $R_d$  can be added as structures (see Fig. 6.2). For each structure, which is selected for display, the outline is visualized with the color assigned to the structure. In addition, each overlap volume, which is selected in the quantitative views, is displayed as filled, half transparent area, which is shown in Fig. 6.8. The resulting color is determined by mixing the colors of the original structures.

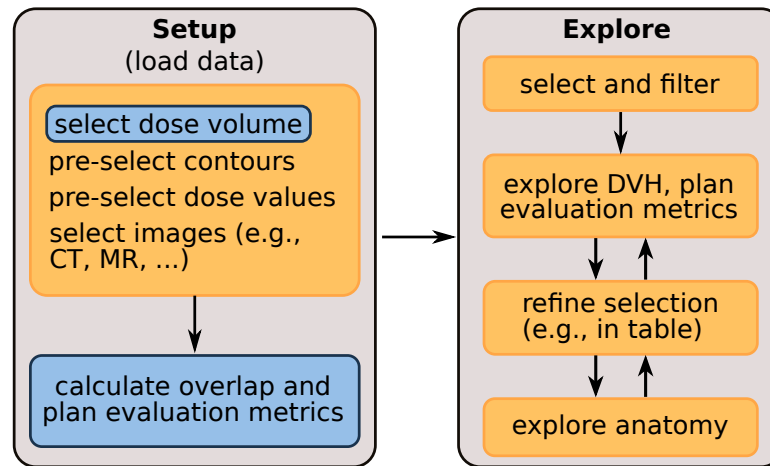


Figure 6.10: Data setup and interaction concept: the blue parts in the setup are mandatory to fill the data structures, and the arrows define the flow of actions.

**3D View** The underlying implementation for volume visualization of the imaging data is based on the approach described in the work of Schlachter et al. [SFA<sup>+</sup>17b], and is used for image fusion, as well as, visualization of target and OAR structures. Furthermore, the implementation allows for “cutting” open the volumes to be able to inspect the inside information, which is shown in Fig. 6.8. There is also the possibility to display dose information as isodose surfaces for defined dose-values (see Fig. 6.9). Additionally, it is possible to highlight the surface of the overlap volume in 3D if required.

## 6.5 Data Exploration and User Interaction

The underlying data structures need to be initialized before starting to interact with the views (see Fig. 6.10). A dose distribution needs to be selected to compute the quantitative metrics and to define dose regions  $R_d$  (see Section 6.3.2). Optional steps in the setup are pre-selecting contours, i.e., reducing the overall data for exploration, and pre-selecting dose values that are used for generating dose regions  $R_d$ . The basic idea is to use the quantitative views to identify candidate overlaps for which the resulting dose could or should be reduced. The calculated metrics, which are displayed in the various views, can be used to reduce the number of possible candidates to a smaller set and further explore them in detail. An overview of the connections between views can be found in Fig. 6.11. In general, we follow an overview first, zoom and filter, then details-on-demand approach [Shn96].

### 6.5.1 Chord Diagram

The chord diagram has two options for making a selection. It is used to select a reference structure as shown in Fig. 6.3a and in Fig. 6.11 A, or to select a single chord as shown in

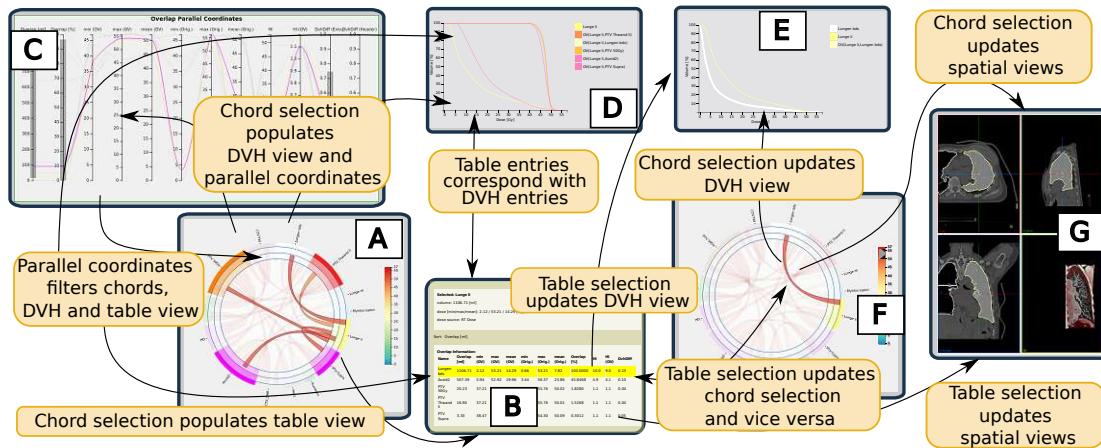


Figure 6.11: Overview of the interaction between individual quantitative views (chord diagram, parallel coordinates, DVH and table view TV-I) and the spatial views. Arrow directions indicate which views are updated after an interaction.

Fig. 6.3b and Fig. 6.11 F.

After selecting a reference structure  $S_r$ , table view TV-I shows all structures, which overlap with  $S_r$  (see Fig. 6.11 A to B). Additionally, the  $S_r$  is added to the spatial views and the center of the slice views is set to the center of  $S_r$ . Furthermore, the data of the parallel coordinates are updated to show only entries, which correspond to the visible chords and entries in TV-I respectively (see Fig. 6.11 A to C). The DVH view is also updated accordingly, it only shows DVHs, which correspond to the overlap volumes of visible chords, including  $S_r$  itself (see Fig. 6.11 A to D).

If a single, outgoing chord of  $S_r$  is selected, then the corresponding entry in TV-I is highlighted in yellow (see Fig. 6.11 F to B), and the DVH view is updated to show only  $S_r$ , the overlapping structure  $S_i$ , and the overlap volume  $OV(S_r, S_i)$  (see Fig. 6.11 F to E). Furthermore, the spatial view is updated to show  $S_r$ ,  $S_i$  and  $OV(S_r, S_i)$  (see Fig. 6.11 F to G). Independently, a single chord can always be selected, but only updates the DVH and spatial view if no  $S_r$  is selected.

### 6.5.2 Parallel Coordinates

The parallel coordinates (PC) are used to filter overlaps depending on plan and overlap evaluation metrics. The data shown in the view depends on whether a reference structure is selected or not.

If a reference structure  $S_r$  is selected the PC view shows all overlaps  $S_r \sim S_i$ . Brushing the coordinates, i.e., selecting a value range on the axis (see Fig. 6.4), filters table entries in TV-I, and fades items, which are not selected by the brush (see Fig. 6.11 C to B). The same applies to outgoing chords of  $S_r$  in the chord diagram (see Fig. 6.11 C to A), and

furthermore the DVH view, which now only shows DVHs of overlaps with the selected criteria (see Fig. 6.11 C to D).

If no  $S_r$  is selected, all overlaps  $S_i \sim S_j$  are displayed, i.e., each line in the PC view corresponds to a chord in the chord diagram. Brushing the coordinates filters the set of overlaps, and updates the chord diagram to show only chords corresponding to the filtered overlaps. Additionally, the DVH view is updated to show only DVHs of filtered overlaps, including the DVHs of the original structures defining the overlap.

### 6.5.3 Table Views

After selecting a reference structure in the chord diagram, the table view TV-I can be used to investigate overlaps by selecting one by one. A selection in the table view (see Fig. 6.11 B to F) is equivalent to a click on a single chord in the chord diagram. This also means that a table entry selection updates the chord diagram, the DVH view, and the spatial views. Overlaps can be deselected and the state before the selection is restored.

A selection in table view TV-II works like a selection TV-I, with the only difference that the crosshair, i.e., the 3D world position, in the spatial views is not repositioned, as this would alter the contents of the table. Instead, a selection only updates the zoom and the displayed structures to be able to investigate overlaps at specific 3D position.

### 6.5.4 Spatial Views

The only interaction which updates the quantitative views, is adjusting the position of the slices. Adjusting the slices automatically updates the content of table view TV-II, and therefore always makes all overlap information at the current position with all calculated metrics available.

The focus is on updating the spatial views depending on selections made in the quantitative views. For instance, if an overlap is selected in TV-I, an automatic repositioning of the slices to the center of gravity of the overlap volume and a zoom depending on the size of the volume is triggered. Furthermore, only the corresponding structures and overlaps of the selection are displayed (see Fig. 6.8). There is an option to automatically set isodose values from the selected overlap volume for 3D display, as well as, an optional automated clipping in the 3D view to the bounding box of the selected overlap volume.

## 6.6 Proposed Workflow for RT Plan Evaluation

We propose the following workflow. First, a target volume is selected in the chord diagram as a reference structure  $S_r$ . Afterwards, all OARs in proximity are visible by the outgoing chords, i.e., all  $S_j$  with  $S_r \sim S_j$ . A first indication of the amount of overlap, as well as the mean dose values for the volumes  $OV(S_r, S_j)$ ,  $S_r$ , and  $S_j$  are encoded in the chord diagram (see Fig. 6.12a). All other plan evaluation metrics are available in the PC view for filtering and also displayed in the table view TV-I. As a next step, the PC view

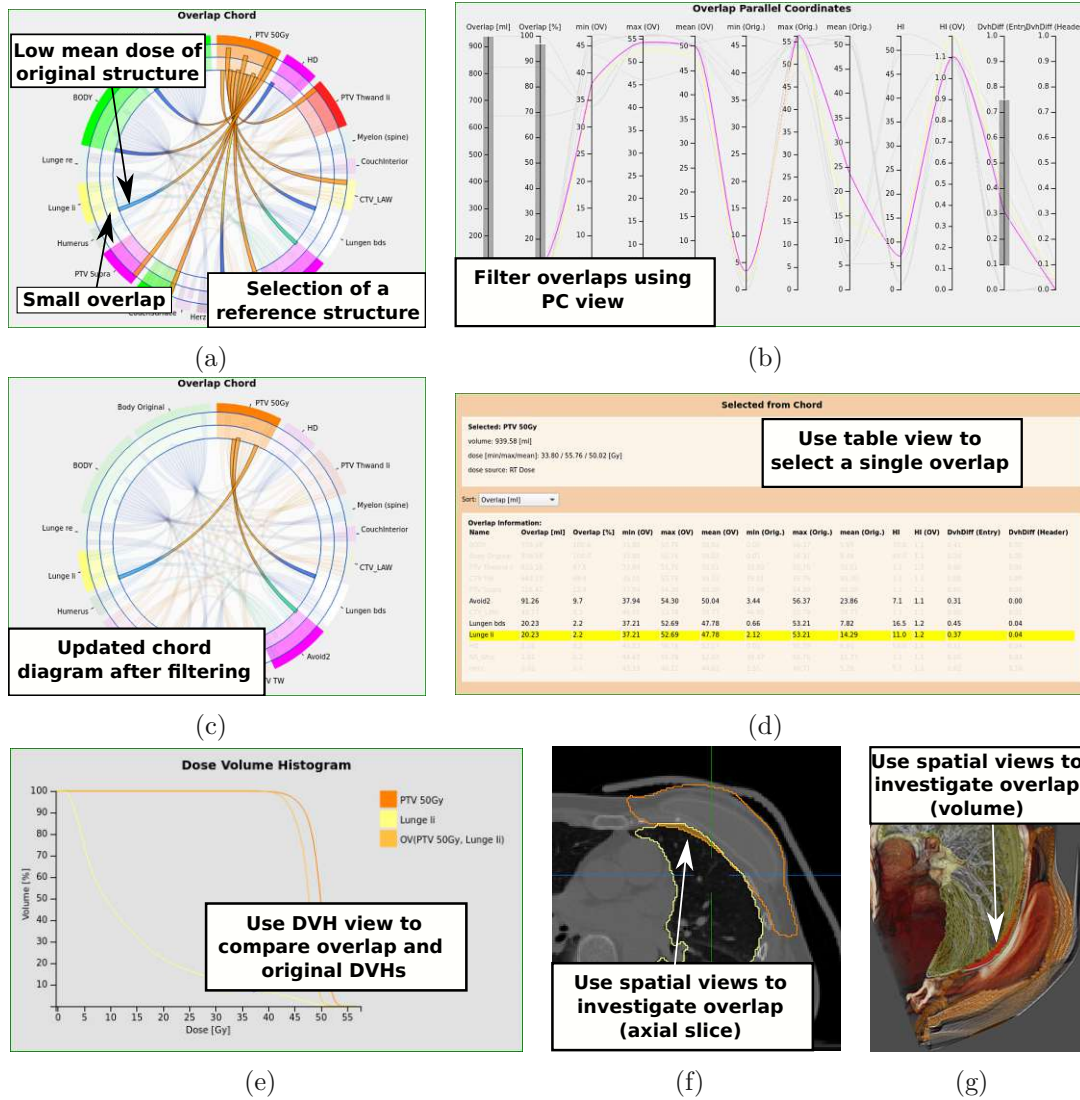


Figure 6.12: Example exploration starting by selecting a reference structure in the cord diagram (a). Filtering in the parallel coordinates (b) reduces possible candidates (c), (d). Finally, a selection of a single overlap (d) shows the DVHs (e) and spatial views (f), (g) of the corresponding structures alongside the overlap volume.

can be used to put further constraints on the candidate volumes (see Fig. 6.12b). The remaining volumes (see Fig. 6.12c) can be inspected one by one, by selecting each entry in the table view TV-I (see Fig. 6.12d). Then for each selection the corresponding DVHs can be evaluated in the DVH view (see Fig. 6.12e), alongside the corresponding anatomy (see Fig. 6.12f and Fig. 6.12g), which is brought automatically into the center of the view with the display of  $OV(S_r, S_j)$ ,  $S_r$ , and  $S_j$ . Further adjustments can be made in the spatial views if the automatic parameter setting is not sufficient.

### 6.6.1 Finding Candidate Overlaps

An example and the necessary steps for finding candidates is depicted in Fig. 6.12. The PTV with dose  $\geq 50$  Gy is selected in the chord diagram as reference structure  $S_r$  (see Fig. 6.12a). Now the chord diagram gives an indication that overlaps are either small, but with a low mean dose of the original structure, or either large (up to 100% overlap) with a similar mean dose as  $S_r$ . The small overlaps are the most interesting, as they might have too much dose in the overlap.

Afterwards, the PC view is used to filter by the amount of overlap in % and in ml, to remove very small volumes, and additionally by the  $D_{HI}$  value (see Fig. 6.12b). The remaining structures are now reduced to three candidates (see Fig. 6.12c and Fig. 6.12d). Now the table view TV-I can be used to inspect all other metrics, and select one overlap as shown in Fig. 6.12d, in this case the left lung, for further investigation using the DVH view and the spatial views.

The result after the selection is shown in Fig. 6.12e. It is now possible to inspect the DVHs of the overlap and the original structures alongside the anatomy with the highlighted overlap region, as shown for the axial slice in Fig. 6.12f. The 3D view can then be further adjusted to produce the final result as depicted in Fig. 6.12g.

### 6.6.2 Hot Spot Detection in OARs

Another possible application is the detection of dose hot spots as depicted in Fig. 6.13. In our application it is possible to define dose regions  $R_d$  as part of the setup and calculate volume-to-dose overlaps (see Section 6.3.2 and Fig. 6.2). This is depicted in Fig. 6.13a, where  $R_d$  was defined with  $d$  as 93% of the reference dose. By selecting  $R_d$  in the chord diagram as reference structure, it is possible to explore the resulting overlap volumes with potential hot spots. All volumes with hot spots can be easily detected and explored (see Fig. 6.13b) in the same way as we described it in Section 6.6.1 for target volumes.

## 6.7 Evaluation and Results

We evaluated our approach in a user study with three experienced domain experts of the field: a radiation oncologist, a medical physicist, and a radiation therapist, all with more than 10 years of experience. They were required to use the software to perform a dose plan evaluation with specific tasks for five data sets and fill in a questionnaire. The tasks



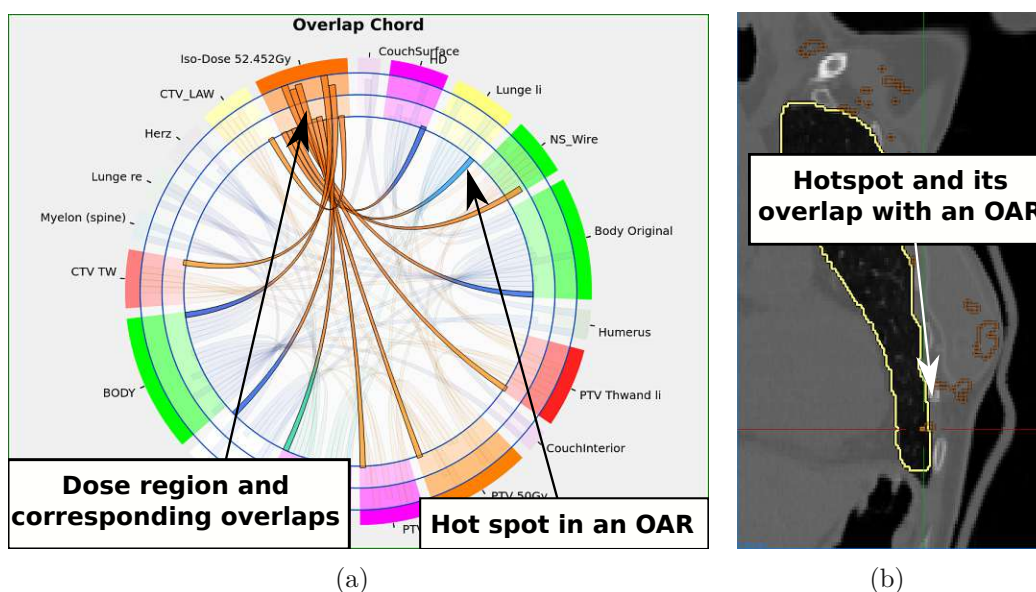


Figure 6.13: Hotspots after defining a dose region with a dose value  $d$  corresponding to 93% of the reference dose. All outgoing chords show structures, which have sub-volumes with a dose value  $\geq d$  (a). Quantitative measures can be explored using the table view, and further selections update the spatial views (b).

Table 6.1: Questionnaire per Data Set (Shortened Version)

Q1	Give a final rating of the plan regarding overlap volumes from 1 to 5.
Q2	Was your final decision in Q1 based on visualization X?
Q3	Is visualization X helpful for finding candidate overlaps? (Rating: 1–5)
Q4	Would you come to the same conclusion as in Q1 by considering only the DVHs of individual OARs using the standard software?
Q5	Are the visualizations suitable for finding hot spots? (Rating: 1–5)

of the domain experts were to investigate five data sets, and explore possible candidates for further dose reduction, as well as finding dose hot spots. The order in which the data sets were evaluated was different for each expert. Each data set covers a different type of cancer, e.g., brain and prostate lesions (see Table 6.3). The dose distributions are expected to be suboptimal, as no prior review was done.

The questionnaire consists of 24 questions covering the individual visualizations and their interactions regarding helpfulness, comprehensibility, intuitiveness, decision-making, speed (subjective scale), and domain expert insights through informal comments. The Questions Q1–Q5 were answered for each of the five data sets (see Table 6.1), whereas Q6–Q24 were answered after finishing the tasks related to the data sets to reflect the gathered

Table 6.2: Questionnaire (Shortened Version)

Q6	Which of the visualizations are helpful for the problem of identifying overlaps to further reduce the dose? (Rating: 1–5)
Q7	Is visualization X suitable for finding candidate overlaps? (Rating: 1–5)
Q8	Intuitiveness: Rate the visualizations for finding candidate overlaps from 1 to 5.
Q9	Speed: How fast did you find the sub-volumes which could potentially benefit from lower doses with visualization X? (Rating: 1–5)
Q10	Measures/Metrics: Is the overlap information / measure X in the PC view and table views helpful?
Q11	Which measures are missing regarding the PC and table views, and could be relevant to include in future work?
Q12	Details: Does the visualization of the X help for detailed inspection of candidate volumes? (Rating: 1–5)
Q13	Does interaction with visualization X give a good spatial overview? (Rating: 1–5)
Q14	Does interaction with the spatial views (reference point selection) help to give an overview of candidate overlaps. (Rating: 1–5)
Q15	Chord diagram: Provides a good overview for candidate overlaps? Are the rings good for an overview of the amount of overlap? Are the chord colors a good indication for the amount of dose on the original and overlap? Is the interaction with the diagram helpful? (Rating: 1–5)
Q16	Parallel Coordinate: Is brushing helpful to filter for candidate overlaps? (Rating: 1–5)
Q17	TV-I: Is the table view helpful for finding candidate overlaps? Is the interaction with the table view good for investigating candidate overlaps? (Rating: 1–5)
Q18	TV-II: Same questions as Q17
Q19	DVH view: Is it helpful to show the originals together with overlap volumes? (Rating: 1–5)
Q20	Use cases: For which of the test use cases are the visualizations more helpful?
Q21	Is adding dose regions helpful for investigating overlap volumes?
Q22	Can you do the same with the standard software, i.e., finding overlap volumes with too high doses or hot spots? Would it take longer?
Q23	Do you see potential to integrate the visualizations in the radiotherapy planning workflow?
Q24	What are missing features with regard to finding sub-volumes of OARs which are receiving too much dose?

Table 6.3: Final rating of the plan with regard to overlap volumes.

Data Set	U1	U2	U3	Same Rating	Agree on Acceptance
Abdomen	3	2	5	0	no
Head & Neck	2	2	5	2	no
Prostate	5	2	5	2	no
Brain	5	4	5	2	yes
Thorax	1	1	2	2	yes

Table 6.4: User ratings for Q2 aggregated over all test data sets in percentages.

	yes	no
Chord Diagram	<b>93</b>	7
Parallel Coordinates	20	<b>80</b>
Table View I	<b>87</b>	13
Table View II	0	<b>100</b>
Dose Volume Histogram	<b>67</b>	33
Spatial Views	<b>87</b>	13

experience (see Table 6.2). The answers were either given as a rating using a scale from 1 to 5, where higher is better, if not mentioned otherwise, as “yes” / “sometimes” / “no”, or as free text. For each question users could provide free comments.

With the first question Q1, the users were asked to give a final rating of the plan with regard to overlap volumes from 1 (cannot be improved) to 5 (must be improved), where 3 means can be improved, but is not critical (see Table 6.3). In four out of the five cases at least two users gave the same rating, although in three cases there was at least one user who disagreed with the other two in terms of acceptance.

They were asked in Q2 on which of the visualizations their final decision was based on (see Table 6.4). In **93%** the chord diagram is used for the decision, followed by the TV-I and spatial views with **87%**, and the DVH view with **67%**. In Q3 we asked which visualizations are helpful for solving the task, which also shows that these views are helpful, whereas TV-II and parallel coordinates are rated as not helpful (see Fig. 6.14). The standard software was not used for comparison, as we can not directly compare it to our approach. But we asked in Q4 if they think they had come to the same conclusion if they would use the standard software of the institution. In **60%** of the cases they think they would have come to the same conclusion. The comments suggest, that this was due to the fact that an OAR is receiving a dose higher than a certain limit, which is visible in the standard software, and was not related to an overlap region. In Q5 we asked if the visualizations are suitable for finding hot spots in OARs. The results show that the spatial views, TV-I and chord diagram are the most suitable for this task (see Fig. 6.14).

## 6. EXPLORATION OF OVERLAP VOLUMES FOR RADIOTHERAPY PLAN EVALUATION

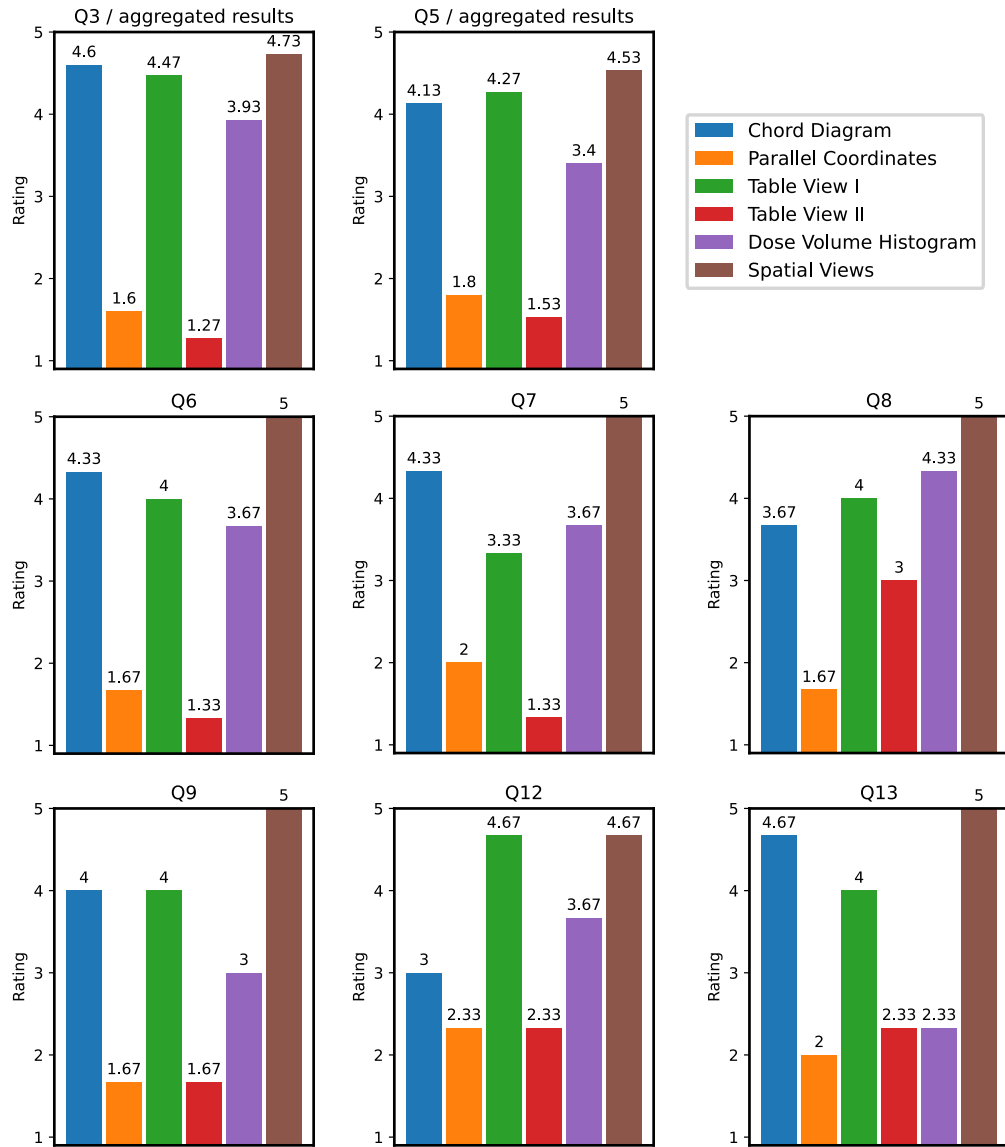


Figure 6.14: User ratings for Q3, Q5–Q9, Q12 and Q13. Q3 and Q5 are aggregated over all test data sets.

Table 6.5: User ratings for Q10 in percentages.

	Parallel Coordinates		Table Views	
	yes	no	yes	no
Overlap in ml	0	<b>100</b>	<b>100</b>	0
Overlap in %	<b>67</b>	33	<b>67</b>	33
Overlap: min/max/mean	0	<b>100</b>	<b>100</b>	0
Original: min/max/mean	<b>100</b>	0	<b>100</b>	0
HI	0	<b>100</b>	0	<b>100</b>
$D_{HI}$	0	<b>100</b>	0	<b>100</b>

Questions Q6–Q9 cover the helpfulness of identifying overlaps to further reduce the dose (Q6), the suitability to identify candidate overlaps for further inspection (Q7), the visualizations’ intuitiveness (Q8), and how fast (subjective scale) candidates can be identified (Q9). The spatial views always received the highest rating. The chord diagram, TV-I and DVH view were always rated greater than **3**, and the parallel coordinates and TV-II were always below or equal to **3** (see Fig. 6.14).

In Q10 they were asked which of the metrics shown in the table views and parallel coordinates they consider helpful. The results depicted in Table 6.5 show that only the overlap and dose values are considered helpful. HI is not considered helpful, as well as the  $D_{HI}$ . For the latter, one comment mentioned, that it was not used because the user could not get familiar with the meaning of the value.

Furthermore, we asked in Q11 for missing metrics as free text. One suggestion was to include also the volume in ml of the original structures in TV-I and the PC view, as only the overlap in ml is shown. Only for the selected reference structure the absolute value is shown at the top of TV-I.

In Q12 we asked which visualizations are helpful for a detailed inspection of candidate volumes. The results show that the spatial views and TV-I are considered most helpful, with the DVH view following (see Fig. 6.14). This is also in line with our proposed workflow.

In Q13 we asked whether using the interaction in the quantitative views to synchronize to the spatial views helps to provide a good spatial overview. The chord diagram and TV-I are considered helpful, besides the spatial views themselves (see Fig. 6.14). The other views received low ratings. In Q14, the interaction in the other direction, which updates TV-II, is not considered helpful with a rating of **2.33**.

Questions Q15–Q19 are specific to individual visualizations. Q15 covers the chord diagram (see Fig. 6.15). In terms of overview of candidate overlaps and the interaction it is perceived as helpful. The outer rings were rated as sometimes helpful. The chord colors received lower ratings, and one comment suggested that the maximum instead

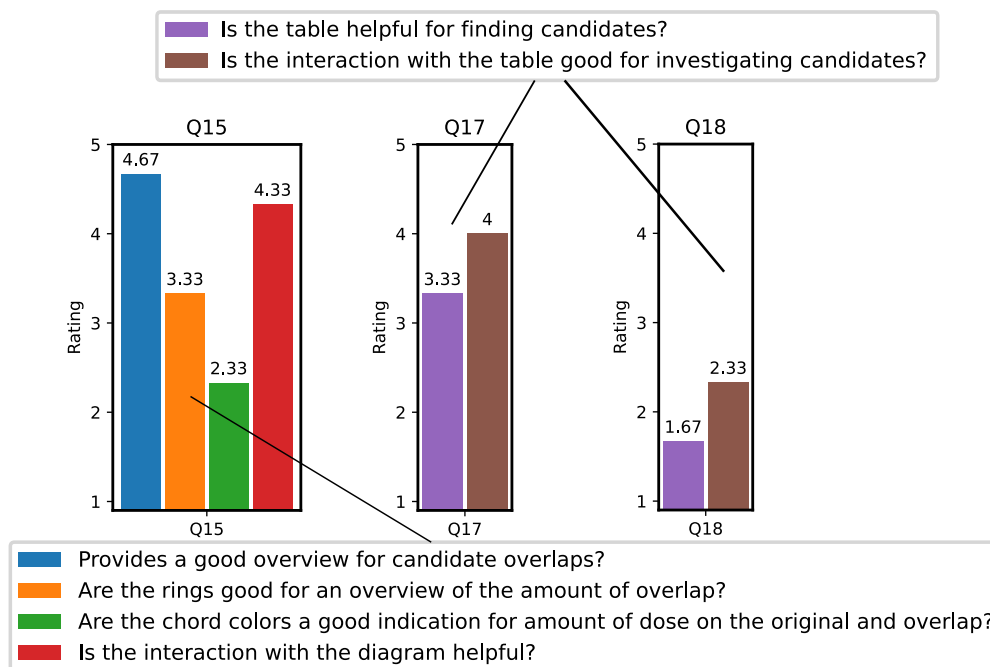


Figure 6.15: User ratings for Q15, Q17 and Q18.

of the mean dose would be more appropriate. In Q16 we asked whether brushing the parallel coordinates is helpful in the filtering of candidate overlaps, and is not regarded helpful with a rating of **2.0**. In Q17 for TV-I, and Q18 for TV-II respectively, we asked whether the table view is helpful for finding candidates, and if the interaction is good for investigating candidates. For TV-I, the first question was answered sometimes helpful and the latter one helpful (see Fig. 6.15). For TV-II both are considered not helpful. In Q19 users were asked if it is helpful in the DVH view to show the original volumes together with the overlap volumes, which received a rating of **33%** “yes” and **67%** “sometimes”.

The remaining questions cover use cases, comparison to existing software, and the integration in the current RT workflow. We asked for which use cases the visualizations are more helpful in Q20. All answers suggest that they are more suitable for overlap volumes, but can be also helpful for hot spots. One comment mentioned the manual effort for the latter, as one still needs to define the dose regions as part of the setup. In Q21 we asked if adding dose regions is also helpful for investigating overlap volumes and not just for investigating hot spots. This is regarded as very helpful, especially if there is no overlap with another structure to identify dose regions of interest in OARs. In Q22 we were interested in the comparison to existing software used by the hospital. We asked if

it is possible to do the same with the standard software, i.e., finding overlap volumes with too high doses or hot spots. Furthermore, we asked if it would take longer, to explore all overlapping structures with the standard software. The first part was answered by all with “sometimes”, and the second part with **67%** “yes” and **33%** “sometimes”. The comments indicate that it would be possible with standard software, but it would take much more time, as the overlaps have to be created manually. In Q23 we asked if there is potential to integrate the visualizations in the RT planning workflow and where. All participants answered “yes”, and suggested that they could be integrated during the plan creation and optimization, and during the plan discussion. Furthermore, the overlaps could be sent directly to the planning system to recalculate the dose and to see if the plan was improved with regard to PTV coverage and OAR sparing. We asked in Q24 which features are missing with regard to finding sub-volumes of OARs that are receiving too much dose. One answer suggests, a way to show highest and lowest doses to all structures and overlaps, not just for the ones shown after a reference structure is selected. Another answer suggests including logical operations for structures to remove, for instance, the PTV from the body structure to find only hot spots outside the PTV. Furthermore, a comment suggests defining a new reference structure from table view TV-I, to be able to see all structures overlapping with a table entry without starting again from the chord diagram.

## 6.8 Discussion

In general the results are promising. The chord diagram was well perceived in many aspects, most notably to gain an overview. One user criticized the fact that it is mandatory to use for selecting a reference structure in order to use table TV-I. Furthermore, it was mentioned that it would be of advantage to sort the structures in the chord diagram, e.g., according to the mean dose.

The table view TV-I was generally perceived as very helpful. Since it is linked with the chord diagram, one user noted that it would be appreciated to see some information about the structures in table views even if there is no reference selected in the chord diagram.

The DVH view was regarded helpful especially in combination with TV-I to investigate the overlaps further. It was noted that if one selects a structure in TV-I, one gets an impression on how big the compromise between PTV dose coverage and dose sparing of an OAR would be. In general, it was regarded helpful to show the originals together with the overlap volumes. One user noted, one can see in one view, if to rather focus on the PTV dose coverage or try to spare the OAR, and how much dose the spared PTV part gets. But this user also mentioned that this needs time to get familiar with, as it is very different from the current evaluation process.

The parallel coordinates were added as a means to reduce information and therefore possible candidates. However, it was barely used for that purpose. It was perceived as too complicated, although the idea of filtering was appreciated.

The measure  $D_{HI}$  was designed for finding volumes, which differ in their DVHs in combination with the parallel coordinates. In the example shown in Fig. 6.7, the DVH of the OAR differs from the overlap volume by a high amount, which is reflected by a high  $D_{HI}$  value of 0.53. For comparison, the value is 0.07 for the PTV. The  $D_{HI}$  can be used in the table and PC views to identify such an overlap. However, since the parallel coordinates were not used intensively, one can also not expect that the  $D_{HI}$  measure is regarded helpful to filter for candidates.

Automatically updating the spatial views depending on selections made in the quantitative views, helps to focus on one reference structure and investigate it further, and was regarded as helpful in many aspects. The table view TV-II was not perceived well, because one needs to manually scan the image by moving the anatomical point without any other information displayed to find a possible candidate.

The three experts were of different professions, which is possibly biasing their view of the cases and the software. This limitation should be considered when interpreting their responses.

## 6.9 Conclusion and Outlook

We present a novel way of exploring radiotherapy plans with a focus on overlap volumes. We demonstrate that the approach can also be used for hot spot detection. Our evaluation shows the validity of our approach.

Volume overlaps with PET-based regions of interest for dose boosting [EvdSZ<sup>+</sup>15], e.g. dose painting in non-small cell lung cancer, could be another possible application. Volumes based on the standard uptake value (SUV) could be added and used similar to the inclusion of dose regions. This could also be extended to show multiple overlaps, for instance, the PTV, the SUV volume, and the dose region overlap. Similarly, overlaps with dose regions using past and current dose distributions could be used for re-planning. Showing also previous dose regions on OARs, could help planners to decide where further reduction might be advisable due to past irradiation.



# Conclusions

The main scientific contributions of this thesis were presented in the Chapters 3 to 6. On its own, each of the presented chapters contributes to a specific part of the radiotherapy planning workflow, and as a whole the chapters contribute towards improving the overall workflow.

## 7.1 Summary of Scientific Contributions

The scientific contributions of the individual methods are summarized as follows:

- Definition of major requirements for a visualization system to provide medical doctors with the necessary visual information to validate tumor delineations, and review the dose distribution of an RT plan.
- Based on the list of requirements, the development and evaluation of a 4D visualization system with dedicated rendering and fusion of 4D multi-modal imaging data in collaboration with radiation oncologists. The benefit of using 4D multi-modal visualization and interaction techniques for defined radiotherapy planning tasks over a treatment planning system used in clinical routine was evaluated in a user study. The performance was evaluated for specific tasks: assessment of internal target volume (ITV) delineation, classification of tumor location, and assessment of dose distribution. For all three tasks, test cases with ground truth data were used for which we measured correctness, certainty, consistency, followed by an additional survey regarding specific visualization features.
- A visualization framework based on dissimilarity measures to indicate locally the registration results. The theoretical framework was implemented and evaluated in a user study to show its validity and performance regarding the detection of errors using landmarks defined on the data sets. It extends the original framework

by different interaction and visualization features for the exploration of candidate regions, and to simplify the process of visual assessment.

- Development of a novel interactive visualization approach for the exploration of radiotherapy treatment plans with a focus on overlap volumes, and with the aim of healthy tissue sparing. Quantitative properties can be interactively explored to identify critical regions and used to steer the visualization for a detailed inspection of candidates. The approach was evaluated with a user study covering the individual visualizations and their interactions regarding helpfulness, comprehensibility, intuitiveness, and decision-making.

### 7.2 Impact on the Field of RT Planning

The impact on the field of RT planning can be summarized as follows:

#### 4D Imaging, Target Volume Definition, and Motion Management

In RT planning medical doctors need to consider a variety of information sources for anatomical and functional target volume delineation. The validation and inspection of the defined target volumes and the resulting RT plan are complex tasks, especially in the presence of moving target areas as it is the case for tumors of the chest and the upper abdomen.

A multi-modal visualization system as proposed in this thesis (see Chapter 3) has the potential to improve the assessment of ITV delineations and the classification of tumor location. In a user study, lower quality of the test ITVs (ground truth quality was available) were more likely to be detected, ITV ratings were more consistent, and the classification of tumor location had a higher accuracy compared to the treatment planning system used in clinical routine. The overall evaluation of the survey (see Chapter 4) indicates that such a system provides a better spatial comprehensibility and simplifies the tasks, which were performed during testing. Furthermore, the visualization features have been identified as being helpful for the assessment of dose distribution during user testing.

#### Deformable Image Registration Quality

An evaluation with three radiation oncologists demonstrates the viability of our approach presented in Chapter 5. In the evaluation, lung regions were rated by the participants with regard to their visual accuracy and compared to the registration error measured with expert defined landmarks. Regions rated as “accepted” had an average registration error of 1.8 mm, with the highest single landmark error being 3.3 mm. Additionally, survey results show that the proposed visualizations support a fast and intuitive investigation of DIR accuracy, and are suitable for finding even small errors.

### Treatment Plan Evaluation and Healthy Tissue Sparing

A user study with domain experts was conducted using our visualization system presented in Chapter 6, using five data sets each representing a different type of cancer and location by performing a set of tasks and filling out a questionnaire. The results show that the visualizations and interactions help to identify and evaluate overlap volumes according to their physical and dose properties. Furthermore, the task of finding dose hot spots can also benefit from our approach. The results have the potential to enhance the current treatment plan evaluation process in terms of healthy tissue sparing.

### Handling of Uncertainties in RT Planning

The proposed methods made an attempt to improve the handling of uncertainties by addressing the goals described in Section 1.1, and thereby address some uncertainty sources — implicitly or explicitly. This includes target volume definition in the presence of breathing motion. The benefit of using the proposed visualization framework has been shown in user studies. Furthermore, the method for image registration quality has the potential to improve motion management by means of a pre-step if using motion modelling, as well as reducing uncertainties present in IGART if using DIR for dose warping [VLM<sup>+</sup>15]. Additionally, the method for exploring overlapping target volumes and OARs, has the potential to improve the overall treatment plan evaluation with respect to healthy tissue sparing.

## 7.3 Future Directions

During the course of this thesis, many aspects of radiotherapy planning and its workflow were discussed with research partners from other domains, which also led to the methods presented in this thesis. Some insights gained from these discussions, but also from the user studies presented in the previous chapters, will be discussed below in an effort to show possible future directions or extensions of the presented methods.

**3D/4D Multi-Modal Visualization:** Multi-modal visualization is important and needed for most steps in the planning. However, depending on the use case 3D and/or 4D visualizations are useful, but in other scenarios, the use of slice views in combination with quantitative visualizations might be more relevant, for instance, exploring overlap volumes. One insight gained is that the use of 3D visualization still has a high setup effort, and even with attempts made to reduce it (see automatic isodose values and clipping in Chapter 6), there might be not enough value added to justify the effort over using slice views. In terms of 3D visualization, reducing the setup effort, i.e. having parameters determined automatically, so that it can be used instantly without the need of manual adjustments, might broaden its use and lead to a more widespread acceptance.

**4D Imaging and Motion Management:** The use of 4D imaging and motion modelling for 4D dose calculation is an active research topic [RMBX15, LHD<sup>+</sup>19, ZBL<sup>+</sup>19].

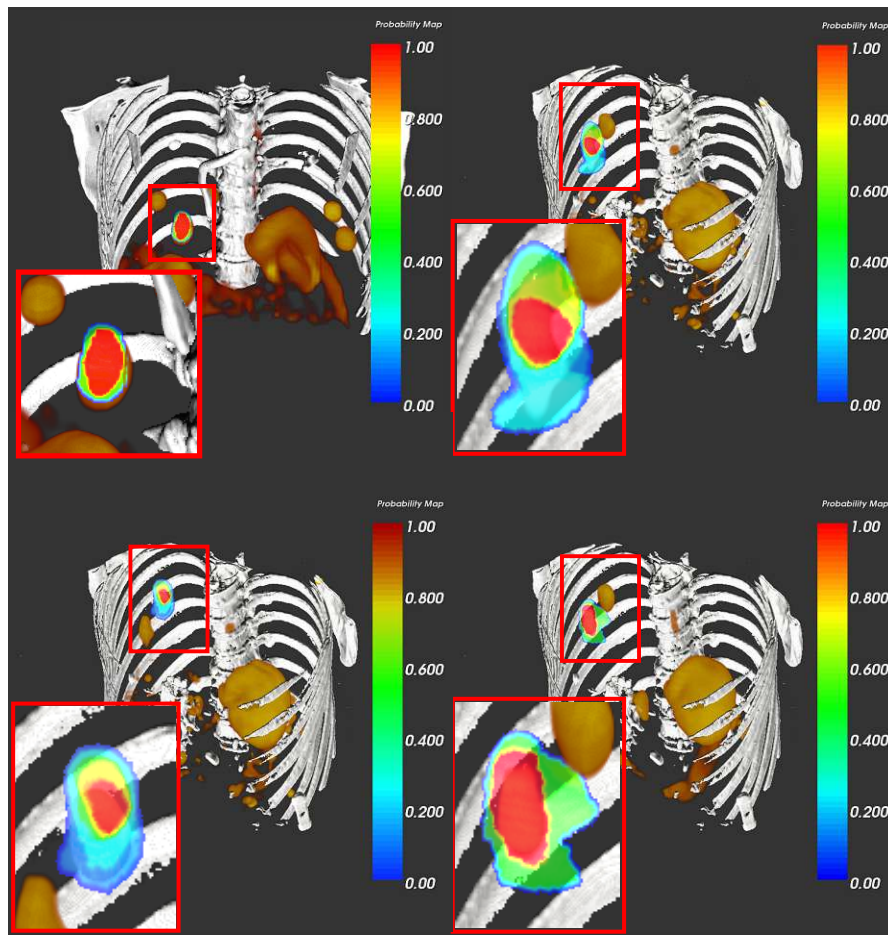


Figure 7.1: Using 4D GTV contour information to calculate the relative frequency for each voxel to be classified as cancer, leads to a probability volume (PV) of tumor tissue over the whole breathing cycle. The visualizations show the PV together with the PET/CT. Image are taken and adapted from Schlachter et al. [SFBN14].

Including 4D dose calculation into RT planning might require additional visualizations to ensure its quality, and approaches as presented in Chapter 6 might find more widespread use.

But motion modelling based on 4D imaging can also be achieved by the use of statistical volumes, for instance, using a calculated single CT scan from 4D-CTs for delineations [GHHLY08, WSvD08]. In general the visualization of tumor (location) probability using 4D GTVs might be another interesting concept. Figure 7.1 shows the time averaged probability map of 4D GTVs over the whole breathing cycle of lung cancer patients. Although the approach was initially designed to evaluate the quality of an automatic 4D GTV algorithm based on 4D-PET images, these probability maps might be used to define ITVs based on 4D GTVs [SFBN14]. Using 4D GTVs requires the delineation of

the tumor over the whole breathing cycle. Again, there might be the potential to use deformable image registration to effectively define only one delineation, and warp it onto the remaining time bins. The methods proposed in Chapters 3–5 can then be applied for quality assurance of the resulting registration result and the resulting contours.

**Deformable Image Registration:** Besides using DIR for motion modelling, another important application area is IGART for which quality assurance of DIR accuracy is essential [GHC14]. For the use in IGART, the framework needs to be evaluated using multi-modal features to show its validity for CT to CBCT registration quality inspection.

Also, the selection of different features that fulfil the requirements stated in Chapter 5 might be another interesting area to investigate. The features used in Chapter 5 are invariant towards rotation and cyclic translations within the patch window, as they are based on the distribution of Hounsfield units. For instance, features such the histogram of oriented gradients [DT05], might be a possible distribution to be used in combination with the histogram intersection method used in Chapter 5.

**Treatment Plan Evaluation and Volume Overlaps:** The use of quantitative views as presented in Chapter 6, to interactively explore overlap regions could be extended to define helper structures based on identified candidate regions. A new dose value could be assigned to these helper structures and the dose distribution could be immediately re-calculated. This would lead to an interactive, iterative process combining the steps of *Treatment Plan Design & Dose Calculation* and *Dose Plan Review & Treatment Evaluation* (see Fig. 1.1) by introducing a feedback loop. Such an interactive planning seems even more feasible given the fact that dose calculation speed is now within minutes. For instance, RayStation (RaySearch, Stockholm, Sweden, 2021) has an average calculation time of  $\leq 5$ min according to the vendor.

Another interesting direction could be dose painting, if volume overlaps with PET based regions of interest are defined and used for dose boosting [EvdSZ<sup>+</sup>15]. Similar to the inclusion of isodose volumes as presented in Chapter 6, the standard uptake value (SUV) could be used to define volumes. These SUV-based volumes could then be incorporated to explore overlaps, e.g., with the PTV, for the possibility of boosting.

This could further be extended to show multiple overlaps, for instance, the PTV, the SUV volume, and the isodose overlap. Again, this could be designed as a feedback loop enabling an interactive dose painting system.

Another challenge often faced in clinical reality is the re-irradiation of patients after relapse. Overlaps of an OAR with isodose volumes from past and present dose distributions for re-planning could be defined similarly. Using information from past and current treatment plans, might assist the planner to identify regions where further reduction is advisable due to past irradiation of OARs.

This work is now concluded with the highlighting of possible future directions. Hopefully, it contributes to strengthening the research foundation on the topic and as such supports

## 7. CONCLUSIONS

---

future works that will build on it for a better treatment outcome of cancer patients. Even though, the presented approaches were designed for RT planning as the primary application, they can be transferred to other application domains, e.g., biology. For instance, the inspection of deformable registration results is independent of RT itself. Furthermore, contributions targeting volume visualization or combining quantitative views with anatomical views have the potential to be applied to other domains.

# APPENDIX **A**

## Supplementary Material: Chapter 4

### Supplementary material for the publication:

**M. Schlachter**, T. Fechter, S. Adebahr, T. Schimek-Jasch, U. Nestle, and K. Bühler. Visualization of 4D multimodal imaging data and its applications in radiotherapy planning. *Journal of Applied Clinical Medical Physics*, 18(6):183–193, 2017. [SFA<sup>+</sup>17b]  
<https://doi.org/10.1002/acm2.12209>

## I. ADDITIONAL STATISTICS AND PLOTS FOR TEST CASES USED DURING TASK T.1

TABLE I. 4D-VS ITV<sub>1</sub>: Hausdorff distance in mm and Dice comparisons to the planning ITV, as well as quality ratings for each of the test cases in the ITV<sub>1</sub> test set using 4D-VS.

	Case 1	Case 2	Case 3	Case 4	Case 5	Case 6	Case 7	Case 8	Case 9	min	max	avg	stddev
Hausdorff Distance (Maximum)	9.99	7.03	6.19	8.29	4.00	7.68	7.34	12.11	6.38	4.00	12.11	7.67	2.33
Hausdorff Distance (Average)	3.28	1.71	1.34	2.21	1.31	1.69	1.88	4.62	2.12	1.31	4.62	2.24	1.07
Hausdorff Distance (95 percent)	5.45	3.88	3.51	5.10	2.85	4.11	4.42	7.01	4.19	2.85	7.01	4.50	1.22
Dice	0.66	0.74	0.81	0.84	0.76	0.89	0.80	0.61	0.70	0.61	0.89	0.76	0.09
Rating U1	5	4	5	3	2	2	4	5	4	2	5	3.78	1.20
Rating U2	5	5	5	5	2	2	5	5	5	2	5	4.33	1.32
Rating Combined	-	-	-	-	-	-	-	-	-	2	5	4.06	1.26

TABLE II. C-TPS ITV<sub>1</sub>: Hausdorff distance in mm and Dice comparisons to the planning ITV, as well as quality ratings for each of the test cases in the ITV<sub>1</sub> test set using C-TPS.

	Case10	Case11	Case12	Case13	Case14	Case15	Case16	Case17	Case18	min	max	avg	stddev
Hausdorff Distance (Maximum)	5.33	52.45	6.95	4.21	17.73	9.92	7.34	4.78	9.42	4.21	52.45	13.13	15.30
Hausdorff Distance (Average)	1.39	8.22	1.60	1.23	3.03	3.08	1.86	0.83	1.90	0.83	8.22	2.57	2.25
Hausdorff Distance (95 percent)	3.30	25.31	3.88	2.85	8.49	6.89	4.10	2.30	5.40	2.30	25.31	6.95	7.17
Dice	0.79	0.52	0.82	0.81	0.78	0.48	0.79	0.86	0.82	0.48	0.86	0.74	0.14
Rating U1	3	4	2	1	1	1	1	1	1	1	4	1.67	1.12
Rating U2	5	3	4	2	3	5	3	2	2	2	5	3.22	1.20
Rating Combined	-	-	-	-	-	-	-	-	-	1	5	2.44	1.38

TABLE III. 4D-VS ITV<sub>2</sub>: Hausdorff distance in mm and Dice comparisons to the planning ITV, as well as quality ratings for each of the test cases in the ITV<sub>2</sub> test set using 4D-VS.

	Case19	Case20	Case21	Case22	Case23	Case24	Case25	Case26	Case27	min	max	avg	stddev
Hausdorff Distance (Maximum)	17.68	16.66	21.46	23.48	4.17	11.72	13.51	14.53	7.61	4.17	23.48	14.54	6.19
Hausdorff Distance (Average)	6.44	3.91	6.29	4.98	1.16	4.04	3.25	7.29	3.74	1.16	7.29	4.57	1.90
Hausdorff Distance (95 percent)	10.25	7.99	11.88	14.49	2.93	7.66	7.09	9.80	5.83	2.93	14.49	8.66	3.41
Dice	0.33	0.46	0.18	0.63	0.72	0.73	0.65	0.37	0.45	0.18	0.73	0.50	0.19
Rating U1	5	5	5	5	4	3	5	5	5	3	5	4.67	0.71
Rating U2	5	5	5	5	5	4	5	5	5	4	5	4.89	0.33
Rating Combined	-	-	-	-	-	-	-	-	-	3	5	4.78	0.55

TABLE IV. C-TPS ITV<sub>2</sub>: Hausdorff distance in mm and Dice comparisons to the planning ITV, as well as quality ratings for each of the test cases in the ITV<sub>2</sub> test set using C-TPS.

	Case28	Case29	Case30	Case31	Case32	Case33	Case34	Case35	Case36	min	max	avg	stddev
Hausdorff Distance (Maximum)	9.13	17.18	9.27	5.86	31.8	9.27	9.24	6.62	18.04	5.86	31.8	12.93	8.25
Hausdorff Distance (Average)	2.20	3.85	3.40	1.46	9.17	2.87	3.07	1.42	3.88	1.42	9.17	3.48	2.32
Hausdorff Distance (95 percent)	5.65	8.71	6.35	3.76	18.48	6.61	5.90	2.94	9.95	2.94	18.48	7.59	4.62
Dice	0.60	0.56	0.59	0.71	0.38	0.52	0.61	0.76	0.61	0.38	0.76	0.59	0.11
Rating U1	5	5	3	5	5	3	3	2	5	2	5	4.00	1.22
Rating U2	5	5	5	5	5	5	5	4	5	4	5	4.89	0.33
Rating Combined	-	-	-	-	-	-	-	-	-	2	5	4.44	0.98





FIG. 1. Graphical overview of individual test cases used in Task T.1. Columns represent results for 4D-VS ITV<sub>1</sub>, C-TPS ITV<sub>1</sub>, 4D-VS ITV<sub>2</sub> and C-TPS ITV<sub>2</sub> (in that order). The first four rows represent the quality measures used to compare ITVs to the planning ITV. From row one to row four these measures are: maximum ( $HD_{\max}$ ), average ( $HD_{\text{avg}}$ ), 95% ( $HD_{95}$ ) Hausdorff distance and the dice coefficient. They also have lines for the minimum (green), average (yellow) and maximum (red) values within one subplot. For plots where the maximum value lines were omitted, the maximum value was cropped to the highest displayed y-coordinate (see Tables I–IV for the exact value). The last two rows represent the user ratings for U1 and U2. The bar colors were chosen as follows. Green bar represents an accepted case, a red bar represents a rejected case, and a gray bar (does not apply to user ratings) represents a case, which was rejected by one user and accepted by the other.



APPENDIX **B**

## Supplementary Material: Chapter 5

### Supplementary material for the publication:

**M. Schlachter**, T. Fechter, M. Jurisic, T. Schimek-Jasch, O. Oehlke, S. Adabahr, W. Birkfellner, U. Nestle, and K. Bühler. Visualization of Deformable Image Registration Quality Using Local Image Dissimilarity. *IEEE Transactions on Medical Imaging*, 35(10):2319–2328, 2016. [SFJ<sup>+</sup>16]  
<https://doi.org/10.1109/TMI.2016.2560942>

# Supplementary Material: Visualization of Deformable Image Registration Quality using Local Image Dissimilarity

Matthias Schlachter, Tobias Fechter, Miro Jurisic, Tanja Schimek-Jasch, Oliver Oehlke, Sonja Adebahr, Wolfgang Birkfellner, Ursula Nestle, and Katja Bühler

## CONTENTS

<b>I</b>	<b>Detailed Landmark Statistics</b>	1
I-A	Overall Landmark Statistics of Test Cases . . . . .	1
I-B	Retrospective Statistics of Dissimilarity measures . . . . .	2
<b>II</b>	<b>Questionnaire</b>	3
<b>III</b>	<b>Comparison Measures: Example Images</b>	4
III-A	Checkerboard and Color Blending Visualization (CB+CB) . . . . .	4
III-B	Entropy Difference (EN) . . . . .	5
III-C	Histogram Intersection (HI) . . . . .	6
III-D	Intensity Difference (Abs) . . . . .	7
III-E	Sum of Squared Differences (SSD) . . . . .	8
III-F	Normalized Cross Correlation (NCC) . . . . .	9
III-G	Kullback-Leibler Divergence (KL) . . . . .	10
III-H	Variation of Information (VI) . . . . .	11
<b>IV</b>	<b>Comparison Measures: Side-by-side Images</b>	12
<b>V</b>	<b>Transfer Function used for CT images</b>	13
<b>VI</b>	<b>Deformation Vector Field Properties</b>	14
VI-A	Jacobian . . . . .	14
VI-B	Magnitude . . . . .	15

## LIST OF TABLES

I	TRE measures of registration results for each case as used in the user evaluation. The TRE per landmark is given in mm units. . . . .	1
II	Retrospective calculation of the correlation coefficient of the TRE with the dissimilarity measure over all data sets used in the user evaluation. . . . .	2
III	Calculation of the correlation coefficient of the TRE with the dissimilarity measure using the artificial data sets from our preselection step. . . . .	2
IV	Questionnaire . . . . .	3

Die approbierte gedruckte Originalversion dieser Dissertation ist an der TU Wien Bibliothek verfügbar. The approved original version of this doctoral thesis is available in print at TU Wien Bibliothek.

## I. DETAILED LANDMARK STATISTICS

### A. Overall Landmark Statistics of Test Cases

TABLE I

TRE MEASURES OF REGISTRATION RESULTS FOR EACH CASE AS USED IN THE USER EVALUATION. THE TRE PER LANDMARK IS GIVEN IN MM UNITS.

TRE	Case 1	Case 2	Case 3	Case 4	Case 5
Mean	1.81	1.52	2.15	8.28	3.28
$\sigma$	1.55	1.06	1.73	5.39	3.22
$\sigma^2$	2.40	1.12	3.01	29.10	10.36
RMS	2.38	1.85	2.76	9.88	4.60
Min	0.15	0.13	0.17	0.30	0.17
Max	9.89	8.61	8.65	20.49	16.44
Median	1.37	1.26	1.55	8.62	1.91
Algorithm	MITK <sup>1</sup>	SlicerRT <sup>2</sup>	SlicerRT <sup>2</sup>	MITK <sup>1</sup>	SlicerRT <sup>2</sup>

<sup>1</sup> MITK: Registered using a demons-based approach [1], which is included in MITK [2].

<sup>2</sup> SlicerRT: Registered using plastimatch [3], a B-Spline based deformable registration method, which is included in SlicerRT [4].

## REFERENCES

- [1] T. Vercauteren, X. Pennec, A. Perchant, and N. Ayache, "Symmetric log-domain diffeomorphic registration: A demons-based approach," in *Medical Image Computing and Computer-Assisted Intervention*. Springer, 2008, pp. 754–761.
- [2] I. Wolf, M. Vetter, I. Wegner, T. Böttger, M. Nolden, M. Schöbinger, M. Hastenteufel, T. Kunert, and H.-P. Meinzer, "The Medical Imaging Interaction Toolkit," *Medical Image Analysis*, vol. 9, no. 6, pp. 594–604, 2005.
- [3] J. A. Shackleford, N. Kandasamy, and G. C. Sharp, "On developing B-spline registration algorithms for multi-core processors," *Physics in Medicine & Biology*, vol. 55, no. 21, pp. 6329–6351, 2010.
- [4] C. Pinter, A. Lasso, A. Wang, D. Jaffray, and G. Fichtinger, "SlicerRT: Radiation therapy research toolkit for 3D Slicer," *Medical Physics*, vol. 39, pp. 6332–6338, 2012.

## B. Retrospective Statistics of Dissimilarity measures

TABLE II  
RETROSPECTIVE CALCULATION OF THE CORRELATION COEFFICIENT OF THE TRE WITH THE DISSIMILARITY MEASURE OVER ALL DATA SETS USED IN THE USER EVALUATION.

$D_{diss}$	Correlation using neighborhood	Correlation using direct position
<b>Intensity Difference (Abs)</b>	0.7034	0.4179
<b>Entropy Difference (EN)</b>	0.6664	0.5016
<b>Histogram Intersection (HI)</b>	0.7371	0.6293
<b>Symmetric Kullback-Leibler Divergence (KL)</b>	0.7125	0.5867
<b>Normalized Cross Correlation (NCC)</b>	0.7473	0.6765
<b>Variation of Information (VI)</b>	0.5130	0.5093
<b>Sum of Squared Differences (SSD) (already includes neighborhood per definition)</b>	0.7534	0.7191

TABLE III  
CALCULATION OF THE CORRELATION COEFFICIENT OF THE TRE WITH THE DISSIMILARITY MEASURE USING THE ARTIFICIAL DATA SETS FROM OUR PRESELECTION STEP.

$D_{diss}$	Correlation as calculated in the preselection step
<b>Intensity Difference (Abs)</b>	0.5602
<b>Entropy Difference (EN)</b>	0.6858
<b>Histogram Intersection (HI)</b>	0.7131
<b>Symmetric Kullback-Leibler Divergence (KL)</b>	0.7296
<b>Normalized Cross Correlation (NCC)</b>	0.6657
<b>Variation of Information (VI)</b>	0.4050
<b>Sum of Squared Differences (SSD)</b>	0.6245

## II. QUESTIONNAIRE

TABLE IV  
QUESTIONNAIRE

Question as asked in the questionnaire	
Q1	Use the visualization modes in X and give a rating of the accuracy of the registration from 1-5 for each of the lung regions 1 = "not acceptable for radiotherapy" 3 = "borderline for radiotherapy" 5 = "visually no difference detected, suitable for radiotherapy"
Q2	On which of the visualization modes would you base your final decision on? Please describe briefly the reasons for using or not using a method for the decision.
Q3	Was visualization mode X helpful for solving the task?
Q4	Which of the visualization modes is helpful for the problem of identifying registration errors? Please Rank them from 1-5 (same ranking is possible) 1 = "worst" 5 = "best"
Q5	Please rate the visualization X from 1-5 1 = "incomprehensible" 5 = "intuitive"
Q6	How fast did you find the errors with method X? 1 = "snail pace" 5 = "very fast"
Q7	Does visualization X give a good spatial overview?
Q8	Is visualization X suitable for finding smaller detailed errors?
Q9	Does the interaction, sliding between fixed and moving image, help or is it necessary for making a decision? Please specify your answer.
Q11	Do you trust the proposed visualizations more than red/green and checkerboard?
Q12	Do you see potential of getting this integrated in the radiotherapy planning workflow? If "Yes", please specify where. If "No", please specify why not.
Q13	Does the visualization of the cross-hair help or is it necessary for making a decision? Please specify your answer.
Q14	Does the visualization with opacity weighting help or is it necessary for making a decision? Please specify your answer.
Q15	What are missing features?

### III. COMPARISON MEASURES: EXAMPLE IMAGES

#### A. Checkerboard and Color Blending Visualization (CB+CB)

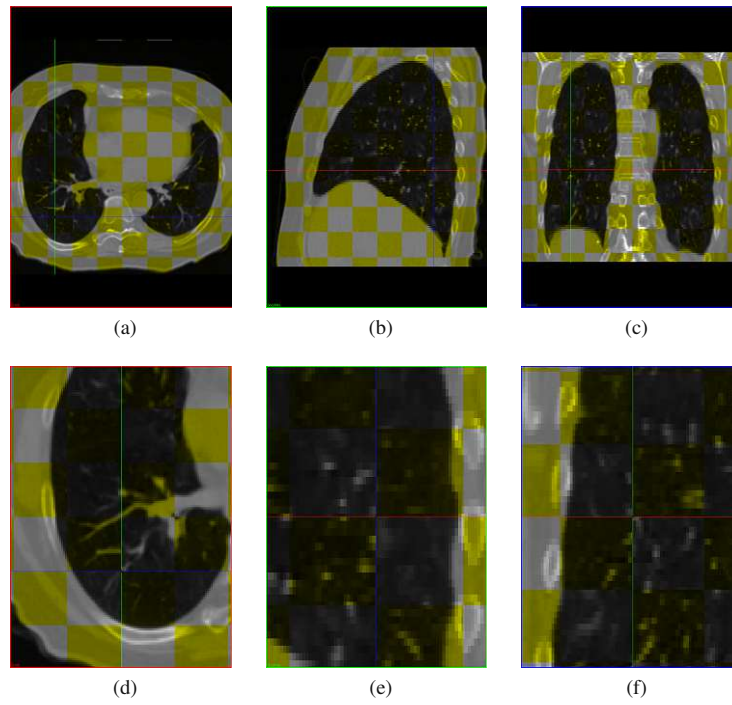


Fig. 1. Overview images of the checkerboard visualization at different zoom levels.

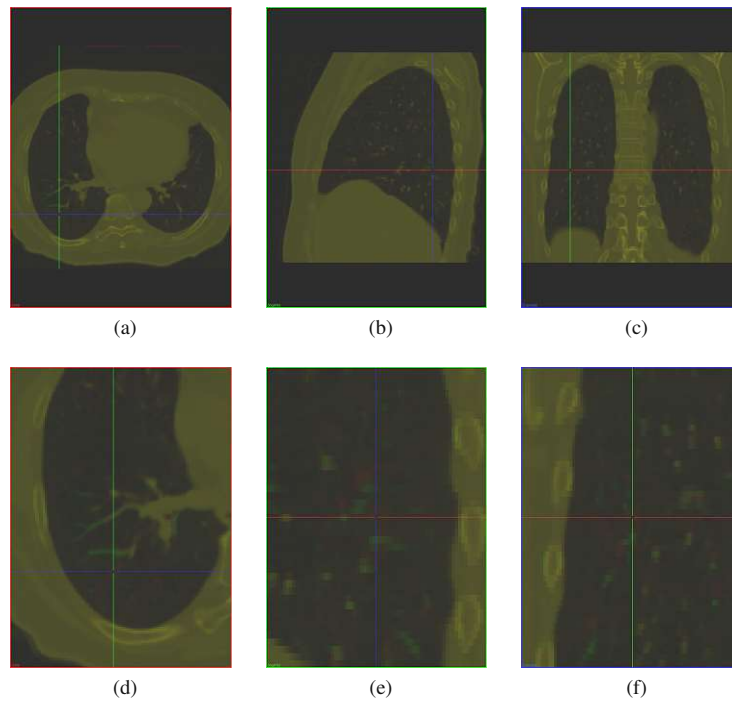
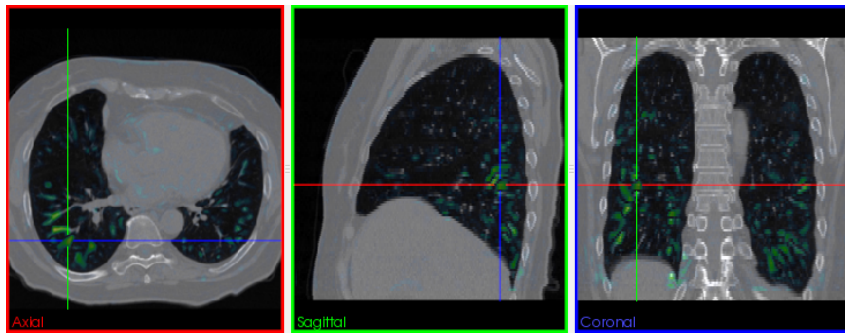


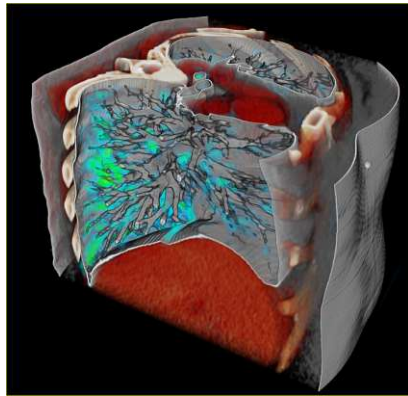
Fig. 2. Overview images of the red/green overlay visualization at different zoom levels.



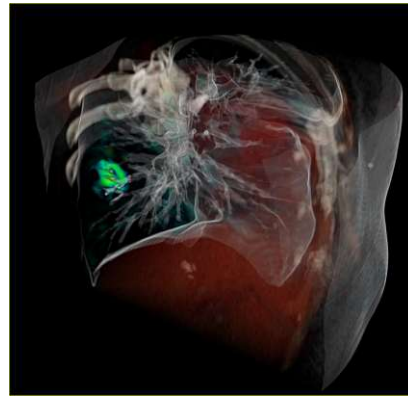
## B. Entropy Difference (EN)



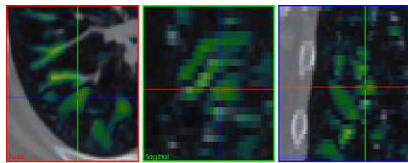
(a) Overview: axial, sagittal, and coronal views



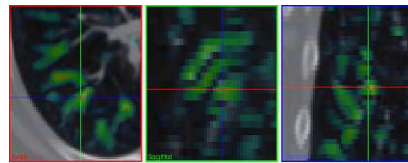
(b) Overview: volume visualization with clipping



(c) Overview: volume visualization with cross-hair lens



(d) Fixed image using the alternative mode of the cross-hair lens for detailed inspection



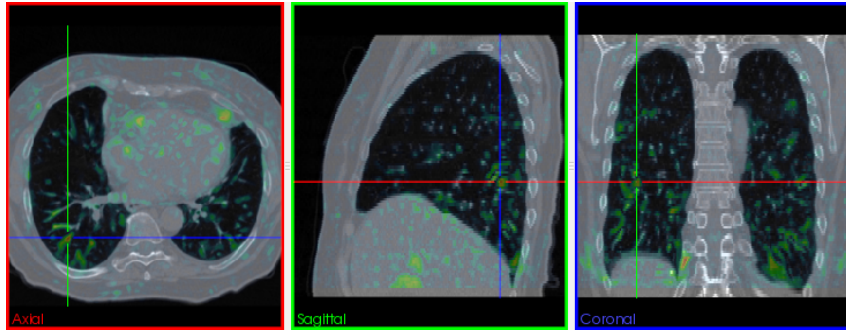
(e) Warped image using the alternative mode of the cross-hair lens for detailed inspection



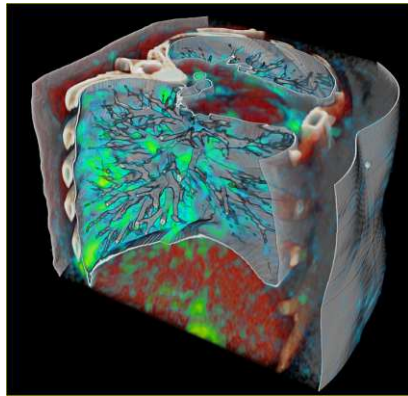
(f) Color bar and value range

Fig. 3. Dissimilarity measure = entropy difference, radius 7 mm. Fig. (d) and (e) use the selected position depicted in (c) and show either the fixed or the warped image fused with the dissimilarity image. Differences between the fixed and the warped image should be indicated by the dissimilarity measure.

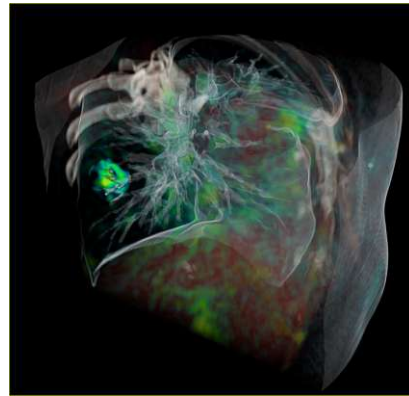
### C. Histogram Intersection (HI)



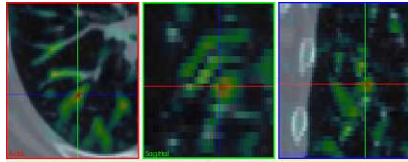
(a) Overview: axial, sagittal, and coronal views



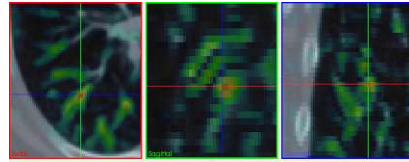
(b) Overview: volume visualization with clipping



(c) Overview: volume visualization with cross-hair lens



(d) Fixed image using the alternative mode of the cross-hair lens for detailed inspection



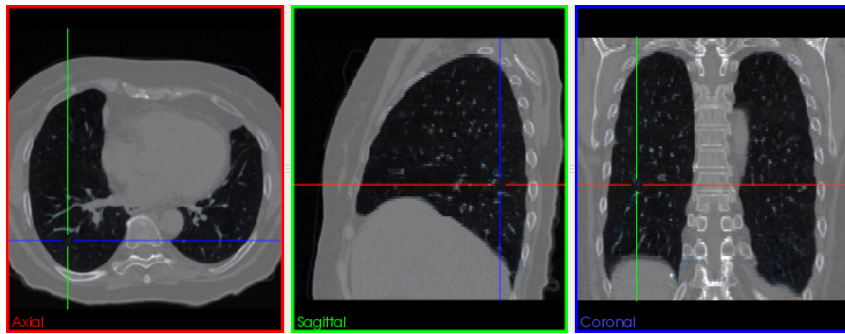
(e) Warped image using the alternative mode of the cross-hair lens for detailed inspection



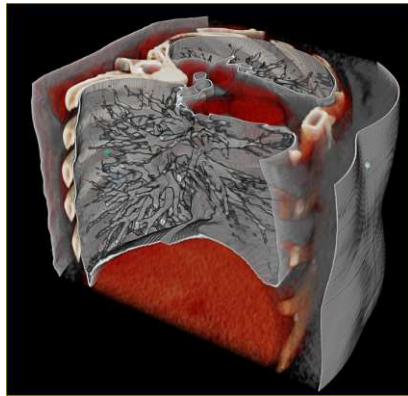
(f) Color bar and value range

Fig. 4. Dissimilarity measure = histogram intersection, radius 7 mm. Fig. (d) and (e) use the selected position depicted in (c) and show either the fixed or the warped image fused with the dissimilarity image. Differences between the fixed and the warped image should be indicated by the dissimilarity measure.

#### D. Intensity Difference (Abs)



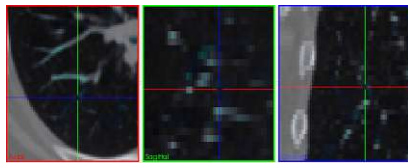
(a) Overview: axial, sagittal, and coronal views



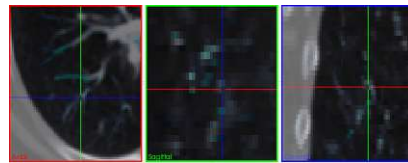
(b) Overview: volume visualization with clipping



(c) Overview: volume visualization with cross-hair lens



(d) Fixed image using the alternative mode of the cross-hair lens for detailed inspection



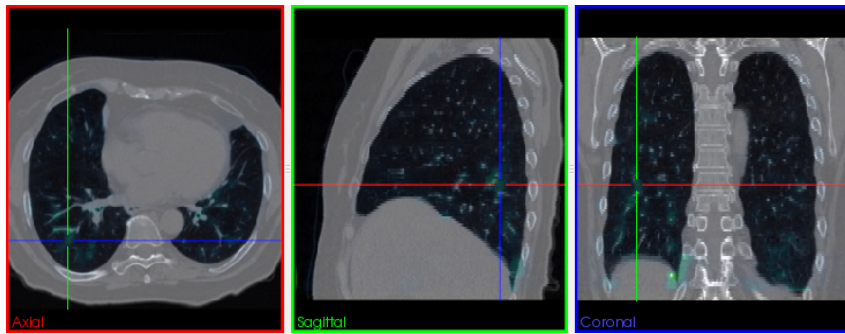
(e) Warped image using the alternative mode of the cross-hair lens for detailed inspection



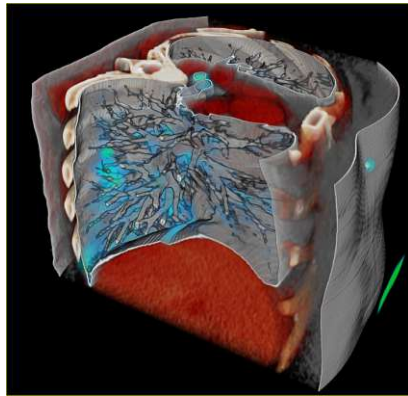
(f) Color bar and value range

Fig. 5. Dissimilarity measure = intensity difference. Fig. (d) and (e) use the selected position depicted in (c) and show either the fixed or the warped image fused with the dissimilarity image. Differences between the fixed and the warped image should be indicated by the dissimilarity measure.

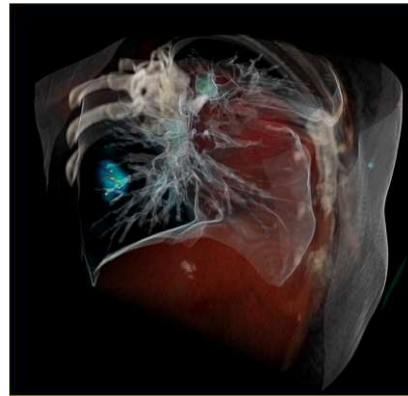
### E. Sum of Squared Differences (SSD)



(a) Overview: axial, sagittal, and coronal views



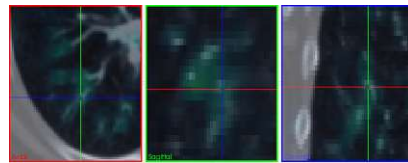
(b) Overview: volume visualization with clipping



(c) Overview: volume visualization with cross-hair lens



(d) Fixed image using the alternative mode of the cross-hair lens for detailed inspection



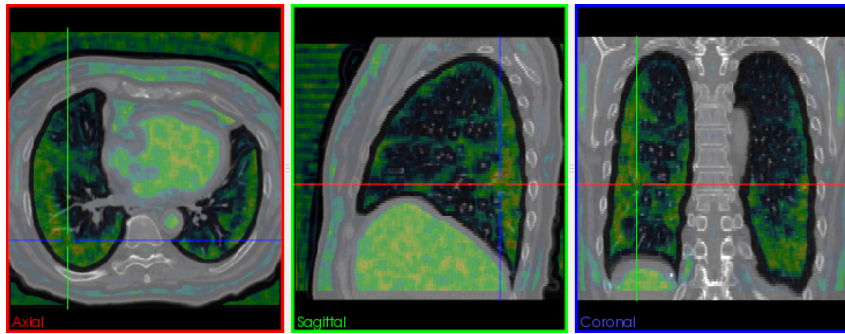
(e) Warped image using the alternative mode of the cross-hair lens for detailed inspection



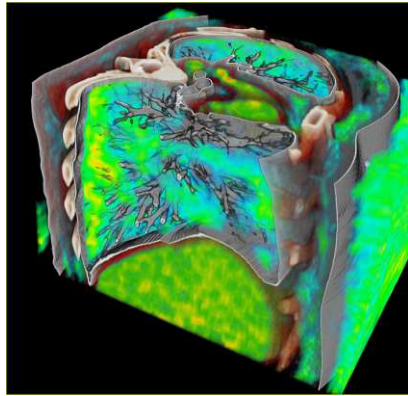
(f) Color bar and value range

Fig. 6. Dissimilarity measure = sum of squared differences, radius 7 mm. Fig. (d) and (e) use the selected position depicted in (c) and show either the fixed or the warped image fused with the dissimilarity image. Differences between the fixed and the warped image should be indicated by the dissimilarity measure.

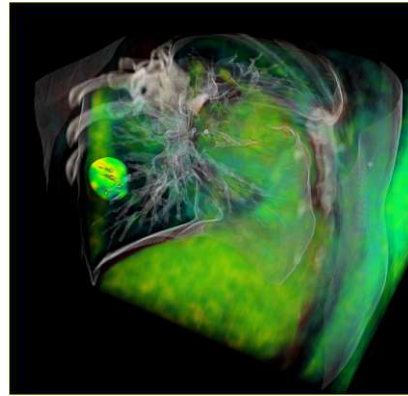
### F. Normalized Cross Correlation (NCC)



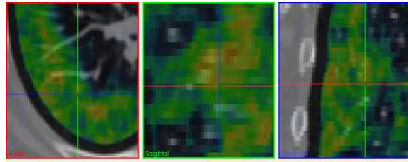
(a) Overview: axial, sagittal, and coronal views



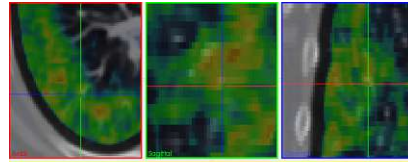
(b) Overview: volume visualization with clipping



(c) Overview: volume visualization with cross-hair lens



(d) Fixed image using the alternative mode of the cross-hair lens for detailed inspection



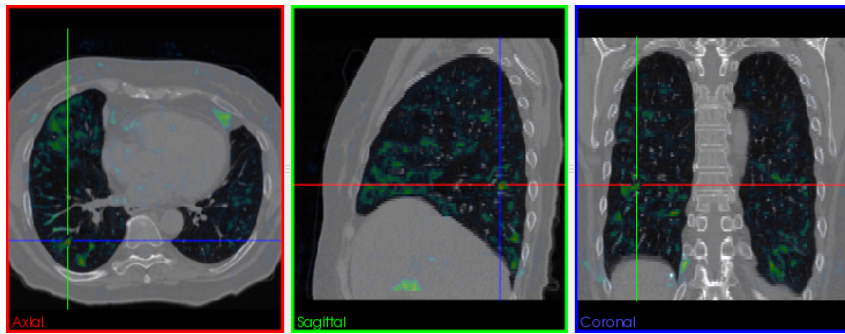
(e) Warped image using the alternative mode of the cross-hair lens for detailed inspection



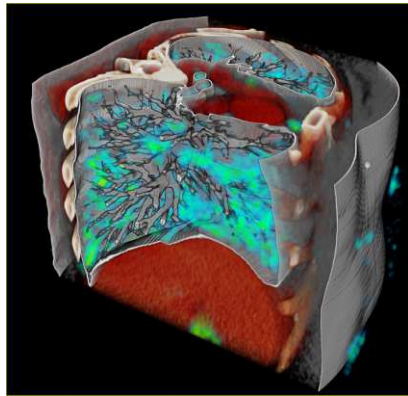
(f) Color bar and value range

Fig. 7. Dissimilarity measure = normalized cross correlation, radius 7 mm. Fig. (d) and (e) use the selected position depicted in (c) and show either the fixed or the warped image fused with the dissimilarity image. Differences between the fixed and the warped image should be indicated by the dissimilarity measure.

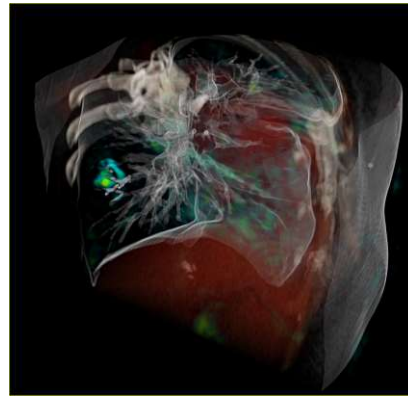
G. Kullback-Leibler Divergence (KL)



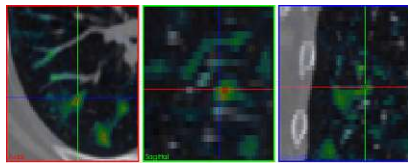
(a) Overview: axial, sagittal, and coronal views



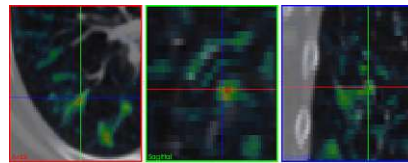
(b) Overview: volume visualization with clipping



(c) Overview: volume visualization with cross-hair lens



(d) Fixed image using the alternative mode of the cross-hair lens for detailed inspection



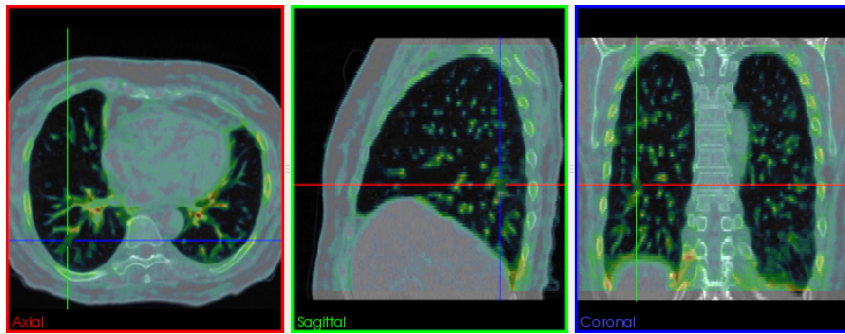
(e) Warped image using the alternative mode of the cross-hair lens for detailed inspection



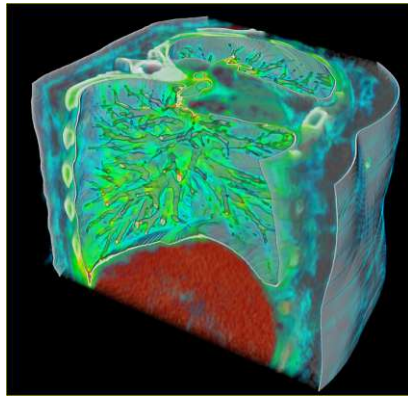
(f) Color bar and value range

Fig. 8. Dissimilarity measure = Kullback-Leibler divergence, radius 7 mm. Fig. (d) and (e) use the selected position depicted in (c) and show either the fixed or the warped image fused with the dissimilarity image. Differences between the fixed and the warped image should be indicated by the dissimilarity measure.

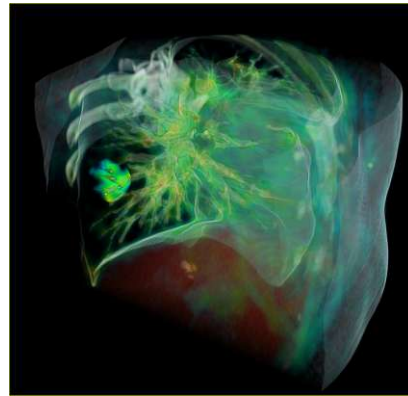
### H. Variation of Information (VI)



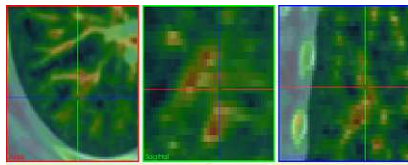
(a) Overview: axial, sagittal, and coronal views



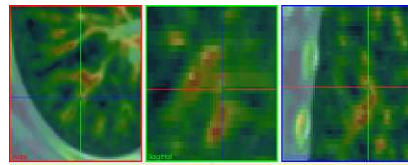
(b) Overview: volume visualization with clipping



(c) Overview: volume visualization with cross-hair lens



(d) Fixed image using the alternative mode of the cross-hair lens for detailed inspection



(e) Warped image using the alternative mode of the cross-hair lens for detailed inspection



(f) Color bar and value range

Fig. 9. Dissimilarity measure = variation of information, radius 7 mm. Fig. (d) and (e) use the selected position depicted in (c) and show either the fixed or the warped image fused with the dissimilarity image. Differences between the fixed and the warped image should be indicated by the dissimilarity measure.

## IV. COMPARISON MEASURES: SIDE-BY-SIDE IMAGES

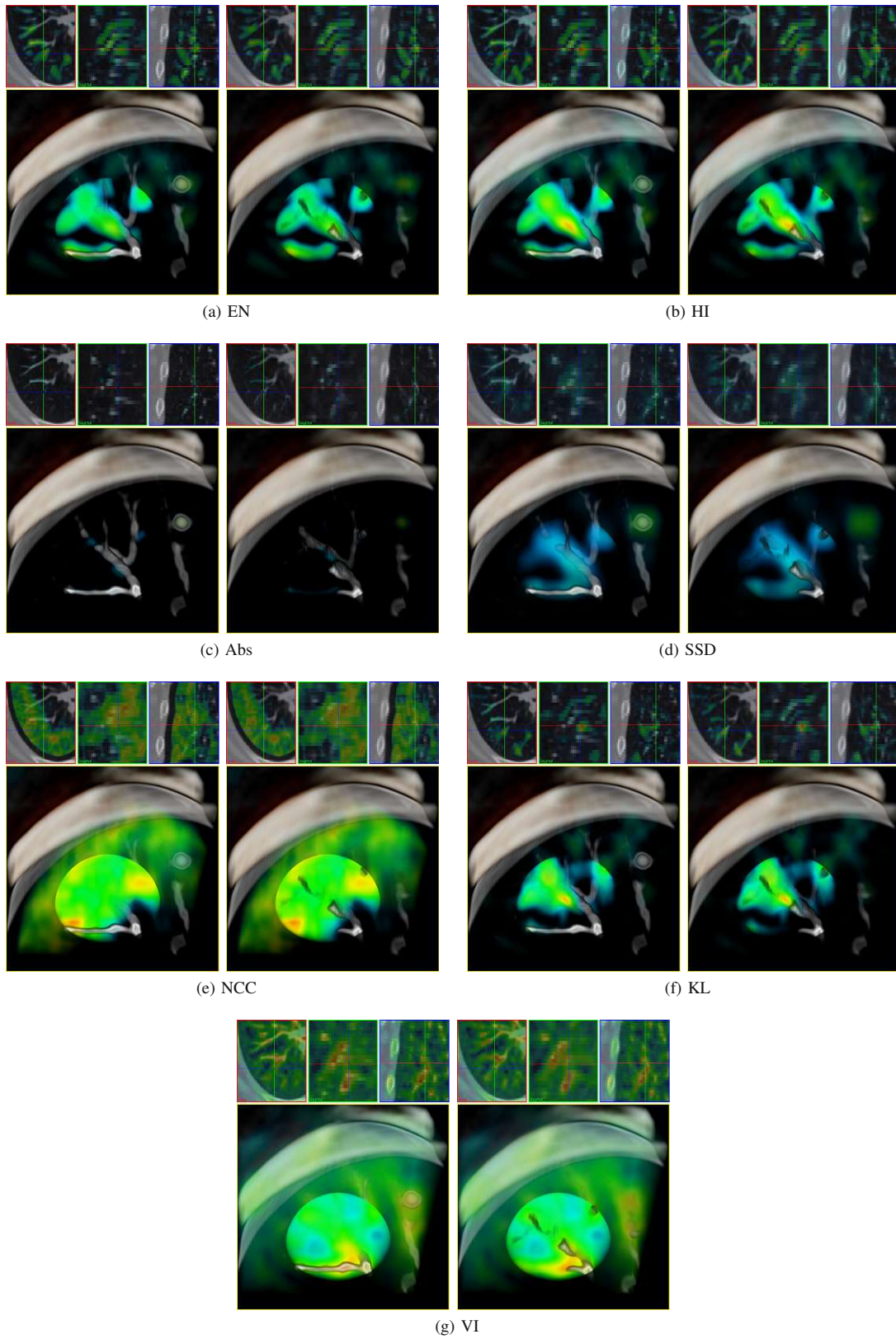


Fig. 10. Fixed and warped images for the different measures side by side.



## V. TRANSFER FUNCTION USED FOR CT IMAGES

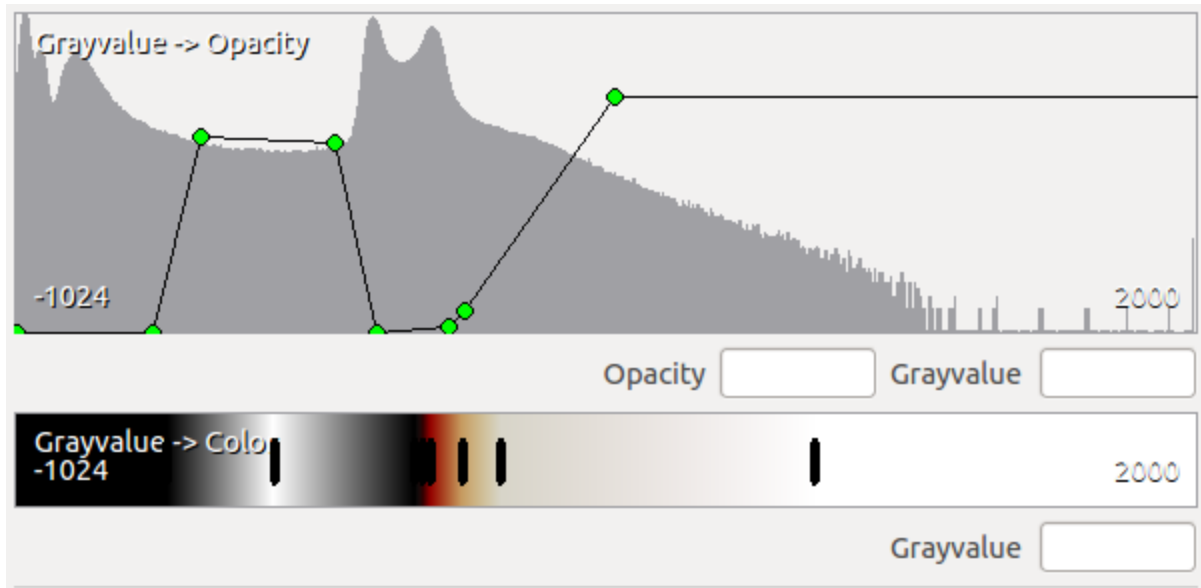


Fig. 11. Example of CT transfer functions for color ( $c_f$  and  $c_w$ ) and opacity ( $k_f$  and  $k_w$ ) used in our visualization system. The functions are not fixed and modifiable by the user.

## VI. DEFORMATION VECTOR FIELD PROPERTIES

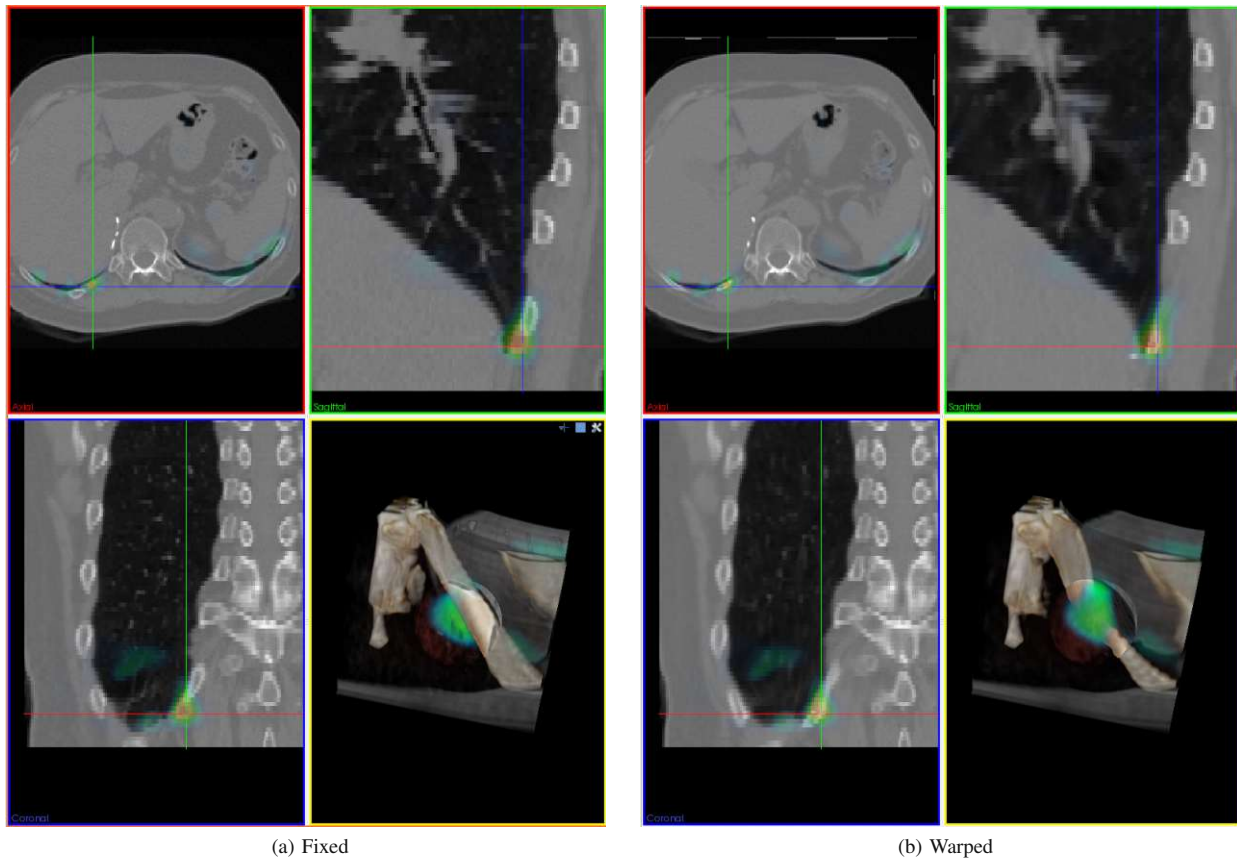
A. *Jacobian*

Fig. 12. The determinant of the Jacobian could be used to detect implausible deformation in rigid structures. In this example we show only values greater than 1.

B. Magnitude

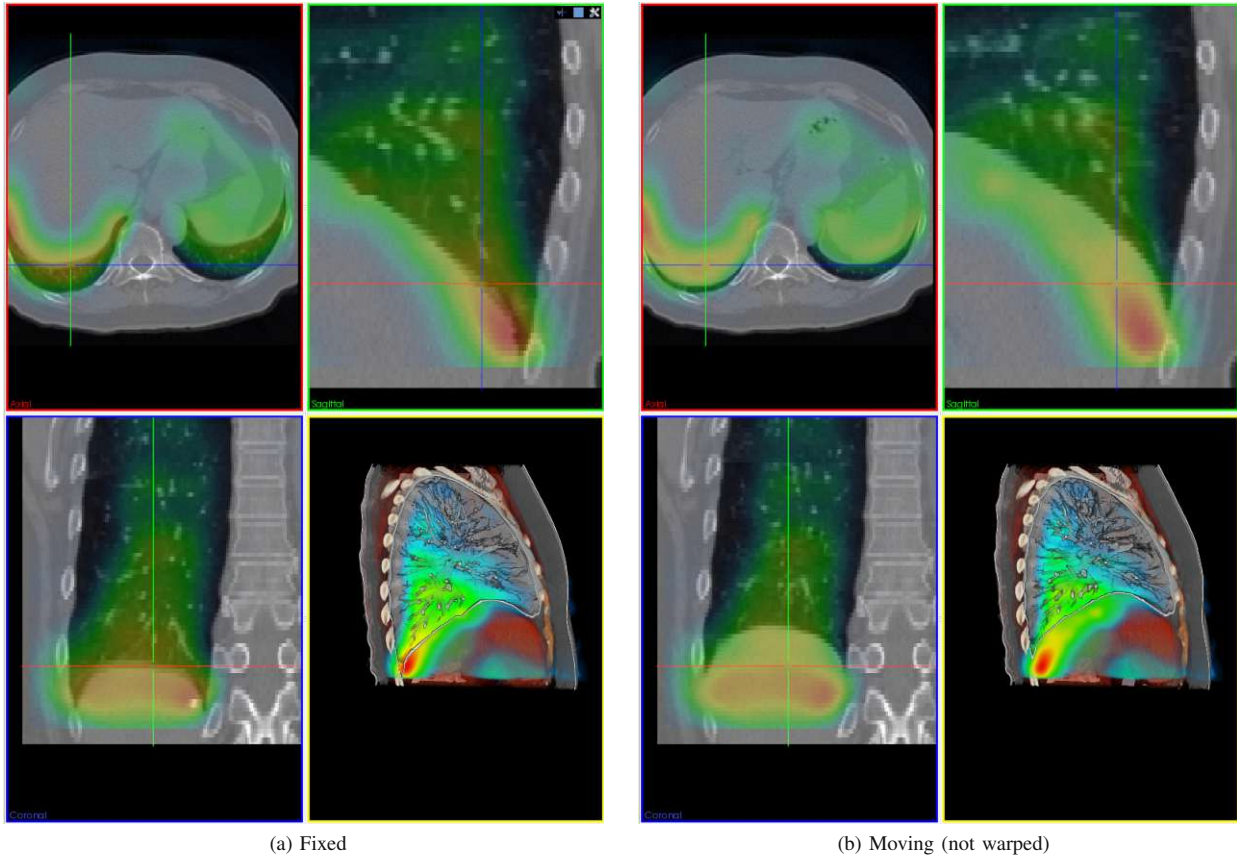


Fig. 13. Example of the overlay using the color coded magnitude of the DVF.

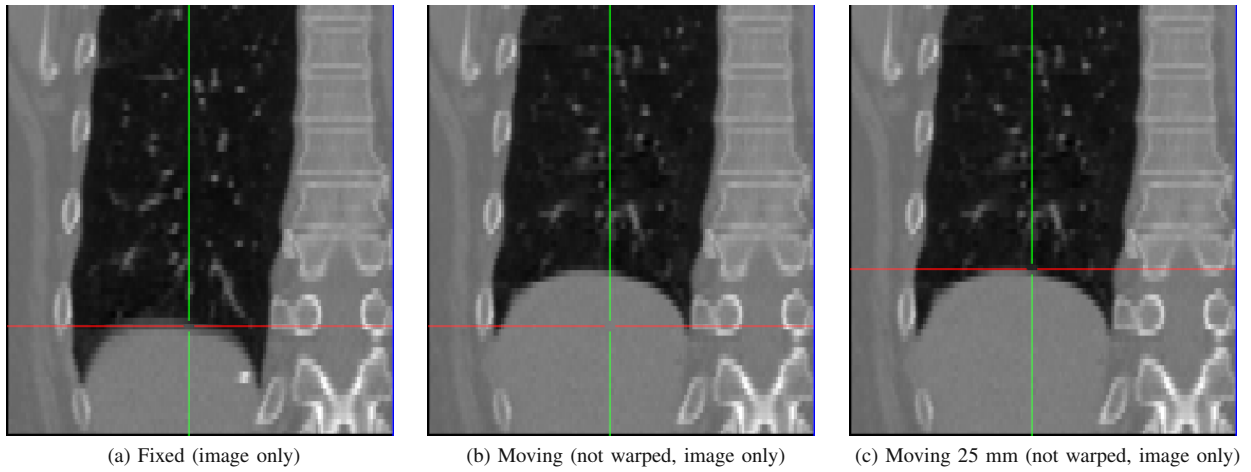


Fig. 14. Example of an axial movement of the diaphragm of about 25 mm in axial direction

Die approbierte gedruckte Originalversion dieser Dissertation ist an der TU Wien Bibliothek verfügbar. The approved original version of this doctoral thesis is available in print at TU Wien Bibliothek.



# List of Figures

1.1	The steps of the workflow of RT planning, as adapted from the book of Washington and Leaver [WL15]. Most workflow steps comprise sub-steps [SRM <sup>+</sup> 19]. The steps for which visual computing plays an important role are denoted with blue squares. . . . .	2
1.2	Volume concepts used in RT planning. The Gross Tumor Volume (GTV), Clinical Target Volume (CTV), Internal Target Volume (ITV), and Planning Target Volume (PTV), as well as the Organ at Risk (OAR) and Planning Organ at Risk Volume (PRV) are denoted. The Treated Volume (TV) is implicitly defined (by a dose value) after dose calculation. The PTV and ITV account for patient setup errors and other sources of inaccuracy. Overlapping volumes can have an impact on the dose calculation, and might lead to insufficient PTV coverage or undesired dose levels for the OAR. . . . .	4
1.3	Fusion of the planning CT with a 4D-PET/CT (top: 4D-CT, bottom: 4D-PET). The structure encompassing the tumor was defined by using 4D imaging. The images on the left and the right showing the maximum inhale and exhale position during the patients breathing cycle. . . . .	5
1.4	Deformable image registration has many applications in radiotherapy. Independent of the application, quality assessment of the resulting displacement vector field is an important step toward clinical acceptance. . . . .	7
1.5	Fusion of different types of information sources relevant in RT planning. . . . .	8
1.6	Overview of the software as used for the overlap volume exploration. The multi-modal interactive visualization framework is visible in part A, the configuration parameters are implemented in part B, and in part C quantitative visualizations were implemented using the MITK platform. . . . .	9
1.7	(a) The SUMMER consortium consisted of seven different research institutions located in different European countries [SUM12]. Chapters 3–5 are the result of collaborations with the University Medical Center Freiburg, Germany and Chapter 5 with the Medical University of Vienna, Austria. (b) Collaborations with other institutes leading to results presented in this thesis: Kantonsspital St. Gallen, Switzerland; Technical University of Vienna, Austria; University of Magdeburg, Germany; Aarhus University Hospital, Denmark. . . . .	10
1.8	Overview of the core software framework and integration. . . . .	11
1.9	Overview of contributions of individual chapters to steps in the radiotherapy treatment planning workflow. . . . .	12
		149

2.1	Schematic depiction of a linear accelerator (LINAC) used in External Beam Radiation Therapy (EBRT) treatment, with its major components and employed axes [SRM <sup>+</sup> 19]. Rotational and translational movements of several parts are depicted with arrows. . . . .	17
2.2	(a) Isodose surface encompassing the ITV. This is a less critical example, due to the location of the tumor (at the lung border close to a rib), where the PTV (ITV with setup error margin) is not representing the TV well. (b) Example of a difficult case (central lung), where the tumor is close to an OAR. The PTV and PRV were overlapping in this case. Figures taken from Schlachter et al. [SRM <sup>+</sup> 19]. . . . .	20
2.3	The axial, sagittal and coronal slices together with a 3D overview to evaluate the simulated dose distribution used to treat prostate cancer. The 3D overview (upper left) shows the previously segmented anatomical structures along with the three orthogonal slices. The slice views employ isolines and colored regions to display the dose distribution as percentage of the target radiation in the tumor (Courtesy of Mathias Walke, Department of Radiation Treatment Planning, University of Magdeburg, taken from the book of Preim and Botha [PB13]). . . . .	22
2.4	The dose volume histogram indicates which percentage of a structure volume receives a certain dose (horizontal axis) to treat an esophageal carcinoma. The orange curve relates to the tumor volume which indicates that 95% of its volume receive at least 95% of the target dose, as shown with the x-mark (Courtesy of Mathias Walke, Department of Radiation Treatment Planning, University of Magdeburg, taken from the book of Preim and Botha [PB13]). . . . .	23
2.5	Schematic overview of how arbitrary slices can be extracted from 3D volumes, and how volumes are defined by a stack of slices commonly acquired by an imaging device [SPBR20]. . . . .	24
2.6	Schematic overview of the ray casting algorithm and volume fusion [SPBR20]. The ray is sampled at discrete positions to evaluate the volume rendering integral. . . . .	24
2.7	(a) MPR views together with volume rendering of a head CT with segmentation data. (b) Surface representation of segmentation data (left) combined with CT data (right). (c) 4D-PET/CT combined with segmentation data and an isodose surface. Figures taken from Schlachter et al. [SPBR20]. . . . .	25
2.8	A widget used for defining a 1-D transfer function [SPBR20]. The upper part shows the histogram of a CT volume and points can be added to define the opacity transfer function, and the lower part is used to define the color transfer function respectively. The concept of <i>window/level</i> is shown on top of the widget. Values outside the window are either black (to the left) or white (to the right). . . . .	26
2.9	The main steps of the volume rendering process [SPBR20]. . . . .	27
2.10	The main components of the visual analytics process (redrawn from Schlachter et al. [SPBR20]). . . . .	30

2.11	An example of a tool for the exploration and analysis of the variability of pelvic organs [RBGR18]. . . . .	31
2.12	Treemap representation of the first dimension of the taxonomy, related to the <b>Steps</b> of the RT workflow addressed in VC literature as presented in [SRM <sup>+</sup> 19]. The categories in the green squares are related work within the scope of this thesis. . . . .	33
3.1	Overview of the fusion pipeline used in our ray casting implementation. . . . .	46
3.2	(a) Overview of the core components of our rendering framework and MITK integration. (b) Screen-shot of the MITK platform with the integration of our 3D multi-modal rendering and plug-in. . . . .	47
3.3	Fusion of a different number of modalities: (a) Fusion of PET, CT. (b), (c) PET, CT, and segmentation. (d) CT and segmentation. Different parameters for clipping were applied to hide parts of the thorax. . . . .	48
3.4	(a) Fusion of PET and CT with surface rendering of binary volumes. (b) Fusion of PET and CT with binary volume information. The different binary volumes represent either background, one modality or the fused PET and CT. (c) Same as (b) without surface rendering of binary volumes. Clipping was applied to hide parts of the thorax. . . . .	49
3.5	Fusion of dose information: (a) Fusion of the planning CT and four different isodose surfaces. (b) Additional fusion of PET. (c) Additional fusion of segmentation data sets. (d) Corresponding DVH of the segmentation data sets from (c). . . . .	50
3.6	Fusion of 4D-PET/CT with segmentation data sets (ITV, SMT) and the 15 Gray isodose surface. (a) and (b) show different time bins of the patients' breathing cycle. Clipping was applied to hide parts of the thorax. . . . .	51
4.1	Schematic overview of image sources, which are combined in the 4D-VS visualization system. . . . .	57
4.2	In (a) the full body CT is fused with 4D-PET and delineations. Data sets can be clipped to a region-of-interest (ROI) (b). Image information can be exchanged, for instance, in (c) the 4D-CT is used instead of the 4D-PET. A slider can be used to navigate time bins (see (b) and (c)) and access all image information over the whole breathing cycle. An example of an ITV, which does not cover the target, is shown in (d). . . . .	59
4.3	Visualization in 4D-VS of binary volumes and fusion with image information are depicted in (a)–(b). Additional features for supporting classification of tumor localization are shown in (c). . . . .	60
4.4	Example of the dose distribution visualization using 4D-VS: (a) the 37.5 Gy isodose surface can be evaluated against the planning ITV. A combination of masking, clipping and isodose rendering of a lower dose surface is shown in (b), and a possible configuration of a target close to an OAR is shown in (c). . . . .	61
4.5	The schematic overview of binary volume picking as implemented in the 4D-VS visualization system. . . . .	62
		151

4.6	Example visualization 4D-PET/CT and ITVs: 2D views and with 4D-VS. Examples show a rejected ITV (a) with a DC = 0.65 and an accepted ITV (b) with a DC = 0.76. . . . .	69
4.7	Using C-TPS for Tasks T.1 and T.2: Contours are visualized together with the planning CT. Clipping is applied, however, only the CT is affected. The ITV is depicted in green, the heart in red and the esophagus in blue. In (b), the heart is made slightly transparent. When compared to (a), the volume covering the heart is not shown correctly anymore. C-TPS does not preserve the depth information of the heart when made transparent. Using C-TPS for Task T.3: Green is the 37.5 Gy isodose. The planning target volume is depicted in violet, and the ITV in yellow. In (c) the isodose surface is visualized as mesh, and as solid surface in (d) . . . . .	71
5.1	Overview of the visualization system. The input data is on the left and indicated by arrows going inside the green box. The green box depicts the core parts of the system, and arrows indicate input and output of the modules.	76
5.2	Core parts of the visualization system: (a) fusion for one sample point as used in the ray casting. (b) Principal of the cross-hair lens visualization. (c) Example visualization of the cross-hair lens for detailed inspection. Inside the sphere normal opacity values are used. Occluding samples are discarded, and all other samples have lower opacity. . . . .	78
5.3	Example of functions for $c_{diss}$ and $k_{diss}$ . We can define $k_{diss} : \text{range}(D_{diss}) \rightarrow [0, 1]$ and $c_{diss} : \text{range}(D_{diss}) \rightarrow [0, 1]^3$ (RGB space). If the range of $D_{diss}$ is known and bounded $d_{max} := \sup\{\text{range}(D_{diss})\} < \infty$ we can, for instance, define a piece-wise linear mapping for the opacity with $k_{diss}(0) = 0$ and $k_{diss}(d_{max}) = 1$ . . . . .	79
5.4	For demonstration purposes (a) shows the linear fusion of the fixed and warped image only for lung tissue. The fixed image is set to red, and the warped one to green so that similar regions will appear in yellow tones. In (b) the dissimilarity measure ranging from blue (similar) to red (dissimilar) is visualized together with the fixed and warped image. In (c) the dissimilarity measure is used to weight the opacity of (a). . . . .	81
5.5	The cross-hair lens visualization mode is designed to check in detail a volume position with a high dissimilarity value. Interaction features allow comparing the fixed and warped image. Here, the region with high dissimilarity was due to a structure disappearing in the warped image. . . . .	82
5.6	Example visualization using $D_{HI}$ with a patch size of 7 mm x 7 mm x 7 mm. The top row shows the 2D views and the bottom the 3D view of the system. The volume was set to the fixed image, and additional clipping was applied to the 3D view. . . . .	84



5.7	Close up of the deformed rib from Fig. 5.6. The top row in (a) shows the 2D views of the fixed image and the bottom of the warped image. (b) shows the cross-hair visualization, which was centered at the rib, for the fixed image on the left and the warped one on the right. . . . .	85
5.8	(a) Lung regions used for the user evaluation. (b) Average ratings per data set. The average was calculated over region ratings of all users that participated in the study. . . . .	89
5.9	Answers to Survey Questions. (a) Average over answers given by all users for Q2–Q3. (b) Average over ratings given by all users for Q4–Q6. (c) Average over answers given by all users for Q7–Q14. . . . .	90
5.10	Illustration of the influence of the transfer functions and the relation to the range of $D_{diss}$ . (a) shows a cropped region with a vessel, which was not correctly registered. From left to right a step-wise transition from the fixed to the moving image is depicted ( $\alpha$ was set to 1, 0.75, 0.25, and 0 in Eq. (5.8) and Eq. (5.9)). (b) shows the overlay of $D_{SSD}$ and the corresponding color transfer $c_{diss}$ in (d). In (c) the overlay shows $D_{SSD}$ with a different value set for $d_{max}$ , as an example of how the boundness of $D_{diss}$ will influence the final visualization. The corresponding $c_{diss}$ is shown in (e). The overlay depicted in (f) is for $D_{EN}$ and in (g) for $D_{HI}$ , with the corresponding $c_{diss}$ shown in (h) and (i) respectively. All overlay images were generated with $\beta = 0.5$ and $\alpha = 1$ for the left, and $\alpha = 0$ for the right image. . . . .	93
6.1	(a) The four major (consecutive) RT planning steps prior to treatment. (b) Schematic overview of important RT volume definitions. (c) Conflicting treatment goals: PTV requires high dose, whereas PRV requires low dose. After dose calculation the desired treatment goals might not be as prescribed. . . . .	97
6.2	Volume-to-Dose Overlaps are defined dose regions $R_d$ (a) (yellow outline where dose is $\geq d$ ) and other structures (b). . . . .	100
6.3	The chord diagram with a selected reference structure (a), and the outer ring indicating the amount of overlap (b). The colors represent the mean dose. . . . .	102
6.4	The parallel coordinates after selecting a reference structure. Filtering overlaps by evaluation metrics updates the other views. The resulting line color is determined by mixing the colors of the original structures. . . . .	103
6.5	Table view TV-I: The reference structure selected in the chord diagram is listed at the top. All table entries correspond to outgoing chords and lines in the parallel coordinates view (greyed-out values are from brushing shown in Fig. 6.4). The entry highlighted in yellow is the currently selected overlap, which updates the spatial and DVH views. . . . .	104
6.6	Table view TV-II: All overlaps defined by the current intersection of the slice views are displayed. . . . .	105
		153

6.7	DVH view with a selected overlap volume of the PTV and an OAR. The resulting line color of the overlap DVH is determined by mixing the colors of the original structures. . . . .	106
6.8	Spatial views after selecting an overlap. The original structures are displayed alongside the overlap volume. The overlap is used to focus the slice views in its center and displayed as filled semi-transparent area after its selection in the quantitative views. . . . .	107
6.9	Dose visualization can be enabled if required either as colorwash (a) or isolines (b) in the slice views, or as iso-surfaces in the 3D view (c). . . . .	107
6.10	Data setup and interaction concept: the blue parts in the setup are mandatory to fill the data structures, and the arrows define the flow of actions. . . . .	108
6.11	Overview of the interaction between individual quantitative views (chord diagram, parallel coordinates, DVH and table view TV-I) and the spatial views. Arrow directions indicate which views are updated after an interaction. . . . .	109
6.12	Example exploration starting by selecting a reference structure in the cord diagram (a). Filtering in the parallel coordinates (b) reduces possible candidates (c), (d). Finally, a selection of a single overlap (d) shows the DVHs (e) and spatial views (f), (g) of the corresponding structures alongside the overlap volume. . . . .	111
6.13	Hotspots after defining a dose region with a dose value $d$ corresponding to 93% of the reference dose. All outgoing chords show structures, which have sub-volumes with a dose value $\geq d$ (a). Quantitative measures can be explored using the table view, and further selections update the spatial views (b). . . . .	113
6.14	User ratings for Q3, Q5–Q9, Q12 and Q13. Q3 and Q5 are aggregated over all test data sets. . . . .	116
6.15	User ratings for Q15, Q17 and Q18. . . . .	118
7.1	Using 4D GTV contour information to calculate the relative frequency for each voxel to be classified as cancer, leads to a probability volume (PV) of tumor tissue over the whole breathing cycle. The visualizations show the PV together with the PET/CT. Image are taken and adapted from Schlachter et al. [SFBN14]. . . . .	124

# List of Tables

4.1	Representative imaging sources with sizes and resolutions of one patient used for the three clinical tasks. . . . .	57
4.2	Task description summary and quality scale. The certainty for all tasks was given as binary answer, i.e., either uncertain or certain. . . . .	64
4.3	Survey questions with answers. Answers given as ( $U_1 / U_2$ ) or “–” if not applicable . . . . .	65
4.4	Feature Comparison of 4D-VS and C-TPS. . . . .	66
4.5	Results of ITV and dose distribution ratings using different systems. . . . .	67
4.6	Dice and Hausdorff distance comparisons to the planning ITV for rejected and accepted ITVs. . . . .	67
4.7	Acceptance and certainty rates for ITV and dose distribution assessments using different systems. . . . .	68
5.1	Questionnaire (Short) . . . . .	87
5.2	Average and maximum landmark (LM) error in mm for accepted regions. . . . .	88
5.3	Computation time for Dissimilarity Measure with a patch size of 7 mm and patch sampling of 1 mm and grid size 256x256x106. . . . .	91
6.1	Questionnaire per Data Set (Shortened Version) . . . . .	113
6.2	Questionnaire (Shortened Version) . . . . .	114
6.3	Final rating of the plan with regard to overlap volumes. . . . .	115
6.4	User ratings for Q2 aggregated over all test data sets in percentages. . . . .	115
6.5	User ratings for Q10 in percentages. . . . .	117



# Bibliography

- [AAMH13] B. Alsallakh, W. Aigner, S. Miksch, and H. Hauser. Radial sets: interactive visual analysis of large overlapping sets. *IEEE Transactions on Visualization and Computer Graphics*, 19(12):2496–2505, Dec 2013.
- [AGL<sup>+</sup>13] A. Aselmaa, R. H. Goossens, A. Laprie, S. Ken, T. Fechter, A. Ramkumar, and A. Freudenthal. Workflow Analysis Report. Technical report, Delft University of Technology, 2013.
- [AHN15] J. C. L. Alfonso, M. A. Herrero, and L. Núñez. A dose-volume histogram based decision-support system for dosimetric comparison of radiotherapy treatment plans. *Radiation Oncology*, 10(1), Dec 2015.
- [ALH97] J. Alakuijala, J. Laitinen, and H. Helminen. Beam’s Light View: Visualization of Radiotherapy Treatment Planning Fields on Anatomic Surfaces. In *Proceedings of the International Conference of the IEEE Engineering in Medicine and Biology Society*, volume 3, pages 970–973, 1997.
- [AMA<sup>+</sup>15] B. Alsallakh, L. Micalef, W. Aigner, H. Hauser, S. Miksch, and P. Rodgers. The State-of-the-Art of Set Visualization. *Computer Graphics Forum*, 35(1):234–260, Nov 2015.
- [AOM<sup>+</sup>14] Y. Akino, R.-J. Oh, N. Masai, H. Shiomi, and T. Inoue. Evaluation of Potential Internal Target Volume of Liver Tumors Using Cine-MRI. *Medical Physics*, 41(11):111704, 2014.
- [BAG<sup>+</sup>17] P. Bruza, J. M. Andreozzi, D. J. Gladstone, L. A. Jarvis, J. Rottmann, and B. W. Pogue. Online Combination of EPID & Cherenkov Imaging for 3-D Dosimetry in a Liquid Phantom. *IEEE Transactions on Medical Imaging*, 36(10):2099–2103, 2017.
- [BBP<sup>t</sup>HR08] R. Brecheisen, A. V. Bartroli, B. Platel, and B. M. ter Haar Romeny. Flexible GPU-Based Multi-Volume Ray-Casting. In *Vision, Modelling, and Visualization*, pages 303–312, 2008.
- [BC87] R. A. Becker and W. S. Cleveland. Brushing Scatterplots. *Technometrics*, 29(2):127–142, 1987.

- [BCD<sup>+</sup>10] S. M. Bentzen, L. S. Constine, J. O. Deasy, A. Eisbruch, A. Jackson, L. B. Marks, R. K. T. Haken, and E. D. Yorke. Quantitative Analyses of Normal Tissue Effects in the Clinic (QUANTEC): An Introduction to the Scientific Issues. *International Journal of Radiation Oncology\*Biography\*Physics*, 76(3):S3–S9, Mar 2010.
- [BCTT08] T. Bortfeld, T. C. Y. Chan, A. Trofimov, and J. N. Tsitsiklis. Robust management of motion uncertainty in intensity-modulated radiation therapy. *Operations Research*, 56(6):1461–1473, 2008.
- [BDK<sup>+</sup>07] A. K. Berthelsen, J. Dobbs, E. Kjellén, T. Landberg, T. R. Möller, P. Nilsson, L. Specht, and A. Wambersie. What’s new in target volume definition for radiologists in ICRU Report 71? How can the ICRU volume definitions be integrated in clinical practice? *Cancer Imaging*, 7(1):104–116, 2007.
- [Ben08] S. M. Bentzen. Dose Painting and Theragnostic Imaging: Towards the Prescription, Planning and Delivery of Biologically Targeted Dose Distributions in External Beam Radiation Oncology. In *Radiation Oncology Advances*, pages 40–61. Springer, 2008.
- [BHWB07] J. Beyer, M. Hadwiger, S. Wolfsberger, and K. Bühler. High-quality multimodal volume rendering for preoperative planning of neurosurgical interventions. *IEEE Transactions on Visualization and Computer Graphics*, 13(6):1696–1703, Dec 2007.
- [Bir14] W. Birkfellner. *Applied Medical Image Processing*. Taylor & Francis Inc, Mar 2014.
- [BJE<sup>+</sup>11] D. Bonekamp, M. A. Jacobs, R. El-Khouli, D. Stoianovici, and K. J. Macura. Advancements in MR Imaging of the Prostate: From Diagnosis to Interventions. *Radiographics*, 31(3):677–703, 2011.
- [BL15] M. Bozorgi and F. Lindseth. GPU-based multi-volume ray casting within VTK for medical applications. *International Journal of Computer Assisted Radiology and Surgery*, 10(3):293–300, 2015.
- [BMA<sup>+</sup>14] N. P. Brodin, M. V. Maraldo, M. C. Aznar, I. R. Vogelius, P. M. Petersen, S. M. Bentzen, and L. Specht. Interactive Decision-Support Tool for Risk-Based Radiation Therapy Plan Comparison for Hodgkin Lymphoma. *International Journal of Radiation Oncology\*Biography\*Physics*, 88(2):433–445, Feb 2014.
- [BOV03] A. Barla, R. Odone, and A. Verr. Histogram intersection kernel for image classification. In *International Conference on Image Processing*, volume 3, pages III–513. IEEE, 2003.

- [BRC<sup>+</sup>12] J. O. Barentsz, J. Richenberg, R. Clements, P. Choyke, S. Verma, G. Villeirs, O. Rouviere, V. Logager, and J. J. Fütterer. ESUR Prostate MR Guidelines 2012. *European Radiology*, 22(4):746–757, 2012.
- [BRP<sup>+</sup>04] D. L. Buckley, C. Roberts, G. J. M. Parker, J. P. Logue, and C. E. Hutchinson. Prostate Cancer: Evaluation of Vascular Characteristics with Dynamic Contrast Enhanced T1 Weighted MR Imaging - Initial Experience. *Radiology*, 233(3):709–715, 2004.
- [BSJS08] V. Boldea, G. C. Sharp, S. B. Jiang, and D. Sarrut. 4D-CT lung motion estimation with deformable registration: quantification of motion nonlinearity and hysteresis. *Medical Physics*, 35(3):1008–1018, 2008.
- [Bur04] N. G. Burnet. Defining the tumour and target volumes for radiotherapy. *Cancer Imaging*, 4(2):153–161, 2004.
- [CCG<sup>+</sup>09] R. Castillo, E. Castillo, R. Guerra, V. E. Johnson, T. McPhail, A. K. Garg, and T. Guerrero. A framework for evaluation of deformable image registration spatial accuracy using large landmark point sets. *Physics in Medicine & Biology*, 54(7):1849, 2009.
- [CCT<sup>+</sup>14] W.-C. Chang, C.-S. Chen, H.-C. Tai, C.-Y. Liu, and Y.-J. Chen. Integration of Multidisciplinary Technologies for Real Time Target Visualization and Verification for Radiotherapy. *OncoTargets and Therapy*, 7:1143–1150, 2014.
- [CGB<sup>+</sup>05] E. Coto, S. Grimm, S. Bruckner, E. Gröller, A. Kanitsar, and O. Rodriguez. MammoExplorer: An Advanced CAD Application for Breast DCE-MRI. In *Vision, Modelling, and Visualization*, pages 91–98, 2005.
- [CGM<sup>+</sup>17] D. Ceneda, T. Gschwandtner, T. May, S. Miksch, H.-J. Schulz, M. Streit, and C. Tominski. Characterizing Guidance in Visual Analytics. *IEEE Transactions on Visualization and Computer Graphics*, 23(1):111–120, Jan 2017.
- [CK09] M. R. Cheung and K. Krishnan. Interactive Deformation Registration of Endorectal Prostate MRI Using ITK Thin Plate Splines. *Academic Radiology*, 16(3):351–357, 2009.
- [CKB09] A. Cockburn, A. Karlson, and B. B. Bederson. A Review of Overview+Detail, Zooming, and Focus+Context Interfaces. *ACM Computing Surveys (CSUR)*, 41(1):2, 2009.
- [CKK<sup>+</sup>07] Y. J. Choi, J. K. Kim, N. Kim, K. W. Kim, E. K. Choi, and K.-S. Cho. Functional MR Imaging of Prostate Cancer. *Radiographics*, 27(1):63–75, 2007.

- [CLS06] K. S. Cover, F. J. Lagerwaard, and S. Senan. Color Intensity Projections: A Rapid Approach for Evaluating Four-Dimensional CT Scans in Treatment Planning. *International Journal of Radiation Oncology\*Biological\*Physics*, 64(3):954–961, 2006.
- [CMS99] S. K. Card, J. D. Mackinlay, and B. Shneiderman. *Readings in Information Visualization: Using Vision to Think*. Morgan Kaufmann, 1999.
- [CS02] S.-H. Cha and S. N. Srihari. On measuring the distance between histograms. *Pattern Recognition*, 35(6):1355–1370, 2002.
- [CT05] T. M. Cover and J. A. Thomas. *Elements of Information Theory*. Wiley-Blackwell, Apr 2005.
- [CT14] S. S. Chavan and S. N. Talbar. Multimodality Image Fusion in Frequency Domain for Radiation Therapy. In *International Conference on Medical Imaging, m-Health and Emerging Communication Systems*, pages 174–178, 2014.
- [DDSL16] R. R. Deshpande, J. DeMarco, J. W. Sayre, and B. J. Liu. Knowledge-driven decision support for assessing dose distributions in radiation therapy of head and neck cancer. *International Journal of Computer Assisted Radiology and Surgery*, 11(11):2071–2083, Apr 2016.
- [DJFB05] G. Delaney, S. Jacob, C. Featherstone, and M. Barton. The Role of Radiotherapy in Cancer Treatment. *Cancer*, 104(6):1129–1137, 2005.
- [DMB<sup>+</sup>91] R. E. Drzymala, R. Mohan, L. Brewster, J. Chu, M. Goitein, W. Harms, and M. Urie. Dose-volume histograms. *International Journal of Radiation Oncology\*Biological\*Physics*, 21(1):71–78, May 1991.
- [DNT09] D. Dinka, J. M. Nyce, and T. Timpka. Situated Cognition in Clinical Visualization: The Role of Transparency in GammaKnife Neurosurgery Planning. *Artificial Intelligence in Medicine*, 46(2):111–118, 2009.
- [DT05] N. Dalal and B. Triggs. Histograms of Oriented Gradients for Human Detection. In *IEEE Computer Society Conference on Computer Vision and Pattern Recognition*. IEEE, 2005.
- [dW96] K. de Geus and A. Watt. Three-Dimensional Stylization of Structures of Interest from Computed Tomography Images Applied to Radiotherapy Planning. *International Journal of Radiation Oncology\*Biological\*Physics*, 35(1):151–159, 1996.
- [EHK<sup>+</sup>06] K. Engel, M. Hadwiger, J. M. Kniss, C. Rezk-Salama, and D. Weiskopf. *Real-time volume graphics*. Ak Peters Natick, 2006.



- [ESS12] M. Erdt, G. Sakas, and S. Steger. Regmentation: A New View of Image Segmentation and Registration. *Journal of Radiation Oncology Informatics*, 4(1):1–23, 2012.
- [Eva08] P. M. Evans. Anatomical Imaging for Radiotherapy. *Physics in Medicine & Biology*, 53(12):R151–R191, 2008.
- [EvdSZ<sup>+</sup>15] A. J. G. Even, J. van der Stoep, C. M. L. Zegers, B. Reymen, E. G. C. Troost, P. Lambin, and W. van Elmpt. PET-based dose painting in non-small cell lung cancer: Comparing uniform dose escalation with boosting hypoxic and metabolically active sub-volumes. *Radiotherapy and Oncology*, 116(2):281–286, Aug 2015.
- [EWR<sup>+</sup>08] J. Ehrhardt, R. Werner, A. S. Richberg, B. Schulz, and H. Handels. Generation of a Mean Motion Model of the Lung Using 4D-CT Image Data. In *Eurographics Workshop on Visual Computing for Biomedicine*, pages 69–76, 2008.
- [FBKC<sup>+</sup>12] A. Fedorov, R. Beichel, J. Kalpathy-Cramer, J. Finet, J.-C. Fillion-Robin, S. Pujol, C. Bauer, D. Jennings, F. Fennessy, M. Sonka, J. Buatti, S. Aylward, J. V. Miller, S. Pieper, and R. Kikinis. 3D Slicer as an image computing platform for the Quantitative Imaging Network. *Magnetic Resonance Imaging*, 30(9):1323–1341, 2012.
- [FC16] T. C. F. Fonseca and T. P. R. Campos. SOFT-RT: Software for IMRT Simulations Based on MCNPx Code. *Applied Radiation and Isotopes*, 117:111–117, 2016.
- [FCC<sup>+</sup>14] T. Fechter, M. Carles, A. Chirindel, U. Christ, and U. Nestle. A threshold and region-growing based algorithm for 18FDG-PET 4D GTV delineation. In Massoptier and Song, editors, *Multimodal imaging towards individualized radiotherapy treatments*, pages 42–48. 2014.
- [FDC<sup>+</sup>15] T. Fechter, J. Dolz, A. Chirindel, M. Schlachter, M. Carles, S. Adebahr, M. Mix, and U. Nestle. Fully Automatic Danger Zone Determination for SBRT in NSCLC. *Journal of Radiation Oncology Informatics*, 7(1):1–27, 2015.
- [Fit01] J. M. Fitzpatrick. Detecting Failure, Assessing Success. In *Medical Image Registration*, pages 117–139. Informa UK Limited, Jun 2001.
- [FSS<sup>+</sup>13] H. Furtado, E. Steiner, M. Stock, D. Georg, and W. Birkfellner. Real-Time 2D/3D Registration Using kV-MV Image Pairs for Tumor Motion Tracking in Image Guided Radiotherapy. *Acta Oncologica*, 52(7):1464–1471, 2013.
- [FVW<sup>+</sup>11] O. Fluck, C. Vetter, W. Wein, A. Kamen, B. Preim, and R. Westermann. A survey of medical image registration on graphics hardware. *Computer Methods and Programs in Biomedicine*, 104(3):e45–e57, Dec 2011.

- [GCC<sup>+</sup>16] J. I. Gear, C. Cummings, A. J. Craig, A. Divoli, C. D. C. Long, M. Tapner, and G. D. Flux. Abdo-Man: A 3D-Printed Anthropomorphic Phantom for Validating Quantitative SIRT. *EJNMMI Physics*, 3(1):17, 2016.
- [GDF<sup>+</sup>00] G. Gambarini, U. Danesi, R. Foroni, M. Mauri, L. Pirola, and C. Birattari. Prompt Imaging of Absorbed Dose in Tissue-Equivalent Gel-Phantoms and New Toolkit for 3D Data Visualization. In *IEEE Nuclear Science Symposium (NSS/MIC)*, volume 3, pages 19/52–19/55, 2000.
- [GEH<sup>+</sup>02] P. Giraud, S. Elles, S. Helfre, Y. De Rycke, V. Servois, M. F. Carette, C. Alzieu, P. Y. Bondiau, B. Dubray, E. Touboul, M. Housset, J. C. Rosenwald, and J. M. Cosset. Conformal Radiotherapy for Lung Cancer: Different Delineation of the Gross Tumor Volume (GTV) by Radiologists and Radiation Oncologists. *Radiotherapy and Oncology*, 62(1):27–36, 2002.
- [GHC14] C. K. Glide-Hurst and I. J. Chetty. Improving radiotherapy planning, delivery accuracy, and normal tissue sparing using cutting edge technologies. *Journal of Thoracic Disease*, 6(4):303–318, Apr 2014.
- [GHHLY08] C. K. Glide-Hurst, G. D. Hugo, J. Liang, and D. Yan. A simplified method of four-dimensional dose accumulation using the mean patient density representation. *Medical Physics*, 35(12):5269–5277, 2008.
- [GLC<sup>+</sup>04] R. Gahbauer, T. Landberg, J. Chavaudra, J. Dobbs, N. Gupta, G. Hanks, J.-C. Horiot, K.-A. Johansson, T. Möller, S. Naudy, J. Purdy, I. Santenac, N. Suntharalingam, and H. Svensson. Prescribing, Recording, and Reporting Electron Beam Therapy. *Journal of the ICRU*, 4(1):1–2, Jun 2004.
- [GPM<sup>+</sup>02] A. Gerbaulet, R. Potter, J.-J. Mazeron, H. Meertens, and E. V. Limbergen. *The GEC ESTRO Handbook of Brachytherapy*. Leuven, Belgium: European Society for Therapeutic Radiology and Oncology, 2002.
- [GPN<sup>+</sup>01] E. E. Graves, A. Pirzkall, S. J. Nelson, D. Larson, and L. Verhey. Registration of Magnetic Resonance Spectroscopic Imaging to Computed Tomography for Radiotherapy Treatment Planning. *Medical Physics*, 28(12):2489–2496, 2001.
- [GS02] R. Gopal and G. Starkschall. Plan Space: Representation of Treatment Plans in Multidimensional Space. *International Journal of Radiation Oncology\*Biological\*Physics*, 53(5):1328–1336, 2002.
- [GS06] H. Griethe and H. Schumann. The visualization of uncertain data: Methods and problems. In *Proceedings of SimVis*, volume 6, pages 143–156, 2006.
- [GW02] R. C. Gonzalez and R. E. Woods. *Digital Image Processing (2nd Edition)*. Prentice-Hall, Inc., Upper Saddle River, NJ, USA, 2002.

- [GW19] Y. Ge and Q. J. Wu. Knowledge-based planning for intensity-modulated radiation therapy: A review of data-driven approaches. *Medical Physics*, 46(6):2760–2775, Apr 2019.
- [HBH03] M. Hadwiger, C. Berger, and H. Hauser. High-quality two-level volume rendering of segmented data sets on consumer graphics hardware. In *Proceedings of IEEE Visualization*, pages 301–308. IEEE, 2003.
- [HBR<sup>+</sup>17] I. Hamdan, J. Bert, C. C. L. Rest, J. P. Tasu, N. BouSSION, A. Valeri, G. Dardenne, and D. Visvikis. Fully Automatic Deformable Registration of Pretreatment MRI/CT for Image-Guided Prostate Radiotherapy Planning. *Medical Physics*, 44(12):6447–6455, 2017.
- [HCE<sup>+</sup>07] H. Hricak, P. L. Choyke, S. C. Eberhardt, S. A. Leibel, and P. T. Scardino. Imaging Prostate Cancer: A Multidisciplinary Perspective. *Radiology*, 243(1):28–53, 2007.
- [HJB<sup>+</sup>12] M. P. Heinrich, M. Jenkinson, M. Bhushan, T. Matin, F. V. Gleeson, S. M. Brady, and J. A. Schnabel. MIND: Modality independent neighbourhood descriptor for multi-modal deformable registration. *Medical Image Analysis*, 16(7):1423–1435, 2012.
- [HJNL06] M. A. Hunt, A. Jackson, A. Narayana, and N. Lee. Geometric factors influencing dosimetric sparing of the parotid glands using IMRT. *International Journal of Radiation Oncology\*Biophysics*, 66(1):296–304, Sep 2006.
- [HKK09] M. Hub, M. L. Kessler, and C. P. Karger. A Stochastic Approach to Estimate the Uncertainty Involved in B-Spline Image Registration. *IEEE Transactions on Medical Imaging*, 28(11):1708–1716, 2009.
- [HMP<sup>+</sup>18] G. G. Hanna, L. Murray, R. Patel, S. Jain, K. L. Aitken, K. N. Franks, N. van As, A. Tree, P. Hatfield, S. Harrow, F. McDonald, M. Ahmed, F. H. Saran, G. J. Webster, V. Khoo, D. Landau, D. J. Eaton, and M. A. Hawkins. UK Consensus on Normal Tissue Dose Constraints for Stereotactic Radiotherapy. *Clinical Oncology*, 30(1):5–14, Jan 2018.
- [HMTH13] F. Heckel, J. H. Moltz, C. Tietjen, and H. K. Hahn. Sketch-Based Editing Tools for Tumour Segmentation in 3D Medical Images. *Computer Graphics Forum*, 32(8):144–157, 2013.
- [Hol06] D. Holten. Hierarchical Edge Bundles: Visualization of Adjacency Relations in Hierarchical Data. *IEEE Transactions on Visualization and Computer Graphics*, 12(5):741–748, Sep 2006.
- [HST87] P. Hahn, S. Shalev, and P. Therrien. Colour Visualization as an Aid to the Comparison of Treatment Plans for Prostatic Carcinoma. *Acta Oncologica*, 26(4):313–315, 1987.

- [HW03] E. J. Hall and C.-S. Wu. Radiation-Induced Second Cancers: The Impact of 3D-CRT and IMRT. *International Journal of Radiation Oncology\*Biophysics*, 56(1):83–88, 2003.
- [HW13] J. Heinrich and D. Weiskopf. State of the Art of Parallel Coordinates. In M. Sbert and L. Szirmay-Kalos, editors, *Eurographics 2013 - State of the Art Reports*. The Eurographics Association, 2013.
- [HWS<sup>+</sup>07] H. Handels, R. Werner, R. Schmidt, T. Frenzel, W. Lu, D. Low, and J. Ehrhardt. 4D medical image computing and visualization of lung tumor mobility in spatio-temporal CT image data. *International Journal of Medical Informatics*, 76:S433–S439, 2007.
- [IFP95] V. Interrante, H. Fuchs, and S. Pizer. Enhancing Transparent Skin Surfaces with Ridge and Valley Lines. In *Proceedings of IEEE Visualization*, pages 52–59, 1995.
- [IFP96] V. Interrante, H. Fuchs, and S. Pizer. Illustrating Transparent Surfaces with Curvature-Directed Strokes. In *Proceedings of IEEE Visualization*, pages 211–218, 1996.
- [Int97] V. Interrante. Illustrating surface shape in volume data via principal direction-driven 3D line integral convolution. In *Proceedings of the 24th annual conference on Computer graphics and interactive techniques*, pages 109–116. ACM Press/Addison-Wesley Publishing Co., 1997.
- [ISNC05] L. Ibanez, W. Schroeder, L. Ng, and J. Cates. *The ITK Software Guide*. Kitware, Inc., second edition, 2005.
- [JD14] A. P. James and B. V. Dasarathy. Medical image fusion: A survey of the state of the art. *Information Fusion*, 19:4–19, 2014.
- [JHP<sup>+</sup>15] S. S. Jang, G. J. Huh, S. Y. Park, P. S. Yang, and E. Cho. Usefulness of target delineation based on the two extreme phases of a four-dimensional computed tomography scan in stereotactic body radiation therapy for lung cancer. *Thoracic Cancer*, 6(3):239–246, Apr 2015.
- [JKF12] Y. Jung, J. Kim, and D. D. Feng. Dual-modal visibility metrics for interactive PET-CT visualization. In *International Conference of the IEEE Engineering in Medicine and Biology Society (EMBC)*, pages 2696–2699. IEEE, 2012.
- [JYW99] D. A. Jaffray, D. Yan, and J. W. Wong. Managing Geometric Uncertainty in Conformal Intensity-Modulated Radiation Therapy. *Seminars in Radiation Oncology*, 9(1):4–19, 1999.

- [JZG<sup>+</sup>14] L. A. Jarvis, R. Zhang, D. J. Gladstone, S. Jiang, W. Hitchcock, O. D. Friedman, A. K. Glaser, M. Jermyn, and B. W. Pogue. Cherenkov Video Imaging Allows for the First Visualization of Radiation Therapy in Real Time. *International Journal of Radiation Oncology\*Biophysics*, 89(3):615–622, 2014.
- [KAF<sup>+</sup>08] D. Keim, G. Andrienko, J.-D. Fekete, C. Görg, J. Kohlhammer, and G. Melançon. Visual Analytics: Definition, Process, and Challenges. In *Information Visualization*, pages 154–175. Springer, 2008.
- [KBD16] A. P. Keszei, B. Berkels, and T. M. Deserno. Survey of Non-Rigid Registration Tools in Medicine. *Journal of Digital Imaging*, 30(1):102–116, 2016.
- [KBP<sup>+</sup>07] M. R. Kaus, K. K. Brock, V. Pekar, L. A. Dawson, A. M. Nichol, and D. A. Jaffray. Assessment of a Model-Based Deformable Image Registration Approach for Radiation Therapy Planning. *International Journal of Radiation Oncology\*Biophysics*, 68(2):572–580, 2007.
- [KCEF07] J. Kim, W. Cai, S. Eberl, and D. Feng. Real-Time Volume Rendering Visualization of Dual-Modality PET/CT Images With Interactive Fuzzy Thresholding Segmentation. *IEEE Transactions on Information Technology in Biomedicine*, 11(2):161–169, 2007.
- [KCUP13] N. Kirby, C. Chuang, U. Ueda, and J. Pouliot. The need for application-based adaptation of deformable image registration. *Medical Physics*, 40(1):011702, 2013.
- [KGB<sup>+</sup>09] B. Kainz, M. Grabner, A. Bornik, S. Hauswiesner, J. Muehl, and D. Schmalstieg. Ray Casting of Multiple Volumetric Datasets with Polyhedral Boundaries on Manycore GPUs. *ACM Transactions on Graphics*, 28(5):152:1–152:9, Dec 2009.
- [KHB<sup>+</sup>08] R. Kashani, M. Hub, J. M. Balter, M. L. Kessler, L. Dong, L. Zhang, L. Xing, Y. Xie, D. Hawkes, J. A. Schnabel, J. McClelland, S. Joshi, Q. Chen, and W. Lu. Objective assessment of deformable image registration in radiotherapy: A multi-institution study. *Medical Physics*, 35(12):5944, 2008.
- [KKEM10] D. A. Keim, J. Kohlhammer, G. Ellis, and F. Mansmann. *Mastering the Information Age - Solving Problems with Visual Analytics*. Eurographics Association, 2010.
- [KKP<sup>+</sup>08] J. H. Kim, J. K. Kim, B.-W. Park, N. Kim, and K.-S. Cho. Apparent Diffusion Coefficient: Prostate Cancer versus Noncancerous Tissue According to Anatomical Region. *Journal of Magnetic Resonance Imaging*, 28(5):1173–1179, 2008.

- [KLPF14] F. King, A. Lasso, C. Pinter, and G. Fichtinger. A tool for intraoperative visualization of registration results. In *Medical Imaging 2014: Image-Guided Procedures, Robotic Interventions, and Modeling*. SPIE-Intl Soc Optical Eng, Mar 2014.
- [KMB<sup>+</sup>06] P. J. Keall, G. S. Mageras, J. M. Balter, R. S. Emery, K. M. Forster, S. B. Jiang, J. M. Kapatoes, D. A. Low, M. J. Murphy, B. R. Murray, C. R. Ramsey, M. B. van Herk, S. S. Vedam, J. W. Wong, and E. Yorke. The management of respiratory motion in radiation oncology report of AAPM Task Group 76a). *Medical Physics*, 33(10):3874–3900, Oct 2006.
- [KMJ<sup>+</sup>14] O. Koybasi, P. Mishra, S. S. James, J. H. Lewis, and J. Seco. Simulation of dosimetric consequences of 4D-CT-based motion margin estimation for proton radiotherapy using patient tumor motion data. *Physics in Medicine & Biology*, 59(4):853, 2014.
- [KMK<sup>+</sup>04] A. Kaiser, L. Moser, W. Kuschke, M. Hinkelbein, A. Buchali, and V. Budach. Virtual Simulation of a Boost Field in Adjuvant Radiotherapy of the Breast. *Strahlentherapie und Onkologie*, 180(10):637–641, 2004.
- [KSB<sup>+</sup>09] M. Krzywinski, J. Schein, I. Birol, J. Connors, R. Gascoyne, D. Horsman, S. J. Jones, and M. A. Marra. Circo: An information aesthetic for comparative genomics. *Genome Research*, 19(9):1639–1645, Jun 2009.
- [KSM<sup>+</sup>09] M. Kazhdan, P. Simari, T. McNutt, B. Wu, R. Jacques, M. Chuang, and R. Taylor. A Shape Relationship Descriptor for Radiation Therapy Planning. In *Medical Image Computing and Computer-Assisted Intervention*, pages 100–108. Springer Nature, 2009.
- [KSS<sup>+</sup>12] T. Kataria, K. Sharma, V. Subramani, K. P. Karrthick, and S. S. Bisht. Homogeneity Index: An objective tool for assessment of conformal radiation treatments. *Journal of Medical Physics*, 37(4):207–213, Oct 2012.
- [KVCC08] J. Kurhanewicz, D. Vigneron, P. Carroll, and F. Coakley. Multiparametric Magnetic Resonance Imaging in Prostate Cancer: Present and Future. *Current Opinion in Urology*, 18(1):71, 2008.
- [KW03] J. Krüger and R. Westermann. Acceleration techniques for GPU-based volume rendering. In *Proceedings of IEEE Visualization*, pages 287–292, Oct 2003.
- [KWCM13] V. Kong, J. Wenz, T. Craig, and M. Milosevic. Image-Guided Adaptive Radiotherapy – Delivering Personalized Radiation Medicine to Improve Treatment Quality and Patients’ Outcome. *Journal of Medical Imaging and Radiation Sciences*, 44(1):55–56, 2013.

- [KZD<sup>+</sup>09] A. Khamene, D. Zikic, M. Diallo, T. Boettger, and E. Rietzel. A Novel Intensity Similarity Metric with Soft Spatial Constraint for a Deformable Image Registration Problem in Radiation Therapy. In *Medical Image Computing and Computer-Assisted Intervention*, pages 828–836. Springer Berlin Heidelberg, 2009.
- [LCS<sup>+</sup>13] K. P. Lam, D. J. Collins, J. Sule-Suso, R. Bhana, and A. Moloney. On Evaluation of a Multiscale-Based CT Image Analysis and Visualisation Algorithm. In *International Conference on Biomedical Engineering and Informatics*, pages 148–153, 2013.
- [LF09] C. Lux and B. Fröhlich. GPU-based Ray Casting of Multiple Multi-Resolution Volume Datasets. *Advances in Visual Computing*, pages 104–116, 2009.
- [LFP<sup>+</sup>90] M. Levoy, H. Fuchs, S. M. Pizer, J. Rosenman, E. L. Chaney, G. W. Sherouse, V. Interrante, and J. Kiel. Volume Rendering in Radiation Treatment Planning. In *Proceedings of the Conference on Visualization in Biomedical Computing*, pages 4–10. IEEE, 1990.
- [LHD<sup>+</sup>19] G. Liu, F. Hu, X. Ding, X. Li, Q. Shao, Y. Wang, J. Yang, and H. Quan. Simulation of dosimetry impact of 4DCT uncertainty in 4D dose calculation for lung SBRT. *Radiation Oncology*, 14(1), Jan 2019.
- [LHG<sup>+</sup>05] A. Leow, S.-C. Huang, A. Geng, J. Becker, S. Davis, A. Toga, and P. Thompson. Inverse Consistent Mapping in 3D Deformable Image Registration: Its Construction and Statistical Properties. In *International Conference on Information Processing in Medical Imaging*, pages 493–503. Springer Berlin Heidelberg, 2005.
- [LHL<sup>+</sup>00] C. C. Ling, J. Humm, S. Larson, H. Amols, Z. Fuks, S. Leibel, and J. A. Koutcher. Towards Multidimensional Radiotherapy (MD-CRT): Biological Imaging and Biological Conformality. *International Journal of Radiation Oncology\*Biological\*Physics*, 47(3):551–560, 2000.
- [Lin91] J. Lin. Divergence measures based on the Shannon entropy. *IEEE Transactions on Information Theory*, 37(1):145–151, 1991.
- [LJP<sup>+</sup>99] J. S. Lee, A. B. Jani, C. A. Pelizzari, D. J. Haraf, E. E. Vokes, R. R. Weichselbaum, and G. T. Y. Chen. Volumetric visualization of head and neck CT data for treatment planning. *International Journal of Radiation Oncology\*Biological\*Physics*, 44(3):693–703, 1999.
- [LJYS05] Z. Li, Z. Jing, X. Yang, and S. Sun. Color transfer based remote sensing image fusion using non-separable wavelet frame transform. *Pattern Recognition Letters*, 26(13):2006–2014, Oct 2005.

- [LKCG12] P. Lee, P. Kupelian, J. Czernin, and P. Ghosh. Current concepts in F18 FDG PET/CT-based radiation therapy planning for lung cancer. *Frontiers in Oncology*, 2, 2012.
- [LKG<sup>+</sup>16] P. Ljung, J. Krüger, E. Gröller, M. Hadwiger, C. D. Hansen, and A. Ynnerman. State of the Art in Transfer Functions for Direct Volume Rendering. *Computer Graphics Forum*, 35(3):669–691, Jun 2016.
- [LL19] A. S. Lundervold and A. Lundervold. An overview of deep learning in medical imaging focusing on MRI. *Zeitschrift für Medizinische Physik*, 29(2):102–127, 2019.
- [LSBP18] K. Lawonn, N. N. Smit, K. Bühler, and B. Preim. A Survey on Multimodal Medical Data Visualization. *Computer Graphics Forum*, 37(1):413–438, 2018.
- [Max95] N. Max. Optical models for direct volume rendering. *IEEE Transactions on Visualization and Computer Graphics*, 1(2):99–108, 1995.
- [MBC15] M. C. Mabray, R. F. Barajas, and S. Cha. Modern Brain Tumor Imaging. *Brain Tumor Research and Treatment*, 3(1):8–23, 2015.
- [MBLM11] K. L. Moore, R. S. Brame, D. A. Low, and S. Mutic. Experience-Based Quality Control of Clinical Intensity-Modulated Radiotherapy Planning. *International Journal of Radiation Oncology\*Biophysics*, 81(2):545–551, Oct 2011.
- [MBLM12] K. L. Moore, R. S. Brame, D. A. Low, and S. Mutic. Quantitative Metrics for Assessing Plan Quality. *Seminars in Radiation Oncology*, 22(1):62–69, Jan 2012.
- [McS11] D. L. McShan. Workflow and Clinical Decision Support for Radiation Oncology. *Efficient Decision Support Systems - Practice and Challenges in Biomedical Related Domain*, Sep 2011.
- [MGLS<sup>+</sup>16] N. Merten, S. Glaßer, B. Lassen-Schmidt, O. S. Großer, J. Ricke, H. Amthauer, and B. Preim. Illustrative PET/CT Visualisation of SIRT-Treated Lung Metastases. In *Eurographics Workshop on Visual Computing for Biology and Medicine*, pages 99–103, 2016.
- [MK11] J. Marino and A. Kaufman. Prostate Cancer Visualization from MR Imagery and MR Spectroscopy. *Computer Graphics Forum*, 30(3):1051–1060, 2011.
- [MKN13] M. Müller, A. Karamalis, and N. Navab. Visualization of Organ Motion during Breathing from 4D Datasets. In *Augmented Environments for Computer-Assisted Interventions*, pages 34–44. Springer, 2013.



- [MLE<sup>+</sup>14] M. D. Mattes, J. C. Lee, S. Elnaïem, A. Guirguis, N. C. Ikoro, and H. Ashamalla. A predictive model to guide management of the overlap region between target volume and organs at risk in prostate cancer volumetric modulated arc therapy. *Radiation Oncology Journal*, 32(1):23–30, 2014.
- [MLJ<sup>+</sup>14] M. McCormick, X. Liu, J. Jomier, C. Marion, and L. Ibanez. ITK: enabling reproducible research and open science. *Frontiers in Neuroinformatics*, 8(13):1–11, 2014.
- [MNR<sup>+</sup>09] M. MacManus, U. Nestle, K. E. Rosenzweig, I. Carrio, C. Messa, O. Belohlavek, M. Danna, T. Inoue, E. Deniaud-Alexandre, S. Schipani, N. Watanabe, M. Dondi, and B. Jeremic. Use of PET and PET/CT for Radiation Therapy Planning: IAEA expert report 2006–2007. *Radiotherapy and Oncology*, 91(1):85–94, Apr 2009.
- [Mun14] T. Munzner. *Visualization Analysis and Design*. CRC Press, 2014.
- [MUO06] D. Maleike, J. Unkelbach, and U. Oelfke. Simulation and visualization of dose uncertainties due to interfractional organ motion. *Physics in Medicine & Biology*, 51(9):2237–2252, 2006.
- [MV98] J. B. A. Maintz and M. A. Viergever. A survey of medical image registration. *Medical Image Analysis*, 2(1):1–36, 1998.
- [MvGK<sup>+</sup>11] K. Murphy, B. van Ginneken, S. Klein, M. Staring, B. J. de Hoop, M. A. Viergever, and J. P. W. Pluim. Semi-automatic construction of reference standards for evaluation of image registration. *Medical Image Analysis*, 15(1):71–84, Feb 2011.
- [MvGR<sup>+</sup>11] K. Murphy, B. van Ginneken, J. M. Reinhardt, S. Kabus, K. Ding, X. Deng, K. Cao, K. Du, G. E. Christensen, V. Garcia, T. Vercauteren, N. Ayache, O. Commowick, G. Malandain, B. Glocker, N. Paragios, N. Navab, V. Gorbunova, J. Sporring, M. de Bruijne, X. Han, M. P. Heinrich, J. A. Schnabel, M. Jenkinson, C. Lorenz, M. Modat, J. R. McClelland, S. Ourselin, S. E. A. Muenzing, M. A. Viergever, D. De Nigris, D. L. Collins, T. Arbel, M. Peroni, R. Li, G. C. Sharp, A. Schmidt-Richberg, J. Ehrhardt, R. Werner, D. Smeets, D. Loeckx, G. Song, N. Tustison, B. Avants, J. C. Gee, M. Staring, S. Klein, B. C. Stoel, M. Urschler, M. Werlberger, J. Vandemeulebroucke, S. Rit, D. Sarrut, and J. P. W. Pluim. Evaluation of registration methods on thoracic CT: the EMPIRE10 challenge. *IEEE Transactions on Medical Imaging*, 30(11):1901–1920, 2011.
- [MvM02] A. McKenzie, M. van Herk, and B. Mijnheer. Margins for Geometric Uncertainty around Organs at Risk in Radiotherapy. *Radiotherapy and Oncology*, 62(3):299–307, 2002.

- [MYE<sup>+</sup>17] C. S. Mayo, J. Yao, A. Eisbruch, J. M. Balter, D. W. Litzenberg, M. M. Matuszak, M. L. Kessler, G. Weyburn, C. J. Anderson, D. Owen, W. C. Jackson, and R. T. Haken. Incorporating big data into treatment plan evaluation: Development of statistical DVH metrics and visualization dashboards. *Advances in Radiation Oncology*, 2(3):503–514, Jul 2017.
- [MYJ<sup>+</sup>10] L. B. Marks, E. D. Yorke, A. Jackson, R. K. Ten Haken, L. S. Constine, A. Eisbruch, S. M. Bentzen, J. Nam, and J. O. Deasy. Use of Normal Tissue Complication Probability Models in the Clinic. *International Journal of Radiation Oncology\*Biophysics*, 76(3):S10–S19, 2010.
- [MYKO91] T. Miyazawa, R. Yoshida, M. Kimura, and T. Otsuki. Visualization of 3D Medical Images for Radiotherapy Planning. In *IEEE Nuclear Science Symposium (NSS/MIC)*, volume 3, pages 1553–1557, 1991.
- [Nje08] C. F. Njeh. Tumor delineation: The weakest link in the search for accuracy in radiotherapy. *Journal of Medical Physics*, 33(4):136–140, 2008.
- [NLK<sup>+</sup>14] M. Nunes, A. Laruelo, S. Ken, A. Laprie, and K. Bühler. A Survey on Visualizing Magnetic Resonance Spectroscopy Data. In *Eurographics Workshop on Visual Computing for Biology and Medicine*, pages 21–30. The Eurographics Association, 2014.
- [NRS<sup>+</sup>14] M. Nunes, B. Rowland, M. Schlachter, S. Ken, K. Matkovic, A. Laprie, and K. Bühler. An integrated visual analysis system for fusing MR spectroscopy and multi-modal radiology imaging. In *IEEE Conference on Visual Analytics Science and Technology (VAST)*, pages 53–62. IEEE, 2014.
- [NS07] B. E. Nelms and J. A. Simon. A survey on planar IMRT QA analysis. *Journal of Applied Clinical Medical Physics*, 8(3):76–90, 2007.
- [NVI11] NVIDIA Corporation. *NVIDIA CUDA C Programming Guide*, June 2011. Available at [https://docs.nvidia.com/cuda/pdf/CUDA\\_C\\_Programming\\_Guide.pdf](https://docs.nvidia.com/cuda/pdf/CUDA_C_Programming_Guide.pdf).
- [NWHG09] U. Nestle, W. Weber, M. Hentschel, and A.-L. Grosu. Biological imaging in radiation therapy: role of positron emission tomography. *Physics in Medicine & Biology*, 54(1):R1–R25, 2009.
- [ODH<sup>+</sup>07] S. Oeltze, H. Doleisch, H. Hauser, P. Muigg, and B. Preim. Interactive Visual Analysis of Perfusion Data. *IEEE Transactions on Visualization and Computer Graphics*, 13(6):1392–1399, 2007.
- [OdXJB<sup>+</sup>07] J. Orban de Xivry, G. Janssens, G. Bosmans, M. De Craene, A. Dekker, J. Buijsen, A. van Baardwijk, D. De Ruyscher, B. Macq, and P. Lambin. Tumour delineation and cumulative dose computation in radiotherapy based on deformable registration of respiratory correlated CT images of lung cancer patients. *Radiotherapy and Oncology*, 85(2):232–238, 2007.

- [OS01] S. D. Olabarriaga and A. W. M. Smeulders. Interaction in the segmentation of medical images: A survey. *Medical Image Analysis*, 5(2):127–142, 2001.
- [Par62] E. Parzen. On estimation of a probability density function and mode. *The Annals of Mathematical Statistics*, pages 1065–1076, 1962.
- [PB13] B. Preim and C. P. Botha. *Visual Computing for Medicine: Theory, Algorithms, and Applications*. The Morgan Kaufmann Series in Computer Graphics. Newnes, 2013.
- [PBC<sup>+</sup>16] B. Preim, A. Baer, D. Cunningham, T. Isenberg, and T. Ropinski. A Survey of Perceptually Motivated 3D Visualization of Medical Image Data. *Computer Graphics Forum*, 35(3):501–525, Jun 2016.
- [PLW<sup>+</sup>12] C. Pinter, A. Lasso, A. Wang, D. Jaffray, and G. Fichtinger. SlicerRT: Radiation therapy research toolkit for 3D Slicer. *Medical Physics*, 39:6332–6338, 2012.
- [PM06] G. Price and C. Moore. Visualisation of Delineation Structure Variability in Radiotherapy. In *International Conference on Medical Information Visualisation - BioMedical Visualisation*, pages 91–96, 2006.
- [PPB15] P. M. Putora, S. Peters, and M. Bovet. Informatics in Radiation Oncology. In *Machine Learning in Radiation Oncology*, pages 57–70. Springer International Publishing, 2015.
- [PPN<sup>+</sup>13] S. Pirozzi, J. Piper, A. Nelson, M. Duchateau, D. Verellen, and M. De Ridder. A Novel Framework for Deformable Registration Evaluation and Quality Assurance. *International Journal of Radiation Oncology\*Biography\*Physics*, 87(2):S719, 2013.
- [PWK<sup>+</sup>12] S. F. Petit, B. Wu, M. Kazhdan, A. Dekker, P. Simari, R. Kumar, R. Taylor, J. M. Herman, and T. McNutt. Increased organ sparing using shape-based treatment plan optimization for intensity modulated radiation therapy of pancreatic adenocarcinoma. *Radiotherapy and Oncology*, 102(1):38–44, Jan 2012.
- [PXP00] D. L. Pham, C. Xu, and J. L. Prince. Current Methods in Medical Image Segmentation. *Annual Review of Biomedical Engineering*, 2(1):315–337, 2000.
- [RA10] D. Rueckert and P. Aljabar. Nonrigid registration of medical images: Theory, methods, and applications [applications corner]. *IEEE Signal Processing Magazine*, 27(4):113–119, 2010.
- [Rai17] R. G. Raidou. *Visual Analytics for Digital Radiotherapy: Towards a Comprehensive Pipeline*. PhD thesis, Department of Biomedical Engineering, TU Eindhoven, 2017.

- [Rai18] R. G. Raidou. Uncertainty Visualization: Recent Developments and Future Challenges in Prostate Cancer Radiotherapy Planning. In *EuroVis Workshop on Reproducibility, Verification, and Validation in Visualization*, pages 13–17, 2018.
- [Rat04] O. Ratib. PET/CT image navigation and communication. *Journal of Nuclear Medicine*, 45 Suppl 1:46S–55S, Jan 2004.
- [RBGR18] O. Reiter, M. Breeuwer, E. Gröller, and R. G. Raidou. Comparative Visual Analysis of Pelvic Organ Segmentations. In *EuroVis - Short Papers*, pages 37–41, 2018.
- [RBV17] R. G. Raidou, M. Breeuwer, and A. Vilanova. Visual Analytics for Digital Radiotherapy: Towards a Comprehensible Pipeline. In *Proceedings of the European Association for Computer Graphics: Dirk Bartz Prize for Visual Computing in Medicine*, pages 1–4, 2017.
- [RCCW05] E. Rietzel, G. T. Y. Chen, N. C. Choi, and C. G. Willet. Four-dimensional image-based treatment planning: Target volume segmentation and dose calculation in the presence of respiratory motion. *International Journal of Radiation Oncology\*Biophysics*, 61(5):1535–1550, Apr 2005.
- [RCM<sup>+</sup>16] R. G. Raidou, O. Casares-Magaz, L. P. Muren, U. A. van der Heide, J. Rørvik, M. Breeuwer, and A. Vilanova. Visual Analysis of Tumor Control Models for Prediction of Radiotherapy Response. *Computer Graphics Forum*, 35(3):231–240, 2016.
- [RDK<sup>+</sup>16] A. Ramkumar, J. Dolz, H. A. Kirisli, S. Adebahr, T. Schimek-Jasch, U. Nestle, L. Massoptier, E. Varga, P. J. Stappers, W. J. Niessen, and Y. Song. User Interaction in Semi-Automatic Segmentation of Organs at Risk: A Case Study in Radiotherapy. *Journal of Digital Imaging*, 29(2):264–277, 2016.
- [RKS<sup>+</sup>16] R. G. Raidou, H. J. Kuijf, N. Sepasian, N. Pezzotti, W. H. Bouvy, M. Breeuwer, and A. Vilanova. Employing Visual Analytics to Aid the Design of White Matter Hyperintensity Classifiers. In *Medical Image Computing and Computer-Assisted Intervention*, pages 97–105. Springer International Publishing, 2016.
- [RMB<sup>+</sup>16] R. G. Raidou, F. J. J. Marcelis, M. Breeuwer, E. Gröller, A. Vilanova, and H. M. M. van de Wetering. Visual Analytics for the Exploration and Assessment of Segmentation Errors. In *Eurographics Workshop on Visual Computing for Biology and Medicine*, pages 193–202, 2016.
- [RMBX15] O. Rouabhi, M. Ma, J. Bayouth, and J. Xia. Impact of temporal probability in 4D dose calculation for lung tumors. *Journal of Applied Clinical Medical Physics*, 16(6):110–118, Nov 2015.

- [Roh12] T. Rohlfing. Image similarity and tissue overlaps as surrogates for image registration accuracy: widely used but unreliable. *IEEE Transactions on Medical Imaging*, 31(2):153–163, 2012.
- [RPHL14] G. Ristovski, T. Preusser, H. K. Hahn, and L. Linsen. Uncertainty in medical visualization: Towards a taxonomy. *Computers & Graphics*, 39:60–73, 2014.
- [RPSWI10] P. Risholm, S. Pieper, E. Samset, and W. M. Wells III. Summarizing and Visualizing Uncertainty in Non-Rigid Registration. In *Medical Image Computing and Computer-Assisted Intervention*, pages 554–561. Springer, 2010.
- [RSO<sup>+</sup>96] V. Rudat, P. Schraube, D. Oetzel, D. Zierhut, M. Flentje, and M. Wannemacher. Combined Error of Patient Positioning Variability and Prostate Motion Uncertainty in 3D Conformal Radiotherapy of Localized Prostate Cancer. *International Journal of Radiation Oncology\*Biophysics*, 35(5):1027–1034, 1996.
- [RvD<sup>+</sup>15] R. G. Raidou, U. A. van der Heide, C. V. Dinh, G. Ghobadi, J. F. Kallehauge, M. Breeuwer, and A. Vilanova. Visual Analytics for the Exploration of Tumor Tissue Characterization. *Computer Graphics Forum*, 34(3):11–20, 2015.
- [RvdMS<sup>+</sup>07] N. Reynaert, S. C. van der Marck, D. R. Schaart, W. V. der Zee, C. V. Vliet-Vroegindewey, M. Tomsej, J. Jansen, B. Heijmen, M. Coghe, and C. D. Wagter. Monte Carlo treatment planning for photon and electron beams. *Radiation Physics and Chemistry*, 76(4):643–686, Apr 2007.
- [SBR<sup>+</sup>17] S. Samanta, S. Balukrishna, K. M. Rafic, B. S. T. Peace, I. R. R. Singh, and S. P. Pavamani. Adding Another Dimension to Plan Evaluation: Visualising the Dose–Volume Histogram Band in Head and Neck Radiotherapy and Exploring Its Utility. *Journal of Radiotherapy in Practice*, 16(4):403–408, 2017.
- [SDB<sup>+</sup>02] W. Sibomana, J.-F. Daisne, A. Bol, M. Lonnew, V. Gregoire, and C. Michel. Head and Neck Multimodality Volumes Visualization Methods. In *IEEE Nuclear Science Symposium (NSS/MIC)*, volume 2, pages 1282–1286, 2002.
- [SDP13] A. Sotiras, C. Davatzikos, and N. Paragios. Deformable Medical Image Registration: A Survey. *IEEE Transactions on Medical Imaging*, 32(7):1153–1190, 2013.
- [SFA<sup>+</sup>05] R. Shimofusa, H. Fujimoto, H. Akamata, K. Motoori, S. Yamamoto, T. Ueda, and H. Ito. Diffusion-Weighted Imaging of Prostate Cancer. *Journal of Computer Assisted Tomography*, 29(2):149–153, 2005.

- [SFA<sup>+</sup>17a] M. Schlachter, T. Fechter, S. Adebahr, T. Schimek-Jasch, U. Nestle, and K. Bühler. Video S1. Supplementary video demonstrating features of 4D-VS. Supporting Information: Visualization of 4D multimodal imaging data and its applications in radiotherapy planning. <https://aapm.onlinelibrary.wiley.com/action/downloadSupplement?doi=10.1002%2Facm2.12209&file=acm212209-sup-0002-MovieS1.mov>, Oct 2017.
- [SFA<sup>+</sup>17b] M. Schlachter, T. Fechter, S. Adebahr, T. Schimek-Jasch, U. Nestle, and K. Bühler. Visualization of 4D multimodal imaging data and its applications in radiotherapy planning. *Journal of Applied Clinical Medical Physics*, 18(6):183–193, Oct 2017.
- [SFBN14] M. Schlachter, T. Fechter, K. Bühler, and U. Nestle. EP-1711: Fast visual quality inspection of 4D PET/CT contouring of manual and semi-automatic contours. *Radiotherapy and Oncology*, 111:S251–S252, 2014.
- [SFJ<sup>+</sup>16] M. Schlachter, T. Fechter, M. Jurisic, T. Schimek-Jasch, O. Oehlke, S. Adebahr, W. Birkfellner, U. Nestle, and K. Bühler. Visualization of Deformable Image Registration Quality Using Local Image Dissimilarity. *IEEE Transactions on Medical Imaging*, 35(10):2319–2328, Oct 2016.
- [SFNB14] M. Schlachter, T. Fechter, U. Nestle, and K. Bühler. Visualization of 4D-PET/CT, Target Volumes and Dose Distribution: Applications in Radiotherapy Planning. In *Proceedings of MICCAI Workshop on Image-Guided Adaptive Radiation Therapy*, Oct 2014.
- [SH02] J. C. Stroom and B. J. M. Heijmen. Geometrical Uncertainties, Radiotherapy Planning Margins, and the ICRU-62 Report. *Radiotherapy and Oncology*, 64(1):75–83, 2002.
- [Shn96] B. Shneiderman. The eyes have it: a task by data type taxonomy for information visualizations. In *Proceedings 1996 IEEE Symposium on Visual Languages*, pages 336–343, 1996.
- [SHS<sup>+</sup>14] N. N. Smit, B. K. Haneveld, M. Staring, E. Eisemann, C. P. Botha, and A. Vilanova. RegistrationShop: An Interactive 3D Medical Volume Registration System. In *Eurographics Workshop on Visual Computing for Biology and Medicine*. The Eurographics Association, 2014.
- [SKH<sup>+</sup>08] H. Seim, D. Kainmueller, M. Heller, H. Lamecker, S. Zachow, and H.-C. Hege. Automatic Segmentation of the Pelvic Bones from CT Data Based on a Statistical Shape Model. In *Eurographics Workshop on Visual Computing for Biomedicine*, pages 93–100, 2008.

- [SKO06] D. A. X. Schinagl, J. H. A. M. Kaanders, and W. J. G. Oyen. From Anatomical to Biological Target Volumes: The Role of PET in Radiation Treatment Planning. *Cancer Imaging*, 6:S107–S116, 2006.
- [SKS10] J. A. Shackelford, N. Kandasamy, and G. C. Sharp. On developing B-spline registration algorithms for multi-core processors. *Physics in Medicine & Biology*, 55(21):6329–6351, 2010.
- [Sla12] J. M. Slater. From X-Rays to Ion Beams: A Short History of Radiation Therapy. In *Ion Beam Therapy – Fundamentals, Technology, Clinical Applications*, pages 3–16. Springer, 2012.
- [SML06] W. Schroeder, K. Martin, and B. Lorensen. *Visualization Toolkit: An Object-Oriented Approach to 3D Graphics*. Kitware, fourth edition, Dec 2006.
- [SPBR20] M. Schlachter, B. Preim, K. Bühler, and R. G. Raidou. Principles of Visualization in Radiation Oncology. *Oncology*, 98(6):412–422, 2020.
- [SPC<sup>+</sup>21] M. Schlachter, S. Peters, D. Camenisch, P. M. Putora, and K. Bühler. Exploration of Overlap Volumes for Radiotherapy Plan Evaluation with the Aim of Healthy Tissue Sparing. *arXiv*, 2021.
- [SPWF12] E. Schreibmann, P. Pantalone, A. Waller, and T. Fox. A measure to evaluate deformable registration fields in clinical settings. *Journal of Applied Clinical Medical Physics*, 13(5):126–139, 2012.
- [SRH<sup>+</sup>10] M. Schlachter, M. Reiser, C. Herz, F. Schlürmann, S. Lassmann, M. Werner, H. Burkhardt, and O. Ronneberger. Harmonic Filters for 3D Multichannel Data: Rotation Invariant Detection of Mitoses in Colorectal Cancer. *IEEE Transactions on Medical Imaging*, 29(8):1485–1495, Aug 2010.
- [SRM<sup>+</sup>19] M. Schlachter, R. G. Raidou, L. P. Muren, B. Preim, P. M. Putora, and K. Bühler. State-of-the-Art Report: Visual Computing in Radiation Therapy Planning. *Computer Graphics Forum*, 38(3):753–779, Jun 2019.
- [SRS<sup>+</sup>10] A. Søvik, J. Rødal, H. K. Skogmo, C. Lervåg, K. Eilertsen, and E. Malinen. Adaptive Radiotherapy Based on Contrast Enhanced Cone Beam CT Imaging. *Acta Oncologica*, 49(7):972–977, 2010.
- [SRV16] P. Silva, R. G. Raidou, and A. Vilanova. Visualization of Variability in Radiotherapy Dose Planning. In *Proceedings of the 10th MedVis Conference*, pages 63–66, 2016.
- [SS11] N. Schubert and I. Scholl. Comparing GPU-based multi-volume ray casting techniques. *Computer Science - Research and Development*, 26(1):39–50, 2011.

- [SSB<sup>+</sup>05] W. Song, B. Schaly, G. Bauman, J. Battista, and J. Van Dyk. Image-Guided Adaptive Radiation Therapy (IGART): Radiobiological and Dose Escalation Considerations for Localized Carcinoma of the Prostate: IGART: Radiobiological and Dose Escalation Considerations. *Medical Physics*, 32(7Part1):2193–2203, 2005.
- [SSC<sup>+</sup>15] T. Song, D. Staub, M. Chen, W. Lu, Z. Tian, X. Jia, Y. Li, L. Zhou, S. B. Jiang, and X. Gu. Patient-specific dosimetric endpoints based treatment plan quality control in radiotherapy. *Physics in Medicine & Biology*, 60(21):8213–8227, Oct 2015.
- [STCS<sup>+</sup>03] J. Schnabel, C. Tanner, A. D. Castellano-Smith, A. Degenhard, M. O. Leach, D. R. Hose, D. L. G. Hill, and D. J. Hawkes. Validation of nonrigid image registration using finite-element methods: application to breast MR images. *IEEE Transactions on Medical Imaging*, 22(2):238–247, 2003.
- [SUM12] SUMMER. Software for the Use of Multi-Modality images in External Radiotherapy. <https://cordis.europa.eu/project/rcn/100561/factsheet/en>, 2012. Accessed on 4 February 2022.
- [SW14] B. W. Stewart and C. P. Wild, editors. *World cancer report 2014*. World Health Organization, 2014.
- [TAKC09] B. Turkbey, P. S. Albert, K. Kurdziel, and P. L. Choyke. Imaging Localized Prostate Cancer: Current Approaches and New Developments. *American Journal of Roentgenology*, 192(6):1471–1480, 2009.
- [TBB<sup>+</sup>99] P. S. Tofts, G. Brix, D. L. Buckley, J. L. Evelhoch, E. Henderson, M. V. Knopp, H. B. W. Larsson, T.-Y. Lee, N. A. Mayr, G. J. M. Parker, R. E. Port, J. Taylor, and R. M. Weisskoff. Estimating Kinetic Parameters from Dynamic Contrast-Enhanced T1-Weighted MRI of a Diffusible Tracer: Standardized Quantities and Symbols. *Journal of Magnetic Resonance Imaging*, 10(3):223–232, 1999.
- [THM<sup>+</sup>13] J. Thariat, J.-M. Hannoun-Levi, A. S. Myint, T. Vuong, and J.-P. Gérard. Past, Present, and Future of Radiotherapy for the Benefit of Patients. *Nature Reviews Clinical Oncology*, 10(1):52–60, 2013.
- [TIP05] C. Tietjen, T. Isenberg, and B. Preim. Combining Silhouettes, Surface, and Volume Rendering for Surgery Education and Planning. In *Proceedings of Eurographics / IEEE VGTC Symposium on Visualization*, pages 303–310, 2005.
- [TM04] M. Tory and T. Möller. Human Factors in Visualization Research. *IEEE Transactions on Visualization and Computer Graphics*, 10(1):72–84, 2004.



- [TMY<sup>+</sup>06] R. Timmerman, R. McGarry, C. Yiannoutsos, L. Papiez, K. Tudor, J. DeLuca, M. Ewing, R. Abdulrahman, C. DesRosiers, M. Williams, and J. Fletcher. Excessive Toxicity When Treating Central Tumors in a Phase II Study of Stereotactic Body Radiation Therapy for Medically Inoperable Early-Stage Lung Cancer. *Journal of Clinical Oncology*, 24(30):4833–4839, Sep 2006.
- [TOG06] K. Tanderup, D. R. Olsen, and C. Grau. Dose Painting: Art or Science? *Radiotherapy and Oncology*, 79(3):245–248, 2006.
- [TTA13] D. Tilly, N. Tilly, and A. Ahnesjö. Dose mapping sensitivity to deformable registration uncertainties in fractionated radiotherapy – applied to prostate proton treatments. *BMC medical physics*, 13(2):1–12, 2013.
- [TUDB12] A. Trofimov, J. Unkelbach, T. F. DeLaney, and T. Bortfeld. Visualization of a variety of possible dosimetric outcomes in radiation therapy using dose-volume histogram bands. *Practical Radiation Oncology*, 2(3):164–171, 2012.
- [VBS<sup>+</sup>12] T. Vik, D. Bystrov, N. Schadewaldt, H. Schulz, and J. Peters. A new method for robust organ positioning in CT images. In *IEEE International Symposium on Biomedical Imaging*, pages 338–341, 2012.
- [VEB10] N. X. Vinh, J. Epps, and J. Bailey. Information theoretic measures for clusterings comparison: Variants, properties, normalization and correction for chance. *Journal of Machine Learning Research (JMLR)*, 11:2837–2854, 2010.
- [vH04] M. van Herk. Errors and margins in radiotherapy. *Seminars in Radiation Oncology*, 14(1):52–64, 2004.
- [vHRL02] M. van Herk, P. Remeijer, and J. V. Lebesque. Inclusion of geometric uncertainties in treatment plan evaluation. *International Journal of Radiation Oncology\*Biophysics*, 52(5):1407–1422, 2002.
- [VKKH13] R. Varadhan, G. Karangelis, K. Krishnan, and S. Hui. A framework for deformable image registration validation in radiotherapy clinical applications. *Journal of Applied Clinical Medical Physics*, 14(1):4066, 2013.
- [VLM<sup>+</sup>15] C. Veiga, A. M. Lourenço, S. Mouinuddin, M. van Herk, M. Modat, S. Ourselin, G. Royle, and J. R. McClelland. Toward adaptive radiotherapy for head and neck patients: Uncertainties in dose warping due to the choice of deformable registration algorithm. *Medical Physics*, 42(2):760–769, Feb 2015.
- [VMK<sup>+</sup>16] M. A. Viergever, J. B. A. Maintz, S. Klein, K. Murphy, M. Staring, and J. P. W. Pluim. A survey of medical image registration – under review. *Medical Image Analysis*, 33:140–144, 2016.

- [VPPA08] T. Vercauteren, X. Pennec, A. Perchant, and N. Ayache. Symmetric log-domain diffeomorphic registration: A demons-based approach. In *Medical Image Computing and Computer-Assisted Intervention*, pages 754–761. Springer, 2008.
- [VTM<sup>+</sup>12] S. Verma, B. Turkbey, N. Muradyan, A. Rajesh, F. Cornud, M. A. Haider, P. L. Choyke, and M. Harisinghani. Overview of Dynamic Contrast-Enhanced MRI in Prostate Cancer Diagnosis and Management. *American Journal of Roentgenology*, 198(6):1277–1288, 2012.
- [WBWK00] M. Q. Wang Baldonado, A. Woodruff, and A. Kuchinsky. Guidelines for Using Multiple Views in Information Visualization. In *Advanced Visual Interfaces*, pages 110–119. ACM, 2000.
- [Web01] S. Webb. *Intensity-Modulated Radiation Therapy*. CRC Press, Taylor & Francis, 2001.
- [WEE02] D. Weiskopf, K. Engel, and T. Ertl. Volume clipping via per-fragment operations in texture-based volume visualization. In *Proceedings of IEEE Visualization*, pages 93–100. IEEE Computer Society, 2002.
- [WL99] A. Wambersie and T. Landgerg. ICRU Report 62: Prescribing, Recording and Reporting Photon Beam Therapy. *ICRU Publ Bethesda MD*, 1999.
- [WL15] C. M. Washington and D. T. Leaver. *Principles and Practice of Radiation Therapy*. Elsevier - Health Sciences Division, 2015.
- [WLF09] C. Y. Wang, T. F. Lee, and C. H. Fang. 3D Volumetric Visualization with Automatic Rigid and Deformable Hybrid Image Registration for Adaptive Radiotherapy. *Journal of Cancer Science and Therapy*, 1:041–046, 2009.
- [WMK13] R. T. Whitaker, M. Mirzargar, and R. M. Kirby. Contour Boxplots: A Method for Characterizing Uncertainty in Feature Sets from Simulation Ensembles. *IEEE Transactions on Visualization and Computer Graphics*, 19(12):2713–2722, 2013.
- [WN93] S. Webb and A. E. Nahum. A Model for Calculating Tumour Control Probability in Radiotherapy Including the Effects of Inhomogeneous Distributions of Dose and Clonogenic Cell Density. *Physics in Medicine & Biology*, 38(6):653–666, 1993.
- [WN12] C. Wachinger and N. Navab. Entropy and Laplacian images: Structural representations for multi-modal registration. *Medical Image Analysis*, 16(1):1–17, 2012.
- [Wor18] World Health Organization (WHO). Cancer Fact Sheets. <https://www.who.int/news-room/fact-sheets/detail/cancer>, 2018. Accessed on 12 September 2018.

- [WRH<sup>+</sup>08] P. Wright, A. T. Redpath, M. Høyer, C. Grau, and L. P. Muren. The Normal Tissue Sparing Potential of Adaptive Strategies in Radiotherapy of Bladder Cancer. *Acta Oncologica*, 47(7):1382–1389, 2008.
- [WRS<sup>+</sup>09] B. Wu, F. Ricchetti, G. Sanguineti, M. Kazhdan, P. Simari, M. Chuang, R. Taylor, R. Jacques, and T. McNutt. Patient geometry-driven information retrieval for IMRT treatment plan quality control. *Medical Physics*, 36(12):5497–5505, 2009.
- [WSS<sup>+</sup>06] J. W. H. Wolthaus, C. Schneider, J.-J. Sonke, M. van Herk, J. S. A. Belderbos, M. M. G. Rossi, J. V. Lebesque, and E. M. F. Damen. Mid-ventilation CT scan construction from four-dimensional respiration-correlated CT scans for radiotherapy planning of lung cancer patients. *International Journal of Radiation Oncology\*Biolog\*Physics*, 65(5):1560–1571, 2006.
- [WSvD08] J. W. H. Wolthaus, J. J. Sonke, M. van Herk, and E. M. F. Damen. Reconstruction of a time-averaged midposition CT scan for radiotherapy planning of lung cancer patients using deformable registration. *Medical Physics*, 35(9):3998–4011, Sep 2008.
- [WWW<sup>+</sup>04] I. Wolf, M. Vetter, I. Wegner, M. Nolden, T. Böttger, M. Hastenteufel, M. Schöbinger, T. Kunert, and H.-P. Meinzer. The medical imaging interaction toolkit (MITK): a toolkit facilitating the creation of interactive software by extending VTK and ITK. In *Medical Imaging 2004: Visualization, Image-Guided Procedures, and Display*, volume 5367, pages 16–27. International Society for Optics and Photonics, 2004.
- [WWW<sup>+</sup>05] I. Wolf, M. Vetter, I. Wegner, T. Böttger, M. Nolden, M. Schöbinger, M. Hastenteufel, T. Kunert, and H.-P. Meinzer. The Medical Imaging Interaction Toolkit. *Medical Image Analysis*, 9(6):594–604, 2005.
- [WZHZ19] C. Wang, X. Zhu, J. C. Hong, and D. Zheng. Artificial Intelligence in Radiotherapy Treatment Planning: Present and Future. *Technology in Cancer Research & Treatment*, 18:1–11, Jan 2019.
- [Yan06] D. Yan. Image-Guided/Adaptive Radiotherapy. In *New Technologies in Radiation Oncology*, pages 321–336. Springer-Verlag, 2006.
- [YBN<sup>+</sup>11] D. Yang, S. Brame, I. E. Naqa, A. Aditya, Y. Wu, S. M. Goddu, S. Mutic, J. O. Deasy, and D. A. Low. Technical Note: DIRART – A software suite for deformable image registration and adaptive radiotherapy research. *Medical Physics*, 38(1):67, 2011.
- [YLL<sup>+</sup>08] D. Yang, H. Li, D. A. Low, J. O. Deasy, and I. E. Naqa. A fast inverse consistent deformable image registration method based on symmetric optical flow computation. *Physics in Medicine & Biology*, 53(21):6143–6165, Oct 2008.

- [ZBL<sup>+</sup>19] M. Ziegler, T. Brandt, S. Lettmaier, R. Fietkau, and C. Bert. Method for a motion model based automated 4D dose calculation. *Physics in Medicine & Biology*, 64(22):225002, Nov 2019.
- [ZCM13] L. Zheng, C. Correa, and K.-L. Ma. Visibility guided multimodal volume visualization. In *IEEE International Conference on Bioinformatics and Biomedicine (BIBM)*, pages 297–304, 2013.
- [ZEP10] Q. Zhang, R. Eagleson, and T. M. Peters. Volume Visualization: A Technical Overview with a Focus on Medical Applications. *Journal of Digital Imaging*, 24(4):640–664, Aug 2010.
- [ZF03] B. Zitova and J. Flusser. Image Registration Methods: A Survey. *Image and Vision Computing*, 21(11):977–1000, 2003.
- [ZM16] C. Zappa and S. A. Mousa. Non-small cell lung cancer: current treatment and future advances. *Translational Lung Cancer Research*, 5(3):288–300, Jun 2016.
- [ZMBL00] E. Zindy, C. Moore, D. Burton, and M. Lalor. Morphological Definition of Anatomic Shapes Using Minimal Datasets. In *IEEE Conference on Information Visualization*, pages 366–370, 2000.
- [ZMN15] R. Zhang, D. Mirkovic, and W. D. Newhauser. Visualization of Risk of Radiogenic Second Cancer in the Organs and Tissues of the Human Body. *Radiotherapy and Oncology*, 10(107):1–9, 2015.

# CURRICULUM VITAE

## Details

### Matthias Schlachter

**Address:** currently living in Wako, Japan

**Email:** matthias.schlachter@riken.jp

## Employment & Research History

03/2022 – present	Researcher <i>RIKEN, Center for Brain Science, Brain Image Analysis Unit, Japan</i>
02/2017 – 02/2022	Software Engineer, Speech Recognition <i>Recognosco GmbH, Austria</i>
02/2017 – present	PhD Student <i>VRVis Research Center, Austria</i>
01/2013 – 01/2017	Researcher / PhD Student (since 10/2014) <i>VRVis Research Center, Austria</i>
06/2011 – 04/2012	Software Engineer <i>Telstra Corporation Ltd, Australia</i>
10/2010 – 03/2011	Voluntary Work <i>Private school in Laos PDR (tadlo.net)</i>
05/2009 – 09/2010	Research Assistant <i>Chair of Image Processing and Pattern Recognition, University of Freiburg, Germany</i>
05/2007 – 08/2008	Research Assistant (Undergraduate) <i>Chair of Image Processing and Pattern Recognition, University of Freiburg, Germany</i>

## Education

10/2014 – present	Doctoral program in Engineering and Computer Sciences <i>TU Wien, Austria</i>
04/2009	Computer Science German Diplom (Master's Degree equivalent) <i>University of Freiburg, Germany</i> Minors: Mathematics

## Work Experience

Recognosco, Austria	<ul style="list-style-type: none"><li>• Part of development team for Speech recognition software</li><li>• Key working areas: automatic model adaptation with user provided pronunciations of words</li></ul>
---------------------	---

- VRVis, Austria
- Part of an interdisciplinary research project called SUMMER (Software for the Use of Multi-Modality images in External Radiotherapy)
  - Research with a focus on multi-modal volume visualization and its applications in radiotherapy planning
  - Specific projects: 4D-PET/CT visualization and quality assessment of deformable image registration
  - Development of a multi-modal rendering framework using GPU acceleration techniques
  - Integration of the rendering framework in a shared platform including developing user interfaces and interaction techniques
- Telstra, Australia
- Engineered a large-scale monitoring cluster for data analysis and reporting based on application server metrics and network devices
  - Multi agent system for data collection and online and offline data evaluation
  - Web frontend for visualizing / graphing of collected / evaluated data
- University of Freiburg, Germany
- Contribution to interdisciplinary research projects
  - Projects: Automated 3D cell detection, 3D segmentation, quantitative analysis of biomedical images
  - Development of algorithms and software systems for image processing and pattern recognition
  - Development of data visualization applications for 3D microscopic data and miscellaneous libraries for reading and writing large data sets

## Academic Experience

- Summer Term 2010      Teaching Assistant, *Prof. Dr. Hans Burkhardt*  
Seminar: “Algorithms for Cluster Analysis”
- Winter Term 2009/10      Teaching Assistant, *Prof. Dr. Hans Burkhardt*
- Lecture Assistance: “Fundamentals of Pattern Recognition”
  - Proseminar: “Image Processing Toolbox with ImageJ”
  - Lab Course on Image Processing
- Winter Term 2006/07      Teaching Assistant, *Prof. Dr. Hans Burkhardt*  
Tutor for Lecture: “Foundations of Image Formation and Picture Analysis – Pattern Recognition”

## Publications

### Peer Reviewed Journals as 1<sup>st</sup> Author

[1] **Schlachter, M.**, Reisert, M., Herz, C., Schlurmann, F., Lassmann, S., Werner, M., Burkhardt, H. and Ronneberger, O.

“Harmonic Filters for 3D Multichannel Data: Rotation Invariant Detection of Mitoses in Colorectal Cancer”

IEEE Transactions on Medical Imaging, Institute of Electrical and Electronics Engineers (IEEE), 2010, Vol. 29(8), pp. 1485-1495

DOI:10.1109/tmi.2010.2049856 [[PDF](#)]

[2] **Schlachter, M.**, Fechter, T., Jurisic, M., Schimek-Jasch, T., Oehlke, O., Adebahr, S., Birkfellner, W., Nestle, U. and Bühler, K.

“Visualization of Deformable Image Registration Quality Using Local Image Dissimilarity”

IEEE Transactions on Medical Imaging, 2016, Vol. 35(10), pp. 2319-2328

DOI:10.1109/TMI.2016.2560942

[3] **Schlachter, M.**, Fechter, T., Adebahr, S., Schimek-Jasch, T., Nestle, U. and Bühler, K.

“Visualization of 4D multimodal imaging data and its applications in radiotherapy planning”

Journal of Applied Clinical Medical Physics, Wiley-Blackwell, 2017, Vol. 18(6), pp. 183-193

DOI:10.1002/acm2.12209

[4] **Schlachter, M.**, Raidou, R. G., Muren, L. P., Preim, B., Putora, P. M. and Bühler, K.

“State-of-the-Art Report: Visual Computing in Radiation Therapy Planning”

Computer Graphics Forum, Wiley, 2019, Vol. 38(3), pp. 753-779

DOI:10.1111/cgf.13726

[5] **Schlachter, M.**, Preim, B., Bühler, K. and Raidou, R. G.

“Principles of Visualization in Radiation Oncology”

Oncology, Karger Publishers, 2020, Vol. 98(6), pp. 412–422

DOI:10.1159/000504940

#### Peer Reviewed Journals as Co-Author

[6] Fechter, T., Dolz, J., Chirindel, A., **Schlachter, M.**, Carles, M., Adebahr, S., Mix, M. and Nestle, U.

“Fully Automatic Danger Zone Determination for SBRT in NSCLC”

Journal of Radiation Oncology Informatics, 2015, Vol. 7(1), pp. 1-27

DOI:10.5166/jroi-7-1-26

#### Peer Reviewed Conferences/Workshops as 1<sup>st</sup> Author

[7] **Schlachter, M.**, Fechter, T., Nestle, U. and Bühler, K.

“Visualization of 4D-PET/CT, Target Volumes and Dose Distribution: Applications in Radiotherapy Planning“

Proc. of MICCAI Workshop on Image-Guided Adaptive Radiation Therapy

The MIDAS Journal, 2014

DOI:10.54294/lgcmkl

#### Peer Reviewed Conferences/Workshops as Co-Author

[8] Nunes, M., Rowland, B., **Schlachter, M.**, Ken, S., Matkovic, K., Laprie, A. and Bühler, K.

“An integrated visual analysis system for fusing MR spectroscopy and multi-modal radiology imaging“

IEEE Conference on Visual Analytics Science and Technology (VAST), 2014, pp. 53-62  
DOI:10.1109/vast.2014.7042481

### Abstract with Poster

[9] **Schlachter, M.**, Fechter, T., Bühler, K. and Nestle, U.  
“EP-1711: Fast visual quality inspection of 4D PET/CT contouring of manual and semi-automatic contours”  
ESTRO 33, Radiotherapy and Oncology, Elsevier BV, 2014, Vol. 111, pp. S251-S252  
DOI:10.1016/s0167-8140(15)31829-6

### Non Peer Reviewed Articles as 1<sup>st</sup> Author

[10] **Schlachter, M.**, Peters, S., Camenisch, D., Putora, P. M. and Bühler, K.  
“Exploration of Overlap Volumes for Radiotherapy Plan Evaluation with the Aim of Healthy Tissue Sparing”  
arXiv, 2021  
<https://arxiv.org/abs/2112.12590>

### Diploma Thesis

**Schlachter, M.** , “Detection and Classification of Mitosis Cells in 3D Tissue Samples of Colorectal Cancer”,  
University of Freiburg, Germany [[PDF](#)]

### Skills

Programming Languages	C++, CUDA, Python, LaTeX, BASH, Java, Matlab, Mathematica
Frameworks, Tool & Libraries	Qt, CUDA, VTK, ITK, MITK, OpenGL, boost, OpenMP, GSL, BLAS, fftw, HDF5, NetCDF, ImageJ, D3, JSON, JUnit, Spring, Hadoop, Hbase, Pig, JSP/Servlets, EJB, RMI, DataNucleus, XML, gcc, gdb, valgrind, autotools, cmake, ant, maven, svn, git
Operating Systems	Linux, Mac OS, Windows, Solaris
Languages	English (fluent), German (Native Tongue)

Date: August 2022